The development of a 3D-printed multi-tissue chip and tubing-free impeller pump to model communication with the lymph node

Sophie Reed Cook

Portland, Oregon

B.A. Chemistry, Bethany College, 2018

A Dissertation presented to the Graduate Faculty of the University of Virginia in Candidacy for the Degree of Doctor of Philosophy

Department of Chemistry

University of Virginia

November, 2023

Abstract

Multi-organs-on-chip (MOOC) technology provides a method to model inter-organ communication. These devices fluidically connect two or more tissue models within a microfluidic chip to enable molecular cross-talk. However, there is an unmet need within the field to build immune-competent MOOCs and, in particular, include immune organs such as the lymph node (LN). This dissertation describes the development of a 3D-printed multi-tissue chip and tubing-free impeller pump to model communication with the LN in the context of inflammation and disease. **Chapter 2** explores the development of the impeller pump, a novel pumping system that generated recirculating fluid flow without the use of tubing. **Chapter 3** focuses on the optimization of resin composition and post-treatment to improve biocompatibility with sensitive immune cells. In **Chapter 4**, a 3D-printed multi-tissue chip for murine LN slice culture and a companion motor-based impeller pump was established and used to model a vaccine injection in the skin draining to a local lymph node. **Chapter 5** describes a 3D-printed multi-media multi-tissue chip designed to support human 2D and 3D cell culture models in commercially available transwells to model brain-immune interactions in the context of neuroinflammation and neurodegeneration. In the future, the impeller pump and multi-tissue chip described here can be used to model complex phenomena such as neurodegeneration, autoimmunity, tumor immunity, and vaccination.

This dissertation is dedicated in memory to my mother, who taught me how to be creative, how to love fiercely, and to “go with the flow”.

Acknowledgements

First, I would like to thank Dr. Rebecca Pompano, my advisor. The excitement you have for the work that we do has always inspired me, and it continues to drive my own excitement for my research from the past 5 years. You gave me a lot of freedom in the lab to be creative in many aspects of my research, and have supported me both in and out of the lab. You have challenged me to be a better writer, critical thinker, leader, and overall scientist. Thank you for making a welcoming and accessible space for me in your lab.

Thank you to my lab mates – both current and past! You all helped me challenge myself, shaped a highly collaborative workplace, and made so many days in the lab a blast. I would like to thank Meg for training and support when I first started graduate school, Jenn for being a great friend and having fun fireplace movie nights (with Max, too!) pre-shutdown, Hannah for constant chats, 3D-printing struggles, and game nights, and Djuro for getting into lab shenanigans, going for coffee, and being my tinkering buddy.

I would also like to thank Dr. Loranelle Lockyear and Dr. Luke McCormick, two chemistry professors from undergrad. Dr. Lockyear – your class in my freshmen year inspired me to pursue chemistry, and your mentorship and support throughout my tumultuous undergraduate career helped me to be where I am today. You introduced me to research and microfluidics, and I haven't looked back since! Dr. McCormick – the way you teach your classes and explain complex ideas inspires me to be a better mentor and teacher, and I will always appreciate your dry humor in and out of class. For both of you – I will always cherish stopping by both of your offices to chat between classes, and will never forget your guidance.

I want to thank my friends that have been there for me over the past few years, whether in person or virtually. Evyn – virtual game nights with you over the past few years has been a well-

needed break, and I will always love catching up over a game of Catan. Francesca – I always had so much fun losing hours talking to you about a million different things, and I am so grateful you were stuck with Mer and I during the beginning years of the pandemic. Katie – you made my last year of undergrad actually good, and I am so glad we randomly facetime to gush about books/tv shows/music/etc. like no time has passed. I also want to shout out some of my Charlottesville friends (you know who you are!) I have met through the queerish community – meeting you all has been one of the highlights of this year!

I'd like to thank Carol – my best ride, my (occasionally useless) moped. Even though you break down at the most inconvenient times (like the day before my candidacy exam), you were the best wheels I could have asked for, even in the rain. For other inanimate objects, I would like to thank the coffee shops of the Charlottesville area – I have done amazing work because of you!

Next, I want to thank my family. Glenn and Vicky – it has been wonderful getting to know you both over the past 5 years, and I love getting all of your questions about my research. Tracy – I love seeing the way that you support my Dad and the joy you both bring to each other, and I really appreciate your support through everything. Dad – you taught me how to be brave and confident no matter what. I owe my self-taught engineering skills to you and the space you gave me to build and tinker with you growing up. Grandma – I have cherished our phone calls during the past 5 years of this program, and I will always appreciate your support, excitement, and curious questions about my research. Syd – you are absolutely the best sister ever. Your fierce loyalty and die-hard support can be felt from states away, and you helped me speak up for myself and to be bold.

Finally, I would like to thank my fiancé, Meredith. I don't think I would have made it through these past few years without your love and support. Thank you for reading and editing

so much of my science writing even though it is a bit over your head. You are always making me laugh, and you are truly the most amazing person I have ever met. I am so extremely lucky to have found you a little over five years ago, and I can't wait to spend the rest of my life with you.

Table of Contents

List of Figures

List of Tables

List of Equations

Chapter 1. Introduction to multi-organs-on-chip

1.1 Inter-organ communication *in vivo*

Homeostasis is critical for proper function in living organisms and is maintained by a network of organs in constant communication. The idea of balance in the body is not a new concept; health was once viewed to be a result of a balance of the four "humors", or the dominant fluids in the body, a concept dating back to Hippocrates in the 5th century BCE.[1] In 1855, Claude Bernard described the first instance of cell signaling via molecular release, where he noted that molecules released into the bloodstream from a gland had an effect on downstream cells.[2] Since then, our understanding of inter-organ communication has increased exponentially with the identification of countless soluble factors and corresponding signaling mechanisms. However, there are still many unexplained phenomena due to the sheer number of tissues releasing molecules simultaneously in an ever-changing system.

As a result of the intricacy of the communication network, tissues can quickly respond to changes in the organ microenvironment. For example, the resident immune cells present in the skin or muscle get activated in the instance of a vaccine injection and drain to local lymph nodes to initiate an immune response.[3] Along with each individual organ's specific function, there is an elaborate system of checks and balances mediated through inter-organ communication to maintain a properly functioning system. In instances of disease and inflammation, these systems have begun to break down or fail altogether.

1.1.1 Messages

Messages between tissues can take many forms. In response to mechanical, electrical, or chemical stimulation, cells will secrete bioactive molecules such as cytokines, neurotransmitters, hormones, and metabolites that can enter the blood or lymphatic vasculature to reach

downstream tissues (Figure 1.1i).[2] In addition to molecules released directly into the extracellular matrix, cells form and release extracellular vesicles (EVs) containing signals such as genetic material, lipids, and proteins within a lipid membrane capsule (Figure 1.1ii).[4,5] For example, adipose tissue releases microRNA-filled vesicles that travel to the liver to help improve glucose tolerance.[6] Cells can also recirculate *in vivo* to carry messages between tissues (Figure 1.1iii). With the immune system specifically, immune cell trafficking throughout the body mediates the transfer of signals either related to damage (i.e. damage-associated molecular patterns, or DAMPs) or pathogens (i.e. pathogen-associated molecular patterns, or PAMPs).[7,8] Some examples of this system include the recruitment of immune cells to a site of infection or the infiltration of immune cells into the brain in instances of inflammation.[7,9]

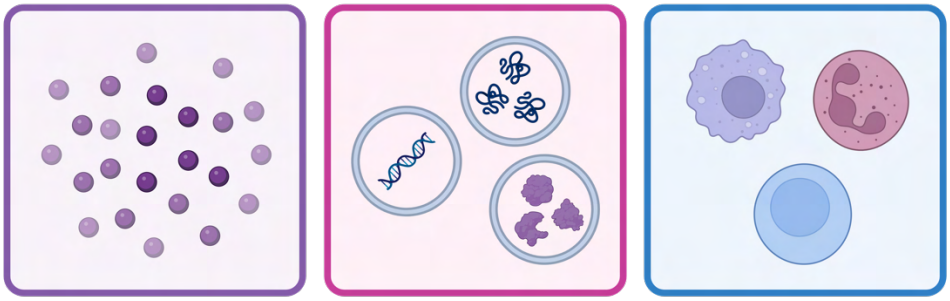

Figure 1.1 Inter-organ messages. *Types of signals include (i) bioactive molecules, (ii) extracellular vesicles, and (iii) cells (Created using BioRender.com).*

1.1.2 Methods of message delivery in the body

The primary route of message delivery *in vivo* is through blood and lymphatic vasculature, similar to a complex highway system (Figure 1.2). Here, the pathway from the skin to a local lymph node (LN) will be explored as an example. The blood capillaries that have vascularized the skin deliver soluble factors into the interstitial fluid that flows slowly through the tissue. The interstitial fluid will pick up messages secreted by the skin, as well as cellular waste, before draining to lymphatic capillaries (Figure 1.2i). Once in the lymph fluid, the

messages and other molecules drain to a nearby LN to be filtered before returning to blood vessels (Figure 1.2ii).

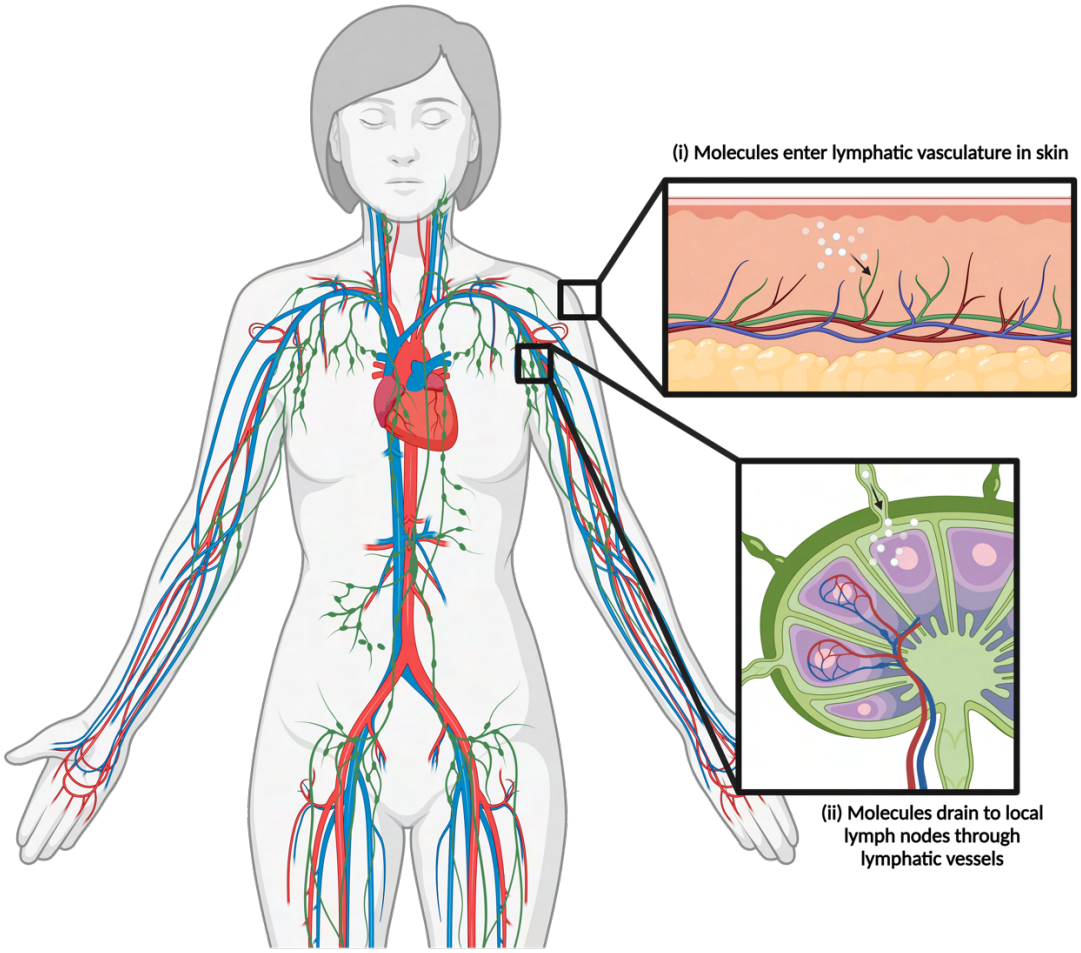

Figure 1.2 Route of message delivery. *(i) Signals from the skin are carried to lymphatic vessels through interstitial fluid flow. (ii) The signals drain to local lymph nodes through lymphatic vasculature (Created using BioRender.com).*

With specific organs, the signaling pathway can follow unique routes. Since the central nervous system (CNS) is immune privileged, thus fluidically isolated via cellular barriers from the rest of the body, the secreted factors from the brain must first enter the meninges to reach the meningeal lymphatics before draining to deep cervical lymph nodes.

1.1.3 Current methods to study inter-organ communication and associated challenges

With the advancement of technology over the last few decades, researchers have developed integral tools to study how organs transmit signals throughout a living organism. The most common way to study inter-organ communication is through the use of animal models (e.g. mice). These animals have been used to test the *in vivo* response to perturbation through the injection of a pathogen or vaccine.[10–12] In addition, it is possible to mimic specific diseases in animal models, typically by injecting inflammatory agents, specific proteins, or even tumor cells.[13–15] For example, CNS antigens are injected in mice to generate experimental autoimmune encephalitis (EAE), which resembles certain features of multiple sclerosis (MS).[16] In 1989, the first knockout mice were created in the lab, which later won researchers a Nobel prize in 2007.[17] This method could target specific genes to remove them, termed "knockout", to better understand that specific gene's role in different biological functions.[18] Similar to knockout animal lines, transgenic animals are genetically modified by incorporating foreign genes to illicit specific change (e.g. increased production of a targeted protein).[19,20]

In addition to high cost and ethical concerns, there are three major limitations with animal models. First, it can be challenging to isolate the signals sent between specific organs due to the magnitude and variety of signals from other organs present *in vivo.* Second, while animal models of diseases can recapitulate certain disease features, they often fall short of the real thing.[15] This is primarily due to the fact that researchers are inducing common disease features in a known method, whereas the origins of many human diseases are unknown. Finally, the established models are in animals, and the results do not directly translate to human physiology. In addition, therapeutics approved through animal-based preclinical trials routinely fail to accurately predict drug efficacy.[21,22]

1.2 Multi-organs-on-chip as a method to model communication between tissues

Multi-organs-on-chip (MOOC) were established as an intermediary between the simple 2D cell culture in a dish and the full complexity found in animal models.[23] By fluidically connecting multiple tissue culture models in tandem, the communication between different organs *in vivo* can be further studied under physiological and pathological conditions (Figure 1.3).

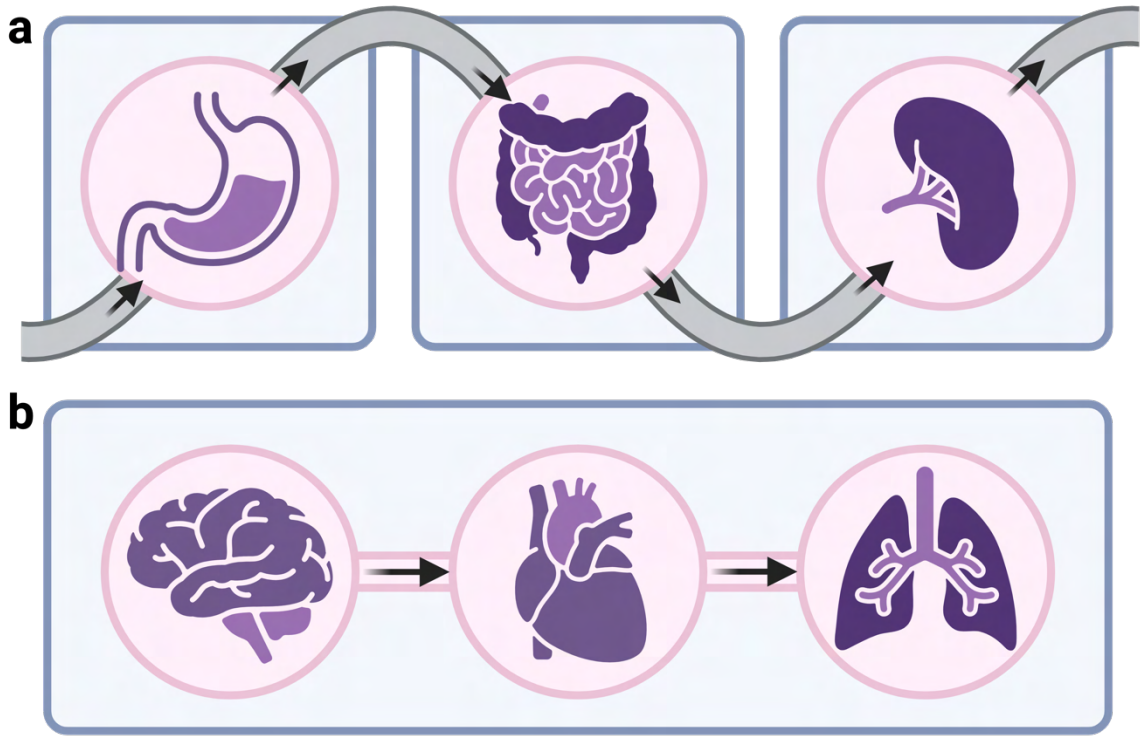

Figure 1.3 Model inter-organ communication using multi-organs-on-chip (MOOC) technology. *Researchers can connect (a) single-organ chips using tubing in a "daisy-chain" or (b) build a single device with multiple tissue compartments (Created using BioRender.com).*

1.2.1 Brief history of organs-on-chip technology

The origin of microfluidic technology dates back to 1993 with a glass device developed for capillary electrophoresis.[24] In the early 2000s, researchers adapted this technology to generate organs-on-chip (OOC), where functional units of various organs were developed in microchannel-based devices.[25] A breathing lung-on-a-chip that cultured endothelial and epithelial cells on a membrane suspended in a chamber bordered by two air channels is

commonly credited as the first OOC model.[26] When researchers applied a vacuum to the side channels, the mechanical strain across the membrane mimicked a breathing lung.

1.2.2 Methods to culture multiple organ models

Single tissue OOCs can be expanded to co-culture multiple tissue models in instances where communication between multiple tissues is integral, such as the modelling of a disease that involves more than one tissue *in vivo*. There are multiple different ways to culture multiple organ models within a microfluidic system. Some labs will make the jump from single tissue chips to multi-tissue culture by connecting multiple different OOCs via tubing in a "daisy-chain" to enable inter-organ crosstalk (Figure 1.3a).[23] Alternatively, labs can develop a multi-compartment device to culture multiple different tissues within the same device, which cuts down on chip size and complexity (Figure 1.3b). Within the field of multi-compartment devices, there are configurable body-on-chip (BOC) systems that enable user customization. These systems allow users to plug any needed tissue model into an established chip and include multiple fluid circuits of different media types.[23,25,27,28]

1.2.3 State of the field and current limitations

Many multi-organ platforms have been developed for disease modeling and drug testing.[29] As therapeutics are traditionally metabolized in the liver, multiple MOOCs have coupled liver cells and organoids with various organ models, like intestine and heart, to test therapeutic effects under a multitude of conditions.[28,30–41] Others are coupling tissue models with related tumor models to gain a better understanding of the tumor microenvironment, metastasis, and response to novel immunotherapies.[30,32,42–45] Some researchers are creating a model of a specific system found *in vivo* traditionally comprised of multiple types of tissue, such as the female reproductive tract[46] or an arthritic joint.[47]

In the future, researchers aim to move away from animal models and utilize human-based MOOCs for robust drug testing and disease modelling. However, these devices are currently unable to replace animal models and remain a complementary tool.[23] There are two major challenges still present that limit device biomimicry: scaling and medium composition.[23] Current approaches for scaling MOOCs range from allometric scaling, where each modeled organ and fluidic connection has a size relative to other MOOC components that correlates to the human body, to functional scaling, where the devices are designed to reproduce specific organ functions found *in vivo*.[48] This will prove to be a critical feature within the organs-on-chip field as size or modeled function may significantly impact the MOOC's ability to accurately model specific diseases or respond to a drug, though there is no consensus on the best method for OOC or MOOC scaling. Some *in vivo* functions such as fluid flow and shear stress are needed for chip biomimicry and remain challenging for a multi-tissue system as it may be difficult to incorporate the different fluid flow speeds or shear stresses needed within each organ compartment on-chip and where many *in vivo* values are still unknown (e.g. interstitial fluid velocity within the lymph node). In addition, there is no standardized blood substitute that supports all modeled organs, so each chip requires media optimization to find a common medium or media compartmentalization with communication across a barrier, which increases device complexity.

Alongside biomimicry, these devices need to be able to be used in clinical laboratories by biological researchers (i.e. labs without trained microfluidics personnel). Current device design, fabrication, and operation is not standardized within the field, where each lab is essentially required to set up the MOOCs themselves. This limitation hinders translation from the lab that developed the technology to outside labs, especially clinical laboratories with biology-focused researchers.[49]

1.3 Key features when designing a biomimetic MOOC

When building a MOOC, there are several key device features to consider to generate a platform that mimics the physiology and pathology found *in vivo*. These features include 1) on-chip pumping; 2) chip fabrication; 3) readouts; 4) organ models; and 5) barriers and compartmentalization (Figure 1.4).

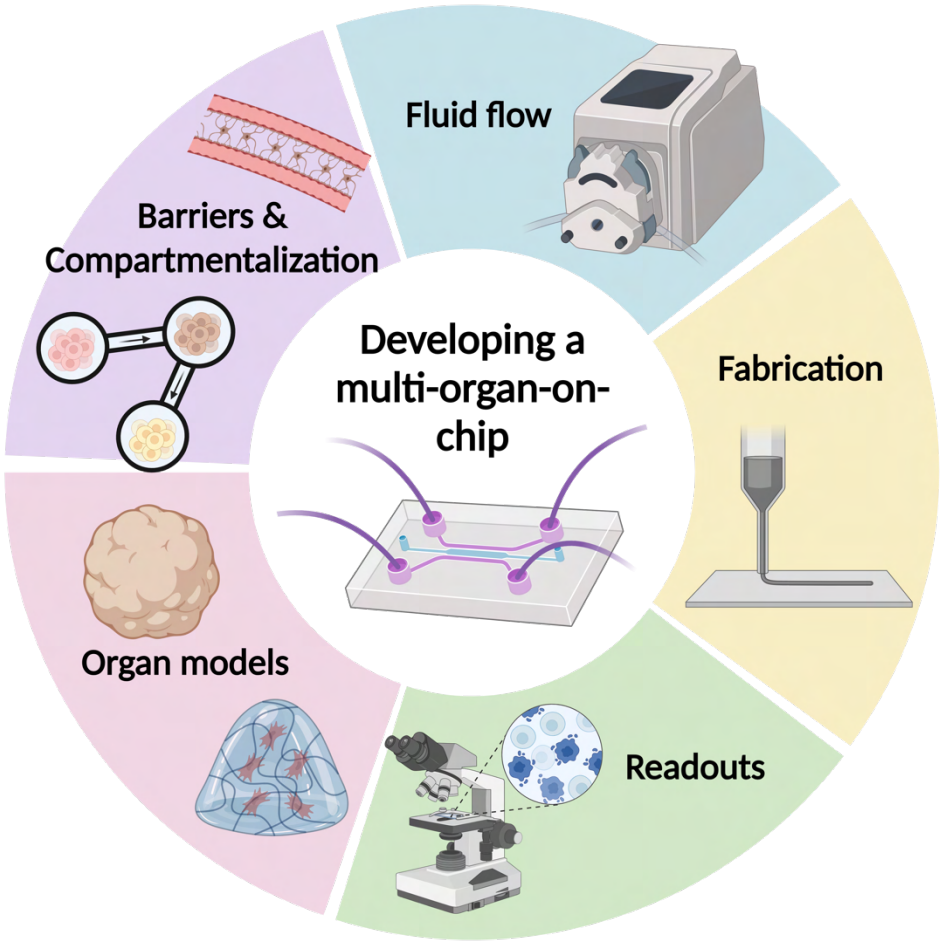

Figure 1.4 Key features to consider when designing a MOOC. *These include fluid flow, fabrication, readouts, organ models, and barriers and compartmentalization (Created using BioRender.com).*

1.3.1 Connecting tissue models using fluid flow

Fluid flow on-chip is responsible for connecting tissue models to enable inter-organ communication. Within the field of microfluidic pumping, there are two categories of pumps: 1)

passive and 2) active. Passive pump methods, such as gravity-driven flow, do not require an external actuator or power source to drive fluid flow on-chip. However, the nature of this pump method can limit the amount of user control over fluid flow speeds.[50,51] Active pumps require an external power source to drive fluid flow and range from external pumps such as syringe and peristaltic pumps,[45,52] to integrated (i.e. on-chip) pumps such as pneumatic and rotating impeller pumps.[30,32,35,53]

Using these pumping methods, MOOCs have utilized either a unidirectional flow path (i.e. flow from liver to lungs) or a recirculating flow path (i.e. flow from liver to lungs and back to liver, etc.) (Figure 1.5). Unidirectional flow typically requires fewer complex pumps (e.g. syringe pump or peristaltic pump) pushing fluid in one direction, but can be experimentally limited, where the user can only observe the upstream organ's effect on the downstream organ and not vice versa (Figure 1.5a). Recirculating flow tends to be more representative of inter-organ communication *in vivo* because complex feedback loops often occur between tissues, but this method is more technically challenging compared to unidirectional flow and typically requires in-line pumping connected to a closed loop of channels (Figure 1.5b). In addition, recirculating fluid flow makes it challenging to determine the tissue of origin due to constant recirculation, though this signal mixing lends more biomimicry. Gravity-driven flow is capable of achieving both unidirectional and recirculating fluid flow depending on the device geometry.

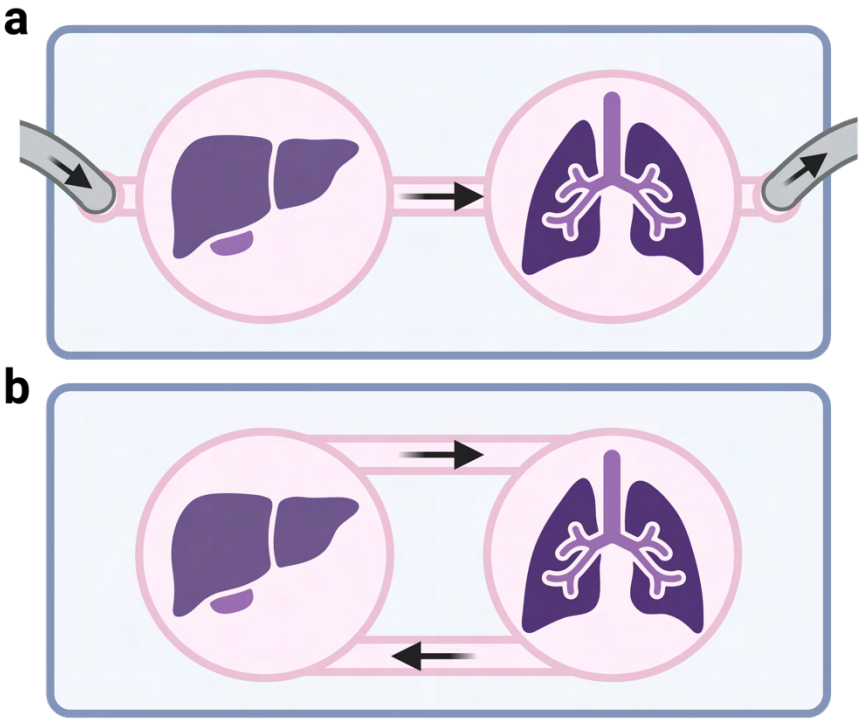

Figure 1.5 MOOC flow paths*. Common flow paths on-chip include (a) unidirectional fluid flow and (b) recirculating fluid flow (Created using BioRender.com).*

In addition to carrying messages to downstream tissues, MOOCs have employed different fluidic modes and speeds to mimic environments found *in vivo*.[54] OOCs can incorporate a pulsatile flow mode similar to blood and lymph flow patterns as well as precise and controllable flow speeds on the µm/s range (0.1-1 µm/s for interstitial flow, 1-20 µm/s in superficial lymphatics, and 10-100 µm/s in blood vessel capillaries)[55–57] to the cm/s range (0.1-2 cm/s in mesenteric lymphatics, 1.5-7.1 cm/s in veins, and 50-100 cm/s in arteries).[58–62] The ideal fluid mode, speed, and pump method can vary depending on the modeled system and the features found *in vivo* that are critical to include.

1.3.2 Device fabrication materials and methods

When selecting a fabrication technique and material, there is no perfect option that works for every single device. It is critical at early stages of device development to have a clear idea of the requirements for the device architecture and use to help select the best fabrication pathway.

The materials and fabrication methods are heavily linked, so depending on the needs of the researcher or the device, either the material or the fabrication method can be selected first.

One of the most common materials for OOCs and MOOCs is polydimethylsiloxane (PDMS), an inert rubber-like material that is fabricated using soft lithography. To fabricate PDMS chips, uncured PDMS is poured on to a mold patterned with photoresist where, when cured, the PDMS is peeled off leaving embossed features behind.[63] PDMS chips are cytocompatible for lengthy periods of time, are optically clear to enable imaging on-chip, and are gas-permeable to allow cell and tissue oxygenation on-chip. Within the OOC field, a major drawback has been the adsorption of small molecules such as drugs into the material, making it challenging to test novel therapeutics. In addition, the nature of the fabrication technique lends itself towards planar devices, where the channels and chambers are all within the same PDMS layer. It is certainly possible to expand these devices into multiple layers with more complex 3D geometry, but it requires skilled alignment of each individual layer and can result in decreased reproducibility and lengthy fabrication times.

Another common material used in OOC technology is thermoplastics, which are traditionally fabricated using hot embossing or injection molding. Both of these techniques utilize complex molds to shape heated plastic.[64,65] The use of these material and fabrication techniques lends itself to mass scale-up, where many of the devices can be produced with high precision and reusability. However, these biocompatible polymers are impermeable to gas and the fabrication cost is high if commercial outsourcing is necessary.

For many years, glass was the gold-standard material used within the microfluidic field. However, it is less and less common, especially within the OOC field, due to the complex fabrication methods required. The wet etching of channels and chambers into glass typically uses

hydrofluoric acid (HF), which is an incredibly hazardous chemical to work with, as well as additional techniques like thermal bonding to generate a closed chip.[66] While less common, these devices are optically clear, reproducible, and biocompatible, with no small molecule adsorption.

The final material highlighted here is photopolymers, which is commonly used in resin 3D printing. With digital light processing (DLP) 3D printing, the device is printed in sequential layers by exposing regions of liquid photopolymer to projected UV light, resulting in a monolithic device.[67] This material and fabrication technique results in fast, reproducible, and relatively low-cost devices with complex 3D architecture, albeit with limited optical clarity, that can be easily shared with collaborators. However, these materials tend to be cytotoxic due to the leaching of unbound materials left over from the fabrication process (e.g. monomers or commercial additives) and can degrade with repeated use.[67,68] In recent years, researchers have developed a method to 3D-print a polymer containing glass particles that can be sintered post-print to generate a fused-glass device.[69]

1.3.3 Readouts

Every MOOC platform has specific readouts at the end of each experiment to measure either changes in the state of the tissue (e.g. activation or drug response) or communication between tissues (e.g. immune cell infiltration from the lymph node into the brain). Common readout methods include fluorescence imaging, flow cytometry, gene expression, and in-line electrodes and sensors to study changes on a tissue-level as well as a wide variety of assays (e.g. ELISA) to analyze supernatant to identify and quantify what tissues are secreting.[70,71] These readouts are highly dependent on the specific organ models used and compatibility with the MOOC. For example, a standard readout for 3D cell culture models in a hydrogel is staining and

imaging the cells using fluorescent microscopy, but it is less common to digest the gel to retrieve cells to run flow cytometry.

In addition to experimental readouts, there are features within the device that are indirectly related, such as the scaling of the device (i.e. how the media volume or tissue model size on-chip compares to *in vivo*), the optical features of the material for imaging, and the ease of use to insert and remove the tissue samples. Another feature to consider is if the testing will be performed over time (i.e. timecourse) or if it will be at the conclusion of the experiment only (i.e. endpoint). With timecourse readouts, the tissue responses can be mapped over time to provide a more robust view of what is occurring on-chip. However, this can add a lot of complexity to the device design to enable sampling over time or easy removal/insertion of the organ model for timecourse imaging. Endpoint readouts tend to require a simpler device design, where the organ model can be used for destructive readouts such as flow cytometry, where the tissue would be crushed or digested into a cell suspension for single-cell analysis.

1.3.4 Organ models: cell and tissue structure and organization

When building a biomimetic MOOC, one of the most important parts is the organ model itself. Here, the user can decide which organ features are critical for their model and determine the best method to incorporate said features. This can be guided either by what is necessary for that specific tissue or what is relevant for the biological question the device will be used to study. Some examples of these attributes include cell type, number of different cells present, cellular organization, tissue scaffolding and geometry, chemical or fluidic environment, presence or lack of mechanical stimulation, organ function, and route of connection for inter-organ communication. Within the OOC field, there are four common methods for building an organ model. The first method is 2D cell culture, where cells are grown in a 2D monolayer, either

across a membrane or within a channel (Figure 1.6i).[26,72] The second method is 3D cell culture, where cells are suspended in a scaffolding material (hydrogel, paper, ceramic, etc.) to recreate the microenvironment surrounding cells *in vivo* (Figure 1.6ii).[73–76] The third method is developing small, self-assembled 3D cell-based structures called organoids for use on-chip (Figure 1.6iii).[36,77,78] Finally, *ex vivo* tissue slices have been cultured on-chip, where a live organ is sliced and placed directly into the device (Figure 1.6iv).[45,79–82] These methods can be coupled as well, like adding an endothelial cell monolayer along the cell-laden hydrogel[83] or adding organoids to a vascularized hydrogel.[84,85] Each of these methods can incorporate some of the attributes needed to model an organ, but no single method can fully recreate an organ.

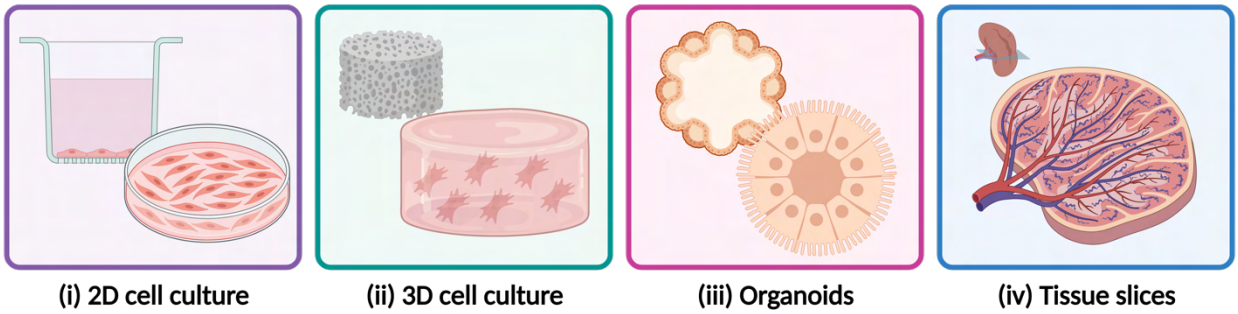

Figure 1.6 Building an organ model. *Common methods include (i) 2D cell culture, (ii) 3D cell culture, (iii) organoids, and (iv) tissue slices (Created using BioRender.com).*

For 2D cell cultures, a 2D lung-on-a-chip on a membrane recapitulated some lung functions using cell monolayers and mechanical stretching to mimic breathing, but it cannot include other features like organized multi-cell type culture, complex 3D microenvironment, and unique tissue geometry.[26,86] On the other hand, tissue slices cultured on-chip such as brain,[80] lymph node,[45,81] intestine,[79] and tumor slices[82] retain cell diversity and organization as well as the geometry and scaffolding in the native tissue, but this method can be challenging to handle and integrate on-chip (i.e. control of chemical or fluidic environment), has increased variability between each sample, and can typically be used for shorter timescales only. As each method has its merits, the type of organ model can be selected that best fits the use of the MOOC platform.

1.3.5 Barriers and compartmentalization

In vivo, there is a high level of compartmentalization on a cellular level and on a tissue level. In simple terms, everything has a place with limited (and controlled) mixing between compartments. For example, the brain is separated from the rest of the body via cellular barriers where there is limited cross-talk to help protect the incredibly sensitive nervous system. On a superficial level, various internal organs such as the lymph node or kidney are contained within a fibrous capsule with specific cells present for a specific function. There are two compartmentalization features found in the MOOC field: 1) spatial compartmentalization and 2) the integration of barriers. With spatial compartmentalization, the device geometry is tailored in such a way to have defined, but separate, tissue environments. Many MOOCs have developed a modular design, where individual organ compartments are inserted into the device, often with multiple fluidic loops with distinct media types connecting the tissues.[28,40,44,47]

In addition to tissue compartments, barriers found *in vivo* are often integrated on chip as a form of compartmentalization. One of the most common barriers in OOCs is the blood-brain barrier (BBB), where countless devices have used membranes, lanes of hydrogel, and sacrificial molding to model key features of this highly selective barrier.[87–89] In addition to the BBB, many researchers have developed compartmentalized chips to model the gut, where the apical and basolateral chambers are often separated by endothelialized villi-like structures.[90] The addition of such barriers can add to the biomimicry of the platform, but should only be incorporated when required for the modeled system, as the device complexity significantly increases.

1.4 Using MOOC technology to study immunity

1.4.1 Overview of innate and adaptive immunity

The immune system is comprised of a collection of cells, organs, and lymphatic vasculature that form a protective network within the body.[91,92] Within immunity, there are essentially two branches: innate and adaptive immunity. Innate immunity is a non-specific defense mechanism that typically occurs within hours of the detection of antigen. This particular pathway has no immunological memory, so it is unable to "learn" more effective treatment pathways for a specific pathogen. Adaptive immunity occurs over a longer timescale (hours to days and weeks) and this is where the immune system's memory comes into play. Upon subsequent exposure to a particular antigen, the adaptive immune response can mount a more robust antigen-specific response.[92] In instances of vaccination, we are using the adaptive immune response to our advantage to build up immune "memory" of a particular antigen (e.g. an inactivated virus) to protect against future infection or exposure.

1.4.2 The lymph node is the hub of the immune system

LNs are secondary lymphoid organs that are responsible for generating an adaptive immune response *in vivo.* Within the human body, there are approximately 500-600 LNs strategically placed along vasculature intersections to surveil blood and lymph fluid for signs of invading pathogens or tissue damage.[93–95] These tiny organs are highly structured, where the spatial organization of different cell types and molecular signals is critical for proper LN function (Figure 1.7).[96,97] This is evident through the complex fluidic network present within the lymph node. Lymph fluid enters the LN through afferent lymphatic vessels, where the majority of the fluid passes through the sinus that borders the tissue to the medulla.[94,98] Some fluid containing immune cells and small molecules (<70 kDa) can enter the lymphoid compartment (i.e. tissue parenchyma containing the cortex, B cell follicles, and paracortex) through the conduit system, a network of collagen fibers that make up the tissue scaffolding.[94,99] Upon arrival

to the lymphoid compartment, antigen-presenting immune cells like dendritic cells can present captured antigen to local B and T cells to mount an immune response. Finally, the fluid flow passing through the sinus or lymphoid compartment gathers in the medulla before exiting the node through the efferent vessel.

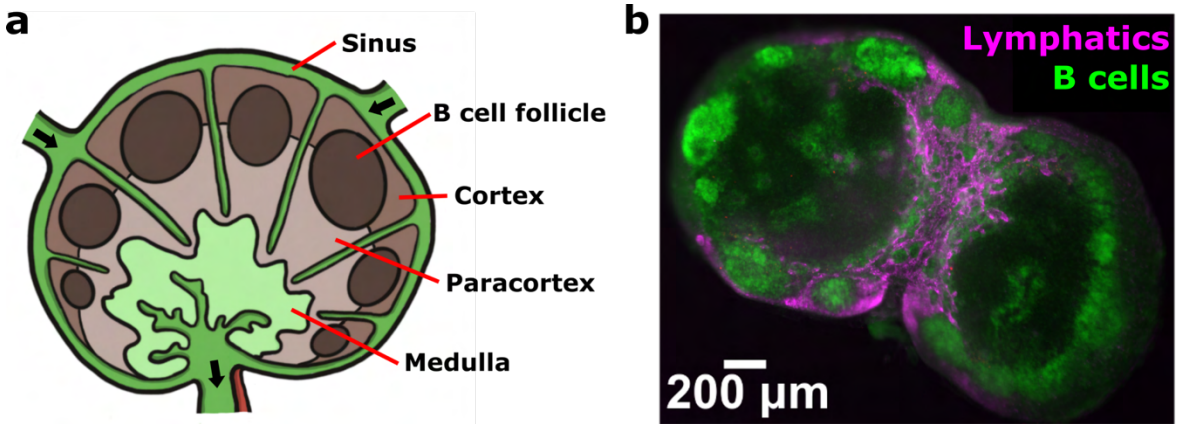

Figure 1.7 Structure of a lymph node (LN). *(a) LNs are highly structured, with different regions containing different cell types. (b) An image of a live murine lymph node slice with B cells (anti-B220) in green and lymphatic vessels (Lyve-1) in magenta (Adapted from Belanger, et al., ACS Pharmacol. Transl. Sci., 2021).*

Due to this incredibly complex tissue organization, it is challenging to generate *in vitro* models (e.g. 3D cell cultures in hydrogel) that mimic LN structure and function. This method, termed the "bottom-up" approach, tends to focus on specific elements within the LN (e.g. formation of a B cell germinal center),[100] whereas the "top-down" approach uses existing live tissue, commonly in the form of tissue slices, as a model system.[97,101,102] Using an established method from the Pompano lab, murine lymph nodes have been embedded in gel and sliced into 300 µm thick slices that can be used for *ex vivo* stimulation both off-chip and on-chip.[45,81,101,103–106]

1.4.3 Methods to study the immune system and current challenges

The primary method to study immunity, especially in the context of other organs, is through animal models, typically by injection of a vaccine or pathogen, or with genetic

modifications. Most of the readouts for this method are endpoint-only, though there has been advancement in recent years for intravital imaging within a live animal.[107] In addition to animal models, researchers have used *ex vivo* tissue slices of immune organs that retain native cellular organization to study the spatiotemporal responses to stimulation in tissues such as the LN, thymus, and spleen.[97,102] However, many of these slices were cultured in isolation and are not used to study communication between organs.

To study multi-tissue immunity, MOOCs provide a platform to either incorporate elements of immunity in established organ models (e.g. recirculating white blood cells in lung, gut, brain, tumor, and islets),[43,108–110] build endothelialized channels to model lymphatic vasculature,[111–113] or add immune organ models (e.g. LN) to a multi-organ system.[102] With the inclusion of immune cells in different OOCs, the model's cellular environment more closely matches the tissue-resident immune cells found in many different organs. However, the immune response may be limited without a dedicated immune organ, i.e. LN, present to mount a biomimetic immune response. Lymphatic vasculature allows for flowing lymph and immune cells to travel between organs *in vivo*, and has been involved in antigen presentation and other key immune functions.[114] Lymphatic vessel OOCs use creative methods to mimic the vasculature, ranging from sacrificial molding in hydrogel to growing cells directly within a microfluidic channel. While these devices have captured many elements found in lymphatics, the models are only cultured in isolation and fail to be considered in many MOOC platforms.

The inclusion of immune organs, specifically the LN, is relatively new, and as a result, there are limited available models.[93,102] Aside from the LN OOC models in isolation,[93,100,104,105,115–117] there are only three published MOOCs that include a LN model: the MIMIC system,[118] and two devices for LN slice co-culture developed in the Pompano lab and

elsewhere.[45,81] Due to the complex cellular organization within the lymph node, tissue slices are ideal models to retain that structure and mimic immune function found *in vivo*.[97] However, this method can be inaccessible for many labs, challenging to integrate into existing chips, and currently limited to animal models only. With the development of more MOOCs that incorporate immunity, researchers can begin to understand human physiology and pathology with regards to the immune system and develop models for robust drug testing for a wide range of diseases.[29]

1.5 Research goals and concluding remarks

In this work, the overall objective was to develop a user-friendly multi-organ-on-chip platform to study communication with the lymph node. To achieve this, I developed a tubing-free impeller pump (Figure 1.8i) and 3D-printed customizable multi-tissue device compatible with tissue slice and 3D cell culture models (Figure 1.8ii). The use of this technology enabled us to begin building models of vaccine immunity and neurodegenerative disease (Figure 1.8iii).

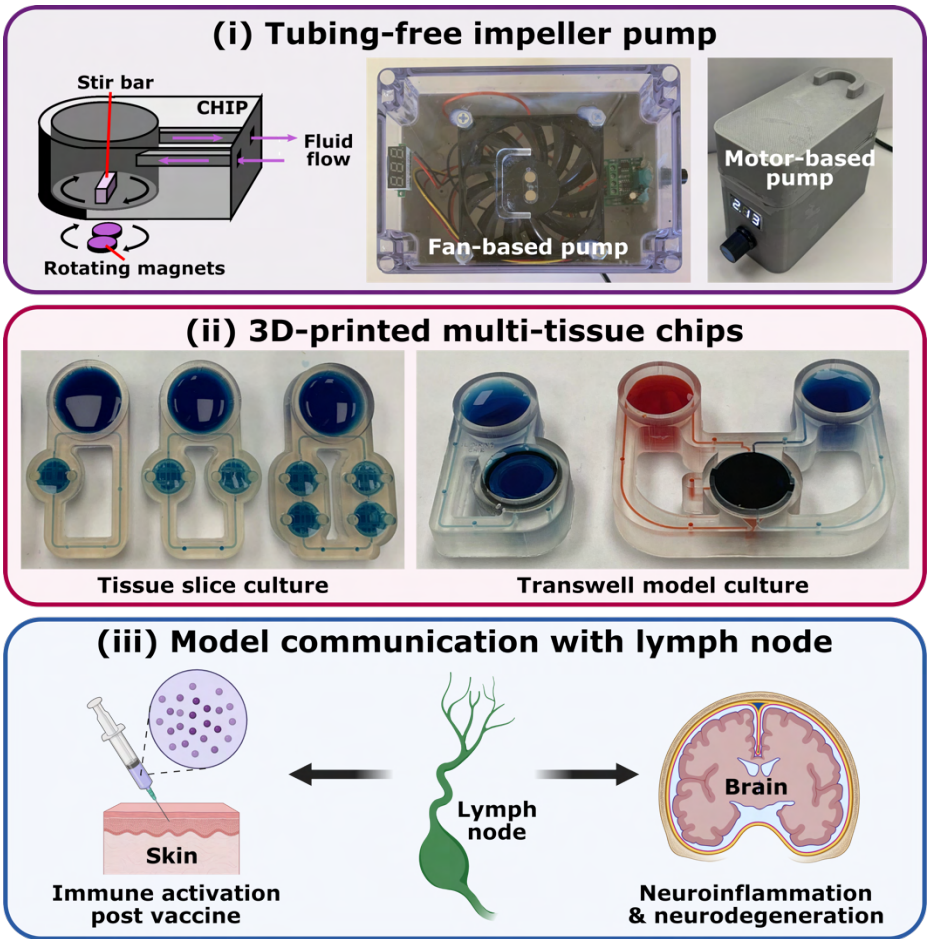

Figure 1.8 Thesis research overview. *This work focuses on the development of the (i) tubing-free impeller pump platform and (ii) 3D-printed multi-tissue chips for tissue slice and transwell model culture to (iii) model communication with the lymph node in the context of vaccination and neuroinflammation/neurodegeneration (Created with BioRender.com).*

Chapter 2 will focus on the development of a magnetically driven fan-based impeller pump to drive fluid recirculation in 3D-printed microfluidic chips. Next, **Chapter 3** will focus on the improvement of biocompatibility of 3D-printed devices with the use of house-made photoresins, post-treatments, and parylene-C coating.

After developing a pump method and biocompatible material, the 3D-printed chip and pump were expanded for cell and tissue culture. In **Chapter 4**, a multi-tissue device and motor-based impeller pump was established to co-culture live tissue slices under recirculating fluid flow. As a proof-of-concept, this platform was used to model a vaccine injection in the skin

draining to a lymph node that was benchmarked against *in vivo* vaccination. In **Chapter 5**, the multi-tissue device was adapted to co-culture human 3D cell culture models in commercially available transwells within a device containing two distinct media compartments. This device was developed to study interactions between the immune system and the brain in instances of neuroinflammation and neurodegeneration. Finally, I will conclude in **Chapter 6** with a discussion of the impact of this research as well as proposed future directions for the impeller pump and multi-tissue chip.

1.6 References

1. Balzer, W. & Eleftheriadis, A. A reconstruction of the hippocratic humoral theory of health. *J. Gen. Philos. Sci.* **22**, 207–227 (1991).
2. Nair, A., Chauhan, P., Saha, B. & Kubatzky, K. F. Conceptual Evolution of Cell Signaling. *Int. J. Mol. Sci.* **20**, 3292 (2019).
3. Roth, G. A. *et al.* Designing spatial and temporal control of vaccine responses. *Nat. Rev. Mater.* **7**, 174–195 (2021).
4. Bobrie, A., Colombo, M., Raposo, G. & Théry, C. Exosome Secretion: Molecular Mechanisms and Roles in Immune Responses. *Traffic* **12**, 1659–1668 (2011).
5. Van Niel, G. *et al.* Challenges and directions in studying cell–cell communication by extracellular vesicles. *Nat. Rev. Mol. Cell Biol.* **23**, 369–382 (2022).
6. Thomou, T. *et al.* Adipose-derived circulating miRNAs regulate gene expression in other tissues. *Nature* **542**, 450–455 (2017).
7. Zundler, S. *et al.* Gut immune cell trafficking: inter-organ communication and immune-mediated inflammation. *Nat. Rev. Gastroenterol. Hepatol.* **20**, 50–64 (2023).

8. Tang, D., Kang, R., Coyne, C. B., Zeh, H. J. & Lotze, M. T. PAMP s and DAMP s: signal 0s that spur autophagy and immunity. *Immunol. Rev.* **249**, 158–175 (2012).

9. Ransohoff, R. M., Schafer, D., Vincent, A., Blachère, N. E. & Bar-Or, A. Neuroinflammation: Ways in Which the Immune System Affects the Brain. *Neurotherapeutics* **12**, 896–909 (2015).

10. Garci-a-Lara, J., Needham, A. J. & Foster, S. J. Invertebrates as animal models for *Staphylococcus aureus* pathogenesis: a window into host–pathogen interaction. *FEMS Immunol. Med. Microbiol.* **43**, 311–323 (2005).

11. Higginson, E. E., Simon, R. & Tennant, S. M. Animal Models for Salmonellosis: Applications in Vaccine Research. *Clin. Vaccine Immunol.* **23**, 746–756 (2016).

12. Chatziandreou, N. *et al.* Macrophage Death following Influenza Vaccination Initiates the Inflammatory Response that Promotes Dendritic Cell Function in the Draining Lymph Node. *Cell Rep.* **18**, 2427–2440 (2017).

13. Ruggeri, B. A., Camp, F. & Miknyoczki, S. Animal models of disease: Pre-clinical animal models of cancer and their applications and utility in drug discovery. *Biochem. Pharmacol.* **87**, 150–161 (2014).

14. Zaragoza, C. *et al.* Animal Models of Cardiovascular Diseases. *J. Biomed. Biotechnol.* **2011**, 1–13 (2011).

15. Gold, R. Understanding pathogenesis and therapy of multiple sclerosis via animal models: 70 years of merits and culprits in experimental autoimmune encephalomyelitis research. *Brain* **129**, 1953–1971 (2006).

16. Hasseldam, H., Rasmussen, R. S. & Johansen, F. F. Oxidative damage and chemokine production dominate days before immune cell infiltration and EAE disease debut. *J. Neuroinflammation* **13**, 246 (2016).

17. Watts, G. Nobel prize is awarded for work leading to “knockout mouse”. *BMJ* **335**, 740.2-741 (2007).

18. Hall, B., Limaye, A. & Kulkarni, A. B. Overview: Generation of Gene Knockout Mice. *Curr. Protoc. Cell Biol.* **44**, (2009).

19. Bowers, B. J. Applications of Transgenic and Knockout Mice in Alcohol Research. **24**, (2000).

20. Dawson, T. M., Ko, H. S. & Dawson, V. L. Genetic Animal Models of Parkinson’s Disease. *Neuron* **66**, 646–661 (2010).

21. Ingber, D. E. Is it Time for Reviewer 3 to Request Human Organ Chip Experiments Instead of Animal Validation Studies? *Adv. Sci.* **7**, 2002030 (2020).

22. Low, L. A., Mummery, C., Berridge, B. R., Austin, C. P. & Tagle, D. A. Organs-on-chips: into the next decade. *Nat. Rev. Drug Discov.* **20**, 345–361 (2021).

23. Picollet-D’hahan, N., Zuchowska, A., Lemeunier, I. & Le Gac, S. Multiorgan-on-a-Chip: A Systemic Approach To Model and Decipher Inter-Organ Communication. *Trends Biotechnol.* S0167779920303097 (2021) doi:10.1016/j.tibtech.2020.11.014.

24. *Lab-on-a-Chip Devices and Micro-Total Analysis Systems: A Practical Guide*. (Springer International Publishing, 2015). doi:10.1007/978-3-319-08687-3.

25. Sung, J. H. *et al.* Recent Advances in Body-on-a-Chip Systems. *Anal. Chem.* **91**, 330–351 (2019).

26. Huh, D. *et al.* Reconstituting Organ-Level Lung Functions on a Chip. *Science* **328**, 1662–1668 (2010).

27. Wang, Y. I., Carmona, C., Hickman, J. J. & Shuler, M. L. Multiorgan Microphysiological Systems for Drug Development: Strategies, Advances, and Challenges. *Adv. Healthc. Mater.* **7**, 1701000 (2018).

28. Edington, C. D. *et al.* Interconnected Microphysiological Systems for Quantitative Biology and Pharmacology Studies. *Sci. Rep.* **8**, 4530 (2018).

29. Hammel, J. H., Zatorski, J. M., Cook, S. R., Pompano, R. R. & Munson, J. M. Engineering in vitro immune-competent tissue models for testing and evaluation of therapeutics. *Adv. Drug Deliv. Rev.* **182**, 114111 (2022).

30. Ong, L. J. Y. *et al.* Self-aligning Tetris-Like (TILE) modular microfluidic platform for mimicking multi-organ interactions. *Lab. Chip* **19**, 2178–2191 (2019).

31. Coppeta, J. R. *et al.* A portable and reconfigurable multi-organ platform for drug development with onboard microfluidic flow control. *Lab. Chip* **17**, 134–144 (2017).

32. Satoh, T. *et al.* A multi-throughput multi-organ-on-a-chip system on a plate formatted pneumatic pressure-driven medium circulation platform. *Lab. Chip* **18**, 115–125 (2018).

33. Esch, M. B., Ueno, H., Applegate, D. R. & Shuler, M. L. Modular, pumpless body-on-a-chip platform for the co-culture of GI tract epithelium and 3D primary liver tissue. *Lab. Chip* **16**, 2719–2729 (2016).

34. Sasserath, T. *et al.* Differential Monocyte Actuation in a Three-Organ Functional Innate Immune System-on-a-Chip. *Adv. Sci.* **7**, 2000323 (2020).

35. Shinha, K. *et al.* A Kinetic Pump Integrated Microfluidic Plate (KIM-Plate) with High Usability for Cell Culture-Based Multiorgan Microphysiological Systems. *Micromachines* **12**, 1007 (2021).

36. Baert, Y. *et al.* A multi-organ-chip co-culture of liver and testis equivalents: a first step toward a systemic male reprotoxicity model. *Hum. Reprod.* **35**, 1029–1044 (2020).

37. Lin, N. *et al.* Repeated dose multi-drug testing using a microfluidic chip-based coculture of human liver and kidney proximal tubules equivalents. *Sci. Rep.* **10**, 8879 (2020).

38. Materne, E.-M. *et al.* A multi-organ chip co-culture of neurospheres and liver equivalents for long-term substance testing. *J. Biotechnol.* **205**, 36–46 (2015).

39. Schimek, K. *et al.* Human multi-organ chip co-culture of bronchial lung culture and liver spheroids for substance exposure studies. *Sci. Rep.* **10**, 7865 (2020).

40. Maschmeyer, I. *et al.* A four-organ-chip for interconnected long-term co-culture of human intestine, liver, skin and kidney equivalents. *Lab. Chip* **15**, 2688–2699 (2015).

41. Oleaga, C. *et al.* Investigation of the effect of hepatic metabolism on off-target cardiotoxicity in a multi-organ human-on-a-chip system. *Biomaterials* **182**, 176–190 (2018).

42. Marzagalli, M. *et al.* A multi-organ-on-chip to recapitulate the infiltration and the cytotoxic activity of circulating NK cells in 3D matrix-based tumor model. *Front. Bioeng. Biotechnol.* **10**, 945149 (2022).

43. Mannino, R. G. *et al.* 3D microvascular model recapitulates the diffuse large B-cell lymphoma tumor microenvironment in vitro. *Lab. Chip* **17**, 407–414 (2017).

44. Chramiec, A. *et al.* Integrated human organ-on-a-chip model for predictive studies of anti-tumor drug efficacy and cardiac safety. *Lab. Chip* **20**, 4357–4372 (2020).

45. Shim, S., Belanger, M. C., Harris, A. R., Munson, J. M. & Pompano, R. R. Two-way communication between ex vivo tissues on a microfluidic chip: application to tumor–lymph node interaction. *Lab. Chip* **19**, 1013–1026 (2019).

46. Xiao, S. *et al.* A microfluidic culture model of the human reproductive tract and 28-day menstrual cycle. *Nat. Commun.* **8**, (2017).

47. Li, Z. *et al.* Human Mesenchymal Stem Cell-Derived Miniature Joint System for Disease Modeling and Drug Testing. *Adv. Sci.* **9**, 2105909 (2022).

48. Wikswo, J. P. *et al.* Scaling and systems biology for integrating multiple organs-on-a-chip. *Lab. Chip* **13**, 3496 (2013).

49. Leung, C. M. *et al.* A guide to the organ-on-a-chip. (2022).

50. Chen, L., Yang, Y., Ueno, H. & Esch, M. B. Body-in-a-Cube: a microphysiological system for multi-tissue co-culture with near-physiological amounts of blood surrogate. *Microphysiological Syst.* **4**, 1–1 (2020).

51. Wang, Y. I. & Shuler, M. L. UniChip enables long-term recirculating unidirectional perfusion with gravity-driven flow for microphysiological systems. *Lab. Chip* **18**, 2563–2574 (2018).

52. Miller, D. R. *et al.* A bistable, multiport valve enables microformulators creating microclinical analyzers that reveal aberrant glutamate metabolism in astrocytes derived from a tuberous sclerosis patient. *Sens. Actuators B Chem.* **341**, 129972 (2021).

53. Kimura, H., Yamamoto, T., Sakai, H., Sakai, Y. & Fujii, T. An integrated microfluidic system for long-term perfusion culture and on-line monitoring of intestinal tissue models. *Lab. Chip* **8**, 741 (2008).

54. Wasson, E. M., Dubbin, K. & Moya, M. L. Go with the flow: modeling unique biological flows in engineered *in vitro* platforms. *Lab. Chip* 10.1039.D1LC00014D (2021) doi:10.1039/D1LC00014D.

55. Griffith, L. G. & Swartz, M. A. Capturing complex 3D tissue physiology in vitro. *Nat. Rev. Mol. Cell Biol.* **7**, 211–224 (2006).

56. Leu, A. J., Berk, D. A., Yuan, F. & Jain, R. K. Flow velocity in the superficial lymphatic network of the mouse tail. *Am. J. Physiol.-Heart Circ. Physiol.* **267**, H1507–H1513 (1994).

57. Nuttall, A. L. Velocity of red blood cell flow in capillaries of the guinea pig cochlea. *Hear. Res.* **27**, 121–128 (1987).

58. Dixon, J. B. *et al.* Lymph Flow, Shear Stress, and Lymphocyte Velocity in Rat Mesenteric Prenodal Lymphatics. *Microcirculation* **13**, 597–610 (2006).

59. Holm-Weber, T., Kristensen, R. E., Mohanakumar, S. & Hjortdal, V. E. Gravity and lymphodynamics. *Physiol. Rep.* **10**, (2022).

60. Klarhöfer, M., Csapo, B., Balassy, Cs., Szeles, J. C. & Moser, E. High-resolution blood flow velocity measurements in the human finger: Blood Flow Velocities in the Human Finger. *Magn. Reson. Med.* **45**, 716–719 (2001).

61. Bovenkamp, P. R. *et al.* Velocity mapping of the aortic flow at 9.4 T in healthy mice and mice with induced heart failure using time-resolved three-dimensional phase-contrast MRI (4D PC MRI). *Magn. Reson. Mater. Phys. Biol. Med.* **28**, 315–327 (2015).

62. Lacy, J. Development and validation of a novel technique for murine first-pass radionuclide angiography with a fast multiwire camera and tantalum 178. *J. Nucl. Cardiol.* **8**, 171–181 (2001).

63. Weibel, D. B., DiLuzio, W. R. & Whitesides, G. M. Microfabrication meets microbiology. *Nat. Rev. Microbiol.* **5**, 209–218 (2007).

64. Ma, X. *et al.* Injection molding and characterization of PMMA-based microfluidic devices. *Microsyst. Technol.* **26**, 1317–1324 (2020).

65. Deshmukh, S. S. & Goswami, A. Hot Embossing of polymers – A review. *Mater. Today Proc.* **26**, 405–414 (2020).

66. Hirama, H. *et al.* Glass-based organ-on-a-chip device for restricting small molecular absorption. *J. Biosci. Bioeng.* **127**, 641–646 (2019).

67. Musgrove, Hannah. B., Catterton, Megan. A. & Pompano, Rebecca. R. Applied tutorial for the design and fabrication of biomicrofluidic devices by resin 3D printing. *Anal. Chim. Acta* **1209**, 339842 (2022).

68. Musgrove, H. B., Cook, S. R. & Pompano, R. R. *Parylene-C coating protects resin 3D printed devices from materials erosion and cytotoxicity*. https://chemrxiv.org/engage/chemrxiv/article-details/643eb6df83fa35f8f6da8d77 (2023) doi:10.26434/chemrxiv-2023-42969.

69. Kotz, F. *et al.* Three-dimensional printing of transparent fused silica glass. *Nature* **544**, 337–339 (2017).

70. Esch, E. W., Bahinski, A. & Huh, D. Organs-on-chips at the frontiers of drug discovery. *Nat. Rev. Drug Discov.* **14**, 248–260 (2015).

71. Fuchs, S. *et al.* In-Line Analysis of Organ-on-Chip Systems with Sensors: Integration, Fabrication, Challenges, and Potential. *ACS Biomater. Sci. Eng.* **7**, 2926–2948 (2021).

72. Papademetriou, I., Vedula, E., Charest, J. & Porter, T. Effect of flow on targeting and penetration of angiopep-decorated nanoparticles in a microfluidic model blood-brain barrier. *PLOS ONE* **13**, e0205158 (2018).

73. Cramer, S. M., Larson, T. S. & Lockett, M. R. Tissue Papers: Leveraging Paper-Based Microfluidics for the Next Generation of 3D Tissue Models. *Anal. Chem.* **91**, 10916–10926 (2019).

74. Ortiz-Cárdenas, J. E. *et al.* Towards spatially-organized organs-on-chip: Photopatterning cell-laden thiol-ene and methacryloyl hydrogels in a microfluidic device. *Organs---Chip* **4**, 100018 (2022).

75. Campisi, M. *et al.* 3D self-organized microvascular model of the human blood-brain barrier with endothelial cells, pericytes and astrocytes. *Biomaterials* **180**, 117–129 (2018).

76. Sieber, S. *et al.* Bone marrow-on-a-chip: Long-term culture of human haematopoietic stem cells in a three-dimensional microfluidic environment. *J. Tissue Eng. Regen. Med.* **12**, 479–489 (2018).

77. Giese, C. *et al.* Immunological substance testing on human lymphatic micro-organoids in vitro. *J. Biotechnol.* **148**, 38–45 (2010).

78. Au, S. H., Chamberlain, M. D., Mahesh, S., Sefton, M. V. & Wheeler, A. R. Hepatic organoids for microfluidic drug screening. *Lab. Chip* **14**, 3290 (2014).

79. Richardson, A. *et al.* A microfluidic organotypic device for culture of mammalian intestines *ex vivo*. *Anal. Methods* **12**, 297–303 (2020).

80. Huang, Y., Williams, J. C. & Johnson, S. M. Brain slice on a chip: opportunities and challenges of applying microfluidic technology to intact tissues. *Lab. Chip* **12**, 2103 (2012).

81. Delong, L. M. & Ross, A. E. Open multi-organ communication device for easy interrogation of tissue slices. *Lab. Chip* **23**, 3034–3049 (2023).

82. Rodriguez, A. D. *et al.* A microfluidic platform for functional testing of cancer drugs on intact tumor slices. *Lab. Chip* **20**, 1658–1675 (2020).

83. Katt, M. E., Linville, R. M., Mayo, L. N., Xu, Z. S. & Searson, P. C. Functional brain-specific microvessels from iPSC-derived human brain microvascular endothelial cells: the role of matrix composition on monolayer formation. *Fluids Barriers CNS* **15**, 7 (2018).

84. Zhang, S., Wan, Z. & Kamm, R. D. Vascularized organoids on a chip: strategies for engineering organoids with functional vasculature. *Lab. Chip* **21**, 473–488 (2021).

85. Nashimoto, Y. *et al.* Vascularized cancer on a chip: The effect of perfusion on growth and drug delivery of tumor spheroid. *Biomaterials* **229**, 119547 (2020).

86. Huh, D. *et al.* A Human Disease Model of Drug Toxicity–Induced Pulmonary Edema in a Lung-on-a-Chip Microdevice. *Sci. Transl. Med.* **4**, 159ra147-159ra147 (2012).

87. DeStefano, J. G., Jamieson, J. J., Linville, R. M. & Searson, P. C. Benchmarking in vitro tissue-engineered blood–brain barrier models. *Fluids Barriers CNS* **15**, 32 (2018).

88. Jamieson, J. J., Searson, P. C. & Gerecht, S. Engineering the human blood-brain barrier in vitro. *J. Biol. Eng.* **11**, 37 (2017).

89. van der Helm, M. W., van der Meer, A. D., Eijkel, J. C. T., van den Berg, A. & Segerink, L. I. Microfluidic organ-on-chip technology for blood-brain barrier research. *Tissue Barriers* **4**, e1142493 (2016).

90. Xiang, J., Cai, Z., Zhang, Y. & Wang, W. A micro-cam actuated linear peristaltic pump for microfluidic applications. *Sens. Actuators Phys.* **251**, 20–25 (2016).

91. Hoebe, K., Janssen, E. & Beutler, B. The interface between innate and adaptive immunity. *Nat. Immunol.* **5**, 971–974 (2004).

92. Warrington, R., Watson, W., Kim, H. L. & Antonetti, F. R. An introduction to immunology and immunopathology. *Clin. Immunol.* 8 (2011).

93. Ozulumba, T., Montalbine, A. N., Ortiz-Cárdenas, J. E. & Pompano, R. R. New tools for immunologists: models of lymph node function from cells to tissues. *Front. Immunol.* **14**, 1183286 (2023).

94. Jafarnejad, M., Woodruff, M. C., Zawieja, D. C., Carroll, M. C. & Moore, J. E. Modeling Lymph Flow and Fluid Exchange with Blood Vessels in Lymph Nodes. *Lymphat. Res. Biol.* **13**, 234–247 (2015).

95. Willard-Mack, C. L. Normal Structure, Function, and Histology of Lymph Nodes. *Toxicol. Pathol.* **34**, 409–424 (2006).

96. Qi, H., Kastenmüller, W. & Germain, R. N. Spatiotemporal Basis of Innate and Adaptive Immunity in Secondary Lymphoid Tissue. *Annu. Rev. Cell Dev. Biol.* **30**, (2014).

97. Belanger, M. C. *et al.* Acute Lymph Node Slices Are a Functional Model System to Study Immunity Ex Vivo. *ACS Pharmacol. Transl. Sci.* **4**, 128–142 (2021).

98. Margaris, K. N. & Black, R. A. Modelling the lymphatic system: challenges and opportunities. *J. R. Soc. Interface* **9**, 601–612 (2012).

99. Roozendaal, R., Mebius, R. E. & Kraal, G. The conduit system of the lymph node. *Int. Immunol.* **20**, 1483–1487 (2008).

100. Goyal, G. *et al.* Ectopic Lymphoid Follicle Formation and Human Seasonal Influenza Vaccination Responses Recapitulated in an Organ-on-a-Chip. *Adv. Sci.* **9**, 2103241 (2022).

101. Groff, B. D., Kinman, A. W. L., Woodroof, J. F. & Pompano, R. R. Immunofluorescence staining of live lymph node tissue slices. *J. Immunol. Methods* **464**, 119–125 (2019).

102. Hammel, J. H., Cook, S. R., Belanger, M. C., Munson, J. M. & Pompano, R. R. Modeling Immunity In Vitro: Slices, Chips, and Engineered Tissues. *Annu. Rev. Biomed. Eng.* **23**, 461–491 (2021).

103. Catterton, M. A., Dunn, A. F. & Pompano, R. R. User-defined local stimulation of live tissue through a movable microfluidic port. *Lab. Chip* **18**, 2003–2012 (2018).

104. Ross, A. E. & Pompano, R. R. Diffusion of cytokines in live lymph node tissue using microfluidic integrated optical imaging. *Anal. Chim. Acta* **1000**, 205–213 (2018).

105. Ross, A. E., Belanger, M. C., Woodroof, J. F. & Pompano, R. R. Spatially resolved microfluidic stimulation of lymphoid tissue ex vivo. *The Analyst* **142**, 649–659 (2017).

106. Ball, A. G., Belanger, M. C. & Pompano, R. R. Detergent wash improves vaccinated lymph node handling ex vivo. *J. Immunol. Methods* **489**, 112943 (2021).

107. Entenberg, D., Oktay, M. H. & Condeelis, J. S. Intravital imaging to study cancer progression and metastasis. *Nat. Rev. Cancer* **23**, 25–42 (2023).

108. Cucullo, L., Marchi, N., Hossain, M. & Janigro, D. A Dynamic *in vitro* BBB Model for the Study of Immune Cell Trafficking into the Central Nervous System. *J. Cereb. Blood Flow Metab.* **31**, 767–777 (2011).

109. Gjorevski, N. *et al.* Neutrophilic infiltration in organ-on-a-chip model of tissue inflammation. *Lab. Chip* **20**, 3365–3374 (2020).

110. Ramadan, Q. & Ting, F. C. W. In vitro micro-physiological immune-competent model of the human skin. *Lab. Chip* **16**, 1899–1908 (2016).

111. Thompson, R. L. *et al.* Design principles for lymphatic drainage of fluid and solutes from collagen scaffolds: Design principles for lymphatic drainage. *J. Biomed. Mater. Res. A* **106**, 106–114 (2018).

112. Gong, M. M. *et al.* Human organotypic lymphatic vessel model elucidates microenvironment-dependent signaling and barrier function. *Biomaterials* **214**, 119225 (2019).

113. Kim, S., Chung, M. & Jeon, N. L. Three-dimensional biomimetic model to reconstitute sprouting lymphangiogenesis in vitro. *Biomaterials* **78**, 115–128 (2016).

114. Card, C. M., Yu, S. S. & Swartz, M. A. Emerging roles of lymphatic endothelium in regulating adaptive immunity. *J. Clin. Invest.* **124**, 943–952 (2014).

115. Shanti, A. *et al.* Multi-Compartment 3D-Cultured Organ-on-a-Chip: Towards a Biomimetic Lymph Node for Drug Development. *Pharmaceutics* **12**, 464 (2020).

116. Kraus, T. *et al.* Evaluation of a 3D Human Artificial Lymph Node as Test Model for the Assessment of Immunogenicity of Protein Aggregates. *J. Pharm. Sci.* **108**, 2358–2366 (2019).

117. Wagar, L. E. *et al.* Modeling human adaptive immune responses with tonsil organoids. *Nat. Med.* **27**, 125–135 (2021).

118. Higbee, R. G. *et al.* An Immunologic Model for Rapid Vaccine Assessment — A Clinical Trial in a Test Tube. *Altern. Lab. Anim.* **37**, 19–27 (2009).

Chapter 2. Microscale impeller pump for recirculating flow in organs-on-chip and microreactors

Adapted from:

Cook, S. R., Musgrove, H. B., Throckmorton, A. L., & Pompano, R. R. *Lab Chip*, 22, 605 (2022)

2.1 Abstract

Fluid flow is an integral part of microfluidic and organ-on-chip technology, ideally providing biomimetic fluid, cell, and nutrient exchange as well as physiological or pathological shear stress. Currently, many of the pumps that actively perfuse fluid at biomimetic flow rates are incompatible with use inside cell culture incubators, require many tubing connections, or are too large to run many devices in a confined space. To address these issues, we developed a user-friendly impeller pump that uses a 3D-printed device and impeller to recirculate fluid and cells on-chip. Impeller rotation was driven by a rotating magnetic field generated by magnets mounted on a computer fan; this pump platform required no tubing connections and could accommodate up to 36 devices at once in a standard cell culture incubator. A computational model was used to predict shear stress, velocity, and changes in pressure throughout the device. The impeller pump generated biomimetic fluid velocities (50-6400 μm/s) controllable by tuning channel and inlet dimensions and the rotational speed of the impeller, which were comparable to the order of magnitude of the velocities predicted by the computational model. Predicted shear stress was in the physiological range throughout the microchannel and over the majority of the impeller. The impeller pump successfully recirculated primary murine splenocytes for 1 hr and Jurkat T cells for 24 hr with no impact on cell viability, showing the impeller pump's feasibility for white blood cell recirculation on-chip. In the future, we envision that this pump will be integrated into single- or multi-tissue platforms to study communication between organs.

3.2 Introduction

Organ-on-chip (OOC) devices aim to mimic a tissue's native environment by integrating single or multiple tissues in tandem into biomimetic perfusion systems.[1,2] One feature that is critical to the function of these devices is directing fluid flow in a highly controlled manner. *In vivo*, there is constant fluid flow at varying velocities.[3] Slower physiological fluid flow rates are found in the interstitium (0.1-1 μm/s)[4] and within lymphatic capillaries (1.4-20.4 μm/s),[5] while faster fluid flow rates are found in the blood vessel capillaries (80-180 μm/s),[6] lymphatic vessels (870 μm/s, with a peak of 2200-9000 μm/s)[7], veins (15,000-71,000 μm/s),[8] and aortic artery (1,000,000 μm/s).[9] As fluid moves, it provides nutrient and waste exchange as well as communication between organs through recirculation of cells, signaling molecules, exosomes, and so on. Flow also applies shear stress that impacts cellular function and viability and can result in cellular adhesion, activation, and extravasation.[10–12] Thus, flow control systems for organs-on-chip must generate flow in a range of physiological and pathological flow rates, while ideally enabling transport of blood-borne cells between organs without damage. In addition to controllable flow rates, additional desirable qualities for flow control systems within OOC platforms include multiplexing capabilities, compatibility with cell culture incubators in terms of temperature output, and ability to recirculate media to enable cell circulation and communication between tissues.

Current technology provides a variety of methods to achieve biologically relevant fluid flow rates on a microfluidic device, but these remain challenging for use when running many organ-on-chip devices simultaneously with fine control over flow rate, particularly for fluid recirculation. External, motorized fluid control systems such as syringe pumps[13,14] and peristaltic pumps[15,16] provide precise fluid control at physiological flow rates, but they can be expensive,

bulky, and require many tubes or wires if running multiple devices at once. Furthermore, these pumps may emit heat, making them incompatible with use inside of an incubator for long-term culture. Recently, an elegant in-plane peristaltic pump was developed that is more compact than commercially available peristaltic pumps and is compatible with incubators.[17] With the ability to switch between multiple fluid inputs, this pump was designed primarily for rapid drug testing rather than for continuous media recirculation within OOC models. Alternatively, on-chip pneumatic peristaltic pumps use changes in pneumatic pressure to drive fluid flow, e.g. by serial compression of microfluidic channel.[18–21] While powerful, this type of pump requires at least three tubing connections per device to drive fluid flow, which introduces complexity in handling for high throughput applications as well as sites for potential leaks.[14,16,19–22] To avoid these issues, passive gravity-driven flow through a microfluidic device greatly simplifies handling by minimizing fluid or pneumatic connections, in exchange for less fine control over the flow rate.[23–26] While most gravity-driven systems provide alternating or pulsatile unidirectional flow,[23,24] cleverly-designed fluidics have also enabled continuous recirculation that is unidirectional through a single channel.[25] However, actively controlled fluid recirculation for organs-on-chip remains a challenge.

A promising alternative means of active flow control uses rotating external magnets and an on-chip stir bar or impeller to drive fluid flow through a microfluidic chip.[27–29] In prior reports, this approach elegantly reduced the need for tubing connections and allowed for controllable flow rates within the device.[27,28,30] However, magnetic flow control has not been widely adopted, likely because the magnetic element within these devices was powered by commercially available stir plates,[27,28,30] most of which are large and lack precise rotational control or quantification. This limitation makes it challenging to run many devices

simultaneously, especially within a culture incubator, and also to achieve consistent flow rates. In addition, the prior example of a rotating stir bar-based pump for OOC applications relied on manual PDMS-based fabrication and yielded a narrow range of flow rates recirculating through the device.[28,30] This system was recently extended to perfuse media between two tissue models in an integrated polystyrene microfluidic plate fabricated by injection molding and laser fusion.[29]

Here, we present a magnetically driven microscale impeller pump platform for recirculating fluid flow that is inexpensive, easy to fabricate and use, has low heat output, and has multiplexing capabilities. We designed and fabricated a prototype impeller pump and tested its ability to achieve a range of physiologically relevant flow rates by varying pump and device features. We conducted computational modeling of the impeller pump geometry to assess fluid flow performance and scalar stress present within the device. As a proof-of-concept, we tested the cytocompatibility of the pump components with primary murine splenocytes and Jurkat T cells, models of recirculating white blood cells, and finally demonstrated the impeller pump's ability to circulate cells across a range of flow rate regimes without loss of cell viability.

2.3 Methods

2.3.1 3D-printed device fabrication

The microfluidic device and impeller piece were designed using Fusion 360. The device consisted of a large well with a micro channel loop intersecting the well tangentially. Channels had a square cross-section and were 0.5 or 1 mm in width. The microfluidic devices were printed using a CADWorks3D MiiCraft Ultra 50 DLP printer (CADWorks3D, Toronto, Canada) and a CADWorks3D MiiCraft P110Y DLP Printer (CADWorks3D, Toronto, Canada) using BV007a (MiiCraft, Jena, Germany) and Clear v.1 (FormLabs, Massachusetts, USA) resins, both recommended for use with microfluidics by their manufacturers. Drain ports were added in the

channels when printing in the Clear resin to enable uncured resin to drain out of the channel during printing. For both resins, printer settings included a 0.10 mm gap adjustment with a slow peel speed. For BV007a in the Ultra 50 printer, a cure time of 1.15 s was used with a base cure time of 9 s for a single base layer with 1 buffer layer. All layers were printed at 50 µm and the light intensity was set to 75% power (9 mW/cm^2) at 405 nm. For the P110Y printer, a cure time of 1.20 s was used with a base cure time of 25 s for a single base layer with 2 buffer layers. The light intensity was set to 100% power (5 mW/cm^2) at 385 nm. For the Clear resin in the Ultra 50 printer, a 5 s cure time was used with a single base layer at a 6 s cure time, with a single buffer layer. Pieces with 1 mm channels used 50-µm layers with an 80% power setting (9.6 mW/cm^2) at 405 nm; pieces with 0.5 mm channels used 100-µm layers with 75% power (9 mW/cm^2) and 405 nm. For the P110Y printer, all pieces printed in the Clear resin had 100-µm layers with a 3.75 s cure time with a base cure time of 8.75 s for 4 base layers with 12 buffer layers. The light intensity was set to 70% power (3.5 mW/cm^2) at 385 nm.

For the hand-washed conditions, all printed parts were rinsed with a spray bottle for 2 min with isopropyl alcohol (IPA) after coming out of the printer to remove any excess resin; parts printed in Clear resin were subsequently soaked in IPA for an additional 10 minutes. For the machine-washed conditions, all printed parts were submerged in IPA within a Form Wash (FormLabs, Massachusetts, USA) for 5 min (BV007a resin) or 8 min (Clear resin). After cleaning with alcohol, the pieces were dried thoroughly with nitrogen and placed in a high-intensity UV light box, either the CureZone (ResinWorks3D, Ontario, CA) UV light box (60 mW/cm^2) or the Form Cure (FormLabs, Massachusetts, USA) UV light box (10 mW/cm^2) for post curing. BV007a pieces were post-cured for 30 s in the CureZone or 1 min in the Form Cure, and Clear pieces were post-cured for 1 hour in both the CureZone or the Form Cure. After post-

curing, Teflon-encapsulated magnetic stir bars (3 x 10 mm, Thomas Scientific, New Jersey, USA) were inserted into printed impeller pieces and glued in place using super glue (Loctite, Düsseldorf, Germany).

2.3.2 Assembly of the impeller pump external platform

Within an ABS plastic Universal Project Enclosure (200 x 120 x 56 mm, uxcell, Hong Kong, China), two 3-pin sleeve bearing computer fans (80 mm, Cooler Master, Taipei, Taiwan) were mounted on 4 screws that were glued to the base of the enclosure, termed the fan project box. Each computer fan was connected to a mini digital DC voltmeter (2.5 – 30 V, MakerFocus, Hong Kong, China) that was mounted within the enclosure so it was visible through the transparent top of the box. Two magnets were glued to the center of each computer fan. The initial prototype used 17.5 mm ceramic ferrite industrial magnets (Clout Science), which were later replaced with 6 mm brushed nickel magnets with a strength of 0.08 T (FINDMAG). The strength of the magnets used in the final prototype was measured using a Bell 610 Gaussmeter (F.W. Bell, Oregon, USA). On the outside of the fan project box, a 3D-printed chip holder (BV007a) was glued above the computer fan to hold the device in place. This project box, which resided within the cell-culture incubator during experimentation, was connected to an ABS plastic IP65 Hinged Junction box (150 x 100 x 70 mm, LMioEtool), which housed the PWM low voltage DC potentiometer (ALDECO) and 12 V DC female power connector (Chanzon), termed the power box. The power connector plugged into the 12 V AC DC power supply adapter wall plug (EWETON) that provides power to the entire pump platform. As the power project box is housed outside of the incubator, it allows for voltage and power control while an experiment is running. While the fan boxes were usually built with two fans, one pump box (Pump 7) was built with a single fan housed alongside a potentiometer; this pump box was not used for cell culture.

All wiring was connected using a tin-lead rosin-core solder wire (ICESPRING) and wrapped in heat shrink tubing (Eventronic, Kommanditgesellschaft, Germany).

2.3.3 Assessment of the external platform

A digital laser photo tachometer (AGPtek, Brooklyn, New York, USA) was used to measure the revolutions per minute (RPM) of the magnetic impeller as it rotated. All RPMs reported were conducted at the onset of each experiment unless stated otherwise, and are the average of three RPM measurements made at a consistent voltage. The impeller pump stability was tested by measuring the impeller RPM over a period of 90 hr at a constant voltage. To monitor heat emission of the impeller pump platform, the single fan pump platform was run with no device for 24 hr in an insulated Styrofoam box at >10 V. For comparison, a peristaltic pump (BT100-1F-B, Langer Instruments, Boonton, New Jersey, USA) was run in the same box at 10 µL/min. Next, to monitor the impact of the pumps on temperature within a cell culture incubator, six external pump platforms with no devices (>10 V) were run for 24 hr in a cell culture incubator that was either off or on, as noted. Temperature was recorded from two locations inside the incubator: at the pump location (front of the top shelf) and at the back of the bottom shelf; the self-reported incubator temperature was also recorded when the incubator was on.

2.3.4 Computational modeling

To investigate the design of the fluid circuit, numerical modeling using computational fluid dynamics (CFD) studies was performed. ANSYS 15.0 CFX (ANSYS Inc., Canonsburg, PA, USA) was employed to mesh the geometry of the fluid circuit, including the impeller. Each fluid circuit consisted of three separate domains: 1) fluid channel; 2) top region of the pump well; and 3) the lower region of the pump well, which included the rotating impeller. Two fluid channel widths of 1 mm and 0.5 mm, with square cross-section, were considered. Each of the regions were connected

via fluid-fluid interfaces. The fluid channel and top region of the pump well were specified to be in the stationary reference frame, while the lower region of the pump well with the impeller was defined to be in the rotating reference frame. A frozen rotor interface connected the top and lower regions of differing reference frames and maintained flow properties without circumferential averaging.

Each domain required separate meshes. The final mesh density for each channel width model was found using a standard grid independence study. Five separate meshes ($5x10^5$, $1x10^6$, $5x10^6$, $7.5x10^6$, $10x10^6$ element numbers), were created for each of the channel widths; the velocity values at multiple locations, pressure drop across the fluid channel, and mass flow rates in fluid channel varied by less than 5% for mesh densities greater than $5x10^6$. The final number of mesh elements for the two channel width models were 5,758,350 and 5,947,380, respectively.

A turbulence modeling approach was employed due to the strong rotational fluid dynamics in the tank reservoir and fluid velocity in the channel. All simulations were performed under steady state, with a no-slip boundary condition on surfaces and a high-resolution advection scheme. In accordance with prior profilometry measurements of 3D printed materials,[31] a surface roughness was specified at 3.5 μm on the internal fluid contacting surfaces; all walls were treated as rigid. To account for the effect of surface roughness, we further utilized a k-ω turbulence model where the y+ criterion ($y+ < 1$) was a design requirement for the mesh construct along the surface walls. Inflation layers were utilized to ensure achievement of the mesh y+ criterion. We verified that the low-Reynolds k-ω turbulence model requirement of a y+ mesh value of less than 1 was satisfied along all of the surfaces and walls of both models.

Mesh quality was confirmed using standard mesh metrics including aspect ratio, Jacobian ratio, skewness and an ANSYS metric called element quality. A hybrid mesh of tetrahedral and/or

hexahedral elements defining its volume was created for each region. The grid structure was designed to satisfy standard quality metrics, including the skewness and aspect ratio.[32] Mesh quality metrics for all of the models met target goals: 1) aspect ratios less than 100, 2) Jacobian ratio less than 10, 3) skewness less than 0.25 and 4) element quality measure greater than 0.75. Convergence was achieved when the residual calculation error for the state variables reached less than 10^{-4}. In line with experimental measurements in this study, water was indicated as the fluid media with Newtonian properties of a dynamic viscosity of 0.001 kg/m∗s and density of 1000 kg/m^3. Rotational speeds of 500 to 900 RPM were modeled.

Simulation results were assessed qualitatively and quantitively. Pressure losses, average velocity profiles, and mass flow rates in the fluid channels were determined. Each plane for analysis was created as a cross-sectional slice of the flow domain. Scalar fluid stress was estimated using the six components of the stress tensor (Equation 2.1). This approach estimates the 3D flow field and calculates a scalar stress (σ) as representative of the level of stress experienced by the fluid traveling through the entire model.[33,34]

$$\sigma = \left(\frac{1}{6}\sum\left(\sigma_{ii} - \sigma_{jj}\right)^2 + \sum \sigma_{ij}^2\right)^{\frac{1}{2}} \qquad \text{Equation 2.1}$$

2.3.5 Experimental fluid flow characterization

To measure the maximum velocity of the fluid flow within the device, a drop of blue food coloring (McCormick Culinary Food Color) was inserted into a reservoir in the device and tracked using a Dino-Lite Edge 3.0 digital microscope (SunriseDino, Torrance, CA, USA). Images were collected over time, and the distance the food coloring front moved over time was measured using DinoXcope software (SunriseDino, Torrance, CA, USA) to determine the fluid velocity. In preliminary experiments, we found that in situ measurement was preferable to

addition of an external in-line flow meter, as the latter offered too high of a flow resistance and slowed the flow rate through the device.

For the experiments comparing channel size, the BV007a resin was used and the devices were printed using the MiiCraft Ultra 50 printer, hand washed, and cured in the CureZone. We later acquired a new, higher capacity printer and automated washer, which were used for subsequent experiments. Therefore, when comparing the changes in inlet size, the devices were printed using BV007a resin on the MiiCraft P110Y printer, washed using the Form Wash, and cured using the Form Cure.

The flow resistance (R) in each condition was calculated via an approximation for resistance in a square channel, where η is viscosity, L is channel length, and w is channel width (Equation 2.2):[35]

$$R = \frac{128\eta L}{\pi w^4} \qquad \text{Equation 2.2}$$

2.3.6 Primary murine splenocyte preparation

All animal work was approved by the Institutional Animal Care and Use Committee at the University of Virginia under protocol #4042, and was conducted in compliance with guidelines from the University of Virginia Animal Care and Use Committee and the Office of Laboratory Animal Welfare at the National Institutes of Health (United States). Spleens were harvested from female and male C57BL/6 mice (Jackson Laboratory, USA) under the age of 6 months following isoflurane anesthesia and cervical dislocation. The spleens were collected into "complete RPMI" media consisting of RPMI (Lonza, Walkersville, MD, USA) supplemented with 10% FBS (VWR, Seradigm USDA approved, Radnor, PA, USA), 1× l-glutamine (Gibco Life Technologies, Gaithersburg, MD, USA), 50 U/mL Pen/Strep (Gibco, MD, USA), 50 µM

beta-mercaptoethanol (Gibco, MD, USA), 1 mM sodium pyruvate (Hyclone, Logan, UT, USA), 1× non-essential amino acids (Hyclone, UT, USA), and 20 mM HEPES (VWR, PA, USA). Spleens were crushed through a 70-µm Nylon mesh filter (Thermo Fisher, Pittsburgh, PA, USA) with 10 mL of complete media, then centrifuged for 5 minutes at 400 x g. To lyse red blood cells, the pellet was resuspended in 2 mL of ACK lysis buffer prepared from 4.15 g NH_4Cl (Sigma-Aldrich, St. Louis, MO, USA), 0.5 g $KHCO_4$ (Sigma, MO, USA), and 18.7 g Na_2EDTA (Sigma, MO, USA) in 0.5 L MilliQ water (Millipore Sigma, Burlington, MA, USA). Cells were lysed for 1 minute, then quenched with 10 mL of complete media, and centrifuged again. The pellet was resuspended in complete media, producing a splenocyte suspension with the density determined by trypan blue exclusion. The suspensions were diluted with complete media to a concentration of 1 x 10^6 cells/mL in preparation for culture.

2.3.7 Jurkat T cell preparation

For 24 hr long culture on 3D-printed devices, human Jurkat T lymphoblast cells (Clone E6-1 TIB-152, ATCC, VA, USA) were used. The cell line was cultured in media consisting of RPMI (Lonza, Walkersville, MD, USA) supplemented with 10% FBS (VWR, Seradigm USDA approved, Radnor, PA, USA), 1× l-glutamine (Gibco Life Technologies, Gaithersburg, MD, USA) and 50 U/mL Pen/Strep (Gibco, MD, USA). Before on-chip culture, the cells were centrifuged at 200 x g for 5 min and resuspended in 10 mL of media, producing a cell suspension whose density was determined by trypan blue exclusion. The suspensions were diluted with additional media to a density of 0.8 – 1 x 10^6 cells/mL in preparation for culture.

2.3.8 Analysis of cell viability

Prior to culture, all prints were post-treated as outlined above, and then subjected to an additional leaching process. For initial 1- and 4-hr tests of resin cytotoxicity and pump

biocompatibility, the prints were soaked in 1x PBS (Lonza, MD, USA) for 24 hr at 37°C (BV007a prints) or 70°C (Clear prints) to mitigate cytotoxicity.[36] Primary splenocytes (3.5 mL, 10^6 cells/mL in complete media) were aliquoted into the pump well of a 3D printed device or into a 12-well polystyrene non-treated tissue culture plate (VWR, Radnor, PA, USA) that served as a control. The wells within the tissue culture plate (23 mm diameter) were similar in diameter to the 3D printed pump wells (26 mm diameter), and the volume of media used was the same, so oxygenation and dilution of secreted factors is expected to be similar in the two systems. Cells were cultured at 37°C with 5% CO_2 for either 4 hours for material cytotoxicity testing or 1 hour for "pump-on" viability testing.

In preparation for 24-hr cell culture on Clear prints, a longer leach step was performed, in which the devices were soaked in 1x PBS for 8 days and in complete media for 2 days at 37°C.[37] Jurkat T cells or primary murine splenocytes were cultured within the printed and leached devices. The Jurkat cells and splenocytes (3.5 mL, 10^6 cells/mL in Jurkat-specific media) were aliquoted into the pump well of a 3D printed device or into a 12-well polystyrene non-treated tissue culture plate (VWR, Radnor, PA, USA) as a control. The cells were cultured at 37°C with 5% CO_2 for 24 hr.

Following the culture period, the cell viability was assessed by flow cytometry using a previously established protocol.[38] Briefly, 500 µL samples at 10^6 cells/mL were stained with Calcein AM (eBioscience, San Diego, CA, USA) at 67 nM for splenocytes and 95 nM for Jurkat T cells in 1x PBS for 20 minutes at 37°C. The stained samples were washed by centrifugation at 400 x g for splenocytes and 200 x g for Jurkat T cells for 5 min, then resuspended in flow buffer (1x PBS with 2% FBS). Following the wash step, 4 µL of 1 mg/mL 7-AAD (AAT Bioquest, Sunnyvale, CA, USA) was added to the cell suspension. Single-stain compensation controls were

prepared using plate control cells (Calcein AM) or cells treated with a 1:1 v/v mix of media and 70% ethanol for 20 minutes (7-AAD); single-stains were mixed 1:1 v/v with unstained cells for analysis. All samples and controls were run on a Guava 4-color cytometer (6-2L) and analyzed with Guava® InCyte™ Software. 7-AAD^{low} was defined as Live, and 7-AAD^{high} was defined as Dead.

The shear stress for each condition was approximated by calculating the fluid shear stress (FSS), where η is viscosity, Q is volumetric flow rate, h is channel height, and w is channel width (Equation 2.3).[39]

$$FSS = \frac{6\eta Q}{h^2 w} \qquad \text{Equation 2.3}$$

2.3.9 Imaging cell recirculation on-chip

Primary splenocytes were suspended at 3x10^6 cells/mL in 1x PBS and labelled with 3 µM Calcein AM for 20 minutes at 37°C. The labelled samples were washed by centrifugation at 400 x g for 5 min, then resuspended in 1x PBS at 3x10^6 cells/mL. Cell circulation was monitored in real time using a Zeiss AxioZoom macroscope (Carl Zeiss Microscopy, Germany) with an Axiocam 506 Mono camera and a filter cube for GFP (Zeiss filter set #38). 300 µL of the cell suspension was pipetted into the pump well of a 1x PBS-filled device, with the impeller off. After 15 minutes, initial images were captured within the pump well and near the reservoir in the channel. The pump was then turned on (~6.20 V), and images were captured of cells moving through the channel and reservoir.

2.4 Results and Discussion

2.4.1 Concept of the microscale impeller pump

When designing the impeller pump platform, the major design goals included 1) small overall size, 2) user-friendly interface, 3) easily expandable to run multiple devices at once, 4)

low heat output to be compatible with use inside cell culture incubators, and 5) ability to achieve controllable recirculating fluid flow at physiologically relevant flow rates. To address many of these design goals, we selected a fluid pumping mechanism inspired by that of the centrifugal water pump.[40] The centrifugal water pump consists of a circular chamber with a rotary impeller that has curved vanes to generate a suction force, converting rotational energy into hydrodynamic energy and inducing fluid flow. Historically, large-scale centrifugal pumps were designed to recirculate and oxygenate water for fish and live bait on a fishing boat, similar to the purpose of media perfusion on a microfluidic device.[40] This design and related waterwheel-based systems have been integrated into smaller-scale pumps for use as an artificial heart pump[41] as well as in microfluidic technology.[27,28,30,42–44]

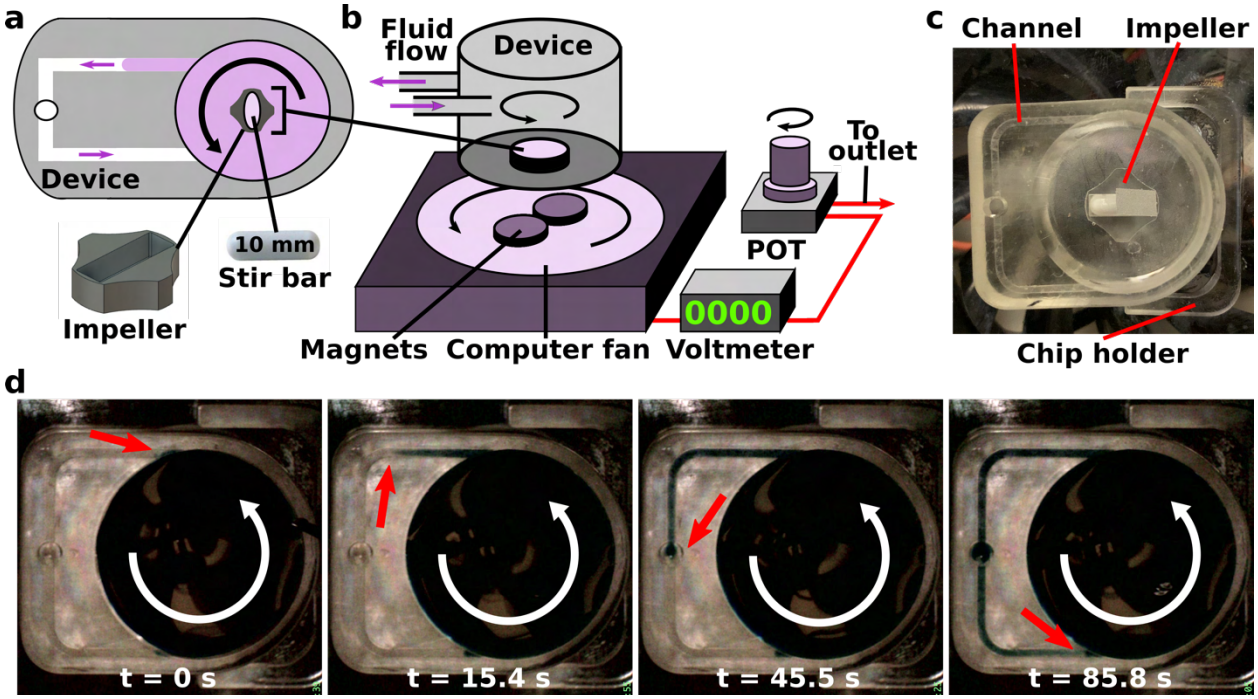

Figure 2.1 Design and prototype of the impeller pump and external pump platform. *(a) The impeller pump consisted of a magnetic stir bar inserted into a 3D-printed impeller placed within a large well on a 3D-printed microfluidic device. (b) The device was placed on top of an external pump platform, where the rotation of magnets on a computer fan caused the impeller to rotate, moving fluid through the device. The computer fan voltage was controlled using a potentiometer (POT), with voltage readout from a voltmeter. (c) An image of the device in place on the external pump platform. A reflective material was placed on half of the impeller piece to allow for RPM detection using a digital laser photo tachometer. Channel width was 1 mm. (d) Time-lapse*

images of recirculating fluid flow. The impeller rotated counter-clockwise (white arrow). Blue dye was inserted into the pump well, and over time, the dye exited the well and traveled through the channel (dye front marked with red arrow). Channel width was 1 mm.

To adapt the centrifugal pump design to be compatible with recirculating fluid flow in a microfluidic device, spinning magnets were used to drive impeller rotation. Unlike rotating the impeller using an external motor, the use of a rotating magnetic field to drive fluid flow resulted in a simple set-up that was readily compatible with microfabrication techniques. The magnetic impeller rested within a large fluid-filled well, similar to the main chamber in a centrifugal water pump, and its rotation was used to drive fluid recirculation through an attached microchannel loop (Figure 2.1). Consistent with the vorticity of the impeller-driven flow in the well, preliminary tests showed that a tangential intersection provided better flow of fluid into the channel loop than a perpendicular intersection (data not shown). The direction of the recirculating fluid flow was determined by the rotational direction of the magnetic impeller (Figure 2.2), which in turn is controlled by the direction of the rotating magnets on the external pump platform.

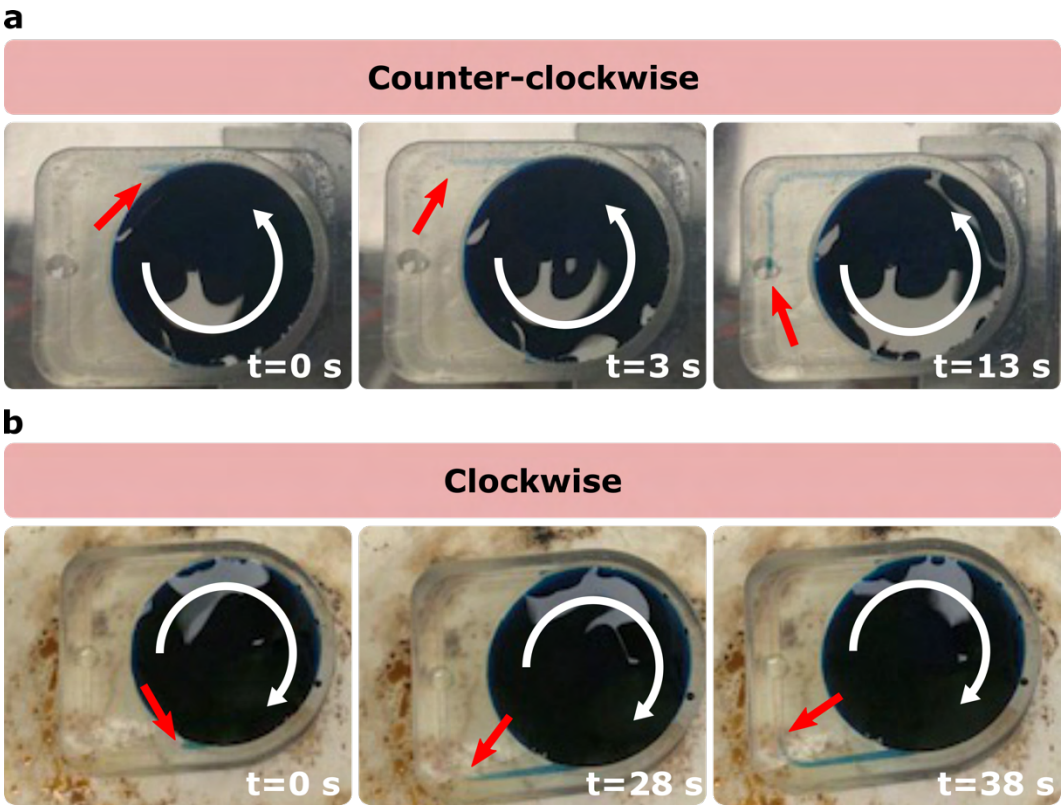

Figure 2.2 Fluid flow direction based off direction of impeller rotation. *Time-lapse images of recirculating fluid flow where the impeller rotated (a) counter-clockwise and (b) clockwise (white arrow). Blue dye was inserted into the pump well, and over time, the dye exited the well and traveled through the channel (dye front marked by red arrows). (a) Counter-clockwise impeller rotation was driven by the external pump platform (6.05 V). (b) Clockwise impeller rotation was driven by a hot plate (high stirring speed, 8). Channel width was 1 mm.*

2.4.2 Design and fabrication of the 3D-printed microfluidic device and impeller insert

To generate a microscale impeller pump for use with microfluidic technology, digital light processing (DLP) 3D printing was used to generate the microdevice and impeller-like part (Figure 2.1c). DLP 3D printing produces highly reproducible devices in a shorter timescale than traditional soft lithography, and the open-source nature of this fabrication allows for easy translation to collaborators.[45,46] Furthermore, this fabrication technique provided access to the required complex architecture, which would be challenging to produce by standard planar fabrication methods. To test the pump, we fabricated a simple chip that contained a large well that was connected to a loop of internal microchannels for recirculating fluid flow (Figure

2.1a,c). To modulate the flow resistance through the microchannel and thus access a wide range of flow rates driven by the impeller pump, we designed two versions of the device with 0.5-mm or 1-mm square channel dimensions. Optically transparent resins were selected to facilitate imaging of flow through the microchannel (Figure 2.1d). Each device print took only 1 hr with an overall materials cost of $1-3 per device, making it easy and relatively inexpensive to produce a large number of chips for experiments. The impeller took 15 min to print at a materials cost of $0.03-0.12 per impeller, and was designed to hold a 10 mm magnetic stir bar in a rectangular hole in its center (Figure 2.1a).

When designing the dimensions of the pump well, impeller, and entry points of the microchannel, we reasoned that the hydrodynamic energy produced in the pump well by the rotating impeller would decrease further from the impeller, due to viscous energy losses. Consistent with this principle, in preliminary work, we found that if the impeller filled the majority of the cross-sectional area of the well, then the hydrodynamic energy generated fluid velocities that were able to reach as high as 33,000 μm/s (Figure 2.3), sufficient to model venous or arterial fluid flow.[8,9] As we were primarily interested in slower capillary and lymphatic vessel flow velocities, a low impeller/well ratio was chosen, with a large well diameter (26 mm) relative to the smaller impeller piece (11.5 mm). Similarly, the intersection height of the channels approximately two-thirds up the side of the well (8.5 mm from the base of a 12-mm deep well) was optimized to slow the flow rates through the corresponding channel compared to a lower intersection height (Figure 2.3). In this manner, a 3-dimensional architecture for the device and impeller was achieved and optimized through rapid 3D printing, enabling the pump to attain biologically relevant fluid flow regimes.

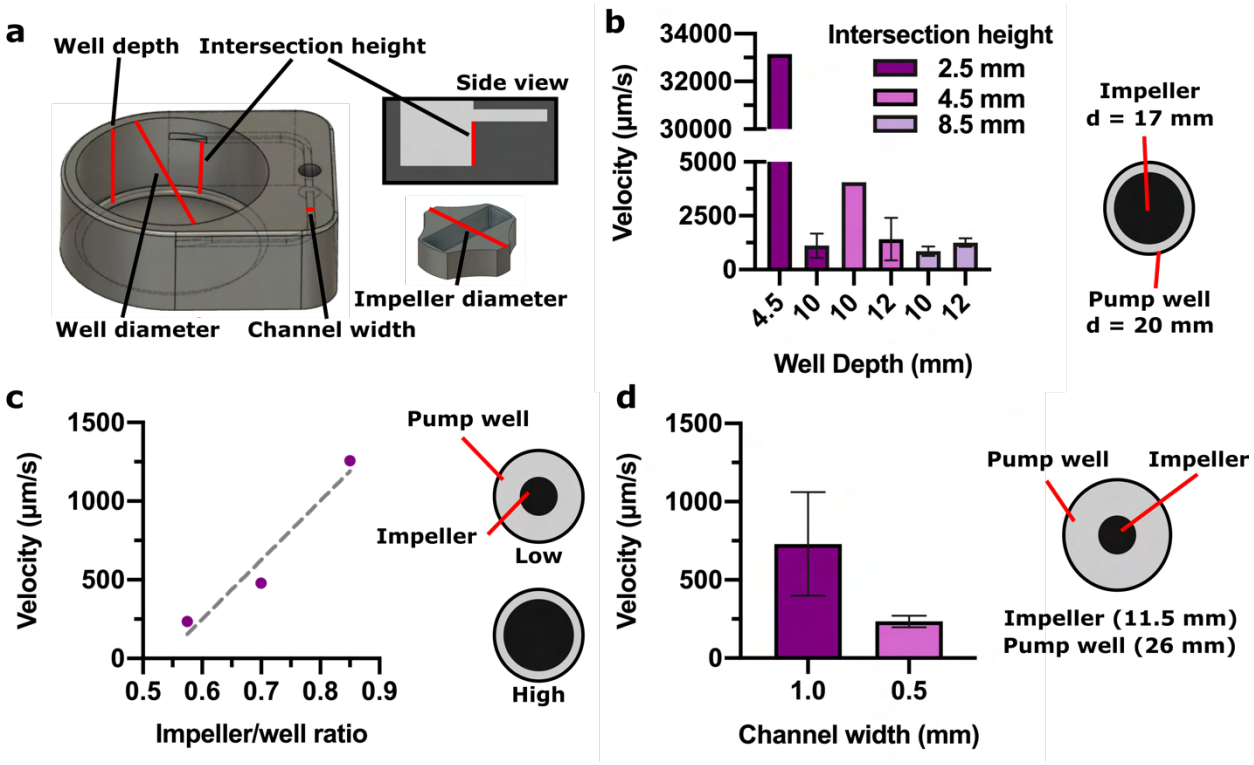

Figure 2.3 Optimization of device parameters. *Using the fluorescent bead method, the velocity across various device parameters was measured. (a) Schematic of the device and impeller piece showing the well depth, well diameter, channel-well intersection height, and impeller diameter. (b-e) Experimentally measured velocity in a water-filled device at 5.42 V when changing specific dimensions of the pump well, impeller, or microchannel. (b) Velocity as a function of well depth and intersection height, with well diameter (20 mm), channel width (1 mm), and impeller diameter (17 mm) held constant. (c) Velocity as a function of impeller/well area ratio, with channel width (1 mm), well depth (12 mm), and channel-well intersection height (8.5 mm) held constant. (d) Velocity as a function of channel dimensions, with channel-well intersection height (8.5 mm), well depth (12 mm), well diameter (26 mm), and impeller diameter (11.5 mm) held constant. The bars represent mean ± standard deviation (n = 4).*

2.4.3 Design and fabrication of the external pump platform

The primary purpose of the external pump platform was to rotate magnets at a controlled and user-selectable rotational speed. Initially, we used a small DC motor that rotated two magnets with an Arduino board to control the rotational speed. However, we found that the DC motor emitted heat over time (data not shown), so we replaced it with a computer fan, which we hypothesized would emit less heat. The two magnets were glued to the center of the fan to control the rotation of the impeller within the microfluidic device (Figure 2.1b, 2.4a). For

simplicity, a DC power adaptor was used that could be plugged into a wall outlet, and a potentiometer (POT) and voltmeter were used to provide voltage control and readout, respectively. The use of a POT and voltmeter minimized the complexity of the pump by removing the need for pump-computer interfacing to select the speeds, and allowed for the external platform to be condensed into a small overall size. To use the pump platform in a humidified incubator, the electronics needed to be sealed within an air-tight enclosure to prevent damage from the water vapor. As a result, the computer fan, POT, and voltmeter were mounted within an air-tight plastic project box (Figure 2.4a). No fluidic or pneumatic tubing was required for pump function in this device, which resulted in a pump platform that was easy to use that avoids leaks and further complications. Furthermore, the use of common, inexpensive items such as small magnetic stirrers and computer fans resulted in an overall materials cost of $50-75, and it took approximately 2 hr to assemble each pump platform. These qualities made the external impeller pump platform easy to replicate to be able to run many devices simultaneously.

Finally, to secure the location of the device relative to the location of the spinning magnets, a 3D-printed chip holder was designed and mounted on the top of the project box (Figure 2.1c). The holder was positioned such that the center of the pump well was aligned over the spinning magnets, thus ensuring stable impeller rotation. The height of the fan and magnet assembly was also fixed relative to the chip holder, thus ensuring consistent magnetic engagement.

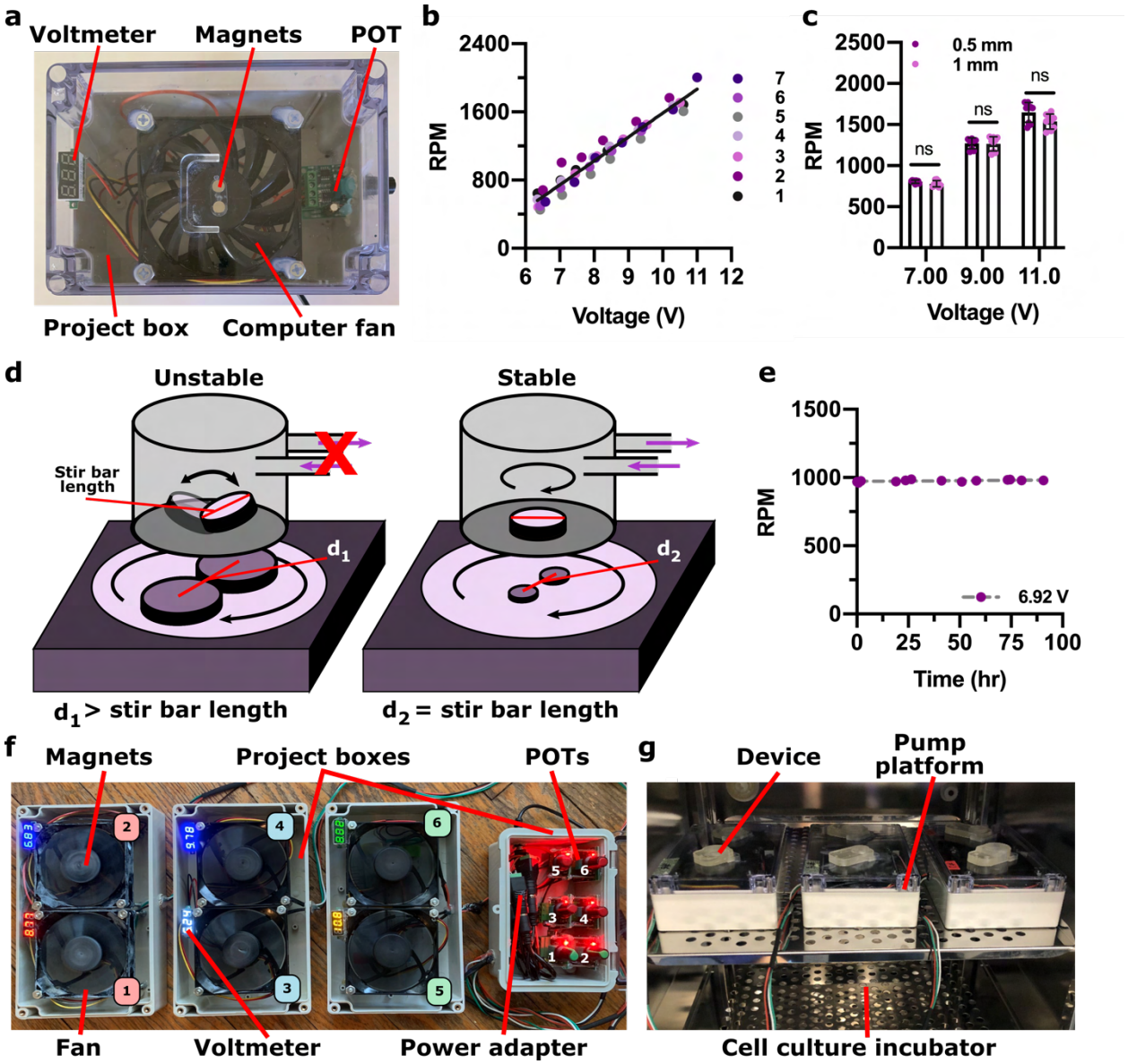

Figure 2.4 Impeller pump control and external platform expansion. *(a) An image of an external pump platform with a single computer fan in a project box with a single voltmeter and POT. (b) As the voltage increased, the RPMs increased for pumps 1-7. The black line represents the line of best fit for the entire data set (y = 281(x) - 1221, R^2 = 0.9522). (c) Impeller RPM was measured at three voltages in devices with varied channel dimensions. Results were compared using a one-way ANOVA (n = 3); ns indicates p > 0.9. (d) The distance between the center of the magnets dictated the stability of the magnetic stirrer within the impeller. When the distance (d_1) was greater than the length of the stirrer, the impeller rotation is unstable, resulting in no fluid flow. When the distance (d_2) was equal to the length of the stirrer, the impeller rotation was stable. (e) Stability of impeller rotation speed over a period of 90 hr. (f) An image of the multiplexed external pump platform with two computer fans per project box, each with their respective voltmeter. Each fan was connected to an individual POT, which were all housed in a shared hinged project box. (g) Six devices placed on a single shelf of a cell culture incubator.*

2.4.4 Tunability and stability of impeller rotation

We tested the ability to control the speed of impeller rotation by tuning the voltage provided by the potentiometer to the computer fan. A digital laser photo tachometer was used to measure the rotations per minute (RPM) of the impeller by placing a reflective material across half of the impeller (Figure 2.1c). As the impeller rotated within a water-filled well, the tachometer counted the number of times the reflective material passed through the laser emitted and provided a numerical value of the RPMs. As expected, the speed of rotation increased linearly with the voltage each computer fan received, which was read out using the voltmeter within the external pump platform (Figure 2.4b). There were variations between the RPMs across seven copies of the pump platform (root-mean-square deviation from line of best fit = 89 RPM), perhaps due to differences in the response of the computer fans to voltage supply. Since this variation was minor, the pump platforms were treated as equivalent. As expected, there was not a significant difference in impeller RPM when used in microchips with different channel dimensions at the same voltage (Figure 2.4c).

As the impeller rotated within the pump well, a vortex of fluid was generated to drive fluid through the channel. In an initial design with large magnets, we observed that unstable impeller rotation failed to form a fluidic vortex and did not drive stable fluid flow (illustrated in Figure 2.4d). In this design, the distance between the center points of the magnets (d_1 = 17.5 mm) was greater than the length of the 10 mm stir bar. To resolve this issue, smaller magnets were used to matched the center-to-center distance to the length of the stir bar (d_2 = 10 mm) (Figure 2.4d).[47] With this design, impeller rotation was stable for at least 90 hr (Figure 2.4e). The steady computer fan rotation provided nonpulsatile unidirectional fluid flow by design; if pulsatile or bidirectional fluid flow were desired, additional electronics such as Arduino could be

added to modulate the voltage the computer fan receives, or a bi-directional, low-heat motor could be used instead of the fan.

2.4.5 Scale up to a multiplexed pump platform

The impeller pump was designed to be used with OOCs, for which simultaneous use of many devices is crucial to reduce the experiment time and increase the power of biological experiments. Therefore, we tested the scale up of the external platform to run multiple micropumps simultaneously. To scale up the prototype external platform, two computer fans were mounted within a single project box. This design was easily scaled up by producing 3 project boxes (Figure 2.4f) to run 6 devices on a single shelf of a cell culture incubator (Figure 2.4g), with total space for up to 36 devices (18 boxes) in the incubator if needed. In the future, use of smaller fans or low-heat motors may enable further miniaturization of the pump platform to fit additional pumps into the incubator, but this was not explored here. We chose a design in which each computer fan was individually connected to a potentiometer so that each fan could run at different speeds. The potentiometers for all six fans were kept in a separate hinged project box that remained outside of the cell culture incubator to increase the available space within the incubator (Figure 2.4g). This feature also reduced the potential for damage of the electrical parts at 37 °C and high humidity. For simplicity, the entire multiplexed system shared a single power adapter, with the voltage split between each fan.

Finally, we tested the variation in impeller rotation across all six of the external pump platforms. Similar to the slight variation in the resulting RPMs at different voltages (Figure 2.4b), we observed variation (26% CV) in the measured fluid velocity at a fixed voltage between copies of the hand-built external pump platform (Figure 2.5). We anticipate that in experiments where accuracy of flow rate is critical, each pump platform will be screened in a quality control

step to verify that it provides flow in a specified range. Alternatively, in the future, automation of production of the platforms would likely reduce variation.

2.4.6 Negligible heat emission for long-term culture

A major design goal for the impeller pump was minimal heat emission to allow for extended cell culture within an incubator. Stable temperatures (±1°C) are critical to maintain viable cell cultures,[48] and we previously found that a peristaltic pump rapidly raised the temperature inside a culture incubator if not countered with cooling packs.[16] To test this feature of the impeller pump, the heat emission was first measured by placing the pump platform at a high rotational speed (> 10 V) or a peristaltic pump at 10 µL/min within an insulated Styrofoam box for 24 hr (Figure 2.5a). After 24 hr, the temperature within the box had increased modestly to 29.0°C with the impeller pump (temperature with no pump, 21.0°C), versus a drastic increase to 52.7°C with the peristaltic pump (Figure 2.5a).

As the pumps will primarily be used within cell culture incubators, we also tested how use of the impeller pump affected the internal temperature of an enclosed incubator. For a rigorous test, we ran six pump platforms simultaneously at a high rotational speed (>10 V) for 24 hr in the incubator. When this test was conducted with the incubator shut down, i.e., without any built-in temperature control, there was a 4°C increase in temperature near the pumps (P1), while the temperature far from the pumps remained comparable to room temperature (P2) (Figure 2.5b,c). Conducting the same test with the incubator on, i.e. to replicate cell culture circumstances, resulted in only a 0.4°C increase at the pumps (P1), which is within the ±1°C acceptable temperature window,[48] and the temperature far from the pumps remained relatively constant (Figure 2.5d). Furthermore, there was no change in the temperature reported by the cell culture incubator (37.0°C), whose sensor is located near the pumps at the top of the incubator.

Collectively, these data indicated that the multiplexed external pump platform did not emit a noticeable amount of heat and was compatible with extended use inside a cell culture incubator.[48]

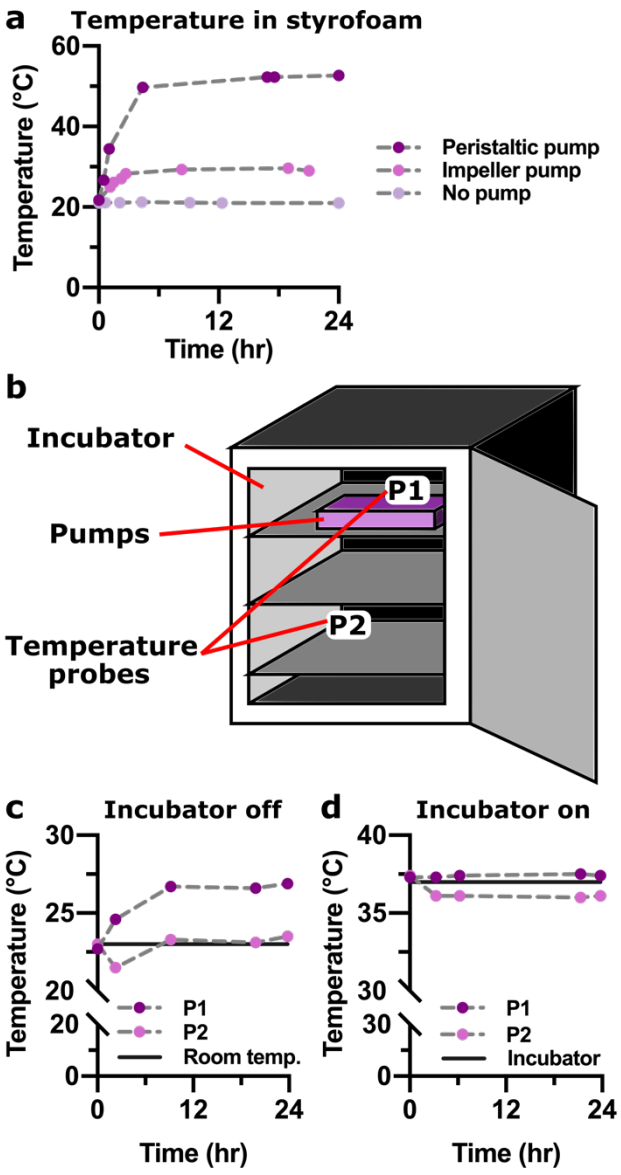

Figure 2.5 Heat emission of the impeller pump. *(a) The temperature within a closed Styrofoam box was measured with no pump, a single impeller pump platform (>10 V), and a peristaltic pump (10 µL/min) over a period of 24 hr. (b) A schematic of a cell culture incubator during the experiment. When measuring the temperature within the incubator, the six pumps were placed on the front of the top shelf to the right. The temperature was measured at the pumps on the top shelf to the right (P1) as well as in the back of the bottom shelf to the left (P2). (c,d) The temperature within a cell culture incubator was measured at positions P1 and P2 while six pumps were run (>10 V) over a period of 24 hr while the incubator was (c) off or (d) on. Black*

lines indicate room temperature (c) and the temperature readout from the incubator when it was on (d).

2.4.7 Predicted fluid flow using a computational model of the impeller pump and microfluidic chip

To model the low (~10-100 μm/s)[6] and high (1-10 mm/s)[7] fluid velocities found within blood and lymphatic vessels, the impeller pump platform must be able to control the flow rate over several orders of magnitude. To understand the factors that controlled impeller-driven fluid flow through the microfluidic device, a computational model was developed (Figure 2.6a). The frozen rotor method was used to model the spinning impeller,[41] with one rotating domain and one stationary domain to avoid discontinuities at the entry to the microchannel. The stationary domain consisted of the top of the pump well and the connecting channel (Figure 2.6bi), while the rotating domain consisted of the base of the pump well and the impeller piece (Figure 2.6bii). The mesh density for each fluid domain was determined using a grid independence study to elucidate when the physics being modeled was no longer dependent upon the mesh resolution (see Experimental). Briefly, to establish mesh independence for each channel geometry, we examined value fluctuations for key study parameters: pressure drop across the channel, mass flow rate in the channel, and fluid velocities on the channel inflow and outflow. The analysis revealed higher value fluctuations (7.6-15.3%) for coarser densities and then leveled to fluctuations of less than 5% for mesh sizes greater than 5 million elements (Figure 2.6b). A turbulence modeling approach was employed due to the strong rotational fluid dynamics in the tank reservoir and fluid velocity in the channel. To account for the effect of surface roughness, a low-Reynolds k-ω turbulence model was adopted (see Experimental). The y+ turbulence mesh parameter was also verified. Mesh quality was confirmed using standard mesh metrics (i.e., aspect ratio, skewness, element quality).

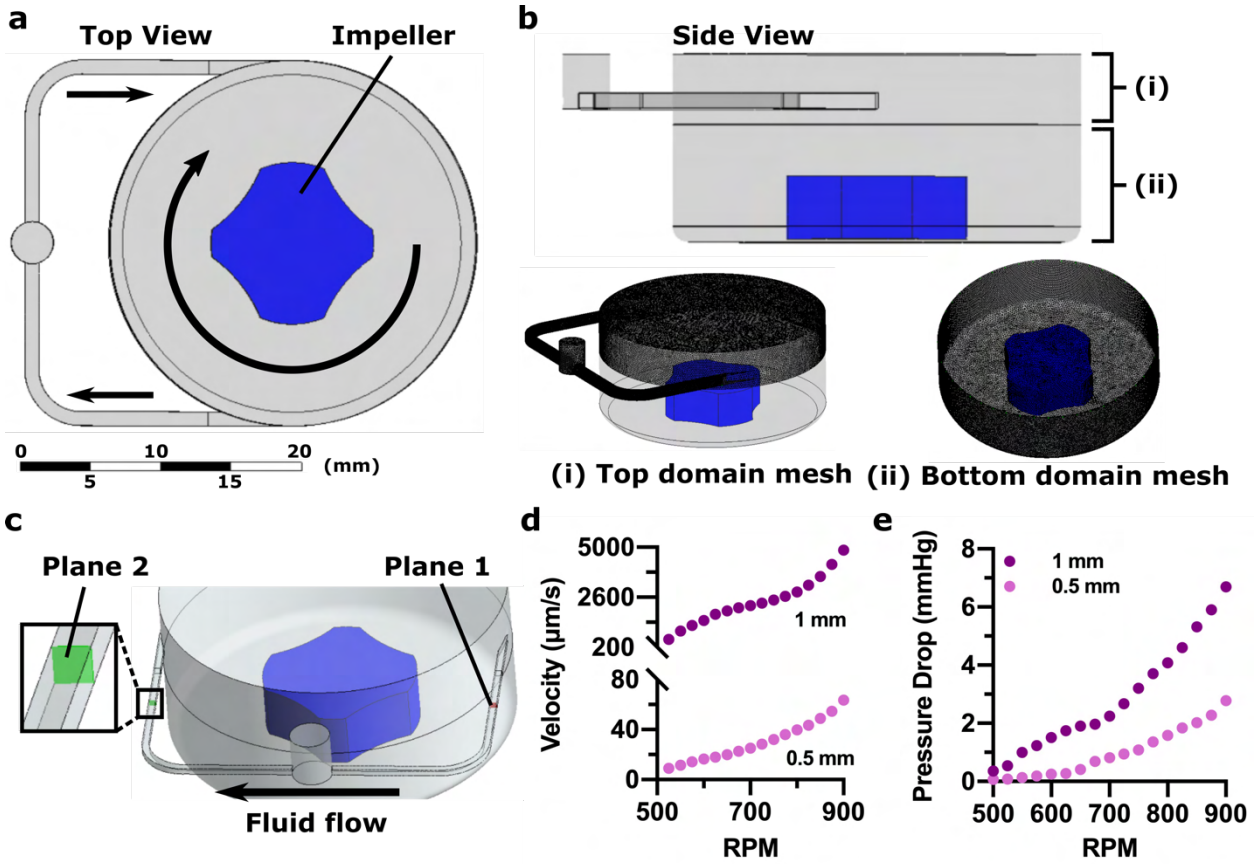

Figure 2.6 Simulated flow control with the microscale impeller pump. *(a) Top view of the fluid circuit model showing the narrow fluid channel, the impeller, and the pump well. Arrows show direction of fluid flow. (b) Side view of the fluid circuit model showing the (i) top domain mesh that contained the top of the pump well and connecting channel and (ii) the bottom domain mesh that contained the lower region of the pump well and the rotating impeller. (c) As the impeller rotated in the simulation, fluid left the pump well and crossed Plane 1, passed through the remaining channel domain, and crossed Plane 2 prior to re-entering the pump well. Flow rate and pressure drops were determined at these two locations. (d) Predicted average velocity across plane 1 and (e) predicted pressure loss between plane 1 and 2 increased with the RPM of the impeller, for both the 0.5 mm and 1 mm channel size.*

The computational model was used to predict the trends in velocity and the pressure drop across a transverse plane in the microfluidic channel as a function of these parameters (Figure 2.6c). As expected, increased rotational speed of the impeller drove increased rates of flow through the microchannels, and the larger channel size resulted in higher average velocities (580-4900 μm/s) than the smaller channel size (9-64 μm/s) (Figure 2.6d).[6,7] There was a more substantial pressure drop for the 1 mm channel, as compared to the 0.5 mm channel (Figure 2.6e); while

initially counter-intuitive, this result is consistent with Hagen-Poiseuille's law, as the increase in velocity for a larger channel size exceeded the decrease in flow resistance. Thus, these computational findings demonstrated that the flow regime can be selected by altering microfluidic circuit geometry and fine-tuned by varying the RPM.

2.4.8 Experimental fluid velocity control over two orders of magnitude

After the computational model was used to predict trends in velocity within the device, we proceeded to experimentally evaluate the velocity in the prototype experimental system across a variety of different conditions. To measure the velocity within the 3D-printed device, reservoirs were added near the pump well for dye insertion. An equilibration period was needed to achieve a consistent velocity after initially starting the impeller rotation, which was observed to be approximately 3-5 minutes. After this time, a drop of dye was inserted into the reservoir, and images were collected as the front of dye moved over time (Figure 2.7a, 2.8).

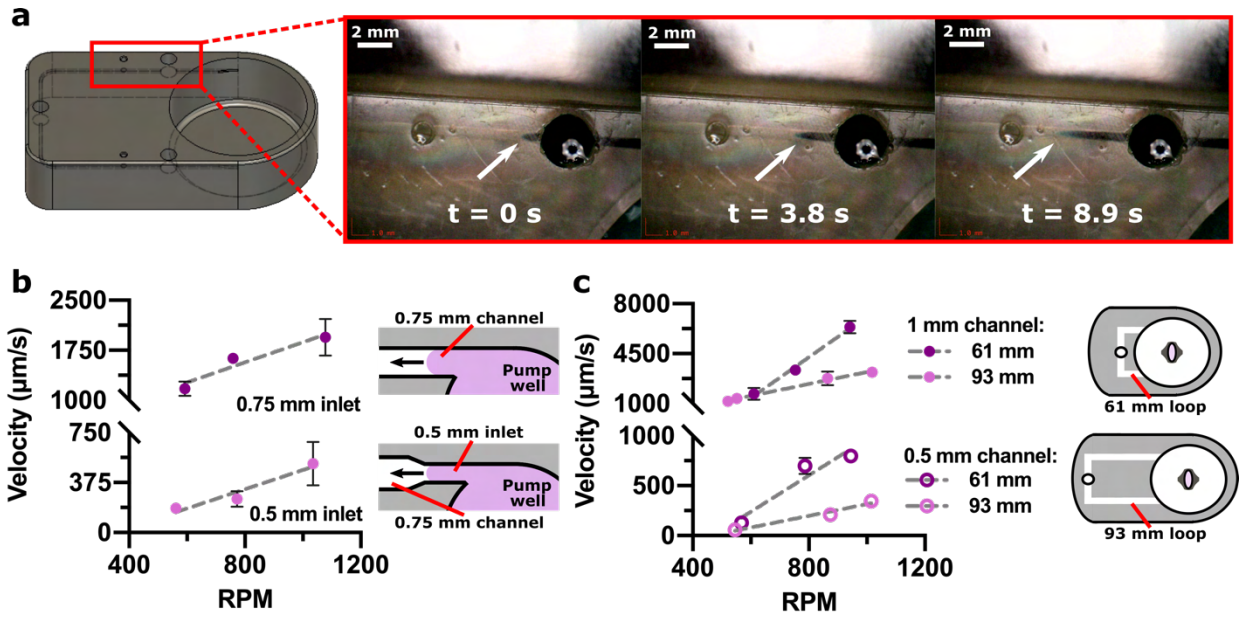

Figure 2.7 Experimental flow control with the microscale impeller pump. *(a) 3D rendering and photos of a 3D printed device (0.5 mm channel size), showing colored dye moving through the channel over time. The white arrow corresponds to the dye front as it moves away from the reservoir over time. (b) Experimentally measured maximum velocity in a 0.75-mm channel without a constriction (0.75-mm inlet; n = 3) and with a constriction (0.5-mm inlet; n = 3) increased as RPM increased. The constriction occupied 16% of the 91-mm total channel length.*

(c) Experimentally measured maximum velocity in 0.5- or 1-mm channels with varied channel length. (n = 3, except for 1 mm, 93 mm long channel where n = 4).

The maximum velocity was measured at the center point of the parabolic flow of the moving front of dye within the channels (Figure 2.8). This in situ measurement method ensured that no additional pressure drop was introduced by adding an external flow rate sensor.

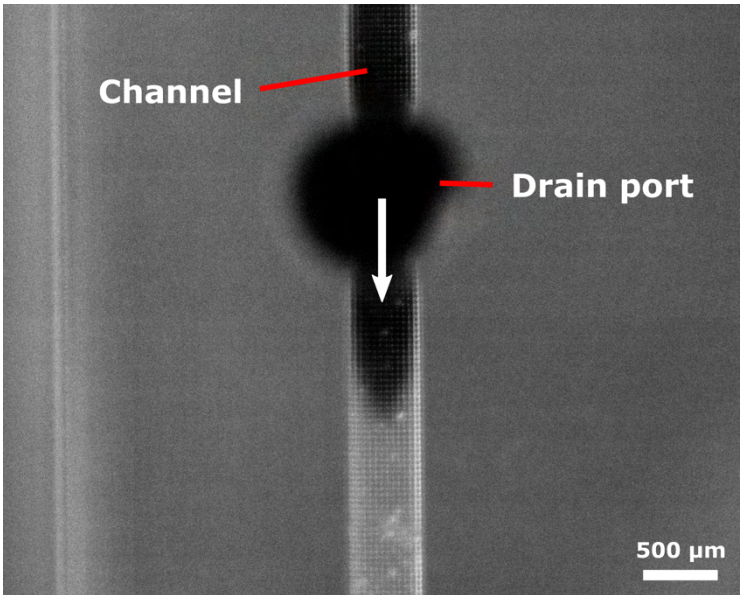

Figure 2.8 Parabolic fluid flow within the channel. *An image of the channel within the device that was pre-filled with water and injected with blue dye as the impeller rotated (7.47 V, 700 µm/s). The direction of fluid flow is marked with a white arrow. The dye moved through the 0.5 mm channel with a parabolic flow profile. Image collected with a Zeiss AxioZoom macroscope with a Axiocam 506 Mono camera.*

We reasoned that as the impeller circulated fluid within the well, a portion of the rotating fluid was pushed through the intersecting channel inlet, driving fluid into the channel. Therefore, the volumetric flow rate (mass flow) at the channel inlet should be driven by both the rotational velocity and the cross-sectional area of the entryway to the channel, with a larger cross-sectional area allowing more fluid entry. As expected, and consistent with the simulated data, the velocity within the channels increased with the rotational speed of the impeller (Figure 2.7b,c). To test the effect of the entry area on flow rate, the inlet size was varied while keeping the cross-sectional

area of the downstream channel (square cross-section) the same. Interestingly, constricting the inlet from 0.75 mm square (11.8 Pa*s/mm^3 flow resistance) to 0.5 mm square (19.8 Pa*s/mm^3) decreased the velocity measured in the channel downstream by over 6-fold (Figure 2.7b), despite the channel itself retaining the same dimensions. As the short constriction only increases flow resistance by < 2-fold, the increased resistance cannot fully account for the significant drop in velocity, so we predict that the reduced inlet area also played a role. The dependence on the cross-sectional area of the entry point in this open system is different from the behavior of pressure-driven flow in a fully closed system, which must maintain a constant volumetric flow rate.

Next, we explicitly tested the prediction that increasing the resistance within the microfluidic loop, e.g., with longer or narrower channels, would result in a lower velocity regime. The larger channel width, 1 mm (2.5 Pa*s/mm^3), resulted in a higher velocity range (1680-6400 μm/s at 61 mm) that was comparable to lymphatic vessels *in vivo* (Figure 2.7c).[7] Reducing the channel width to 0.5 mm (39.8 Pa*s/mm^3) yielded a lower velocity range (130-800 μm/s at 61 mm) that was comparable to blood vessel capillaries *in vivo* (Figure 2.7c).[6] This trend matched that of the computational model and combines an increase in flow resistance with a decrease in entry area. Lengthening the total channel from 61 mm to 93 mm (60.5 Pa*s/mm^3 for 0.5 mm channel, 3.8 Pa*s/mm^3 for 1 mm channel), which changes flow resistance alone, resulted in a slower velocity as expected, though interestingly only for higher impeller rotational speeds (Figure 2.7c), again potentially attributable to the open system.

These results confirm that changes in the resistance of the microfluidic network impact the velocity of impeller-driven flow, and also indicate that experimental calibration of flow rate versus impeller rotation speed must be performed for each microdevice design. While the

experimental trends were similar to the computational model, the magnitudes of the experimental and predicted velocities differed quantitatively, especially for the smaller channel size. We speculate that the experimental system is subject to additional forces not yet captured by the model, such as the generation of vortex flow within the pump well upon impeller rotation,[49] surface tension and wetting at the air-water interface in the pump well, varied surface roughness, and small variations in channel dimensions (Figure 2.9). While the model will be further refined in the future, changes in resins, print quality, and device architecture also would be expected to impact difficult-to-control parameters such as surface roughness and shrinkage, which alter the precise dimensions of the channels. Therefore, calibration of the velocity across a range of impeller rotational speeds should be performed for quantitative flow rate control, similar to calibration of peristaltic pumps.

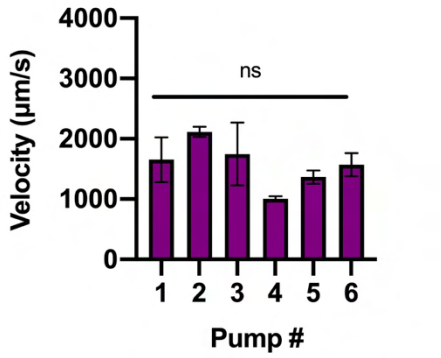

Figure 2.9 Velocity variation between replicates of the external pump platform. *Using the food coloring front method, variations in fluid velocity across 6 different copies of the external pump platform were measured at a fixed voltage of 5.6 V. The same microdevice and impeller were used across all velocity measurements. Channel width was 1 mm. The bars represent an average velocity (n = 2) and the error bars show standard deviation. Results were compared using a one-way ANOVA, ns indicates p > 0.07.*

2.4.9 Shear stress approximation across device

Having validated the trends of the computational model, we used it to predict the levels of shear stress within the device during impeller-driven fluid flow. Shear stress is a major

consideration for cell recirculation, as high shear stress can damage the cells and diminish viability. Physiological shear stress spans 0.6-12 dyn/cm^2 in lymphatic vessels and 0.35-70 dyn/cm^2 in normal blood vasculature.[7,50] 100 dyne/cm^2 is sometimes considered the threshold for pathological shear, which reaches >1500 dyn/cm^2 in diseased or stenotic vessels.[50] Using the computational model, fluid shear stress levels during high impeller rotational speeds (900 RPM) were estimated at various regions within the device. Looking at the impeller surface, 93.2% of the surface was < 100 dynes/cm^2 (Figure 2.10a), i.e. within the physiological range. The highest shear stress, 400 dynes/cm^2, was found along the edges of the impeller; we reasoned that the cells suspended in the circulating media would rarely contact the impeller surface or edges due to centrifugal forces and the large volume of the pump well. Within the channels, the surface shear stress approximations were much lower and well within the physiological range: 0.04-0.10 dynes/cm^2 in the 0.5 mm channel (Figure 2.10b), and 0.40-1.22 dynes/cm^2 in the 1 mm channel (Figure 2.10c), with the highest stress in the corners of the channel. Based off of these results, we predicted that the impeller rotation would not have a significant impact on the viability of circulating cells.

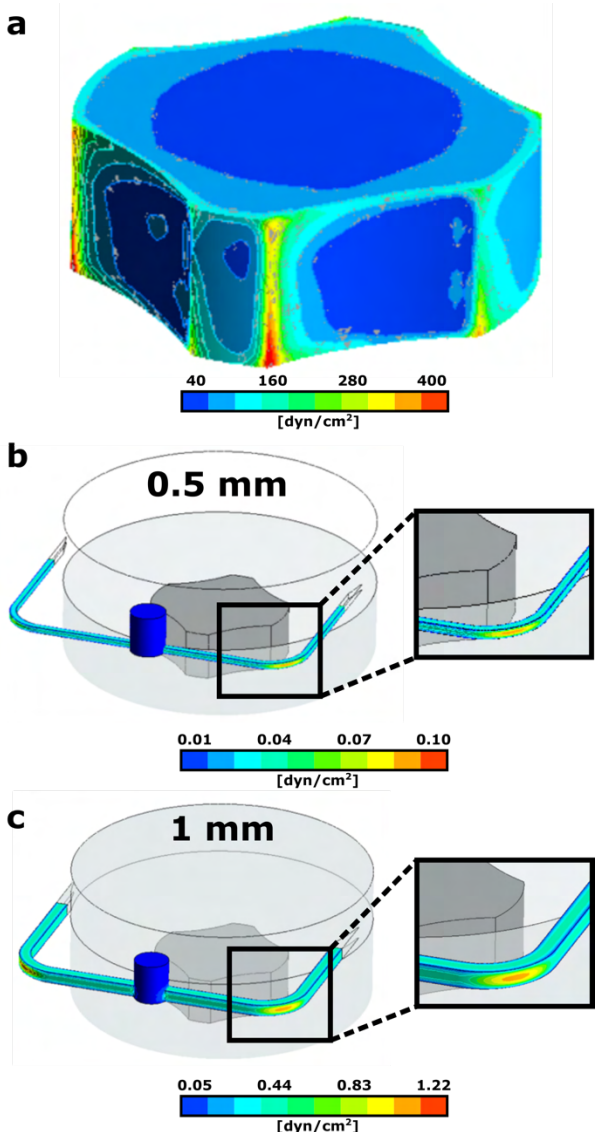

Figure 2.10 Predicted shear stress within the device. *The scalar stress was approximated using the computational model across the surface of (a) the impeller, (b) the 0.5 mm channel, (c) and the 1 mm channel. (a) Along the impeller, the highest scalar stress was present along the edges. (b,c) The scalar stress was highest at the corners of the channel in both channel designs.*

2.4.10 Selection of a sufficiently biocompatible resin for the 3D-printed micropump

As the impeller pump platform is intended to recirculate fluid and cells within OOCs and other biological model systems, the material used to fabricate the device and impeller must be cytocompatible for the timescale of the experiment. While 3D printing is an easy way to reproducibly fabricate microfluidic devices with complex architecture in a short period of time, the liquid photopolymer resins used for stereolithography (SLA) and digital light processing (DLP)

3D printing are often cytotoxic.[51] The use of additives such as optical absorbers and plasticizers can enhance the print resolution, enabling smaller internal channel sizes and smaller port diameters, such as with the MiiCraft BV007a resin, but these may result in increased toxicity if these molecules leach out of the device.[36,51–53] Some photopolymer resins designed for biomedical applications, such as FormLabs Clear, may have reduced cytotoxic additives but also reduced print resolution.[53]

To identify a cytocompatible resin for the microscale impeller pump, the device and impeller were printed in two different resins, MiiCraft BV007a and FormLabs Clear (Figure 2.11a), and tested with primary murine splenocytes as a model for circulating white blood cells. Primary splenocytes provided a rigorous cytotoxicity test because they are more susceptible to damage than immortalized cell lines. To remove cytotoxic leachates, the BV007a and Clear devices were soaked in PBS for 24 hr at 37°C and 70°C, respectively ("post-treatment") prior to use.[36,53] After 4 hr of culture in complete media in the pump well without impeller rotation, primary splenocytes cultured on the BV007a piece had significantly decreased viability compared to off-chip controls, with less than 30% viable cells (Figure 2.11b). In contrast, culture on the Clear piece yielded no significant difference in viability compared to the off-chip controls, though there was a non-significant drop (Figure 2.11b).

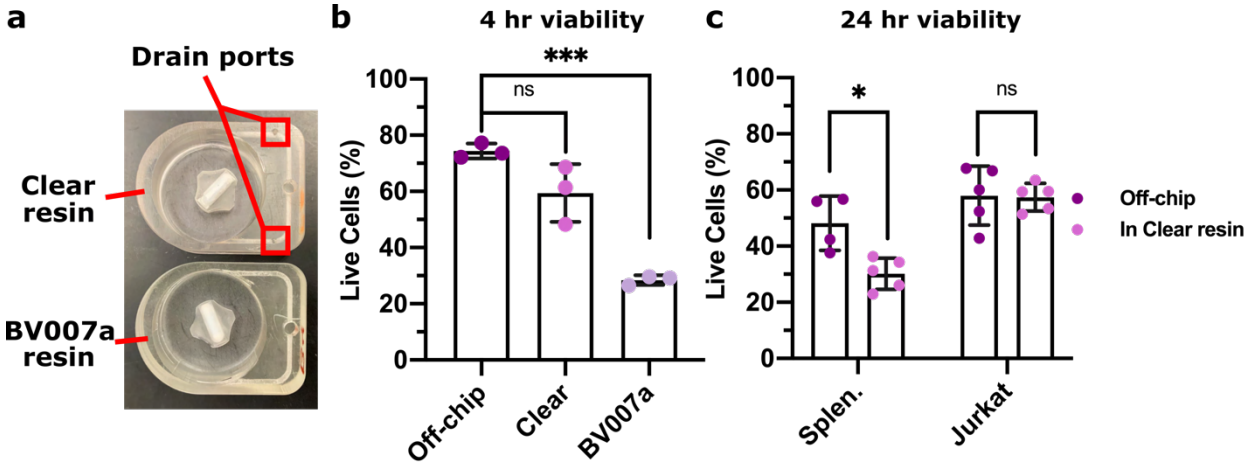

Figure 2.11 Assessment of the biocompatibility of 3D-printed pump chambers with primary splenocytes and an immortalized lymphocyte cell line. *(a) Image of devices printed in the Clear resin and BV007a resin for cytotoxicity testing. The device printed in the Clear resin required drain ports along the channel to print internal channels. (b) Primary splenocytes were cultured for 4 hr without impeller rotation in devices post-treated with a 24 hr soak, and viability was analyzed by flow cytometry. Quantification of live (7-AAD^{low}) cells after culture off-chip, in the Clear pump well, or in the BV007a pump well. Results were compared using a one-way ANOVA with Tukey post-hoc tests (n = 3). *** indicates p <0.0006; ns indicates p > 0.08. (c) Primary splenocytes (Splen.) and Jurkat T cells were cultured for 24 hr without impeller rotation in devices printed using the Clear resin with a 10-day post-treatment ,and viability was analyzed by flow cytometry. Quantification of live (7-AAD^{low}) cells after culture both off-chip and in resin for both cell types. Results were compared using a one-way ANOVA with Tukey post-hoc tests (n = 5, except for off-chip splenocytes where n = 4). * indicates p < 0.02; ns indicates p > 0.2.*

Having identified the Clear resin as the more promising material, we further tested it for overnight cell culture using primary and immortalized cells, since the latter are hardier. To ensure that all possible leachates were removed, devices printed in the Clear resin were soaked in PBS for 8 days and then in media for 2 days at 37°C, according to a published protocol.[37] Primary murine splenocytes and Jurkat T cells were cultured within the 3D-printed microfluidic pump wells for 24 hr without impeller rotation. Whereas primary splenocytes showed a significant decrease in viability, the viability of Jurkat T cells was not significantly different compared to off-chip controls (Figure 2.11c). Therefore, we concluded that the Clear resin was sufficiently compatible for use in experiments of 4 hr or shorter duration with primary cells, and that the use of cell lines expanded compatibility to at least 24 hr. Biocompatibility of SLA/DLP resins for primary cell culture was improved in our lab and others using parylene C coating, discussed here in **Chapters 3** and **4**.

2.4.11 Recirculation of lymphocytes under biomimetic flow regimes

Cell recirculation is a key feature of inter-organ communication *in vivo,* and a new pump for organs on chip should be able to drive cell recirculation without impairing viability. Here, we tested the ability of the impeller pump to drive continuous white blood cell recirculation under fluid velocities found within lymphatic vessels and vasculature *in vivo*. Given the depth and size

of the pump well, it was possible that cells would settle to the bottom of the pump well instead of remaining suspended for recirculation through the microfluidic channel, especially at low RPM. To address this concern, primary splenocytes were stained with Calcein AM and deliberately allowed to settle to the base of the pump well of a pre-filled device while the impeller was off (Figure 2.12a). Imaging at this time confirmed that the cells settled along the base of the pump well (Figure 2.12b) and that no cells were present within the channels (Figure 2.12c). Once the impeller began to rotate at a low rotational speed (6.20 V, 420 RPM), the cells resting on the base of the pump well were resuspended and began to recirculate through the channels, where they were visible entering the reservoir (Figure 2.12d). Cells moved much faster through the 1-mm channel, as evidenced by the blurring of fluorescently-labeled cells moving through the center of the reservoir, than through the 0.5 mm channel, consistent with the slower flow rate in narrower channels (Figure 2.12d). Thus, the rotation of the impeller pump successfully resuspended cells even from rest and achieved continuous cell recirculation through the device.

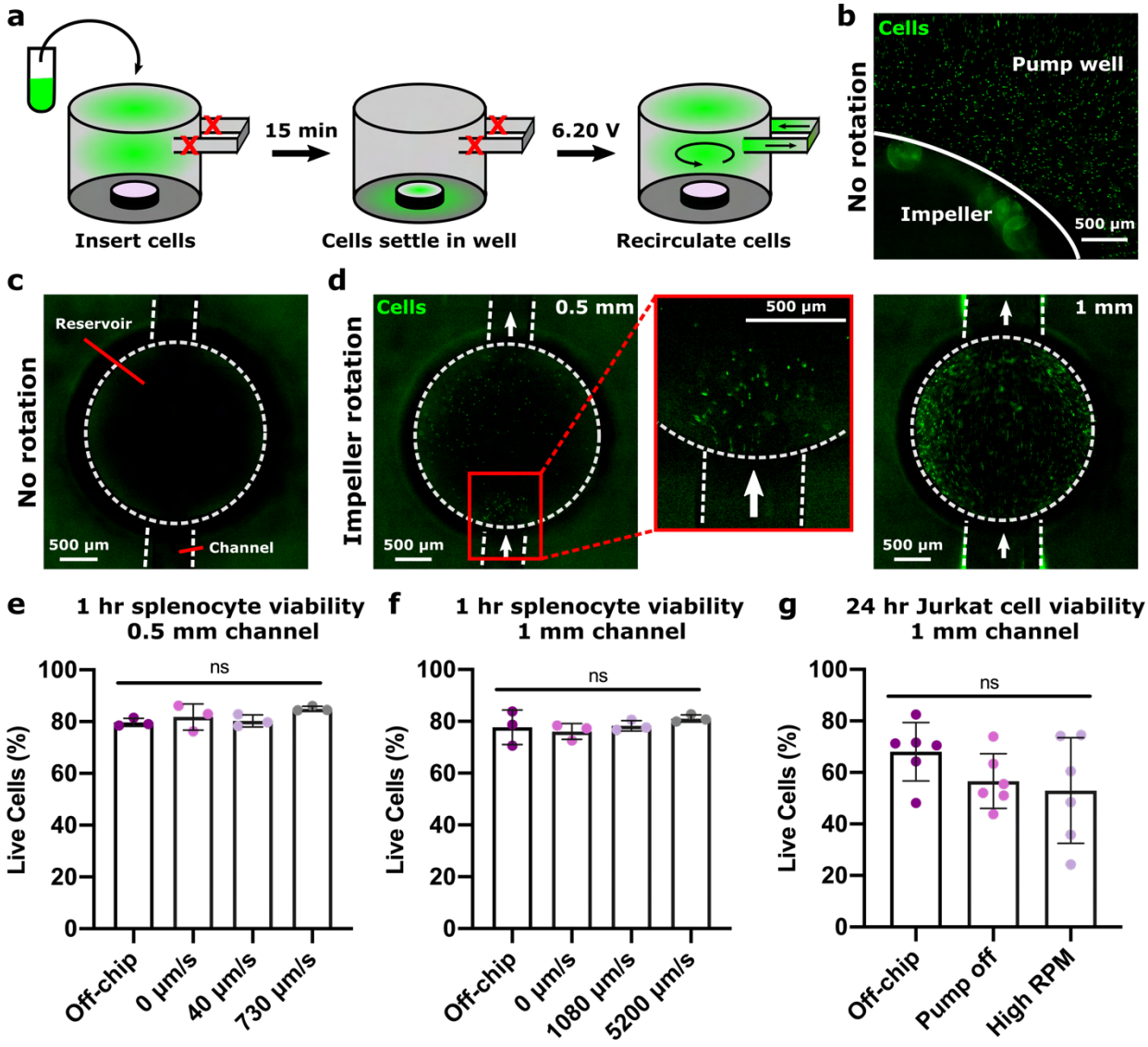

Figure 2.12 Recirculating cells under different flow regimes. *(a) Schematic of the cell recirculation procedure. Cells were labeled with Calcein-AM and inserted into the pump well of a pre-filled device with no impeller rotation. (b) Image of the fluorescently-labelled cells resting on the base of the pump well after a 15 min rest period with the pump off. (c) Image of the reservoir in the channel of the device with no impeller rotation. There are no cells present. (d) Images of cells passing through the reservoir as the impeller rotated for devices with 0.5 mm channels (left, expanded in center) and 1 mm channels (right). (e,f) Quantification by flow cytometry of live (7-AAD^{low}) primary murine splenocytes cultured for 1 hr off-chip, on-chip with no impeller rotation, or circulated at low (6.10 V, 490 RPM) or high speed (7.45 V, 870 RPM) through (e) 0.5 mm channels or (f) 1 mm channels. Viability results were compared using a one-way ANOVA with Tukey post-hoc tests (n = 3). ns indicates p > 0.1. (g) Quantification by flow cytometry of live (7-AAD^{low}) Jurkat T cells cultured for 24 hr off-chip, on-chip with no impeller rotation, or circulated at high impeller RPM (870 RPM, 5200 µm/s) through 1 mm channels. Viability results were compared using a one-way ANOVA with Tukey post-hoc tests (n = 6). ns indicates p > 0.2.*

Next, we tested the impact of impeller rotation at various biomimetic fluid velocities on viability of primary splenocytes. We hypothesized that 1 hr would be sufficient to see any impact on cell viability from mechanical damage from impeller rotation. Cells were continuously recirculated through the chip (24-hr post-treated, FormLabs Clear) by the impeller pump for 1 hr, while the whole system was inside a cell culture incubator. Based on the results above, a 0.5 mm channel was used to achieve low velocities similar to those measured within blood capillaries *in vivo* (Figure 2.12e),[5] and a 1 mm channel was used to achieve higher velocities similar to those measured within lymphatic vessels *in vivo* (Figure 2.12f).[7] Compared to the off-chip control and cells in the pump well without impeller rotation, there were no significant differences in viability for the cells in fluid moving at 40 μm/s (shear stress of 0.0003 dynes/cm^2), 730 μm/s (0.005 dynes/cm^2), 1080 μm/s (0.03 dynes/cm^2), or 5200 μm/s (0.16 dynes/cm^2) (Figure 2.12e,f). The shear stresses listed are estimated from the flow rate in the channel, which is separate from any stress imparted on cells from impeller rotation (Figure 2.10). We concluded the impeller-driven micropump did not cause mechanical damage to primary cells even at the higher impeller rotational speeds or flow velocities.

Finally, to model long-term white blood cell recirculation and further test the rotating impeller's impact on cell viability, Jurkat T cells were circulated at a high speed for 24 hr using the impeller pump platform. The T cells were continuously recirculated on-chip (10-day post-treated, FormLabs Clear resin) at a high impeller rotational speed (7.45 V, 870 RPM, 5200 μm/s, 0.3 dynes/cm^2) through 1-mm channels (Figure 2.12g). Recirculation and impeller rotation did not significantly reduce the viability of the cells compared to static culture in the pump well or off-chip controls (Figure 2.12g), although variability was high. Variability may be related to the inherent differences between copies of the pump platforms (Figure 2.5), e.g., due to slight

variations in impeller RPM, though this was not tested here. In summary, the microscale impeller pump provided cell recirculation at high impeller rotational speeds for at least 24 hr, making it suitable for future use in microscale cultures and OOCs. We note that separate from compatibility of the resin, the compatibility of impeller-driven recirculation may vary as a function of cell type and impeller speed, and should be tested for each cell type and flow rate of interest.

2.5 Conclusions

Here, we have reported a novel and user-friendly magnetically driven impeller pump system for recirculating fluid flow through microfluidic devices. The pump design allowed for the use of inexpensive parts to enable magnetic impeller rotation, which resulted in a simple user interface, no tubing connections, and negligible heat output, making the pump compatible with cell culture incubators. A computational model of the impeller pump was developed to predict the fluid flow through the pump and associated microfluidic chip by using a frozen rotor approach. By varying the dimensions of the channel and inlet as well as the rotational velocity of the impeller, the impeller pump achieved a wide range of physiologically relevant flow rates, from <50 to >5200 μm/s, and the trends of flow rate as a function of channel cross-sectional area and impeller speed were comparable to the predictions of the computational model. The model predicted low shear stress in the microfluidic channels, with the highest shear at the edges of the rotating impeller where cells were not concentrated, suggesting biocompatibility of the system with recirculating cells. As a proof-of-concept, primary murine splenocytes and Jurkat T cells were recirculated through a microfluidic chip at various biomimetic fluid flow regimes while maintaining high cell viability for up to 24 hr. Current limitations of this technology include a large on-chip volume, minor variability between pumps, inconsistent fluid flow direction, and

high shear stress around the rotating impeller. In the future, the impeller pump will be further optimized to drive recirculating fluid flow through multi-organ-on-chip platforms to model communication between tissues on-chip.

2.6 References

1. Watson, D. E., Hunziker, R. & Wikswo, J. P. Fitting tissue chips and microphysiological systems into the grand scheme of medicine, biology, pharmacology, and toxicology. *Exp Biol Med (Maywood)* **242**, 1559–1572 (2017).
2. Bhatia, S. N. & Ingber, D. E. Microfluidic organs-on-chips. *Nat Biotechnol* **32**, 760–772 (2014).
3. Buerck, J. P. *et al.* A Flow Induced Autoimmune Response and Accelerated Senescence of Red Blood Cells in Cardiovascular Devices. *Sci Rep* **9**, 19443 (2019).
4. Munson, J. & Shieh, A. Interstitial fluid flow in cancer: implications for disease progression and treatment. *CMAR* 317 (2014) doi:10.2147/CMAR.S65444.
5. Leu, A. J., Berk, D. A., Yuan, F. & Jain, R. K. Flow velocity in the superficial lymphatic network of the mouse tail. *American Journal of Physiology-Heart and Circulatory Physiology* **267**, H1507–H1513 (1994).
6. Nuttall, A. L. Velocity of red blood cell flow in capillaries of the guinea pig cochlea. *Hearing Research* **27**, 121–128 (1987).
7. Dixon, J. B. *et al.* Lymph Flow, Shear Stress, and Lymphocyte Velocity in Rat Mesenteric Prenodal Lymphatics. *Microcirculation* **13**, 597–610 (2006).

8. Klarhöfer, M., Csapo, B., Balassy, Cs., Szeles, J. C. & Moser, E. High-resolution blood flow velocity measurements in the human finger: Blood Flow Velocities in the Human Finger. *Magn. Reson. Med.* **45**, 716–719 (2001).
9. Lacy, J. Development and validation of a novel technique for murine first-pass radionuclide angiography with a fast multiwire camera and tantalum 178. *Journal of Nuclear Cardiology* **8**, 171–181 (2001).
10. Pisano, M., Triacca, V., Barbee, K. A. & Swartz, M. A. An in vitro model of the tumor–lymphatic microenvironment with simultaneous transendothelial and luminal flows reveals mechanisms of flow enhanced invasion. *Integr. Biol.* **7**, 525–533 (2015).
11. Malek, A. M. Hemodynamic Shear Stress and Its Role in Atherosclerosis. *JAMA* **282**, 2035 (1999).
12. Wasson, E. M., Dubbin, K. & Moya, M. L. Go with the flow: modeling unique biological flows in engineered *in vitro* platforms. *Lab Chip* 10.1039.D1LC00014D (2021) doi:10.1039/D1LC00014D.
13. Bhargava, K., Ermagan, R., Thompson, B., Friedman, A. & Malmstadt, N. Modular, Discrete Micromixer Elements Fabricated by 3D Printing. *Micromachines* **8**, 137 (2017).
14. Owens, C. E. & Hart, A. J. High-precision modular microfluidics by micromilling of interlocking injection-molded blocks. *Lab on a Chip* **18**, 890–901 (2018).
15. Skardal, A. *et al.* Multi-tissue interactions in an integrated three-tissue organ-on-a-chip platform. *Scientific Reports* **7**, (2017).
16. Shim, S., Belanger, M. C., Harris, A. R., Munson, J. M. & Pompano, R. R. Two-way communication between ex vivo tissues on a microfluidic chip: application to tumor–lymph node interaction. *Lab on a Chip* **19**, 1013–1026 (2019).

17. Miller, D. R. *et al.* A bistable, multiport valve enables microformulators creating microclinical analyzers that reveal aberrant glutamate metabolism in astrocytes derived from a tuberous sclerosis patient. *Sensors and Actuators B: Chemical* **341**, 129972 (2021).
18. Ong, L. J. Y. *et al.* A pump-free microfluidic 3D perfusion platform for the efficient differentiation of human hepatocyte-like cells: Pump-Free Microfluidic 3D Perfusion Platform. *Biotechnology and Bioengineering* **114**, 2360–2370 (2017).
19. Edington, C. D. *et al.* Interconnected Microphysiological Systems for Quantitative Biology and Pharmacology Studies. *Sci Rep* **8**, 4530 (2018).
20. Satoh, T. *et al.* A multi-throughput multi-organ-on-a-chip system on a plate formatted pneumatic pressure-driven medium circulation platform. *Lab Chip* **18**, 115–125 (2018).
21. Maschmeyer, I. *et al.* A four-organ-chip for interconnected long-term co-culture of human intestine, liver, skin and kidney equivalents. *Lab on a Chip* **15**, 2688–2699 (2015).
22. Ong, L. J. Y. *et al.* Self-aligning Tetris-Like (TILE) modular microfluidic platform for mimicking multi-organ interactions. *Lab Chip* **19**, 2178–2191 (2019).
23. Oleaga, C. *et al.* Investigation of the effect of hepatic metabolism on off-target cardiotoxicity in a multi-organ human-on-a-chip system. *Biomaterials* **182**, 176–190 (2018).
24. Esch, M. B., Ueno, H., Applegate, D. R. & Shuler, M. L. Modular, pumpless body-on-a-chip platform for the co-culture of GI tract epithelium and 3D primary liver tissue. *Lab Chip* **16**, 2719–2729 (2016).
25. Wang, Y. I. & Shuler, M. L. UniChip enables long-term recirculating unidirectional perfusion with gravity-driven flow for microphysiological systems. *Lab Chip* **18**, 2563–2574 (2018).

26. Narayanamurthy, V. Advances in passively driven microfluidics and lab-on-chip devices: a comprehensive literature review and patent analysis. *RSC Advances* 29 (2020).
27. Ryu, K. S., Shaikh, K., Goluch, E., Fan, Z. & Liu, C. Micro magnetic stir-bar mixer integrated with parylene microfluidic channels. *Lab Chip* **4**, 608 (2004).
28. Kimura, H., Yamamoto, T., Sakai, H., Sakai, Y. & Fujii, T. An integrated microfluidic system for long-term perfusion culture and on-line monitoring of intestinal tissue models. *Lab on a Chip* **8**, 741 (2008).
29. Shinha, K. *et al.* A Kinetic Pump Integrated Microfluidic Plate (KIM-Plate) with High Usability for Cell Culture-Based Multiorgan Microphysiological Systems. *Micromachines* **12**, 1007 (2021).
30. Kimura, H., Ikeda, T., Nakayama, H., Sakai, Y. & Fujii, T. An On-Chip Small Intestine–Liver Model for Pharmacokinetic Studies. *Journal of Laboratory Automation* **20**, 265–273 (2015).
31. Catterton, M. A., Montalbine, A. N. & Pompano, R. R. Selective Fluorination of the Surface of Polymeric Materials after Stereolithography 3D Printing. *Langmuir* acs.langmuir.1c00625 (2021) doi:10.1021/acs.langmuir.1c00625.
32. Hirschhorn, M., Bisirri, E., Stevens, R. & Throckmorton, A. L. Fluid-structure interaction analysis of a collapsible axial flow blood pump impeller and protective cage for Fontan patients. *Artif Organs* **44**, (2020).
33. Bludszuweit, C. Three-Dimensional Numerical Prediction of Stress Loading of Blood Particles in a Centrifugal Pump. *Artif Organs* (1995) doi:https://doi-org.proxy01.its.virginia.edu/10.1111/j.1525-1594.1995.tb02386.x.

34. Throckmorton, A. L. & Untaroiu, A. CFD Analysis of a Mag-Lev Ventricular Assist Device for Infants and Children: Fourth Generation Design. *ASAIO Journal* **54**, 423–431 (2008).
35. Oh, K. W., Lee, K., Ahn, B. & Furlani, E. P. Design of pressure-driven microfluidic networks using electric circuit analogy. *Lab Chip* **12**, 515–545 (2012).
36. Hart, C., Didier, C. M., Sommerhage, F. & Rajaraman, S. Biocompatibility of Blank, Post-Processed and Coated 3D Printed Resin Structures with Electrogenic Cells. *Biosensors* **10**, 152 (2020).
37. Rimington, R. P. *et al.* Feasibility and Biocompatibility of 3D-Printed Photopolymerized and Laser Sintered Polymers for Neuronal, Myogenic, and Hepatic Cell Types. *Macromol. Biosci.* **18**, 1800113 (2018).
38. Ball, A. G., Belanger, M. C. & Pompano, R. R. Detergent wash improves vaccinated lymph node handling ex vivo. *Journal of Immunological Methods* **489**, 112943 (2021).
39. Varma, S. & Voldman, J. A cell-based sensor of fluid shear stress for microfluidics. *Lab Chip* **15**, 1563–1573 (2015).
40. Kusiak, J. L., Seevers, J. E. & Corporation, A. Centrifugal Water Pump. 8 (1990).
41. Fox, C. *et al.* New versatile dual-support pediatric heart pump. *Artif Organs* **43**, 1055–1064 (2019).
42. Kim, S. *et al.* Monolithic 3D micromixer with an impeller for glass microfluidic systems. *Lab Chip* **20**, 4474–4485 (2020).
43. Joswig, L., Vellekoop, M. J. & Lucklum, F. Miniature 3D-Printed Centrifugal Pump with Non-Contact Electromagnetic Actuation. *Micromachines* **10**, 631 (2019).
44. Xue, R. *et al.* Small universal mechanical module driven by a liquid metal droplet. *Lab Chip* 10.1039.D1LC00206F (2021) doi:10.1039/D1LC00206F.

45. Amin, R. *et al.* 3D-printed microfluidic devices. *Biofabrication* **8**, 022001 (2016).
46. Au, A. K., Bhattacharjee, N., Horowitz, L. F., Chang, T. C. & Folch, A. 3D-printed microfluidic automation. *Lab Chip* **15**, 1934–1941 (2015).
47. Stir Bars. *K&J Magnetics, Inc.* https://www.kjmagnetics.com/blog.asp?p=stir-bars.
48. Sureshkumar, G. K. & Mutharasan, R. The influence of temperature on a mouse-mouse hybridoma growth and monoclonal antibody production. *Biotechnol. Bioeng.* **37**, 292–295 (1991).
49. Halász, G., Gyüre, B., Jánosi, I. M., Szabó, K. G. & Tél, T. Vortex flow generated by a magnetic stirrer. *American Journal of Physics* **75**, 1092–1098 (2007).
50. Sakariassen, K. S., Orning, L. & Turitto, V. T. The impact of blood shear rate on arterial thrombus formation. *Future Science OA* **1**, fso.15.28 (2015).
51. Carve, M. & Wlodkowic, D. 3D-Printed Chips: Compatibility of Additive Manufacturing Photopolymeric Substrata with Biological Applications. *Micromachines* **9**, 91 (2018).
52. Voet, V. S. D. *et al.* Biobased Acrylate Photocurable Resin Formulation for Stereolithography 3D Printing. *ACS Omega* 6 (2018).
53. Musgrove, Hannah. B., Catterton, Megan. A. & Pompano, Rebecca. R. Applied tutorial for the design and fabrication of biomicrofluidic devices by resin 3D printing. *Analytica Chimica Acta* **1209**, 339842 (2022).

Chapter 3. Optimization of photopolymerizable resin formulation and treatment to improve biocompatibility for primary immune cell culture

Some figures adapted from:

Musgrove, H. B., Cook, S. R., & Pompano, R. R. *ACS Applied Bio Materials*, 6, 8 (2023)

3.1 Abstract

While 3D printing is becoming more commonplace for biomicrofluidics fabrication, many 3D-printed devices have high levels of toxicity for use with cell culture. Established methods to improve biocompatibility were tested with hardy cell lines, but these materials remain toxic for more sensitive cells, i.e. immune cells. Here, we reduced 3D-printed material toxicity by testing house-made resin formulations, post-treatments, and biocompatible coating with primary immune cells, a rigorous benchmark for cell viability. We found that coating the devices with parylene C maintained cell viability, while the post-treatments and house-made resin remained toxic for sensitive cells.

3.2 Introduction

For the last few decades, microfluidic technology has gained popularity for biomedical applications due to the ability to model a wide variety of biologically relevant events (e.g. cell chemotaxis when exposed to a molecular gradient)[1] and environments (e.g. fluid flow through an endothelialized channel).[2] These devices are commonly fabricated using molding techniques such as soft lithography with polydimethylsiloxane (PDMS), which results in a biocompatible, but planar, device.[3] However, due to the manual fabrication process, it is challenging for biology-centered collaborators to utilize this technology.[3,4] Stereolithographic (SL) 3D printing has become a viable alternative fabrication method, where users can design assembly-free

devices with complex, 3D architecture using a technique geared towards reproducible rapid prototyping of small batches of chips.[3,5]

SL 3D printing, or resin printing, is a form of additive manufacturing where photocrosslinkable resins are cured into a monolithic device by exposing the liquid resin to UV light in sequential layers based off of a digital device design.[4,5] Digital light processing (DLP) 3D printing is a form of SL printing where a digital light source projects UV light in the shape of a design layer by layer into the vat of liquid resin to build up the 3D object, unlike traditional SL printers that use a scanning UV laser as a light source. Each photocurable resin consists of two key ingredients: a monomer base and a photoinitiator (Figure 3.1a). When exposed to a specific wavelength of light, the photoinitiator will form a radical and react with carbon-carbon double bonds on the monomer to form polymeric chains, eventually resulting in a solid material. Along with these components, there are common additives included in resin such as photoabsorbers to improve print resolution, plasticizers to make the final print less brittle, and more (Figure 3.1a).

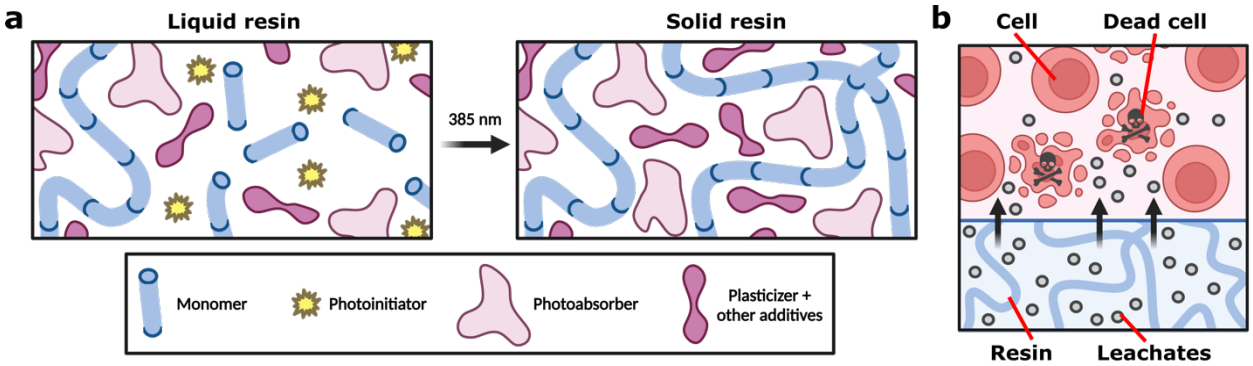

Figure 3.1 Principles of photocrosslinkable resin for 3D printing. *(a) Resin is typically comprised of acrylate-based monomers, photoinitiator, photoabsorber, and other additives. When exposed to UV light, the resin polymerizes to form a solid material. (b) 3D-printed materials are cytotoxic when used for cell culture due to the leaching of harmful resin components (Created using BioRender.com).*

A common issue with 3D printing for use with biomicrofluidics is that unbound toxic compounds will leach out of the material resulting in a significant drop in cell viability (Figure 3.1b).[3,4,6–8] The unbound compounds could be leftover monomer, initiator, or radical species as

well as any resin additives.[9,10] With commercially available resins, this may be especially challenging as there can be many different additives that are a mystery due to a proprietary recipe.

As resin toxicity is a major roadblock for many researchers, there are a few common approaches to improve this issue: 1) leach out (or bind) all of the unbound toxins, 2) develop a house-made resin using biocompatible materials, and 3) coat the device to block the release of toxic leachates (Figure 3.2). However, none of these methods have been shown to be universally effective for a wide variety of cell types including sensitive immune cells. Here, we aimed to improve resin cytotoxicity for primary immune cells by testing poly(ethylene glycol) diacrylate (PEGDA) house-made resins developed previously in the Folch[4] and Nordin[7] labs with a variety of post-treatments (e.g. 24 hr soak or UV exposure)[5] as well as coating the printed material in parylene-C, an established biocompatible impermeable coating.[10,11]

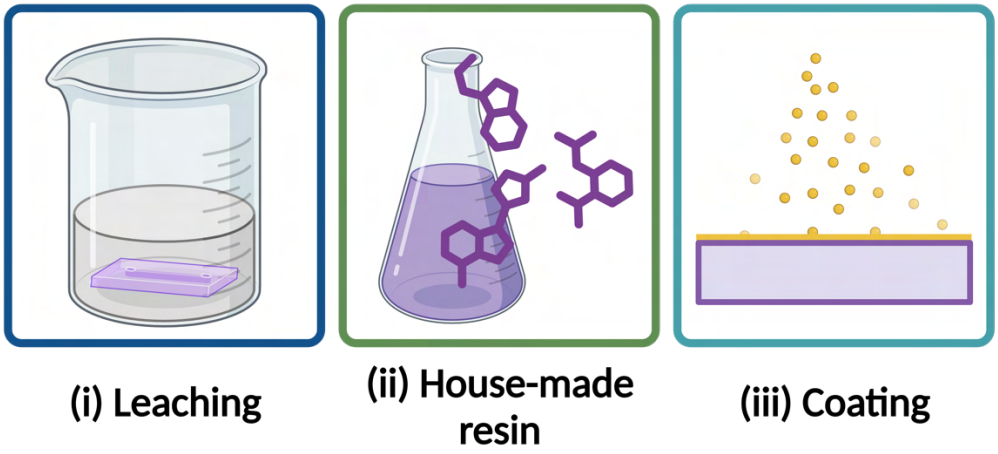

Figure 3.2 Common approaches to reduce 3D-printed material cytotoxicity. *These methods include (i) leaching out unbound toxins, (ii) making house-made resins with biocompatible materials, and (iii) coating the material to limit toxin release (Created with BioRender.com)*

3.3 Methods

3.3.1 Fabrication of 3D-printed wells

3D-printed wells were designed using Fusion 360 and were printed using a CADWorks3D MiiCraft P110Y DLP printer (CADWorks3D, Toronto, Canada). The ITX-PEGDA resin consisted of poly(ethylene glycol) diacrylate (PEGDA, 250 MW, Sigma Aldrich) as the monomer, phenylbis(2,4,6-trimethylbenzoyl)phosphine oxide (Irgacure 819, Sigma Aldrich) as the photoinitiator, and isopropylthioxanthone (ITX, Fisher Scientific, New Hampshire, USA) as the photoabsorber, based off of a previously developed recipe.[4] Irgacure 819 and ITX were mixed with PEG-DA (0.4% w/w) and dissolved for 30 min at 70°C. The A-PEGDA followed a similar recipe, with 0.4% w/w avobenzone (Making Cosmetics, Lot no. AVB-20190603, USA) added to the PEGDA and Irgacure 819 mixture. The commercially available resins used were FormLabs Clear (FL Clear, FormLabs, Massachusetts, USA) and BV007a (MiiCraft Clear, CADworks3D, Canada).

For each print, all layers were printed at a step size of 50 μm at 100% power (5 mW/cm^2), 1.25 s cure time, 4 s base cure time, 6 base layers, and 4 buffer layers. All printed parts were submerged in isopropyl alcohol (IPA) within a Form Wash (FormLabs, Massachusetts, USA) for 5 min. After cleaning with alcohol, the prints were dried thoroughly with nitrogen and placed in the Form Cure high-intensity UV light box (FormLabs, Massachusetts, USA) for 1 min. Various post-treatments were tested to improve material biocompatibility: 1 hr in Form Cure at 10 mW/cm^2, 24 hr soak in 25 mM ascorbic acid solution at room temperature, 24 hr soak in 1 x PBS (Lonza, Maryland, USA) within a cell culture incubator at 37°C, and 24 hr dry bake at 70°C. Prior to culture of tissue in any 3D-printed material, the print was sterilized by submerging in 70% ethanol for 5 min, followed by two 10 min rinses in PBS. Once rinsed, the materials were allowed to air dry for at least 30 min before use.

3.3.2 Resin autofluorescence

ITX-PEGDA resin autofluorescence was measured using a Zeiss AxioZoom macroscope (Carl Zeiss Microscopy, Germany) with an Axiocam 506 Mono camera using Zeiss filter cubes channels including Cy5 (Ex 640/30, Em525/50, #64), rhodamine (Ex 550/25, Em 605/70, #43), EGFP (Ex 470/40, Em 525/50, #38), and DAPI (Ex ~320-385 nm, Em 445/50, #49). Image analysis was completed using ImageJ software.[12]

3.3.3 Animal model

All animal work was approved by the Institutional Animal Care and Use Committee at the University of Virginia under protocol #4042, and was conducted in compliance with guidelines from the University of Virginia Animal Care and Use Committee and the Office of Laboratory Animal Welfare at the National Institutes of Health (United States). Spleens were harvested from female and male C57BL/6 mice (Jackson Laboratory, USA) under the age of 6 months following humane isoflurane anesthesia and cervical dislocation. The spleens were collected into "complete RPMI" media consisting of RPMI (Lonza, Maryland, USA) supplemented with 10% FBS (VWR, Seradigm USDA approved, Pennsylvania, USA), 1 x l-glutamine (Gibco Life Technologies, Maryland, USA), 50 U mL^{-1} Pen/Strep (Gibco Life Technologies, Maryland, USA), 50 µM beta-mercaptoethanol (Gibco Life Technologies, Maryland, USA), 1 mM sodium pyruvate (Hyclone, Utah, USA), 1x non-essential amino acids (Hyclone, Utah, USA), and 20 mM HEPES (VWR, Pennsylvania, USA).

3.3.4 Preparation of primary murine splenocytes

Spleens were collected from C57/BL6 mice and a cell suspension was generated by crushing the spleen through a 70 µm Nylon mesh filter (Thermo Fisher, Pennsylvania, USA) with 10 mL of complete media, then centrifuged for 5 min at 400 x g. The red blood cells were

lysed by resuspending the pellet in 2 mL of ACK lysis buffer prepared from 4.15 g NH_4Cl (Sigma-Aldrich, Missouri, USA), 0.5 g $KHCO_4$ (Sigma-Aldrich, Missouri, USA), and 18.7 g Na_2-EDTA (Sigma-Aldrich, Missouri, USA) in 0.5 L MilliQ water (Millipore, Sigma, Massachusetts, USA). Cells were lysed for 1 min, then quenched with 8 mL of complete media, and centrifuged. The pellet was resuspended in complete media, producing a splenocyte suspension with the density determined by trypan blue exclusion. The suspensions were diluted with complete media to a concentration of 1 x 10^6 to 3 x 10^6 cells per mL in preparation for culture.

3.3.5 Flow cytometry

Following the culture period, the cell viability was assessed by flow cytometry using a previously established protocol.[13] Briefly, 500 µL samples at 1 x 10^6 cells/mL were stained with Calcein AM (eBioscience, San Diego, CA, USA) at 67 nM in PBS for 20 minutes at 37°C. The stained samples were washed by centrifugation at 400 x g then resuspended in flow buffer (1x PBS with 2% FBS). Following the wash step, 4 µL of 1 mg/mL 7-AAD (AAT Bioquest, Sunnyvale, CA, USA) was added to the cell suspension. Single-stain compensation controls were prepared using plate control cells (Calcein AM) or cells treated with a 1:1 v/v mix of media and 70% ethanol for 20 minutes (7-AAD); single-stains were mixed 1:1 v/v with unstained cells for analysis. All samples and controls were run on a Guava 4-color cytometer (6-2L) and analyzed with Guava® InCyte™ Software. Calcein-AM^{high} and 7-AAD^{low} was defined as Live, and Calcein-AM^{low} and 7-AAD^{high} was defined as Dead.

3.3.6 MTS and LDH assays

Following the culture period, cell viability was assessed using a CellTiter 96® AQ_{ueous} One Solution Cell Proliferation Assay (MTS assay, Promega, Wisconsin, USA). In conjunction,

cellular cytotoxicity was assessed using a CyQUANT™ LDH Cytotoxicity Assay Kit (LDH assay, Fisher Scientific, New Hampshire, USA). For the MTS assay, 100 µL of splenocytes at a cell density of 3 x 10^6 (unless stated otherwise) were added to a 96 well plate in triplicate. A killed control was generated by adding 10 µL of Lysis Buffer (LDH assay kit) for 30 min at 37ºC. Then, 20 µL of CellTiter One Solution Reagent was added to each well of the 96 well plate containing killed controls, media only controls, and sample wells. The plate was then incubated for 3 hrs at 37ºC. For the LDH assay, 100 µL samples at 3 x 10^6 were added to a 96 well plate in triplicate. A killed control was generated by adding 10 µL of Lysis Buffer from the LDH assay kit for 30 min at 37ºC. Then, the cells were spun down in the centrifuge for 5 min at 400 x *g*. 50 µL of media from each condition was removed and added to a fresh 96 well plate for the LDH assay. Next, 50 µL of the LDH substrate was added to each well of the 96 well plate containing killed controls, media only controls, and sample wells. The plate was incubated at room temperature for 30 min. After the incubation period for both assays, any bubbles present were popped by spinning down the plate on a centrifuge for 5 min at 400 x *g*. The absorbance within each well was measured at 490 nm using a CLARIOstar plate reader (BMG LabTech, Germany). The background absorbance from media-only controls were subtracted from the killed controls and samples.

3.4 Results and Discussion

3.4.1 Formulation of PEGDA-based resins for DLP printing

The components of photocrosslinkable resin can be critical for print resolution and cell viability. This includes not only the materials selected, but also the ratios of each ingredient added. We began with a base recipe of poly(ethylene glycol) diacrylate (PEGDA) as the monomer and Irgacure 819 as the photoinitiator (Figure 3.3). With PEGDA-based resins, there

were three different photoabsorbers used by different labs to achieve high print resolution: 2-nitrophenyl phenyl sulfide (NPS),[7,14] isopropylthioxanthone (ITX),[4] and avobenzone (A).[7] All three of these absorbers are effective at the wavelength used in our DLP printer (385 nm).

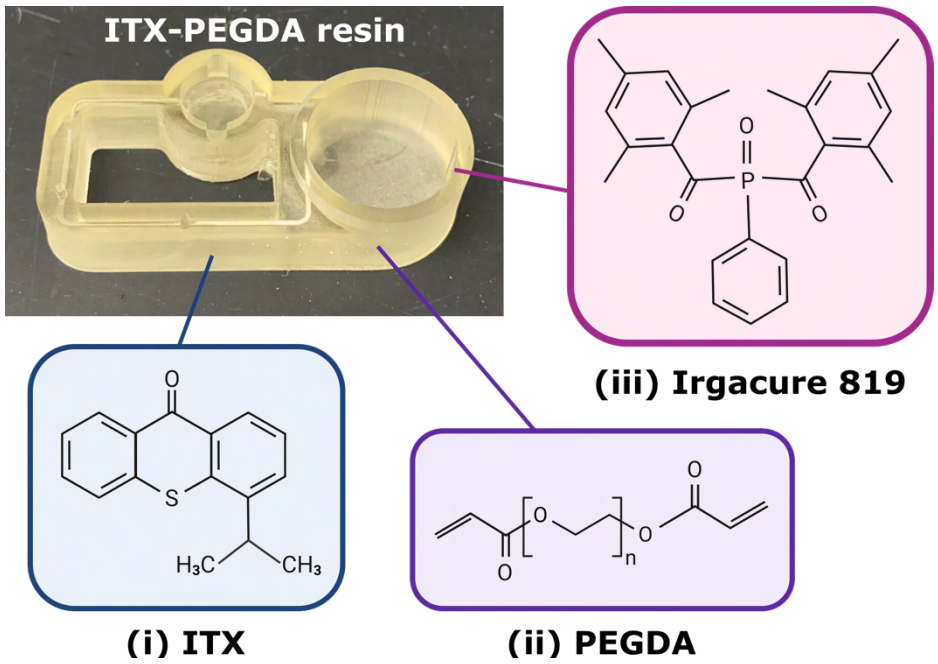

Figure 3.3 Components of ITX-PEGDA resin. *The resin is comprised of (i) isopropylthioxanthone (ITX) as a photoabsorber, (ii) PEGDA as a monomer, and (iii) Irgacure 819 as a photoinitiator (Created using BioRender.com).*

NPS has been commonly used in photocurable resins and was found to be biocompatible following a 24 hr leaching step in ethanol.[7] However, this absorber resulted in a print that was tinted a yellow-orange color which may impact optical clarity and autofluorescence. In comparison, ITX maintained device transparency with little tint (Figure 3.3) and was shown to be viable following a 12 hr leaching step in buffer.[4] Avobenzone appeared to be an ideal candidate, where the resulting device had no colored tint and was shown to be non-toxic with no additional post-treatments.[7] While all of these absorbers were reported to be biocompatible, the cell types tested for each study were hardy cell lines,[4,7] where the material may still be cytotoxic for sensitive primary immune cells. We selected avobenzone and ITX photoabsorbers for initial

resin formulations, excluding NPS due to the resulting color of prints and lengthy post-processing required. Before we tested material characteristics and biocompatibility, we first optimized the printer settings to be able to print intact devices. The ITX-PEGDA resin was able to print reproducibly with a minimum enclosed channel size of 400 µm, while the channels were unable to be fully cleared in the A-PEGDA resin.

3.4.2 ITX selected as photoabsorber based off of preliminary viability results

It was critical to get a baseline level of cytotoxicity in early stages of resin formulation to select one absorber to streamline further optimization of either the resin recipe or the print settings. Here, we cultured primary murine splenocytes for 24 hrs in wells printed in ITX-PEGDA, A-PEGDA, and a commercially available Clear resin (FL Clear) with no additional post-treatments alongside cells cultured in a well plate (off-chip) (Figure 3.4a). After 24 hr culture, the cell viability was quantified using flow cytometry. While the results were non-significant, the ITX-PEGDA resin trended higher than the A-PEGDA and FL Clear, which has been shown to be toxic at 24 hrs,[5,15] when compared to the off-chip condition (Figure 3.4b). Due to the viability trending higher for the ITX-PEGDA resin as well as the ability to reproducibly print internal channels, we moved forward with ITX as the photoabsorber.

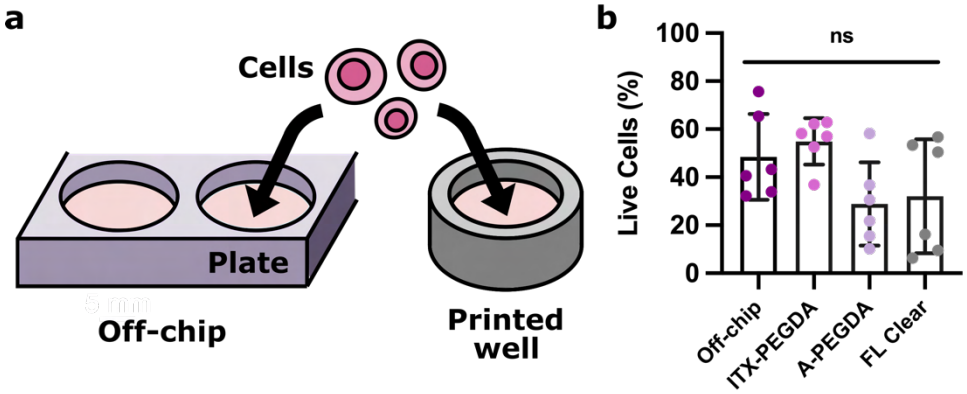

Figure 3.4 Preliminary 24 hr viability of PEGDA-based resins. *(a) Primary murine splenocytes were cultured off-chip and in printed wells (ITX-PEGDA, A-PEGDA, and FL Clear) for 24 hrs before viability quantification using flow cytometry. (b) Viability of live primary murine splenocytes after 24 hr culture. Live cells were determined via flow cytometry as the percent of*

Calcein-AM^{high} and 7AAD^{low} out of all of the cells. Results were compared using a one-way ANOVA with Tukey post-hoc tests (n = 6). ns indicates p > 0.08. Each dot represents one sample under the listed media conditions. The bars represent standard deviation. Results were pooled from two separate experiments.

3.4.3 Characteristics of ITX-PEGDA resin

When using DLP 3D-printing for biomicrofluidic applications, there are a few features of the material to consider such as print resolution, optical clarity, and autofluorescence. While DLP 3D printing has limited print resolution compared to other microfluidic fabrication techniques,[5,15] 500 x 500 µm internal channels have previously printed reproducibly with a commercially available resin, BV007a. One feature of these materials that impacts print resolution is resin viscosity.[5] For the viscous resins such as FormLabs Clear, which is comparable to honey, the resin often gets trapped in internal channels when printing instead of draining out and will begin to crosslink, causing the print to fail. In contrast, BV007a resin is less viscous, comparable to egg whites, and can reproducibly print smaller internal channels.[5] After optimization of the ratio of ITX-PEGDA resin components, we were able to generate a low-viscosity resin[16] that reproducibly printed devices with 500 µm channels (Figure 3.4, 3.5a). Print failure with channels <400 µm is likely due to light scattering passing through the resin during the printing process, and can be improved by further optimizing the amount of photoabsorber added.

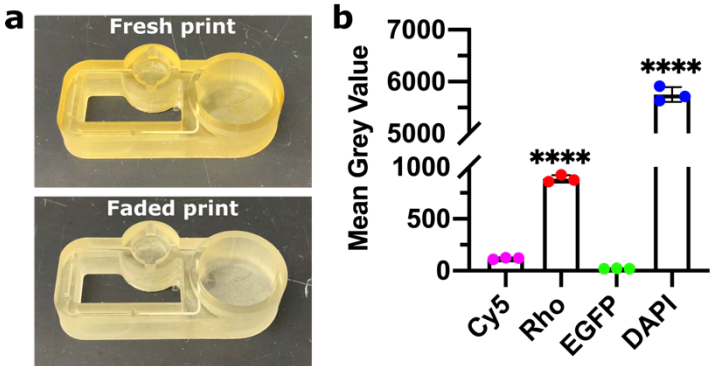

Figure 3.5 ITX-PEGDA characteristics. *(a) Images of a microfluidic device printed in ITX-PEGDA resin that was freshly printed (top) and had rested for a few hours (bottom). (b) Mean grey value of ITX-PEGDA prints in Cy5, rhodamine (Rho), EGFP, and DAPI channels. Results were compared using a one-way ANOVA with Tukey post-hoc tests (n = 3). **** indicates p < 0.0001. Each dot represents the MGV of a single printed device. The bars represent standard deviation.*

For many devices, the ideal material would be optically clear with limited background fluorescence to enable imaging on-chip.[5] The ITX-PEGDA was found to be relatively clear, however the material appeared to be tinted, especially when freshly printed or re-exposed to UV light (Figure 3.5a). This feature did not appear to impact the optical clarity. In addition, the resin was autofluorescent in both the rhodamine channel and the DAPI channel (Figure 3.5b). As a result, imaging on-chip using this resin would be limited to the Cy5 and EGFP channels and imaging off-chip for rhodamine and DAPI.

3.4.4 Principles of MTS and LDH assays for high-throughput primary cell viability testing

Flow cytometry is a robust and reliable method for cell viability quantification.[5,10,15,17] However, it was challenging run many replicates with a single-tube cytometer as the time required to stain and run the samples resulted in cell death. An alternative for high-throughput viability quantification is formazan-based colorimetric assays. Here, we selected two different assays: 1) MTS assay for cell metabolic activity, and 2) LDH assay for cell cytotoxicity (Figure 3.6). These two quick, user-friendly assays provide complementary results, similar to live and dead stains used for flow cytometry.[18–21]

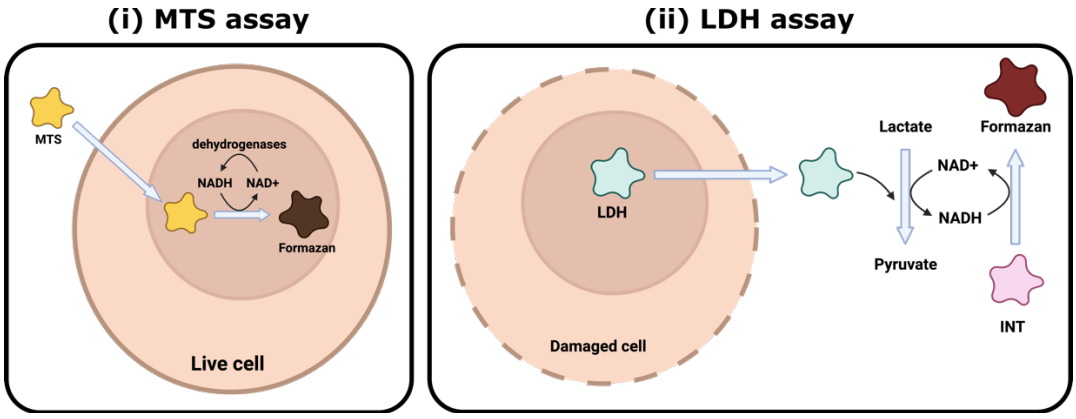

Figure 3.6 Working principles of the cell viability assays. *(i) In the MTS assay, the MTS reagent is internalized in live cells and reduced to formazan by active dehydrogenases. (ii) In the LDH assay, lactate dehydrogenase (LDH) leaves damaged cells and accumulates in the culture media, where it triggers the formation of formazan through a coupled enzymatic reaction (Created using BioRender.com).*

The CellTiter 96 AQ_{ueous} One Solution Cell Proliferation assay, or MTS assay, probes cell viability with the addition of a "One Solution" reagent in a suspension of cells. The reagent consists of an MTS tetrazolium compound paired with an electron coupling reagent, phenazine ethosulfate (PES). Once added to the cell suspension, the One Solution reagent enters the cell, where the active dehydrogenases present in live cells reduce the MTS compound to formazan, a colored product that absorbs at 490 nm (Figure 3.6i). This assay is as simple as adding the One Solution reagent to samples and measuring absorbance after a 1-4 hr culture period.

Lactate dehydrogenase (LDH) is an enzyme present in the cytosol of many different cell types. Upon damage to the cell membrane, LDH will exit the cell and accumulate in the cell culture media. The CyQUANT LDH Cytotoxicity assay, shortened to LDH assay, provides a method to quantify the amount of LDH present in media alone as a measurement of cell death and damage. When the reaction mixture containing the assay substrate and buffer is added to the sample media, the LDH present in the media catalyzes the conversion of lactate to pyruvate via NAD+ reduction. A diaphorase enzyme present in the reaction mixture oxidates NADH to

NAD+, which converts a tetrazolium salt (INT) to formazan (Figure 3.6ii). Similar to the MTS assay, the formazan absorbance is measured at 490 nm after a 30 min culture period.

3.4.5 Optimization of MTS and LDH assays for use with primary murine splenocytes

For both MTS and LDH assays, there can be varying amounts of signal present depending on both the cell type and the cell density. Different cell types across different species can have different metabolic activities as well as varying levels of LDH present in the cell cytosol. If the signal is low for a specific type of cell, having more cells present in the sample by increasing cell density is an easy method to increase assay signal. Another factor that may impact assay signal is the presence of ß-mercaptoethanol (ß-ME), which is a strong reducing agent present in dilute quantities in cell culture media used for splenocyte culture to limit the amount of toxic oxygen radicals present. A study from Wang et al. found that the presence of ß-ME artificially inflated MTS assay signal with greater inflation at higher ß-ME concentrations.[20]

Here, we cultured primary splenocytes off-chip for 24 hrs at a range of cell densities with and without ß-ME to determine optimum culture conditions to generate a high, but accurate, assay signal for each sample (Figure 3.7). As expected, the MTS signal from live samples (Figure 3.7a) and LDH signal from killed samples (Figure 3.7a) increased linearly as the cell density increased. The inclusion of ß-ME for both assays appeared to increase the resulting signal, with a significant difference at $2x10^6$ cells per mL and $4x10^6$ cells per mL (Figure 3.7a,b). As the cell density increases with cell culture, there is a greater chance of the cells consuming all available nutrients in the cell culture media creating a cytotoxic cell environment. While the cell density of $4x10^6$ cells per mL yielded the greatest signal, we chose to move forward with $3x10^6$ cells per mL as it still resulted in a boosted signal compared to $1x10^6$ cells per mL while mitigating cell crowding.

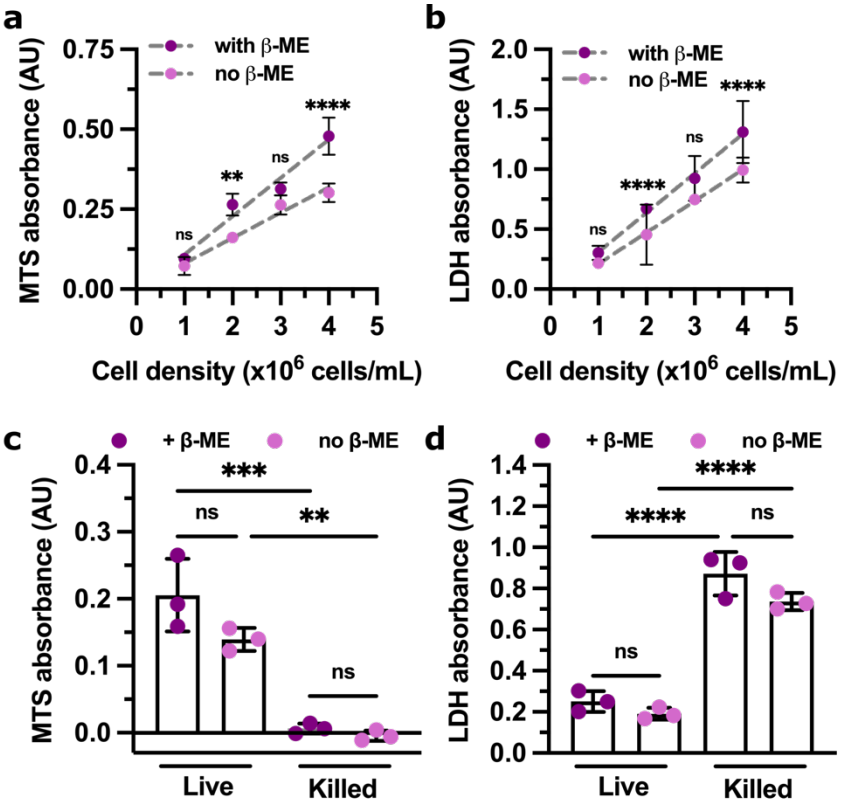

Figure 3.7 Optimization of MTS and LDH assays off-chip for use with primary splenocytes. *(a) MTS assay absorbance of the primary murine splenocytes live controls at varying cell density after 24 hr culture. (b) LDH assay absorbance of the primary murine splenocytes killed control at varying cell density after 24 hr culture. Results from (a) and (b) were compared using a one-way ANOVA with Tukey post-hoc tests (n = 3). ns indicates p > 0.2, ** indicates p < 0.002, **** indicates p < 0.0001. Dots and error bars represent an average and standard deviation, respectively. (c) MTS assay absorbance of primary murine splenocytes with and without ß-ME at 3 mil cells per mL after 24 hr culture. (d) LDH assay absorbance of primary murine splenocytes with and without ß-ME at 3 mil cells per mL after 24 hr culture. Results from (c) and (d) were compared using a one-way ANOVA with Tukey post-hoc tests (n = 3). ns indicates p > 0.08, ** indicates p < 0.002, *** indicates p < 0.0002, **** indicates p < 0.0001. Each dot represents a single sample. The bars represent standard deviation.*

Next, we compared live and killed samples at $3x10^6$ cells per mL with and without ß-ME for both assays after 24 hr culture. For the MTS assay, the addition of ß-ME did not significantly impact the absorbance for both live and killed samples (Figure 3.7c). However, this cell density yielded a significant difference between the live and killed samples, which is critical when utilizing this assay for cell viability quantification. Similarly, the addition of ß-ME in the LDH assay did not result in a significant change for both the live and killed samples while maintaining

a significant difference between live and killed sample absorbance (Figure 3.7d). Based off of these results, there may be a minor impact on the absorbance values with the presence of ß-ME, although it is challenging to identify if this increase in signal is due to the ß-ME artificially inflating the formazan production or if it improves cell viability. This can be tested more in the future by measuring cell viability using flow cytometry. In addition, we used a low working concentration (50 µM) for these experiments, whereas the concentrations that were reported to significantly inflate assay signal were 100-500 µM.[20] Based off of these results, we determined that the ideal conditions for optimum assay signal were a cell density of $3x10^6$ cells per mL and the inclusion of 50 µM ß-ME.

3.4.6 Resin post-treatments do not improve cell viability

Resin cytotoxicity is a common issue within the field of 3D printing. This toxicity is thought to be a result of harmful chemicals leaching out of the printed material. As a result, many of the available methods to improve biocompatibility include different ways to promote further polymerization to crosslink unbound resin components (e.g. UV cure), remove leachates (e.g. soaking, baking), or reduce radicals present from polymerization process (e.g. Vitamin C treatment) (Figure 3.8). These post-treatments may result in material degradation, i.e. layer delamination, as some of the leachates may have been important for structural integrity of the material.[10]

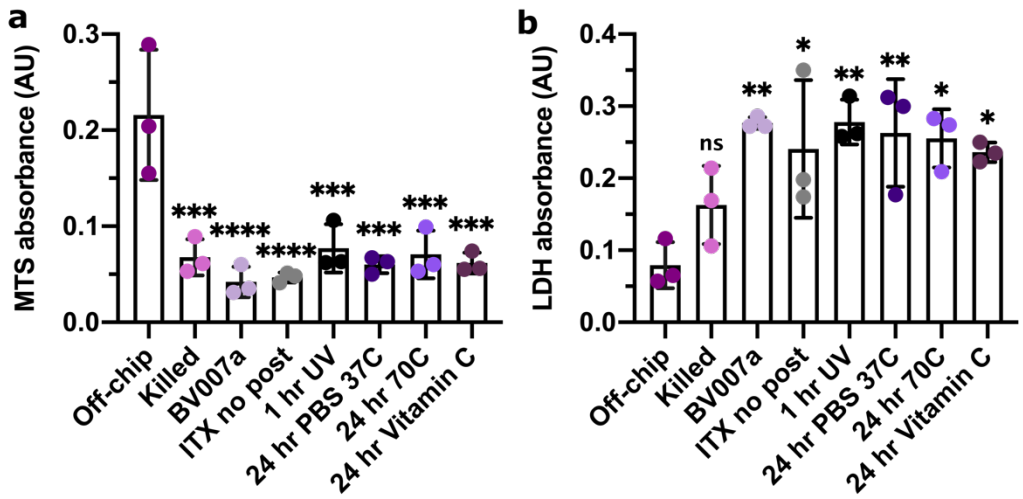

Figure 3.8 Resin post-treatments did not improve cell viability. *(a) MTS assay absorbance of primary murine splenocytes after 24 hr culture in 3D-printed wells with various different post-treatments. (b) LDH assay absorbance of primary murine splenocytes after 24 hr culture in 3D-printed wells with various different post-treatments. Results were compared using a one-way ANOVA with Tukey post-hoc tests (n = 3). ns indicates p > 0.2 , * indicates p < 0.03, ** indicates p < 0.005, *** indicates p < 0.0002, **** indicates p < 0.0001. Each dot represents a single sample. The bars represent standard deviation.*

Here, we treated ITX-PEGDA resin with a range of different post-treatments and measured the resulting impact on cell viability in comparison with a cytotoxic commercially available resin, BV007a. After 24 hr culture, the splenocytes in all resin conditions had significantly lower viability compared to the live plate control for both the MTS (Figure 3.8a) and LDH (Figure 3.8b) assays. The post-treatments did not have a significant impact on the cell viability, as there was no improvement when assay signal was compared to the ITX-PEGDA resin with no post-treatments. As a result, we decided to try another method used to improve material biocompatibility in the field of 3D printing: parylene-C coating.

3.4.7 Restored cell viability with biocompatible parylene-C coating

As resin 3D printing has become more commonplace in the fabrication of microfluidics and organs-on-chip technology, there has been an unmet need for a biocompatible material that is suitable for a wide range of different cell types. Within the past 5 years, some labs have

adopted parylene-C coating, which is a method commonly used to coat medical devices and computer chips to improve biocompatibility and waterproof electronics, respectively.[10,11,22] A thin layer of parylene was deposited on the material of choice through chemical vapor deposition, which generated a barrier across the entire device surface to inhibit the accumulation of toxic leachates in the cell culture media (Figure 3.9).[10,11] In addition to viability, parylene-C has been shown to slow down device degradation as well as limit small molecule absorption.[10,11] Here, we coated 3D-printed wells with parylene-C to measure the impact on viability of sensitive primary immune cells.

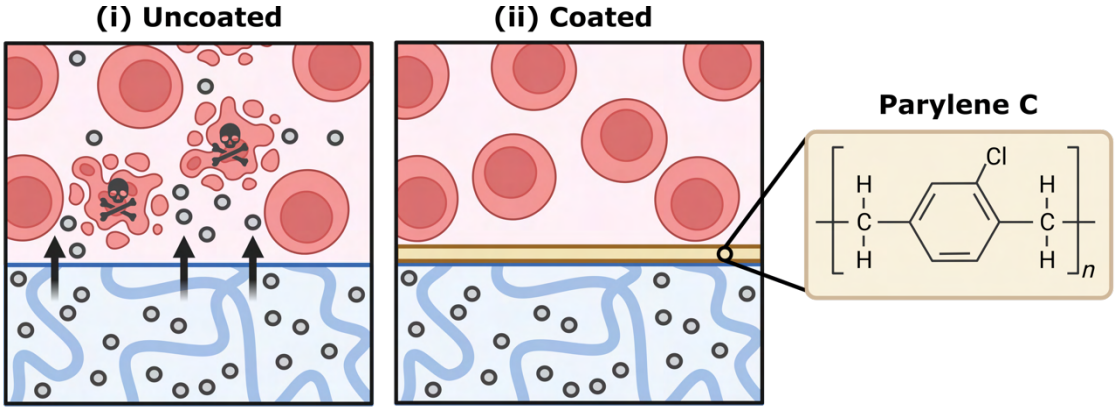

Figure 3.9 Parylene-C coating generated a protective layer on 3D-printed materials to improve cell viability *(Created using BioRender.com).*

For initial characterization of parylene-C coating, we used wells printed in commercially available resin with known cytotoxicity, BV007a, as a rigorous test of this coating method.[5] After 24 hrs, we found that the parylene-C coating was fully protective, where the coated wells had similar viability compared to the samples cultured off-chip (Figure 3.10). In contrast, the untreated BV007a condition had low viability, which was evident especially in the MTS assay results where the untreated absorbance was comparable to the killed controls (Figure 3.10a). The LDH assay showed a minor but insignificant increase in signal with the untreated wells compared to the live off-chip samples and the parylene-C coated samples (Figure 3.10b). Based

off of these results, we conclude that parylene-C coating was the best method to reproducibly produce biocompatible 3D-printed materials.

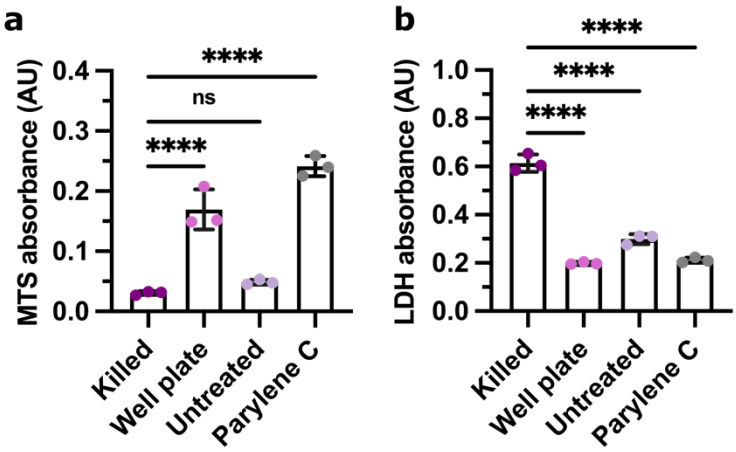

Figure 3.10 Parylene-C coating improves cell viability after 24 hr culture in resin. *(a) MTS absorbance of primary murine splenocytes after 24 hr culture on uncoated and parylene-coated wells printed in BV007a resin. (b) LDH absorbance of primary murine splenocytes after 24 hr culture on uncoated and parylene-coated wells printed in BV007a resin. Results were compared using a one-way ANOVA with Tukey post-hoc tests (n = 3). ns indicates p > 0.6, **** indicates p < 0.0001. Each dot represents a single sample. The bars represent standard deviation.*

3.5 Conclusions

Here, we have reported the optimization of resin formulation and post-treatment to improve primary immune cell viability while maintaining a high print resolution, reproducibility, and optical characteristics for use in biomicrofluidics. For high throughout viability quantification, we improved the signal from two complementary viability assays for cell proliferation (MTS assay) and cell death (LDH assay). Finally, we found that the most effective method to reproducibly improve cell viability when using 3D-printed materials was to coat with a thin layer of parylene-C.

3.6 References

1. Lin, F. & Butcher, E. C. T cell chemotaxis in a simple microfluidic device. *Lab Chip* **6**, 1462–1469 (2006).

2. Fathi, P., Holland, G., Pan, D. & Esch, M. B. Lymphatic Vessel on a Chip with Capability for Exposure to Cyclic Fluidic Flow. *ACS Appl. Bio Mater.* **3**, 6697–6707 (2020).
3. Bhattacharjee, N., Urrios, A., Kang, S. & Folch, A. The upcoming 3D-printing revolution in microfluidics. *Lab Chip* **16**, 1720–1742 (2016).
4. Kuo, A. P. *et al.* High-Precision Stereolithography of Biomicrofluidic Devices. *Adv. Mater. Technol.* **4**, 1800395 (2019).
5. Musgrove, Hannah. B., Catterton, Megan. A. & Pompano, Rebecca. R. Applied tutorial for the design and fabrication of biomicrofluidic devices by resin 3D printing. *Analytica Chimica Acta* **1209**, 339842 (2022).
6. Urrios, A. *et al.* 3D-printing of transparent bio-microfluidic devices in PEG-DA. *Lab Chip* **16**, 2287–2294 (2016).
7. Warr, C. *et al.* Biocompatible PEGDA Resin for 3D Printing. *ACS Appl. Bio Mater.* **3**, 2239–2244 (2020).
8. Oskui, S. M. *et al.* Assessing and Reducing the Toxicity of 3D-Printed Parts. *Environ. Sci. Technol. Lett.* **3**, 1–6 (2016).
9. De Almeida Monteiro Melo Ferraz, M., Nagashima, J. B., Venzac, B., Le Gac, S. & Songsasen, N. 3D printed mold leachates in PDMS microfluidic devices. *Sci Rep* **10**, 994 (2020).
10. Musgrove, H. B., Cook, S. R. & Pompano, R. R. Parylene-C Coating Protects Resin-3D-Printed Devices from Material Erosion and Prevents Cytotoxicity toward Primary Cells. *ACS Applied Bio Materials* **6**, 3079–3083 (2023).
11. O'Grady, B. J. *et al.* Rapid prototyping of cell culture microdevices using parylene-coated 3D prints. *Lab Chip* **21**, 4814–4822 (2021).

12. Schneider, C. A., Rasband, W. S. & Eliceiri, K. W. NIH Image to ImageJ: 25 years of image analysis. *Nat Methods* **9**, 671–675 (2012).
13. Ball, A. G., Belanger, M. C. & Pompano, R. R. Detergent wash improves vaccinated lymph node handling ex vivo. *Journal of Immunological Methods* **489**, 112943 (2021).
14. Gong, H., Bickham, B. P., Woolley, A. T. & Nordin, G. P. Custom 3D printer and resin for 18 μm × 20 μm microfluidic flow channels. *Lab Chip* **17**, 2899–2909 (2017).
15. Cook, S. R., Musgrove, H. B., Throckmorton, A. L. & Pompano, R. R. Microscale impeller pump for recirculating flow in organs-on-chip and microreactors. *Lab Chip* **22**, 10.1039.D1LC01081F (2022).
16. Gong, H., Beauchamp, M., Perry, S., Woolley, A. T. & Nordin, G. P. Optical approach to resin formulation for 3D printed microfluidics. *RSC Adv.* **5**, 106621–106632 (2015).
17. Belanger, M. C. *et al.* Acute Lymph Node Slices Are a Functional Model System to Study Immunity Ex Vivo. *ACS Pharmacol. Transl. Sci.* **4**, 128–142 (2021).
18. Herath, K. H. I. N. M. *et al.* Differential modulation of immune response and cytokine profiles of Sargassum horneri ethanol extract in murine spleen with or without Concanavalin A stimulation. *Biomedicine & Pharmacotherapy* **110**, 930–942 (2019).
19. Yazdi, M. H., Mahdavi, M., Setayesh, N., Esfandyar, M. & Shahverdi, A. R. Selenium nanoparticle-enriched Lactobacillus brevis causes more efficient immune responses in vivo and reduces the liver metastasis in metastatic form of mouse breast cancer. *DARU J Pharm Sci* **21**, 33 (2013).
20. Wang, Y. *et al.* A Modified MTS Proliferation Assay for Suspended Cells to Avoid the Interference by Hydralazine and β-Mercaptoethanol. *ASSAY and Drug Development Technologies* **19**, 184–190 (2021).

21. Manna, K. *et al.* Naringin inhibits gamma radiation-induced oxidative DNA damage and inflammation, by modulating p53 and NF-κB signaling pathways in murine splenocytes. *Free Radical Research* **49**, 422–439 (2015).
22. van den Driesche, S., Lucklum, F., Bunge, F. & Vellekoop, M. 3D Printing Solutions for Microfluidic Chip-To-World Connections. *Micromachines* **9**, 71 (2018).

Chapter 4. A 3D-printed multi-compartment chip and tubing-free pump applied to model short-term responses to the lymph node after vaccination

4.1 Abstract

Multi-organs-on-chip (MOOC) systems provide a biomimetic platform to study molecular and cellular communication between two or more tissues by co-culturing organ models (e.g. 2D/3D cell cultures, tissue slices, etc.) in circulating media. This technology can be used to study basic tissue function, model disease, and test tissue response to different drugs. These devices will only reach its full power once they can translate to clinical settings with biomedical experts. However, many existing devices are difficult for non-experts to implement due to extensive tubing, complex pump mechanisms, and challenging device use. In addition, there are limited existing MOOCs that incorporate immune organs like the lymph node (LN). To address these issues, we developed a customizable, user-friendly platform for the co-culture of two or more tissue slices under recirculating fluid flow using a 3D-printed device and companion tubing-free impeller pump. Using this multi-tissue chip and pump, we modeled the acute response to vaccination in the lymph node on-chip and benchmarked it against vaccination *in vivo* and in a dish.

4.2 Introduction

Communication between organs through recirculation of molecular and cellular signals is essential for life, both in maintenance of homeostasis and for rapid responses to perturbation in health and disease.[1] For example, vaccines are effective only if proper drainage of signals occurs from the skin or muscle at the site of injection to the draining lymph node, which responds to the stimulation with early inflammatory activity and ultimately generates protective immunity. However, it can be challenging to isolate the communication between specific organs using *in*

vivo models, in part because so many organs contribute simultaneously and through often indirect blood and lymphatic vasculature connections.

Using multi-organ-on-chip (MOOC) technology, this challenge has been addressed by coupling models of select organs together to predict their interactions in physiological and pathological conditions.[2–8] These devices deliberately reduce the full complexity of a living organism to a subset of fluidically connected 2D and 3D cultures, containing cells and functionalities as needed to answer the question at hand. MOOCs were first developed to predict the responses to therapeutics, i.e., ADMETox (absorption, distribution, metabolism, excretion, toxicity),[7,9–14] and more recently to model mechanisms of disease pathology.[3,15–18] Similar to *in vivo*, each organ in a MOOC is compartmentalized, with communication mediated by circulating media designed to emulate blood and lymph flow.[7] *In vivo,* flow through the blood and lymphatic vasculature delivers nutrients, clears waste, connects tissues, and enables the delivery of a vaccine or drug.[2] Interstitial flow through the tissue itself also plays a major role in both mass transport and shear-sensitive responses in organs such as tumors and lymph nodes.[19,20] Given the variable and dynamic flow rates seen *in vivo*, MOOCs designed to mimic these properties need to have precise and controllable flow speeds, including with thick 3D cultures. Furthermore, MOOCs with recirculating fluid flow have the advantages of enabling biological feedback loops between organs, reducing media consumption, and allowing accumulation of otherwise dilute secreted factors. However, recirculating flow is often more challenging to achieve than simple one-way flow from an inlet to an outlet.

MOOCs will reach their full power only once biomedical experts and clinical laboratories with no microfluidics expertise are able to adopt them. With this in mind, ease of use, reproducible and affordable fabrication, and robustness are just as critical as biomimicry when

designing a system. Unfortunately, most standard methods for precisely controlled, continuous recirculating flow through MOOCs are challenging for non-experts to implement due to extensive tubing or complex electrical or pneumatic control systems. Standard pumps and pneumatic pressure controllers are bulky, expensive, or incompatible with cell culture incubators, and furthermore they may require tubing that is prone to bubbles, contamination, or disconnection. These challenges make it difficult to scale up the pumps to many simultaneous biological replicates.[16] Gravity-driven systems are far simpler to implement, but often generate unsteady or pulsatile flow.[21–24] We and others previously reported a magnetic impeller pump as an alternative, but although low in heat emission and inexpensive, these required a large fluid volume and/or footprint.[10,25,26] Another challenge is that many OOCs are closed by design, for example with cell cultures located on a membrane inside of a microchannel, making it difficult to add tissues on demand or to remove tissues for imaging, flow cytometry, and gene expression during or after the experiment. In terms of fabrication, a movement away from hand-assembled polydimethylsiloxane (PDMS) is desirable to facilitate reproducible fabrication, e.g. by 3D printing, high-throughput machining, or embossing. Thus, there is a major unmet need for a multi-organ chip platform that remains accessible and user-friendly while incorporating well-controlled fluid flow around and through biomimetic 3D cultures.

Incorporation of organs of the immune system into MOOCs is an additional frontier and is particularly dependent on well-controlled fluid flow. So far, MOOCs have primarily incorporated tissue-resident immune cells or recirculating white blood cells into existing models of lung, gut, brain, tumor, islets, etc.[3,17,27–29] However, models of dedicated immune organs such as the lymph node (LN) are crucial to model the systemic immune responses more directly. LNs are small organs located along lymphatic vessels where the they filter flowing lymph fluid to

detect and respond to foreign pathogens (e.g. viruses) (Figure 4.1a).[30,31] Vaccination takes advantage of this system by inducing the adaptive immune response to protect against infection.[32] Currently, most microscale or organoid models of LN tissue or its subregions have been of the organ in isolation.[33–40] Two exceptions include the MIMIC system[41] and prototype devices for microfluidic lymph node slice co-cultures by us and others.[16,42] However, our prototype platform was not scalable due to multiple large peristaltic pumps and time-intensive manual fabrication in PDMS, and the chip provided endpoint-only imaging capabilities.

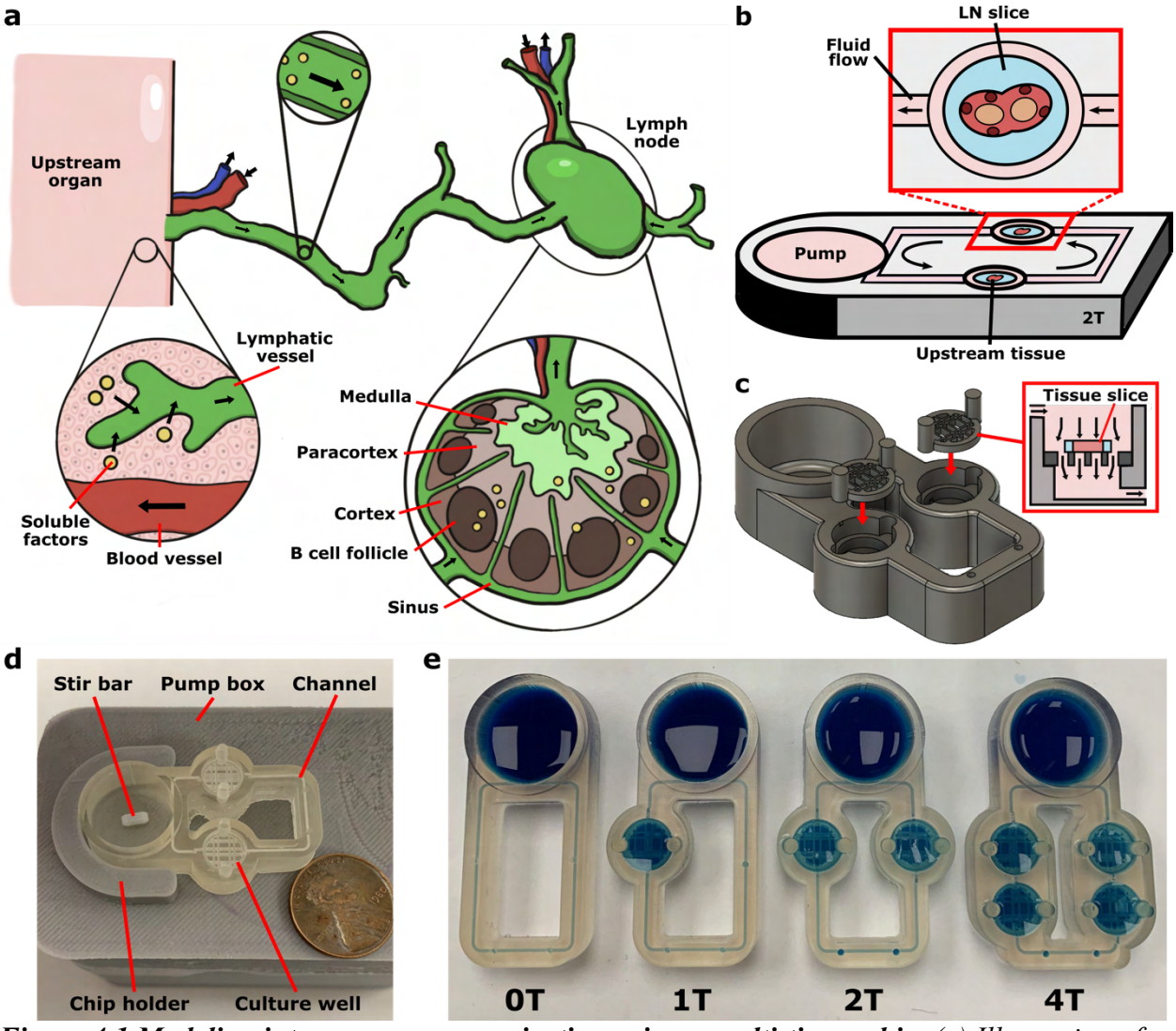

Figure 4.1 Modeling inter-organ communication using a multi-tissue chip. *(a) Illustration of communication via soluble factors (yellow dots) from an upstream organ to local lymph nodes,*

via lymphatic vessels and interstitial fluid flow through each organ. (b) Schematic of the multi-organ device, which consisted of a loop of channels containing wells for tissue slice culture connected to a large pump well. (c) A 3D rendering of the device showing the insertion of the removable mesh support through the open top of the culture well, where the mesh support held the slice suspended within the well to enable flow perpendicular to the tissue. (d) Photo of a two-tissue device (ITX-PEGDA resin) mounted on the motor-based impeller pump external platform, with a US penny for scale. (e) Photo of four variations of the device (ITX-PEGDA resin), containing zero (0T), one (1T), two (2T), and four (4T) wells for tissue slice culture. Each chip was filled with blue food dye to visualize the channels.

Here, we developed a user-friendly, self-contained system for multi-tissue culture under continuous recirculating fluid flow using a 3D-printed device and companion tubing-free motor-based impeller pump, and applied it to model communication with the LN. As a proof of principle, we developed a model of the acute response to vaccination in lymph node slices using the device and impeller pump platform.

4.3 Methods

4.3.1 Device fabrication and assembly

The microfluidic devices and removable mesh supports were designed using Fusion 360. The devices and mesh supports were printed using a CADWorks3D MiiCraft P110Y digital light processing (DLP) printer (CADWorks3D, Toronto, Canada). Devices were printed in MiiCraft Clear resin (BV007a, CADworks3D, Toronto, Canada) and in a custom ITX-PEGDA resin formulated from a previously developed recipe.[43] The ITX-PEGDA resin consisted of poly(ethylene glycol) diacrylate (PEGDA, 250 MW, Sigma Aldrich) as the monomer, phenylbis(2,4,6-trimethylbenzoyl)phosphine oxide (Irgacure 819, Sigma Aldrich) as the photoinitiator, and isopropylthioxanthone (ITX, Fisher Scientific, New Hampshire, USA) as the photoabsorber. Irgacure 819 and ITX were mixed with PEGDA (0.4% w/w) and dissolved for 30 min at 70°C.

All layers were printed at 50 μm at 100% power (5 mW/cm^2), 1.25 s cure time, 4 s base cure time, 6 base layers, and 4 buffer layers. For post-processing, all printed parts were submerged in isopropyl alcohol (IPA) in a Form Wash (FormLabs, Massachusetts, USA) for 5 min, dried thoroughly with nitrogen, and placed in a Form Cure high-intensity UV light box (10 mW/cm^2, FormLabs, Massachusetts, USA) for 1 min. Prior to use with cells or tissue, the device and mesh support were sterilized by soaking in 70% ethanol for 5 min and rinsed for 20 min in 1xPBS (Lonza, Maryland, USA).

4.3.2 Modular chip assembly

Modules were printed in MiiCraft Clear resin as described above, and posts were printed in MiiCraft Black resin (BV002a, Creative CADworks, Ontario, Canada). All printed parts were processed as described above. Before module assembly, the o-ring wells on each module was coated with Rain-X (Rain-X, Texas, USA) using a small paint brush and allowed to dry for at least 1 hr. To assemble, a rubber o-ring (3 x 1 mm, HJ Garden Store, Amazon) was placed in an o-ring well and sandwiched between two modules. While pressing the modules together, two pins were inserted vertically through both sets of holes on the connecting modules to hold the pieces together. After assembly, the device was used similar to the monolithic version.

4.3.3 Preparation of 3D-printed material for tissue culture

To improve biocompatibility of the 3D-printed material, the device and mesh supports were coated in Parylene-C as described previously.[44] In brief, a film of ~1 μm was achieved by adding 1.1 g of mixed isomers of Parylene-C (SCS, Inc. Indianapolis, IN, USA) to the Labcoater 2 parylene coater (SCS, Inc. Indianapolis, IN, USA) for gas-phase deposition onto the prints. Prior to culture of tissue in any 3D-printed device, the print, removable mesh, and stir bar were sterilized by submerging in 70% ethanol for 5 min, followed by two 10 min rinses in 1xPBS.

Once rinsed, the materials were allowed to air dry for at least 30 min before use. The removable mesh supports were loaded into the devices as needed and filled with complete media to the specified volume per device. The chips were then loaded on to the external pump platforms, which were turned on and placed in the incubator for at least 30 min before use to reach 37 ºC.

4.3.4 Motor-based impeller pump assembly

The 3D-printed external housing, chip holder, and chip cover was designed using Fusion 360 and printed using 1.75 mm polylactic acid (PLA) filament (Flashforge, China) using a Monoprice Voxel 3D printer (Monoprice, California, USA). To assemble the motor-based impeller pump, a 6-12 V Mini DC motor (AUTOTOOLHOME) was inserted into the base of the printed housing. A custom magnet holder containing a small fan was 3D printed using the DLP printer described above in the ITX-PEGDA resin. The fan was included on the magnet mount to help push air down through the vents on the top of the motor and mitigate any heat buildup. Two 6-mm brushed nickel magnets (FINDMAG) with a strength of 0.008 T were glued into the magnet holder and mounted on the rotating pin of the DC motor.[25] Each motor was connected to a mini digital DC voltmeter (2.5-30 V, MakerFocus, China) and a pulse-width modulation (PWM) low voltage DC potentiometer (ALDECO), both mounted to their respective holes within the housing base. Within each pump, three anodized aluminum heatsinks (1 g, Easycargo) were mounted along the sides to help distribute heat away from the DC motor. Once assembled, the housing top was initially glued together with hot glue, and the seam was sealed with an epoxy to generate a moisture-free environment within the box (info). The chip holder was glued to the top of the external housing centered over the DC motor. Each pump was connected to a 12 V DC female power connector (Chanzon), which was plugged into the 12 V AC DC power supply adapter wall plug (EWETON). A cord splitter was used to connect all 8 pumps to a single

power supply. All wiring was connected using a tin-lead rosin-core solder wire (ICESPRING) and wrapped in heat shrink tubing (Eventronic, Germany).

A Teflon PTFE encapsulated 2 x 5 mm magnetic stir bar, either 2 x 5 mm (VWR, Pennsylvania, USA) or 3 x 10 mm (Thomas Scientific, New Jersey, USA) were used as impellers. The 2 x 5 mm stir bar was used for all experiments unless noted otherwise. A digital laser photo tachometer (AGPtek, New York, USA) was used to measure the revolutions per minute (RPM) of the magnetic stir bar as it rotated. All RPMs reported were conducted for each individual pump for corresponding voltages, and are the average of three RPM measurements made at a consistent voltage.

4.3.5 Characterization of fluid flow and shear stress in tissue on-chip using COMSOL Multiphysics

The fluid flow profile through the tissue culture well was modeled in three dimensions using the free and porous media flow module and transport of diluted species in porous media module of COMSOL Multiphysics (Version 6.1). The model matched the 3D geometry of the tissue culture well. The culture chamber was split into two cylinders, where the bottom chamber had a diameter of 6.2 mm with a height of 1.5 mm and the top chamber had a diameter of 7.7 mm with a height of 2.5 mm. Both inlet and outlet channels had similar geometry (0.5 x 0.5 mm cross-section, length = 15 mm), where the inlet channel connected to the top of the top chamber and the outlet channel connected to the base of the bottom chamber on the opposite side. The tissue slice was modeled as a cylinder with a diameter of 5 mm and a height of 0.3 mm, where the inner 3 mm represented tissue and the surrounding 1 mm ring represented the 6% agarose. Aqueous media was modeled as an incompressible fluid with a viscosity of 1.00 mPa s and a density of 1000 kg/m^3. The tissue was modeled as a porous matrix with a viscosity of 1.00 mPa

s, a density of 1000 kg/m^3, a porosity of 0.2, and a permeability ranging from 1E-10 m^2 to 1E-12 m^2.[35,45] The 6% agarose was modeled as a porous matrix with a viscosity of 1.00 mPa s, a density of 1000 kg/m^3, porosity of 0.2, and a permeability of 4.26 x 10^{-18} m^2.[46] The mesh support geometry was excluded from the physics to generate a wall around the geometry. A "normal" triangular mesh was used as generated by the software. The simulation was solved in time-dependent mode, and the readouts were reported at 5 min after reaching steady state unless noted otherwise. The inlet velocity was set to a maximum velocity of 30 μm/s within the channel, unless stated otherwise. The outlet was set to atmospheric pressure. The velocity and shear stress through the tissue were measured along cut lines through the center of the slice (z = 0.15), 10 μm from the top (z = 0.29), and 10 μm from the bottom (z = 0.01). Unless otherwise noted, the central cut line was used. When testing different inlet speeds, the inlet velocity was set to a maximum velocity of 10 μm/s, 20 μm/s, 30 μm/s, 50 μm/s, 75 μm/s, 100 μm/s, and 150 μm/s within the channels.

The computational model was used to predict the fluid shear stress (FSS) and shear rate at the channel wall and the central tissue cutline. The inlet velocity was set to the range of maximum velocities listed above. The FSS (dyn/cm^2) was approximated using Equation 1, where γ is shear rate (1/s) and η is viscosity (Pa s) and converted from Pa to dyn/cm^2 by multiplying by 0.1.

$$FSS = 0.1\gamma\eta \qquad \text{Equation 4.1}$$

4.3.6 Characterization of experimental velocity within the device

The maximum velocity was measured experimentally as described previously.[25] In brief, a drop of blue food coloring was inserted into a port within the device and tracked using a Dino-

Lite Edge 3.0 digital microscope (SunriseDino, California, USA). Images were collected over time, and the distance the dye front moved over time was measured to determine fluid velocity.

4.3.7 Animal model

All animal work was approved by the Institutional Animal Care and Use Committee at the University of Virginia under protocol #4042, and was conducted in compliance with guidelines from the University of Virginia Animal Care and Use Committee and the Office of Laboratory Animal Welfare at the National Institutes of Health (United States). Inguinal, axial, and brachial lymph nodes were harvested from female and male C57BL/6 mice (Jackson Laboratory, USA) under the age of 6 months following humane isoflurane anesthesia and cervical dislocation. The lymph nodes were collected into "complete RPMI" media consisting of RPMI (Lonza, Maryland, USA) supplemented with 10% FBS (Corning, New York, USA), 1 x l-glutamine (Gibco Life Technologies, Maryland, USA), 50 U mL^{-1} Pen/Strep (Gibco Life Technologies, Maryland, USA), 50 µM beta-mercaptoethanol (Gibco Life Technologies, Maryland, USA), 1 mM sodium pyruvate (Hyclone, Utah, USA), 1x non-essential amino acids (Hyclone, Utah, USA), and 20 mM HEPES (VWR, Pennsylvania, USA).

4.3.8 Preparation of lymph node slices

To generate lymph node slices, the inguinal, axial, and brachial lymph nodes were inserted into 6% w/v low melting point agarose (Lonza, Maryland, USA) in 1xPBS (Lonza, Maryland, USA) and punched into 5 mm blocks using a disposable biopsy punch (Royaltek).[47] The slices were generated using a Leica VT10000S vibratome (Illinois, USA) set to a speed of 90 (0.17 mm/s) and a frequency of 3 (30 Hz). Slices were collected and placed in a 6-well plate containing ~3 mL per well of complete media and placed in a sterile cell culture incubator (37 ºC with 5% CO_2) for 1 hr to rest prior to use.

4.3.9 Measurement of viability of primary murine LN tissue

For resin cytotoxicity, simple wells similar in size to the pump well were 3D printed and parylene coated as described above. The printed wells were inserted into a 12 well plate and filled with 1000 µL of fresh media, with empty wells used as a plate control. The plate was equilibrated in the cell culture incubator at 37 ºC for at least 30 min, after which LN slices from different nodes were randomly added to each well and cultured for 24 hrs.

For on-chip culture, the chips, mesh inserts, and stir bars were sterilized and dried as described above. Once dry, the mesh support(s) and stir bar were loaded into each device before filling with 1600 µL of fresh media. The channels were flushed through the ports using a pipette to ensure there were no bubbles hindering fluid flow. Chips were loaded onto the pump platforms and covered with a FDM 3D-printed cover, and the pumps were set to the required speed. The whole chip and pump assembly was equilibrated in the cell culture incubator for at least 30 min before tissue slices were added, after which slices from different nodes were randomly added to the culture wells containing mesh supports and cultured for 24 hrs. All cell and tissue viability experiments consisted of two identical experiments performed on different days to test reproducibility.

Following the culture period, cell and tissue viability was assessed using a CellTiter 96® AQ_{ueous} One Solution Cell Proliferation Assay (MTS assay, Promega, Wisconsin, USA). For measuring LN slice viability, intact slices were added directly to 100 µL of media in a 96 well plate. A killed control was generated by adding 15 µL of 10X Lysis Buffer (CyQUANT LDH Cytotoxicity Assay Kit, Invitrogen, Massachusetts, USA) to the media for 30 min at 37ºC. Next, 50 µL of fresh media was added to each well. Then, 30 µL of CellTiter One Solution Reagent was added to each well and incubated for 3 hrs at 37ºC. At the end of the culture period, 100 µL

of media was transferred to fresh wells on the same plate. Bubbles were removed by centrifugation for 5 min at 400 x *g*. Absorbance was measured at 490 nm using a CLARIOstar plate reader (BMG LabTech, Germany). The background absorbance from media-only controls were subtracted from the killed controls and samples.

4.3.10 Soluble factor recirculation and capture on-chip

To generate mock tissue, biotinylated magnetic beads (0.5 μm beads, RayBiotech, Georgia, USA) were embedded in 3% w/v agarose (Lonza, Maryland, USA) in 1x PBS (Lonza, Maryland, USA), which was cast in a 3 mm punched hole within a 35 mm petri dish filled with solidified 6% w/v agarose. This was punched into 5 mm blocks with the bead-laden gel in the center using a disposable biopsy punch (Royaltek). Blocks were sliced to a thickness of 300 μm using previously reported methods.[35,47–49] Slices were collected and placed in a 6-well plate containing 1xPBS.

Prior to protein insertion, the channels of the device (ITX-PEGDA resin) were blocked with BSA (bovine serum albumin) by filling the device 1% BSA (Fisher Scientific, New Hampshire, USA) in 1 x PBS (Lonza, Maryland, USA) and recirculating at 1250 RPM (1.7 V, 75 μm/s maximum channel velocity) for 1 hr. Fluid flow direction was confirmed using a drop of blue dye inserted into the channel. A biotin-bead loaded slice was added to a culture well within the device, and 5 μL of 200 μg/mL NeutrAvidin™ Rhodamine Red™-X (NRho, Fisher Scientific, New Hampshire, USA) was pipetted to the opposite culture well. The biotin-bead loaded slices were removed from the device using the removable mesh insert and imaged at various time points using a Zeiss Axio Zoom macroscope (Carl Zeiss Microscopy, Germany) and analyzed in ImageJ, where the background-subtracted mean grey value of the entire tissue slice was calculated.[50]

4.3.11 DQ-OVA capture in live LN slices on-chip

LNs were sliced as described above. During the 1 hr rest period post tissue slicing, a portion of the slices were removed to generate a killed control for on-chip and off-chip culture. Individual slices were each added to a well in a 24 well plate containing 2 mL of 35% ethanol for 30 min, then moved to a new well containing 1xPBS for a 30 min rinse. Live and killed slices were cultured both on-chip and off-chip in the presence of DQ-ovalbumin (DQ-OVA, Invitrogen, Massachusetts, UVA). Following the 1 hr rest/kill periods, the slices were added to either a well plate or the downstream tissue culture well of a 2T chip, both filled with 1800 µL of complete media. For the on-chip conditions, 10 µL of 500 µg/mL DQ-OVA was added to the upstream culture well. Similarly, 10 µL of 500 µg/mL DQ-OVA was added directly to each off-chip culture well of the well plate. The slices were imaged at 0 hr (before DQ-OVA addition), 2 hr, 4 hr, and 24 hr on the Zeiss Axio Zoom macroscope. The off-chip slices were imaged within the well plate, while the on-chip slices were removed on the mesh supports and placed on a sterile petri dish for imaging before re-insertion. The slices were analyzed using ImageJ, where the background-subtracted mean grey value of the entire tissue slice was calculated. All images were leveled the same unless stated otherwise. The data presented consisted of two identical experiments performed on different days to demonstrate reproducibility.

4.3.12 Comparative vaccination in vivo, off-chip, and on-chip

For *in vivo* vaccinations, C57Bl/6 mice were vaccinated subcutaneously with four 50 µL injections at the shoulders and hips of 100 µg/mL R848 and 500 µg/mL rhodamine-labeled ovalbumin (Rho-OVA) in sterile 1x PBS, or PBS as a vehicle control. The skin-draining lymph nodes (axillary, brachial, and inguinal) were harvested 24 hours later and sliced as described above. For off-chip and on-chip vaccination, LN slices were collected from naive animals and

were either incubated with 0.2 μg/mL R848 and 2 μg/mL Rho-OVA or PBS for 6 hours, at which time the LN slices were collected.

Upon collection, all slices were immunostained as described previously.[51] Briefly, slices were blocked with anti-mouse CD16/32 for 30 mins in a cell culture incubator. An antibody cocktail containing: BV421 CD86, AF488 CD69, AF647 CD40, and Starbright Violet 670 CD19, was added for 1 hour (Table 4.1). Prior to imaging, the slices were washed for 30 mins in 1x PBS. Confocal microscopy was performed on a Nikon A1Rsi confocal upright microscope using 400, 487, 561 and 638 nm lasers paired with 450/50, 525/50, 525/50 and 685/70 nm PMTs on a GaAsP detector, respectively. Starbright Violet 670 was excited off the 400 laser and detected with the 685/70 PMT. Images were collected with a 40×/0.45NA Plan Apo NIR WD objective.

Images were analyzed using Image J (version: vt1. 53t). Three regions of interest (ROIs), the entire slice, CD19+, and CD19- region, were defined by thresholding the outline of the tissue or the CD19 signal in the Cy5 channel. In each ROI, the mean grey value (MGV) of CD86, CD69 and CD40 were quantified. Each image was corrected for spillover from other channels by subtracting average MGV from three fluorescent minus one (FMO) images. The reported results are pooled from three identical experiments performed on different days.

Table 4.1 Antibody Information

Target	Clone	Fluorophore	Product Number	Lot Number	Vendor
CD16/32	93	N/A	101302	B366439	Biolegend
CD86	GL-1	Brilliant Violet 421	105032	B364400	Biolegend
CD69	H1.2F3	Alexa Fluor 488	104516	B371402	Biolegend
CD40	3/23	Alexa Fluor 647	124614	B380619	Biolegend

CD19	N/A	Starbright Violet 670	MCA1439SBV670	100004959	Bio-Rad

4.4 Results and Discussion

4.4.1 Customizable 3D-printed platform for tissue slice co-culture

The major design goals when designing the multi-tissue chip were 1) fast and reproducible fabrication; 2) expandable design to enable the co-culture of two or more tissue samples; 3) easy tissue insertion and removal to allow for timecourse imaging without tissue damage; 4) biocompatibility with tissue slice culture; and 5) recirculating fluid flow on-chip. Inspired by the principles of our previous hand-built PDMS prototype,[16] we developed a monolithic 3D-printed device that consisted of a loop of channels that connected varying numbers of tissue culture wells in line with a pump well[25] for recirculation of media and secreted molecular cues (Figure 4.1b-d). The use of DLP 3D printing provided a semi-transparent, easily customizable device. This fabrication method enabled complex 3D architectures such as sloped channels and mesh supports for slice culture, which would be challenging to produce using traditional soft lithography fabrication.[25,52] Each device only required <1 hr to print, including cleaning and post-treatment. Inspired by other modular OOCs,[9,53,54] we designed a series of monolithic devices with zero to four culture wells (0T – 4T) to illustrate the flexibility of the platform while retaining its simplicity (Figure 4.1e). The 2T device was used throughout the majority of this work (Figure 4.1d).

In principle, this system is compatible with 2D, 3D, or explant cultures inserted into the culture wells.[3] Here, we incorporated live LN tissue slices to maintain the spatiotemporal organization of this organ and make it accessible for imaging and stimulation.[16,47,55] To allow for fragile slices to be easily added on demand and removed repeatedly for timecourse imaging, tissue slices were loaded into the device on top of a custom mesh support (Figure 4.1c). The

mesh support was designed to position the tissue between the channel inlet and outlet, to ensure fluid flow transverse to the tissue to carry signals downstream while providing gaps around the tissue to limit resistance through the fluidic loop.[16]

4.4.2 Alternative modular design for LEGO-like device assembly

Modular microfluidics is growing in popularity, where each device is comprised of a set of pre-made parts that are reconfigured into a range of device orientations. These devices have been made out of a variety of materials (e.g. PDMS, 3D-printed resin) for different applications (e.g. micromixing, organs-on-chip).[53,54,56,57] Here, we designed an alternative modular device comprised of individual modules that assemble to form a loop of channels similar to the monolithic device design (Figure 4.2a,b). This modular design was intended especially for collaborators, where they would receive a set number of each module and any orientation can be achieved without designing, printing, or purchasing another device. We formed a leak-free seal between modules using an o-ring gasket, where an o-ring well surrounded the channel inlet or outlet on the end of a module to allow a fluidic connection between modules (Figure 4.2c). The o-ring well was pre-treated with Rain-X to increase hydrophobicity of the 3D-printed material to prevent leaks. Once the o-ring was placed between two modules, 3D-printed pins were inserted vertically to hold the modules together and compress the o-ring (Figure 4.2d). Varying numbers of tissue modules (T) and straight channel modules (S) were added to either increase the number of tissues cultured and/or increase the channel length (Figure 4.2e). Due to the pressure from the o-ring seal between two modules, the printed material would often crack, which resulted in leaks between the modules. This issue would likely be resolved by either switching to a more durable material that is less prone to cracking or by developing a different method to generate a leak-free connection, such as the “pop-it” connection[58] or a magnetic interface.[11,59]

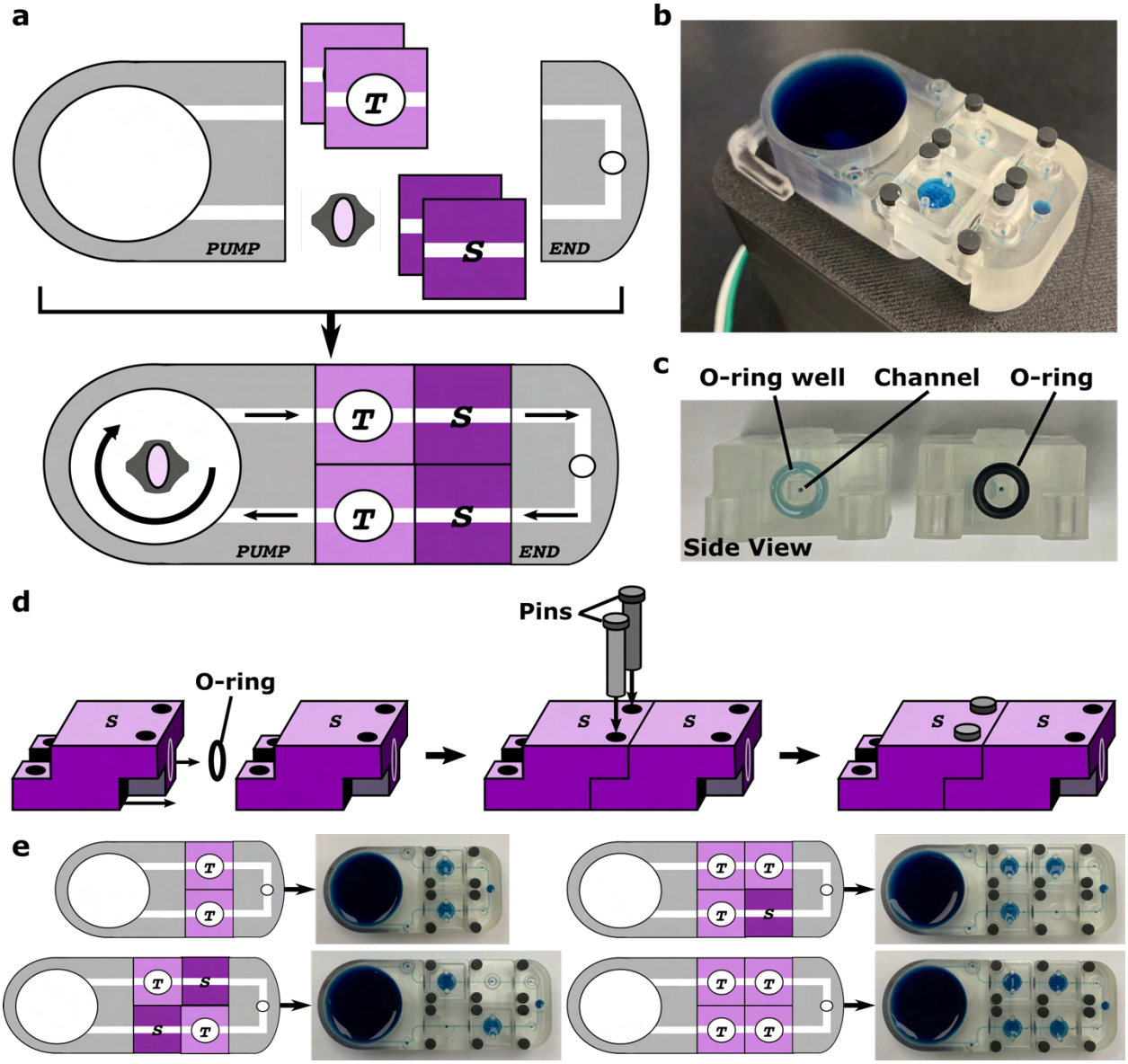

Figure 4.2 Modular device design increased user customization. *(a) The device was comprised of individual modules that assemble to form a device with a simple loop of channels connecting tissue culture wells together. Each device contained variable numbers of tissue modules (T) and straight channel modules (S), with a pump module and an end module on either side to create a closed channel. (b) An image of a fully assembled modular chip with a tissue module and a straight channel module filled with blue dye. (c) The connections between modules consisted of an o-ring in an o-ring well surrounding the channel inlet and outlet. (d) An o-ring was placed between two modules in the o-ring well and the modules were pushed together. The modules were held together by pins that were inserted vertically on either side of the o-ring. (e) Varying numbers of tissue modules and straight channel modules were combined to generate a wide variety of different device layouts and channel lengths.*

4.4.3 Compact, tubing-free motor-based impeller pump platform

In parallel with the chip, we developed a companion pump with the following major design criteria: 1) no tubing, few wires, and simple controls for ease of use; 2) tunable recirculating fluid flow at biomimetic rates; 3) minimal media volume to reduce soluble factor dilution; 4) low overall cost; 5) small pump footprint for high-throughput experiments; and 6) low heat output to maintain stable temperatures (±1°C) in cell culture incubators. To achieve the first two criteria, we started with a tubing-free impeller pump that drove recirculating flow at biomimetic velocities through a simple microchannel loop by using computer fans to rotate magnets.[25] Here, we redesigned the pump to reduce the volume of the chip by > 2-fold and the footprint of the pump external housing by 2-fold. A simple stir bar was used as the impeller (visible in Figure 4.1e), and small DC motors were used to drive magnet rotation inside a custom box that held all of the electronics (Figure 4.3a,b; see Methods). As the motor shaft rotated, the spinning magnets drove the rotation of the stir bar within the device, which generated recirculating fluid flow in the connecting channel loop (Figure 4.3a).

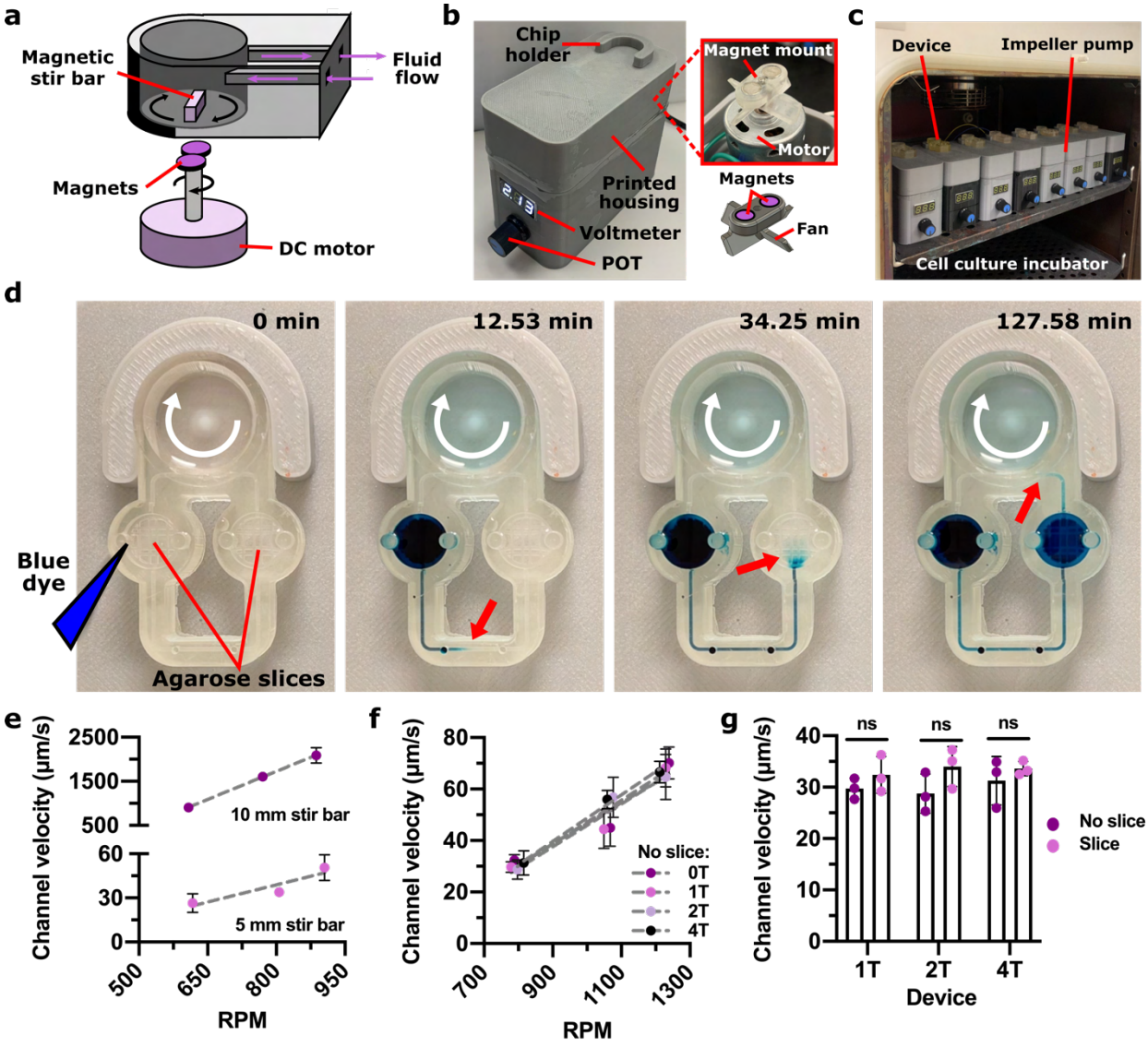

Figure 4.3 Motor-based impeller pump for fluid flow recirculation and control on-chip. *(a) Schematic of the approach for stir bar rotation. (b) Photos of the pump platform showing the (left) outside of the pump box and (right) interior of the pump. (c) Photo of eight impeller pumps on a shelf in a standard cell culture incubator, each holding a single multi-tissue chip. (d) Time-lapse images of recirculating fluid flow on a 2T device (Clear resin) with an agarose slice in each well (5 mm stir bar, 1000 RPM). Blue dye was inserted in the upstream culture well, and over time, moved through the channel to the downstream culture well and then the pump well (dye front marked with red arrow). The stir bar rotated clockwise within the pump well (white arrow). (e-f) Experimentally measured maximum velocity within the channel in (e) a 0T device using a 10 mm stir bar and a 5 mm stir bar, and (f) in varied device designs (0T – 4T) with a 5 mm stir bar. Dots and error bars represent mean and standard deviation; some error bars too small to see. (g) Experimentally measured maximum velocity in the channel at a low RPM (1.2 V, 780 RPM) with and without the addition of an agarose slice in the 1T, 2T, and 4T devices with*

a 5 mm stir bar. Each dot represents one velocity measurement. Results were compared using an unpaired t test (n = 3). ns indicates p > 0.1.

With this design, the overall cost of materials in the pump was approximately $35, and eight pumps fit in a line within the incubator (Figure 4.3c) for a theoretical total of 48 pumps per incubator. We confirmed that the stir bar revolutions per minute (RPM) increased linearly with voltage (Figure 4.4a) and was stable for 90 hrs, as expected (Figure 4.4b).[25] In a 10-day test of heat output, temperatures remained within the acceptable range (+/- 1 deg),[60] even with 8 motors on throughout the culture period (Figure 4.4c).

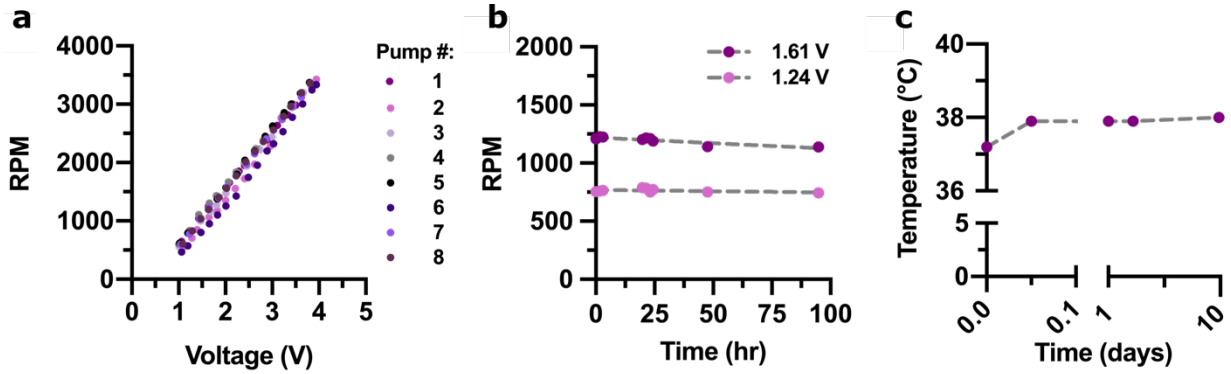

Figure 4.4. Motor-based impeller pump characterization. *(a) As the voltage increased, the RPMs for each pump increased linearly, with little variation between pumps. (b) The RPM stability at two different pump voltages over a 90 hr time period. (c) The temperature within a cell culture incubator over 10 days with eight impeller pumps running at 4 V.*

4.4.4 On-chip fluid recirculation at controllable speeds

Blood and lymph velocity varies greatly *in vivo*, with slower speeds in superficial lymphatics (1-20 µm/s)[61] and blood vessel capillaries (10-100 µm/s),[62] and greater speeds in the mesenteric lymphatics (0.1-2 cm/s),[63,64] veins (1.5-7.1 cm/s),[65] and arteries (50-100 cm/s).[66,67] To test the ability of the multi-organ chip and pump to connect tissue compartments at physiological flow rates, we first confirmed that fluid recirculated within the 2T device when fully assembled with agarose slices as mock tissue in each well (Figure 4.3d). Blue dye inserted in the upstream culture well reached the downstream culture well in 30 min and the pump well in 130 min

(Figure 4.3d). Next, we quantified the velocities through the channel as a function of user-controllable parameters.[25] Doubling the length of the stir bar from 5 to 10 mm increased the channel velocity from 10s of μm/s to mm/s, respectively, thus providing access to different flow regimes (Figure 4.3e).

In the absence of tissue or agarose slices in the wells, channel velocities were comparable between each device variation (0T, 1T, 2T, and 4T) (Figure 4.3f). Furthermore, the addition of an agarose slice within each culture well of the 1T, 2T, and 4T devices did not impact the channel velocity, at least at the moderate RPM that was tested (780 RPM; Figure 4.3g). These results demonstrated that there was negligible additional resistance added to the microfluidic loop with the addition of the culture well or mock tissue slices. We anticipate that with the ability to achieve a wide range of fluid flow regimes, the pump can be tuned to fit the needs of most tissue models.

4.4.5 Tissue permeability and channel flow rate control interstitial fluid velocity and soluble factor delivery to tissue in 3D computational model

Having established experimental control over flow rates through the microchannel, we sought to predict interstitial flow rates, molecular delivery, and shear stress through the tissue as a function of tissue permeability and pump speed. We developed a three-dimensional finite element model using COMSOL Multiphysics of the tissue culture well (as in Figure 4.1c), in which the tissue slice and agarose were modeled as porous matrices. The tissue domain sat atop an impermeable meshwork structure where its geometry matched to the 3D printed mesh support (Figure 4.5a,b).

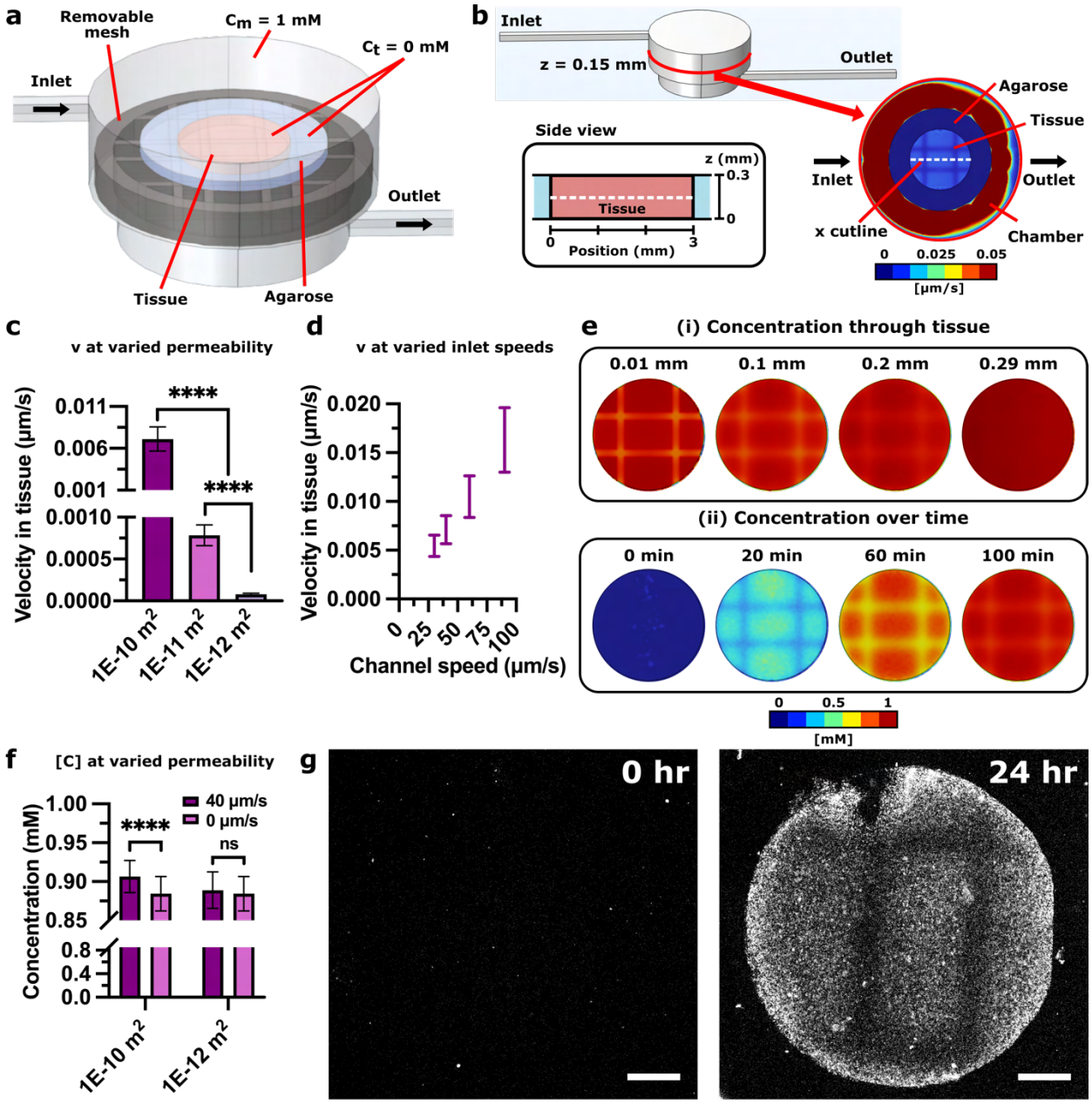

Figure 4.5 Simulated fluid velocity and tracer concentration in a tissue slice on-chip. *(a) Geometry of the 3D COMSOL simulation colored to show the tissue (pink) embedded in agarose (blue) resting on the removable mesh support (dark grey). The inlet channel intersects the top of the culture well, while the outlet channel intersects the bottom on the opposite side. (b) The velocity and tracer concentration was measured along cutlines along the x axis in line with the inlet and outlet channels at different z planes, with the position corresponding to a position of 0 – 3 mm along the tissue region as noted here. (c-d) Predicted velocity in tissue at a (c) range of tissue permeabilities and a (d) range of inlet speeds. Results in c were compared using a one-way ANOVA with Tukey post-hoc tests. **** indicates $p < 0.0001$. The bars represent variability of velocity along the cutline. (e) Color plots of protein concentration in the tissue domain at a permeability of 1E-10 m^2 showing (i) different z planes through tissue and (ii) the middle of the tissue (z = 0.15 mm) over time. (f) Predicted protein concentration in tissue as a function of*

*tissue permeability at a central cutline (z = 0.15 mm), with flow (40 μm/s) and without flow (0 μm/s) at 100 min). Bars represent standard deviation. Results were compared using a one-way ANOVA with Tukey post-hoc tests. **** indicates p < 0.0001, ns indicates p > 0.2. (g) Representative images of the effect of the mesh support, with NRho (white) captured within the biotin region of the agarose slices at 0 hrs and 24 hrs.*

First, we asked how interstitial fluid flow rates scaled with tissue permeability and channel flow rate, and how these compared with physiological interstitial flow rates. Interstitial flow rates through different tissues are widely variable, with estimates ranging from 0.01 – 10 μm/s.[19,20,68] Here, we used the LN as our model tissue, where the tissue permeability is largely unknown, with predictions ranging from 10^{-10} to 10^{-12} m^2,[35,45] and it likely varies by tissue region and the immunological state of the organ. We found that when the tissue was more permeable (1E-10 m^2), the fluid velocity in tissue was 0.006 μm/s (Figure 4.5c). This velocity in tissue was below the lower bound of physiological interstitial fluid flow, which limits the biomimicry of this system as this fluid velocity is likely not generating an environment comparable to that found *in vivo*. This is likely due to the open space in the mesh around the slice, which was initially incorporated in the mesh design to reduce the resistance in the fluidic loop to allow for fluid recirculation using the impeller pump. In the future, the open space in the removable mesh support around the slice could be reduced to encourage more flow to pass through the tissue. Finally, we confirmed that the interstitial fluid speed increased linearly with channel speed, as expected (Figure 4.5d).

One of the critical functions of a multi-tissue chip is to transport molecular cues to downstream tissues. Given the slow interstitial flow rates in the prior simulations, we tested the relative contribution of convection versus diffusion alone to the penetration of soluble molecules into the tissue domain. Consistent with a small role for convection at 1E-10 m^2, both the tracer concentration (Figure 4.5ci, Figure 4.6a) and fluid velocity (Figure 4.6b) were lower in the

locations directly above the bars of the mesh support, although uniformity increased both at a greater z plane in the tissue and over time due to diffusion (Figure 3e). In simulations with and without fluid flow, the flow increased the amount of tracer accumulated in the tissue domain only at high tissue permeability (1E-10 m^2) (Figure 4.5f). Since the permeability of LN tissue is highly variable and uncertain, we conclude that there is little fluid passing through the slice and that the main mode of molecular delivery would be through diffusion.

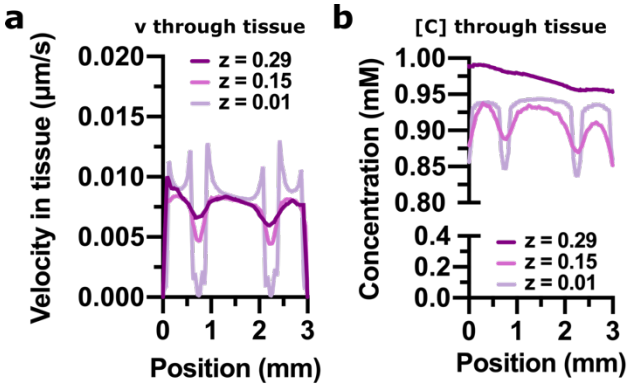

Figure 4.6 Predicted velocity and concentration throughout tissue. *Predicted (a) velocity and (b) protein concentration in tissue with a permeability of 1E-10 m^2 at different z planes at t = 100 min with an inlet speed = 40 μm/s.*

Next, we tested the impact of recirculating fluid flow on the delivery and distribution of soluble factors to a downstream tissue slice by using a fluorescently-labeled soluble ligand (NeutrAvidin Rhodamine Red-X, or NRho) paired with a receptor (biotinylated beads) in a model tissue (agarose).[16] In chips pre-filled uniformly with NRho, we found that the presence of fluid flow increased the amount of captured protein initially as NRho was replenished around the slice (Figure 4.7). We also examined the distribution of delivered protein in the downstream slice, and found that as predicted by the COMSOL model, more protein was delivered through the regions above open areas of the mesh support (Figure 4.6g). In the future, the mesh design can be further optimized to reduce the area of the crossbars as needed.

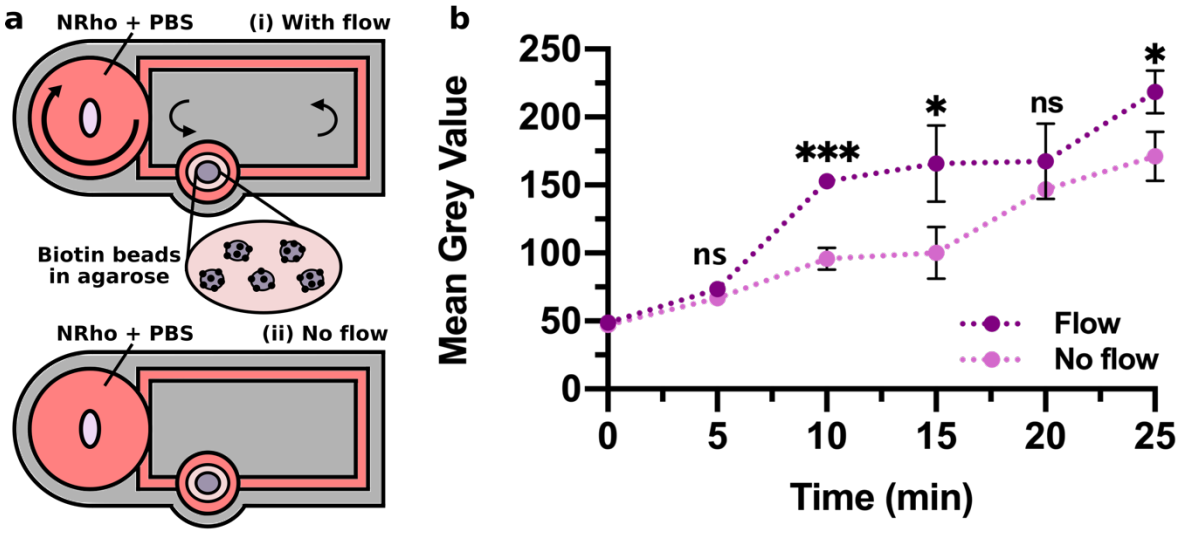

Figure 4.7 Protein capture with and without flow on-chip. *(a) A single compartment chip (1T) was filled with NRho and PBS and a biotinylated mock tissue slice was added to the culture well, either (i) with flow or (ii) without flow. (b) Quantification of NRho MGV with and without flow over time (n = 3). Results were compared using a one-way ANOVA with Tukey post-hoc tests (n = 3). *** indicates $p < 0.006$, * indicates $p < 0.02$, ns indicates $p > 0.2$. Dots and error bars represent mean and standard deviation, respectively.*

4.4.6 Low predicted shear stress expected to have limited impact on tissue viability

The movement of fluid through vasculature and tissue parenchyma imparts mechanical forces, or shear stress, on the surrounding cells.[69] In microphysiological models, shear stress must be kept low enough to avoid damage, if not matched to physiological values to study its effect. Using the computational model described above, we found that at a channel speed of 30-40 µm/s, the wall shear stress in the inlet channel ranged from 0.02-0.04 dyn/cm^2 (Figure 4.8a), well below the shear stress found in lymphatic vessels (0.6-12 dyn/cm^2)[63] and blood vasculature (0.35-70 dyn/cm^2).[69] In addition, the shear stress within tissue with a permeability of 1E-10 m^2 was <1.5E-6 dyn/cm^2 (Figure 4.8b), which was on the lower end of shear stress as a result of physiological interstitial flow (<0.1-0.5 dyn/cm^2).[70,71] Thus, shear stress was not expected have a significant impact on tissue viability in this device at these flow rates.

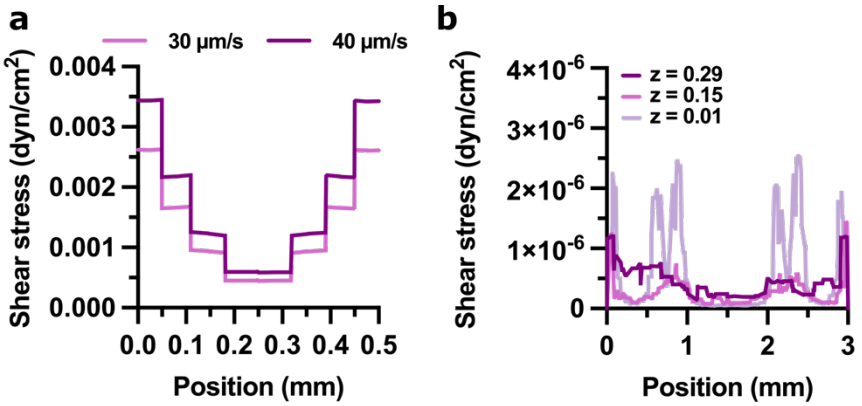

Figure 4.8 Predicted shear stress on-chip. *(a) Predicted shear stress in the inlet channel at an inlet speed of 30 and 40 µm/s. (b) Predicted shear stress through tissue at an inlet speed of 40 µm/s with a tissue permeability of* $1x10^{10}$ m^2.

4.4.7 Lymph node tissue slices remain viable for 24 hr culture under recirculating flow on-chip

With organ-on-chip technology, it is critical that the material and culture conditions are not toxic to cells and tissue. This is particularly challenging with fragile primary cells and tissue of the immune system. Although 3D-printed materials fabricated from commercially available resins are highly cytotoxic to primary murine splenocytes,[25,52] we recently showed that coating the materials with a layer of parylene C was sufficient to protect splenocytes for at least 24 hr.[44] Here, we found that parylene C coating similarly restored viability of primary LN slices on 3D printed devices to the same level as slices cultured off-chip after 24 hr culture using an MTS assay (Figure 4.9a). Due to the heterogeneity of cell number across lymph node slices, a greater deviation in MTS signal occurred in live samples as the assay is sensitive to number of cells present. Next, we tested for any impact of recirculating flow or co-culture on the 2T chip. LN slice viability was not significantly different on-chip under flow than in the live off-chip control (Figure 4.9b). We note that although not statistically significant, the high pump speed (75 µm/s) trended lower in viability than the other conditions, indicating possible damage that should be explored further in the future. At the low speed (30 µm/s), viability was similar whether one or two slices were cultured in the device, and not different between upstream and downstream

culture wells (Figure 4.9c). These results confirm that tissue slices can be cultured in either well and in tandem without loss of viability.

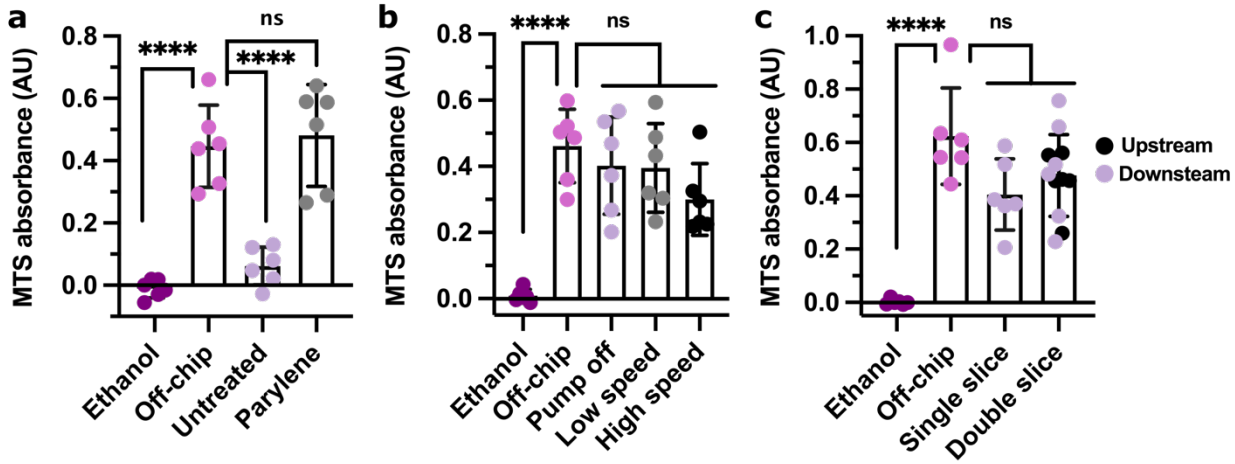

Figure 4.9 Lymph node slices were viable for 24 hr culture on-chip. *(a) MTS assay absorbance of LN slices cultured in untreated and parylene-coated 3D-printed wells (Clear resin) for 24 hrs, without fluid flow, compared to live (off-chip) and killed (ethanol) slices cultured off-chip. (b) MTS assay absorbance of LN slices cultured for 24 hrs on the parylene-coated 2T device (Clear resin) with the pump off, at low speed (1.2 V, 35 µm/s), or at high speed (1.7 V, 75 µm/s) compared to live (off-chip) and killed (ethanol) slices cultured off-chip. (c) MTS assay absorbance of LN slices cultured for 24 hrs on the 2T device (Clear resin) with one or two slices cultured per device at a low pump speed (1.2 V, 30 µm/s) compared to live (off-chip) and killed (ethanol) slices cultured off-chip. Assay results from (a) - (c) were compared using a one-way ANOVA with Tukey post-hoc tests (n = 6). **** indicates $p < 0.0001$, ns indicates $p > 0.1$. Bars represent mean and standard deviation. Each dot represents one LN slice. All results pooled from two independent experiments.*

4.4.8 Two-compartment chip mimics antigen drainage to and processing in lymph node slices

Having established that the chip and pump provided recirculating fluid flow and molecular communication between samples, we sought to use this multi-compartment system to model lymphatic drainage to the live lymph node tissues. *In vivo*, LNs continually filter lymph fluid to pick up and process draining antigen. The concentration of antigen the LN receives can vary depending on the drainage pathway, either a direct route through lymphatic connection or indirect route through systemic vasculature. Here, we tested the extent to which the drainage and capture of proteins within the LN was emulated on-chip.

First, we tested the extent to which the multi-compartment chip modeled these effects by injecting NRho dye into a compartment directly upstream of a biotinylated model tissue (channel first) versus one connected through the pump well (well first) (Figure 4.10a). For the first hour, the channel-first condition had a nearly 10-fold greater rate of capture compared to the well-first condition (Figure 4.10b), resulting in a level of signal that took the well-first condition 24 hr to attain. Rates were similar after the first hour, and we anticipate that eventually, both conditions would reach equilibrium with comparable NRho capture.

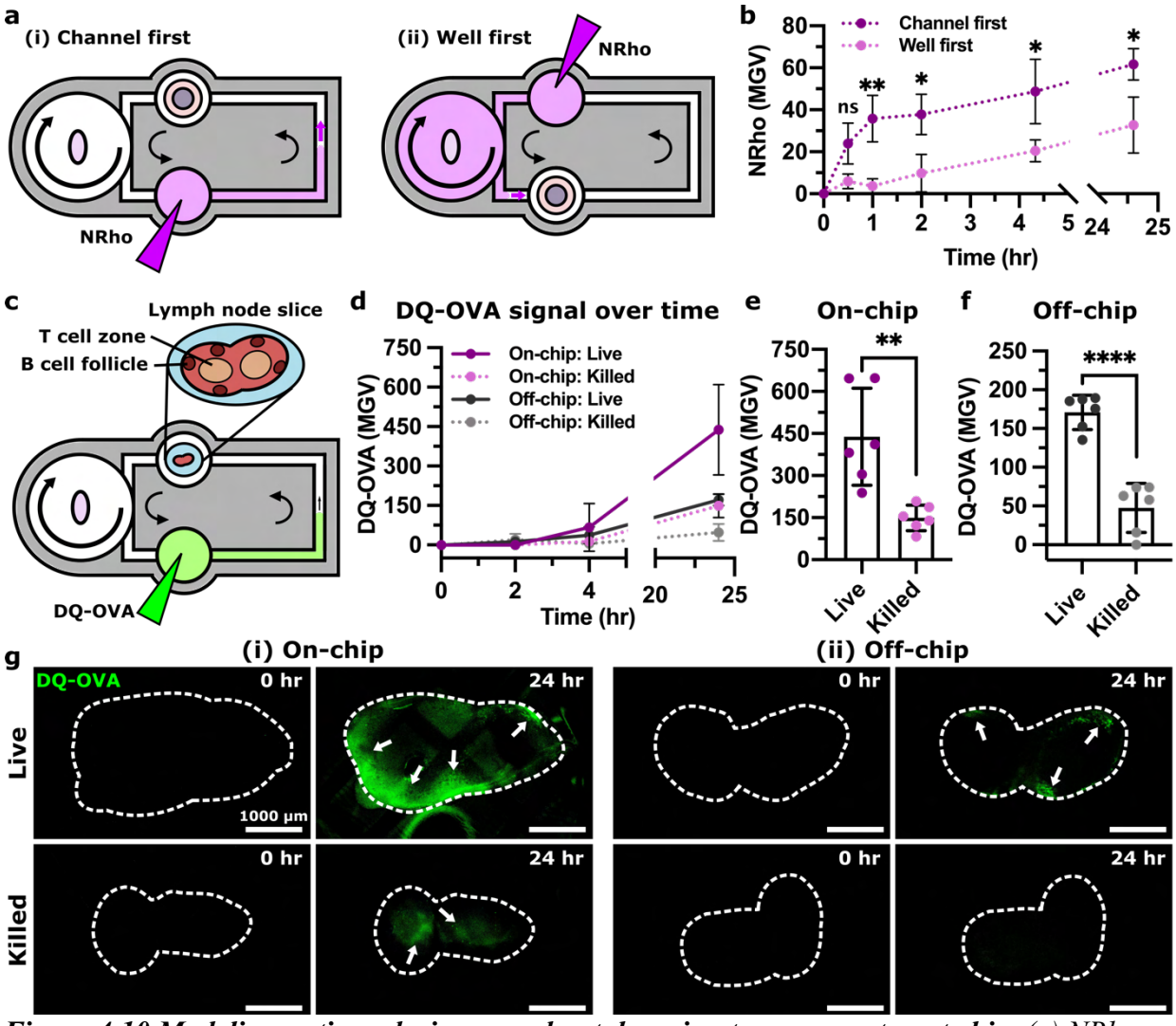

Figure 4.10 Modeling antigen drainage and uptake using two-compartment chip. *(a) NRho was inserted in a filled 2T device (uncoated ITX-PEGDA resin) in the (i) channel first orientation and the (ii) well first orientation. (b) Quantification of NRho MGV in channel first*

*and well first conditions over time (n = 3). Results were compared using a one-way ANOVA with Tukey post-hoc tests. ns indicates p > 0.3, * indicates p < 0.03, and ** indicates p < 0.007. Dots and error bars represent mean and standard deviation, respectively (c) A lymph node slice was inserted in a 2T device (parylene-coated Clear resin) with a DQ-OVA injection in the upstream culture well. (d) Mean gray value (MGV) of DQ-OVA in LN slices over time, showing processing of protein antigen. Dots and error bars represent mean and standard deviation; some error bars too small to see. (e,f) MGV of DQ-OVA in live or ethanol-treated LN slices cultured on-chip or off-chip at 24 hr. Unpaired t test (n = 6). **** indicates p < 0.0001, ** indicates p < 0.003. Each dot represents one LN slice. (g) Representative images of DQ-OVA signal (green) in live and killed slices cultured (i) on-chip and (ii) off-chip at 0 hr and 24 hr. Slices outlined with dashed white line from brightfield images (not shown). Arrows indicate regions that appear to have processed DQ-OVA. All results pooled from two independent experiments.*

Next, we selected DQ-ovalbumin (DQ-OVA) as a model antigen for use with live LN tissue on-chip, as it becomes fluorescent only once proteolytically cleaved within cells. When added to murine LN slices in static culture, DQ-OVA signal was observed primarily in the sinuses and lymphatic vessels, similar the distribution after *in vivo* injection.[47,49] To model lymphatic drainage, DQ-OVA was injected under low speed fluid flow (1.2 V, 30 μm/s) into the upstream culture well, similar to the "channel first" configuration (Figure 4.10c), or added to a well plate in static conditions (no flow) as a reference to traditional culture.

As expected, the DQ-OVA signal increased at a greater rate in live LN slices than in ethanol-treated killed controls (Figure 4.10d-f), both on-chip and off-chip, confirming that the live slices remained metabolically active and able to process antigen on-chip. A slow appearance of signal in ethanol-treated slices may have been due to residual protease activity (Figure 4.10d);[72,73] we observed similar results in formalin fixed tissues previously.[47] Processed antigen was brighter in slices on-chip than off-chip (Figure 4.10d), consistent with better delivery by fluid flow than in static culture. We note that the DQ-OVA signal magnitude and distribution was variable between different lymph node slices, a feature commonly observed due to the heterogenous cell distributions found in the tissue. After 24 hrs, the live slices cultured on-chip showed the mesh support pattern in certain regions (Figure 4.10gi), similar to the protein capture

experiment discussed above (Figure 4.5g). Nevertheless, processed antigen appeared in similar regions of the lymph node as observed previously, near the outer sinus regions.[47,49] Thus, the multi-tissue chip successfully modeled lymphatic drainage, phagocytosis, and processing of whole protein antigens in a lymph node.

4.4.9 Acute immune response to vaccination on-chip was comparable to in vivo

Within hours of a vaccine injection, vaccine components drain from the site of injection to local LNs where the adaptive immune response begins to develop (Figure 4.11a).[32] Here, we modeled this process by co-culturing a mock injection site modeled using a block of soft hydrogel with a downstream murine LN slice on the multi-organ chip (Figure 4.11b). As a model vaccine, we chose rhodamine-labeled ovalbumin (Rho-OVA) and R848 (TLR7/TLR8 agonist) as the antigen and adjuvant, respectively. To assess the accuracy of the multi-organ microphysiological model, we benchmarked the on-chip response to the vaccine against both *in vivo* and static petri dish (off-chip) vaccination. As vaccine delivery is more direct *ex vivo* than *in vivo*, we chose a shorter time for off- and on-chip vaccination (6 hrs) compared to *in vivo* vaccination (24 hrs).

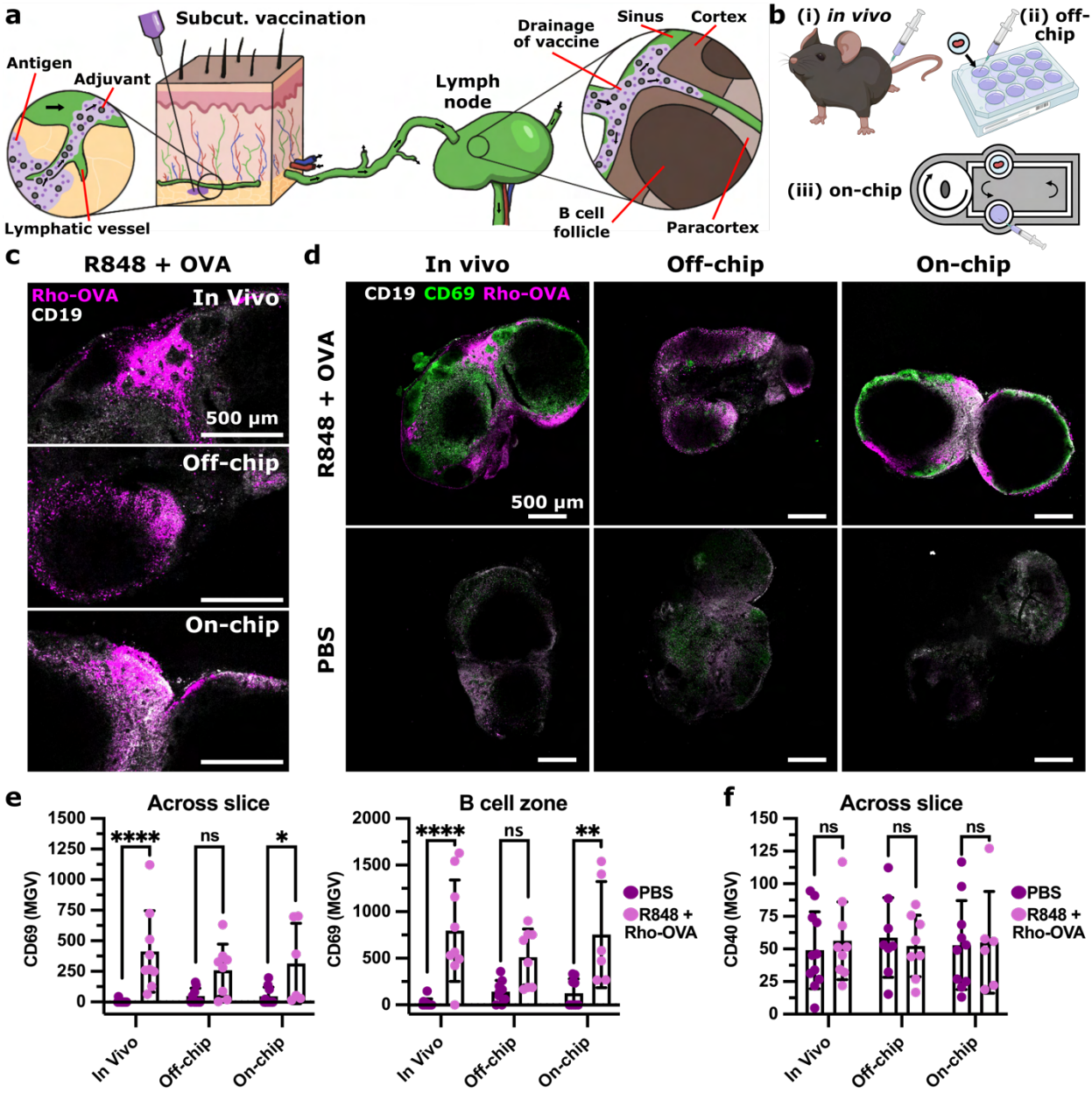

Figure 4.11 Comparative vaccination between* in vivo, *off-chip, and on-chip conditions. *(a) With a subcutaneous vaccine injection (purple) in the skin, the vaccine adjuvant and antigen enter the lymphatic vessels via interstitial fluid flow and drain to local lymph nodes. (b) Three conditions were tested: (i) in vivo vaccination, (ii) off-chip vaccination, and (iii) on-chip vaccination in a 2T device (parylene-coated Clear resin). The vaccine consisted of R848 as the adjuvant, and Rho-OVA as the antigen (Created using BioRender.com). (c) Representative images of Rho-OVA distribution in R848 + OVA condition. B cells (CD19) are shown in grey; antigen (Rho-OVA) is shown in magenta. (d) Representative images of lymph node slices with R848 + OVA and PBS only from in vivo culture, off-chip culture, and on-chip culture. B cells (CD19) are shown in grey; a lymphocyte activation marker (CD69) is shown in green; and the antigen (Rho-OVA) is shown in magenta. (e) Comparison of the MGV of CD69 across the whole slice (left) and B cell zone (CD19+, right) in R848 + OVA and PBS only LN slices from in vivo, off-chip, and on-chip conditions. (f) Comparison of the MGV of CD40 across the whole slice*

*R848 + OVA and PBS only LN slices from in vivo, off-chip, and on-chip conditions. Results in (e)-(f) were compared using a two-way ANOVA and were pooled from three independent experiments . **** indicates $p < 0.0001$, ** indicates $p < 0.003$, * indicates $p < 0.04$, and ns indicates $p > 0.07$. Each dot represents a single LN slice. Bars represent standard deviation.*

First, we assessed the tissue-level response to vaccination across *in vivo*, off-chip, and on-chip conditions by confocal microscopy. Antigen distribution was similar in location across all three stimulated conditions, where the Rho-OVA appeared to be primarily in the sinus region as observed previously (Figure 4.11c).[47] Consistent with early activation of lymphocytes by the vaccine, the on-chip and *in vivo* conditions had a similar statistically significant increase in CD69 signal in R848 + OVA slices compared to PBS only slices (Figure 4.11d,e), whether measured across the entire slice or specifically in the B cell zone (CD19+) (Figure 4.11e). In the slices cultured off-chip, the increase in CD69 signal was smaller and not statistically significant. We also quantified two markers of antigen-presenting cell activation, CD40 (Figure 4.11f) and CD86 (data not shown), where the *ex vivo* vaccination off- and on-chip mimicked the *in vivo* outcome of no significant increase in signal compared to the unvaccinated conditions. These results indicate that the multi-tissue device was able to successfully replicate features of the *in vivo* vaccination better than static culture for some markers.

4.5 Conclusions

Here, we have reported a user-friendly 3D-printed multi-tissue device and motor-based impeller pump for the culture of one or more tissue slices under biologically relevant recirculating fluid flow. Our end goal was for users to simply pipet media into the chip, load their tissues, and plug in a small, inexpensive control box. Towards this goal, we eliminated the bulky, heat-producing peristaltic pumps in favor of the tubing-free impeller pump. We designed the device using concepts from modular microfluidics and traditional cell cultures, e.g. removable tissue supports and open-top chambers, to obtain a customizable multi-tissue platform

for tissue slice culture. Instead of using 3D cell culture, we chose to incorporate live tissue slices within the device to maintain the spatiotemporal organization found within the lymph node, which is critical for proper immune function, while still being accessible for imaging and stimulation.[3,16,47,55] By connecting tissue slices using recirculating fluid flow, this platform was used to model drainage of soluble factors from an upstream organ to a LN. In the future, the fluidic connection of a lymph node module into a user-friendly MOOC platform may enable the modeling of complex phenomena such as neurodegeneration, autoimmunity, tumor immunity, and vaccination.

4.6 References

1. Castillo-Armengol, J., Fajas, L. & Lopez-Mejia, I. C. Inter-organ communication: a gatekeeper for metabolic health. *EMBO Rep* **20**, (2019).
2. Wasson, E. M., Dubbin, K. & Moya, M. L. Go with the flow: modeling unique biological flows in engineered *in vitro* platforms. *Lab Chip* 10.1039.D1LC00014D (2021) doi:10.1039/D1LC00014D.
3. Hammel, J. H., Cook, S. R., Belanger, M. C., Munson, J. M. & Pompano, R. R. Modeling Immunity In Vitro: Slices, Chips, and Engineered Tissues. *Annu. Rev. Biomed. Eng.* **23**, 461–491 (2021).
4. Ronaldson-Bouchard, K. & Vunjak-Novakovic, G. Organs-on-a-Chip: A Fast Track for Engineered Human Tissues in Drug Development. *Cell Stem Cell* **22**, 310–324 (2018).
5. Watson, D. E., Hunziker, R. & Wikswo, J. P. Fitting tissue chips and microphysiological systems into the grand scheme of medicine, biology, pharmacology, and toxicology. *Exp Biol Med (Maywood)* **242**, 1559–1572 (2017).

6. Boeri, L. *et al.* Advanced Organ-on-a-Chip Devices to Investigate Liver Multi-Organ Communication: Focus on Gut, Microbiota and Brain. *Bioengineering* **6**, 91 (2019).
7. Picollet-D'hahan, N., Zuchowska, A., Lemeunier, I. & Le Gac, S. Multiorgan-on-a-Chip: A Systemic Approach To Model and Decipher Inter-Organ Communication. *Trends in Biotechnology* S0167779920303097 (2021) doi:10.1016/j.tibtech.2020.11.014.
8. Leung, C. M. *et al.* A guide to the organ-on-a-chip. (2022).
9. Xiao, S. *et al.* A microfluidic culture model of the human reproductive tract and 28-day menstrual cycle. *Nature Communications* **8**, (2017).
10. Shinha, K. *et al.* A Kinetic Pump Integrated Microfluidic Plate (KIM-Plate) with High Usability for Cell Culture-Based Multiorgan Microphysiological Systems. *Micromachines* **12**, 1007 (2021).
11. Ong, L. J. Y. *et al.* Self-aligning Tetris-Like (TILE) modular microfluidic platform for mimicking multi-organ interactions. *Lab Chip* **19**, 2178–2191 (2019).
12. Edington, C. D. *et al.* Interconnected Microphysiological Systems for Quantitative Biology and Pharmacology Studies. *Sci Rep* **8**, 4530 (2018).
13. Chramiec, A. *et al.* Integrated human organ-on-a-chip model for predictive studies of anti-tumor drug efficacy and cardiac safety. *Lab Chip* **20**, 4357–4372 (2020).
14. Hammel, J. H., Zatorski, J. M., Cook, S. R., Pompano, R. R. & Munson, J. M. Engineering in vitro immune-competent tissue models for testing and evaluation of therapeutics. *Advanced Drug Delivery Reviews* **182**, 114111 (2022).
15. Sasserath, T. *et al.* Differential Monocyte Actuation in a Three-Organ Functional Innate Immune System-on-a-Chip. *Adv. Sci.* **7**, 2000323 (2020).

16. Shim, S., Belanger, M. C., Harris, A. R., Munson, J. M. & Pompano, R. R. Two-way communication between ex vivo tissues on a microfluidic chip: application to tumor–lymph node interaction. *Lab on a Chip* **19**, 1013–1026 (2019).
17. Mannino, R. G. *et al.* 3D microvascular model recapitulates the diffuse large B-cell lymphoma tumor microenvironment in vitro. *Lab Chip* **17**, 407–414 (2017).
18. Li, Z. *et al.* Human Mesenchymal Stem Cell-Derived Miniature Joint System for Disease Modeling and Drug Testing. *Advanced Science* **9**, 2105909 (2022).
19. Munson, J. & Shieh, A. Interstitial fluid flow in cancer: implications for disease progression and treatment. *CMAR* 317 (2014) doi:10.2147/CMAR.S65444.
20. Swartz, M. A. & Fleury, M. E. Interstitial Flow and Its Effects in Soft Tissues. *Annu. Rev. Biomed. Eng.* **9**, 229–256 (2007).
21. Esch, M. B., Ueno, H., Applegate, D. R. & Shuler, M. L. Modular, pumpless body-on-a-chip platform for the co-culture of GI tract epithelium and 3D primary liver tissue. *Lab Chip* **16**, 2719–2729 (2016).
22. Walker, G. M. & Beebe, D. J. A passive pumping method for microfluidic devices. *Lab Chip* **2**, 131 (2002).
23. Chen, L., Yang, Y., Ueno, H. & Esch, M. B. Body-in-a-Cube: a microphysiological system for multi-tissue co-culture with near-physiological amounts of blood surrogate. *Microphysiol Syst* **4**, 1–1 (2020).
24. Fathi, P., Holland, G., Pan, D. & Esch, M. B. Lymphatic Vessel on a Chip with Capability for Exposure to Cyclic Fluidic Flow. *ACS Appl. Bio Mater.* **3**, 6697–6707 (2020).

25. Cook, S. R., Musgrove, H. B., Throckmorton, A. L. & Pompano, R. R. Microscale impeller pump for recirculating flow in organs-on-chip and microreactors. *Lab Chip* **22**, 10.1039.D1LC01081F (2022).
26. Kimura, H., Yamamoto, T., Sakai, H., Sakai, Y. & Fujii, T. An integrated microfluidic system for long-term perfusion culture and on-line monitoring of intestinal tissue models. *Lab on a Chip* **8**, 741 (2008).
27. Cucullo, L., Marchi, N., Hossain, M. & Janigro, D. A Dynamic *in vitro* BBB Model for the Study of Immune Cell Trafficking into the Central Nervous System. *J Cereb Blood Flow Metab* **31**, 767–777 (2011).
28. Gjorevski, N. *et al.* Neutrophilic infiltration in organ-on-a-chip model of tissue inflammation. *Lab Chip* **20**, 3365–3374 (2020).
29. Ramadan, Q. & Ting, F. C. W. In vitro micro-physiological immune-competent model of the human skin. *Lab Chip* **16**, 1899–1908 (2016).
30. Willard-Mack, C. L. Normal Structure, Function, and Histology of Lymph Nodes. *Toxicol Pathol* **34**, 409–424 (2006).
31. Buettner, M. & Bode, U. Lymph node dissection - understanding the immunological function of lymph nodes: The technique of lymph node dissection. *Clinical & Experimental Immunology* **169**, 205–212 (2012).
32. Roth, G. A. *et al.* Designing spatial and temporal control of vaccine responses. *Nat Rev Mater* **7**, 174–195 (2021).
33. Shanti, A. *et al.* Multi-Compartment 3D-Cultured Organ-on-a-Chip: Towards a Biomimetic Lymph Node for Drug Development. *Pharmaceutics* **12**, 464 (2020).

34. Ross, A. E. & Pompano, R. R. Diffusion of cytokines in live lymph node tissue using microfluidic integrated optical imaging. *Analytica Chimica Acta* **1000**, 205–213 (2018).
35. Ross, A. E., Belanger, M. C., Woodroof, J. F. & Pompano, R. R. Spatially resolved microfluidic stimulation of lymphoid tissue ex vivo. *Analyst* **142**, 649–659 (2017).
36. Ozulumba, T., Montalbine, A. N., Ortiz-Cárdenas, J. E. & Pompano, R. R. New tools for immunologists: models of lymph node function from cells to tissues. *Front. Immunol.* **14**, 1183286 (2023).
37. Kraus, T. *et al.* Evaluation of a 3D Human Artificial Lymph Node as Test Model for the Assessment of Immunogenicity of Protein Aggregates. *Journal of Pharmaceutical Sciences* **108**, 2358–2366 (2019).
38. Goyal, G. *et al.* Ectopic Lymphoid Follicle Formation and Human Seasonal Influenza Vaccination Responses Recapitulated in an Organ-on-a-Chip. *Advanced Science* **9**, 2103241 (2022).
39. Shah, S. B. *et al.* Combinatorial treatment rescues tumour-microenvironment-mediated attenuation of MALT1 inhibitors in B-cell lymphomas. *Nat. Mater.* **22**, 511–523 (2023).
40. Wagar, L. E. *et al.* Modeling human adaptive immune responses with tonsil organoids. *Nat Med* **27**, 125–135 (2021).
41. Higbee, R. G. *et al.* An Immunologic Model for Rapid Vaccine Assessment — A Clinical Trial in a Test Tube. *Altern Lab Anim* **37**, 19–27 (2009).
42. Delong, L. M. & Ross, A. E. Open multi-organ communication device for easy interrogation of tissue slices. *Lab Chip* **23**, 3034–3049 (2023).
43. Kuo, A. P. *et al.* High-Precision Stereolithography of Biomicrofluidic Devices. *Adv. Mater. Technol.* **4**, 1800395 (2019).

44. Musgrove, H. B., Cook, S. R. & Pompano, R. R. Parylene-C Coating Protects Resin-3D-Printed Devices from Material Erosion and Prevents Cytotoxicity toward Primary Cells. *ACS Applied Bio Materials* **6**, 3079–3083 (2023).
45. Cooper, L. J., Heppell, J. P., Clough, G. F., Ganapathisubramani, B. & Roose, T. An Image-Based Model of Fluid Flow Through Lymph Nodes. *Bull Math Biol* **78**, 52–71 (2016).
46. Rodriguez Corral, J., Mitrani, H., Dade-Robertson, M., Zhang, M. & Maiello, P. Agarose gel as a soil analogue for development of advanced bio-mediated soil improvement methods. *Can. Geotech. J.* **57**, 2010–2019 (2020).
47. Belanger, M. C. *et al.* Acute Lymph Node Slices Are a Functional Model System to Study Immunity Ex Vivo. *ACS Pharmacol. Transl. Sci.* **4**, 128–142 (2021).
48. Catterton, M. A., Dunn, A. F. & Pompano, R. R. User-defined local stimulation of live tissue through a movable microfluidic port. *Lab Chip* **18**, 2003–2012 (2018).
49. Ball, A. G., Belanger, M. C. & Pompano, R. R. Detergent wash improves vaccinated lymph node handling ex vivo. *Journal of Immunological Methods* **489**, 112943 (2021).
50. Schneider, C. A., Rasband, W. S. & Eliceiri, K. W. NIH Image to ImageJ: 25 years of image analysis. *Nat. Methods* **9**, 671–675 (2012).
51. Groff, B. D., Kinman, A. W. L., Woodroof, J. F. & Pompano, R. R. Immunofluorescence staining of live lymph node tissue slices. *Journal of Immunological Methods* **464**, 119–125 (2019).
52. Musgrove, Hannah. B., Catterton, Megan. A. & Pompano, Rebecca. R. Applied tutorial for the design and fabrication of biomicrofluidic devices by resin 3D printing. *Analytica Chimica Acta* **1209**, 339842 (2022).

53. Ong, L. J. Y. *et al.* A pump-free microfluidic 3D perfusion platform for the efficient differentiation of human hepatocyte-like cells: Pump-Free Microfluidic 3D Perfusion Platform. *Biotechnology and Bioengineering* **114**, 2360–2370 (2017).
54. Loskill, P., Marcus, S. G., Mathur, A., Reese, W. M. & Healy, K. E. μOrgano: A Lego®-Like Plug & Play System for Modular Multi-Organ-Chips. *PLoS ONE* **10**, e0139587 (2015).
55. Horowitz, L. F., Rodriguez, A. D., Ray, T. & Folch, A. Microfluidics for interrogating live intact tissues. *Microsyst Nanoeng* **6**, 69 (2020).
56. Bhargava, K., Ermagan, R., Thompson, B., Friedman, A. & Malmstadt, N. Modular, Discrete Micromixer Elements Fabricated by 3D Printing. *Micromachines* **8**, 137 (2017).
57. Lee, K. G. *et al.* 3D printed modules for integrated microfluidic devices. *RSC Adv.* **4**, 32876–32880 (2014).
58. Abbasi, R., LeFevre, T. B., Benjamin, A. D., Thornton, I. J. & Wilking, J. N. Coupling fluid flow to hydrogel fluidic devices with reversible “pop-it” connections. *Lab Chip* **21**, 2050–2058 (2021).
59. Yuen, P. K. A reconfigurable stick-n-play modular microfluidic system using magnetic interconnects. *Lab on a Chip* **16**, 3700–3707 (2016).
60. Sureshkumar, G. K. & Mutharasan, R. The influence of temperature on a mouse-mouse hybridoma growth and monoclonal antibody production. *Biotechnol. Bioeng.* **37**, 292–295 (1991).
61. Leu, A. J., Berk, D. A., Yuan, F. & Jain, R. K. Flow velocity in the superficial lymphatic network of the mouse tail. *American Journal of Physiology-Heart and Circulatory Physiology* **267**, H1507–H1513 (1994).

62. Nuttall, A. L. Velocity of red blood cell flow in capillaries of the guinea pig cochlea. *Hearing Research* **27**, 121–128 (1987).

63. Dixon, J. B. *et al.* Lymph Flow, Shear Stress, and Lymphocyte Velocity in Rat Mesenteric Prenodal Lymphatics. *Microcirculation* **13**, 597–610 (2006).

64. Holm-Weber, T., Kristensen, R. E., Mohanakumar, S. & Hjortdal, V. E. Gravity and lymphodynamics. *Physiological Reports* **10**, (2022).

65. Klarhöfer, M., Csapo, B., Balassy, Cs., Szeles, J. C. & Moser, E. High-resolution blood flow velocity measurements in the human finger: Blood Flow Velocities in the Human Finger. *Magn. Reson. Med.* **45**, 716–719 (2001).

66. Bovenkamp, P. R. *et al.* Velocity mapping of the aortic flow at 9.4 T in healthy mice and mice with induced heart failure using time-resolved three-dimensional phase-contrast MRI (4D PC MRI). *Magn Reson Mater Phy* **28**, 315–327 (2015).

67. Lacy, J. Development and validation of a novel technique for murine first-pass radionuclide angiography with a fast multiwire camera and tantalum 178. *Journal of Nuclear Cardiology* **8**, 171–181 (2001).

68. Jafarnejad, M., Woodruff, M. C., Zawieja, D. C., Carroll, M. C. & Moore, J. E. Modeling Lymph Flow and Fluid Exchange with Blood Vessels in Lymph Nodes. *Lymphatic Research and Biology* **13**, 234–247 (2015).

69. Sakariassen, K. S., Orning, L. & Turitto, V. T. The impact of blood shear rate on arterial thrombus formation. *Future Science OA* **1**, fso.15.28 (2015).

70. Wirtz, D., Konstantopoulos, K. & Searson, P. C. The physics of cancer: the role of physical interactions and mechanical forces in metastasis. *Nat Rev Cancer* **11**, 512–522 (2011).

71. Hyler, A. R. *et al.* Fluid shear stress impacts ovarian cancer cell viability, subcellular organization, and promotes genomic instability. *PLoS ONE* **13**, e0194170 (2018).
72. Bertheloot, D., Latz, E. & Franklin, B. S. Necroptosis, pyroptosis and apoptosis: an intricate game of cell death. *Cell Mol Immunol* **18**, 1106–1121 (2021).
73. Tóth, M. E., Vígh, L. & Sántha, M. Alcohol stress, membranes, and chaperones. *Cell Stress and Chaperones* **19**, 299–309 (2014).

Chapter 5. The development of a 3D-printed dual-media multi-organ-on-chip to model brain-immune interactions in neuroinflammation and neurodegeneration

5.1 Abstract

In vivo, antigens in the brain are picked up by interstitial fluid flow, enter the meningeal lymphatics, and drain to cervical lymph nodes (LNs). In instances of neuroinflammation and neurodegeneration, brain-LN communication is still poorly understood and challenging to study using traditional mouse models. Multi-organ-on-chips (MOOCs) may provide an experimentally accessible platform to study communication by connecting multiple tissue models using biomimetic fluid flow. Here, we developed a 3D-printed microfluidic device that co-cultures tissue engineered models (TEMs) of the brain, meningeal lymphatics, and LN paracortex established in the Munson lab under two distinct media loops. As a proof-of-principle, the device will be used to model brain-specific antigen drainage from the brain into the LN during neurodegenerative disease.

5.2 Introduction

The brain is in constant communication with cervical lymph nodes (LNs) through a lymphatic vasculature connection. Interstitial fluid slowly perfuses through brain parenchyma, where it picks up brain antigens and other waste before draining to the lymphatic vessels within the meninges (Figure 5.1).[1–3] Once in the lymphatics, the flowing lymph fluid carries the antigens and waste to cervical LNs, where these tiny immune organs can surveil the state of the brain and respond to instances of infection, damage, or disease.[4,5] As a result of this drainage, there is a constant interplay between the brain, meningeal lymphatics, and cervical LNs, where the brain antigens may result in changes in the LN microenvironment such as the priming of

immune cells to recognize components related to the pathogenesis of neurodegenerative disease. However, it is unclear what the LN's role is in the development and progression of neurodegenerative diseases as it is challenging to study with available *in vivo* and *in vitro* tools.

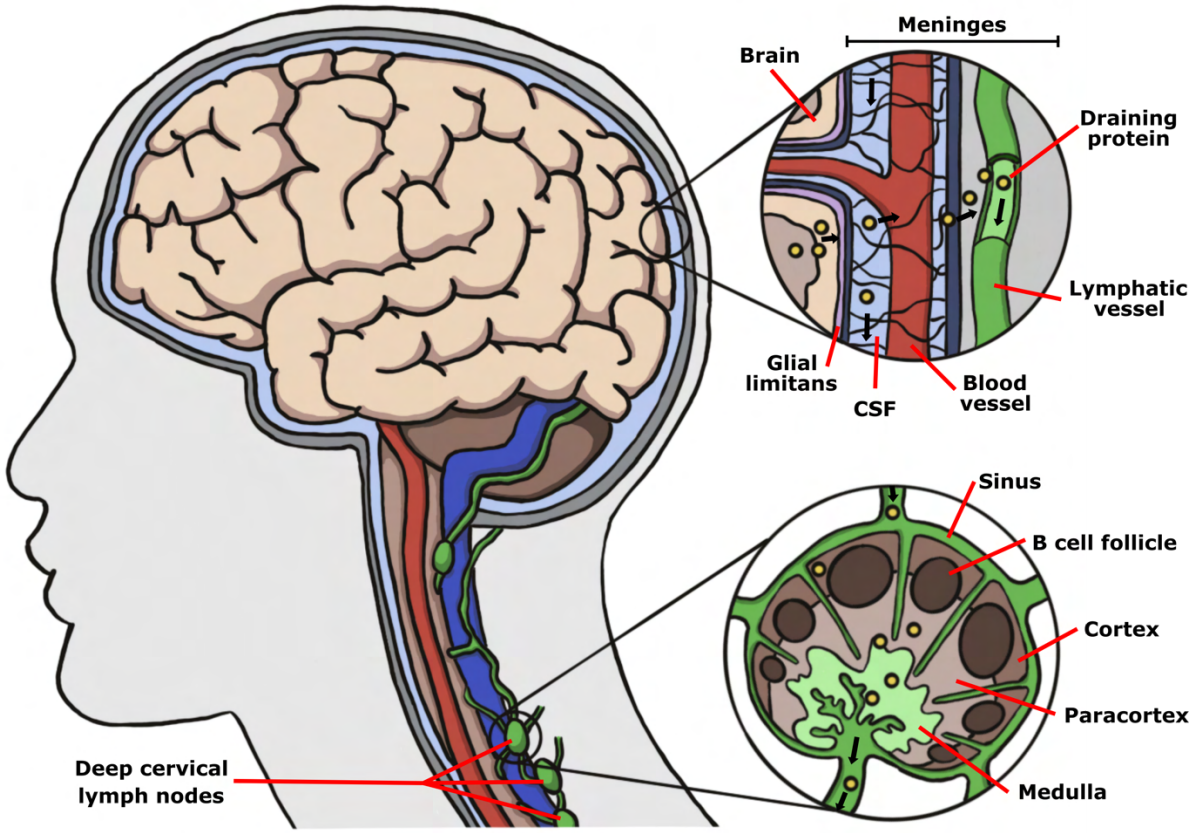

Figure 5.1 Illustration of the brain-lymph node drainage pathway. *Soluble factors (yellow dots) drain from the brain into the meningeal lymphatics, where lymph flow carries the messages to the deep cervical lymph nodes.*

To gain a better understanding of this pathway in the context of brain inflammation, the specific tissues involved (i.e. brain, meningeal lymphatics, and LN) can be isolated from the complex biology found *in vivo* and co-cultured *ex vivo* using multi-organs-on-chip (MOOC) technology.[6,7] Single organs-on-chip models of the brain and blood-brain barrier (BBB) are well established,[8–12] though there are limited chips that co-culture the brain with other organ models.[13,14] Of these devices, some will incorporate elements of immunity such as brain-resident microglia and astrocytes or infiltrating immune cells from the periphery with no inclusion of

immune organs such as the LN.[12,13] To date, there are no devices that capture the interactions between the brain, meningeal lymphatics, and LNs despite the involvement in neurodegenerative diseases.

To address this gap, we are developing an innovative 3D-printed microfluidic platform to model the lymphatic connection between the brain and the LN. Our strategy builds on connecting tissue engineered models (TEMs) of the human brain, meninges, and LN paracortex recently established in the Munson lab in a 3D-printed MOOC with tubing-free fluidic control via impeller pump. Transwell models enable a modular design, where 2D or 3D cell cultures can be customized for each modeled system. The device contained distinct media compartments to mimic the separation of the central nervous system (CNS) from the periphery *in vivo*, where communication would occur across the meningeal barrier. We aim to use this device to model brain-immune interactions in instances of neuroinflammation and neurodegeneration to gain insight in disease pathogenesis and progression.

5.3 Methods

5.3.1 3D-printed device fabrication and post-processing

The dual-media chip, single-media chip, and barrier-only chip (Figure 2.1) was designed using Fusion 360 and printed with a CadWorks3D MiiCraft P110Y DLP printer (CADWorks3D, Toronto, Canada) using MiiCraft Clear resin (BV007a, CADWorks3D, Toronto, Canada). This fabrication method allowed for complex 3D geometry (e.g. overlapping channels in different z planes) and was printed as a single monolithic device in under 45 min. Device post-processing included cleaning in an isopropyl alcohol (IPA)-filled FormWash (FormLabs, Massachusetts, USA) for 4 min and a post-cure in a FormCure (10 mW/cm^2, FormLabs, Massachusetts, USA) for 1 min at room temperature. Prior to use with cells or tissue, the 3D-printed devices were

coated in parylene-C to make the material biocompatible, as established previously.[15] In brief, a film of ~1 μm was achieved by adding 1.1 g of mixed isomers of Parylene-C (SCS, Inc. Indianapolis, IN, USA) to the Labcoater 2 parylene coater (SCS, Inc. Indianapolis, IN, USA). The prints, stir bars, and o-rings were sterilized before use with cells by submerging in 70% ethanol for 5 min, followed by two 10 min rinses in 1xPBS.

5.3.2 Cutting commercially available transwells using hot wire foam cutter

When developed in the Munson lab, the TEMs for meningeal lymphatics, LN paracortex, and brain were housed in commercially available transwell inserts (MilliCell Standing Cell Culture Inserts, 8 μm pore size, 12 mm diameter, Sigma-Aldrich, USA). These inserts were cut from a height of 10 mm to ~3 mm to interface with channels above the transwell membrane. To cut the transwells, a Hot Wire Foam Cutter (Genround, USA) was mounted on a fused deposition modeling (FDM) 3D-printed slider with a removable transwell mount printed in polylactic acid filament (1.75 mm PLA, Flashforge, China). The slider enabled level cutting at a reproducible height. The cutter was powered using a 12 V AC DC power supply adapter wall plug (EWETON) and was used at maximum available voltage. Once cut with the foam cutter, the transwell was removed from the mount and the top was removed by cutting it with cutting pliers and removing the top of the transwell with tweezers. Cut transwells were sterilized post-cutting for use with cells.

Different forms of transwells were used in various different experiments. To generate blocked transwells, hot glue was used to fully cover the membrane, either the top of the membrane or the bottom of the membrane. To make gel-laden cut transwells, cut transwells were first placed on droplets of 1 x PBS (Lonza, Maryland, USA) to wet the membrane. Next, 2 mg/mL collagen type I hydrogel (rat tail collagen, ibidi GmbH, Germany) was made according

to standard protocol, where either 100 µL or 50 µL of gel was added to the pre-wet transwells and allowed to set at 37 °C for 30 min. Gel thickness was approximated by imaging the transwells while sideways using a Zeiss Axio Zoom macroscope (Carl Zeiss Microscopy, Germany) and analyzed in ImageJ.

The meningeal lymphatics TEM was made according to Munson lab protocol, where human lymphatic endothelial cells (LECs, Sciencell) were first seeded on the bottom of a sterile cut transwell and allowed to adhere for 2 hrs before the transwells were flipped over and human meningeal fibroblast cells (hMCs, Sciencell) were seeded on the top of the transwell membrane overnight (~18 hrs).

5.3.3 Device assembly and filling

Before filling the device with liquid of choice, a nitrile rubber o-ring (13 mm ID, 17 mm OD, 2 mm width, uxcell, China) was inserted into the culture well where it fits in place in a ring around the culture well. Next, the cut transwell is placed flat resting gently on top of the edge of the o-ring in the culture well. Tweezers with a curved tip were placed across the top of the transwell walls to push the transwell down so the feet of the transwell touch the base of the well. If using a plug for barrier TEM culture, insert the plug by placing the two wings in the matching holes on either side of the culture well, and twist to lock it in place. Each device has a specific fill volume to maintain a consistent channel speed. This volume was determined by finding the volume where the whole chip is filled and the pump well will not overflow when the stir bar rotated. For the barrier chip, both the LN media loop (L) and brain media loop (R) were filled with 1200 µL, respectively. The single-media chip and brain-immune chip designs are still in the optimization phase, so there is no set fill volume, ranging from 1200-2000 µL per media loop.

To fill the barrier chip, fill the LN media loop (L) first by pipetting in liquid through the fill channel port so the entire region under the transwell has been filled with fluid. Next, use the channel ports to fill both channels connecting the transwell culture well to the pump well and add the remaining volume to the pump well. Once that media loop has been filled, fill the brain media loop (R) by filling the chamber above the transwell membrane either by pipetting directly into the well or by pipetting around either side of the plug. Once filled, use the channel ports to fill both channels connecting the transwell culture well to the pump well and add the remaining volume to the pump well. The single-media loop was filled similarly, where the fill channel port was used to fill the chamber below the transwell before filling the chamber above the transwell, the channels, and the pump well.

5.3.4 Dual-motor pump fabrication and assembly

The 3D-printed external housing and chip holder was designed using Fusion 360 and printed using 1.75 mm PLA filament (Flashforge, China) using an Ender 3 V2 Neo printer (Creality 3D, China). Each dual-motor pump box contained two motor circuits, each with individual power sources. To assemble a motor circuit, wires were attached to the positive and negative mounts on the base of a 6-12 V Mini DC motor (AUTOTOOLHOME) and connected to PWM low voltage DC potentiometer (ALDECO) along with a mini digital DC voltmeter (2.5-30 V, MakerFocus, China). The potentiometer was then connected to a 12 V DC female power connector (Chanzon), which is plugged into the 12 V AC DC power supply adapter wall plug (EWETON). A cord splitter was used to enable six to eight motor circuits to be used with a single power supply. All wiring was connected using a tin-lead rosin-core solder wire (ICESPRING) and wrapped in heat shrink tubing (Eventronic, Germany).

Once the motor circuits were assembled, they were inserted into the 3D-printed housing, where there are specific places to insert the motor, potentiometer, and voltmeter. After assembly, 6 mm brushed nickel magnets with a strength of 0.008 T[16] were glued into a DLP 3D-printed magnet holder and mounted on the rotating pin of the DC motor. The lid for each pump box was attached to the base using hot glue as a reversible seal. Once assembled, the pump boxes were sealed with Clear Repair Tape (TortugaTape). The chip holders were glued to the top of the external housing centered over both of the DC motors.

A Teflon PTFE encapsulated 3 x 10 mm (Thomas Scientific, New Jersey, USA) was used as an impeller alone. A digital laser photo tachometer (AGPtek, New York, USA) was used to measure the revolutions per minute (RPM) of the magnetic stir bar as it rotated. All RPMs reported were conducted for each individual pump for corresponding voltages, and are the average of three RPM measurements made at a consistent voltage.

5.3.5 Characterization of fluid flow for each TEM interface using COMSOL Multiphysics

The fluid flow profile through the tissue culture well was modeled in three dimensions using the free and porous media flow module of COMSOL Multiphysics (Version 6.1). We developed four different computational models to fully encompass all fluidic environments with the TEMs: 1) brain hydrogel, 2) LN hydrogel, 3) chamber above meningeal barrier, and 4) chamber below meningeal barrier. As the flow was intended to pass across the cell monolayers of the meningeal lymphatics model and not actively cross, we split the culture well into two separate models.

The model matched the 3D geometry of the brain and lymph node tissue culture well. The culture chamber was split into three cylinders, representing the chamber below the transwell, the fluid in the transwell, and the chamber above the transwell. The bottom chamber had a

diameter of 14 mm and a height of 1 mm, the fluid inside the transwell region had a diameter of 10 mm and a height of either 2.8 mm for the brain hydrogel and 2.9 mm for the LN hydrogel, and the chamber above the transwell had a diameter of 15 mm and a height of 1 mm. Both inlet and outlet channels had similar geometry (0.5 x 0.5 mm cross-section, length = 15 mm), where the inlet channel connected to the chamber above the transwell and the outlet channel connected to the chamber below the transwell on the opposite side. The hydrogel was modeled as a cylinder with a diameter of 10 mm and a height of 0.2 mm for the brain model and 0.1 mm for the LN model. Hydrogel heights were based off of approximate TEM thicknesses provided by the Munson lab. The hydrogel region was located between the chamber below the transwell and the region inside the transwell. The hydrogel was modeled as a porous matrix with a viscosity of 1.00 mPa s, a density of 1000 kg/m^3, a porosity of 0.3, and a permeability of 1x10^{-10} m^2.[17] Aqueous media was modeled as an incompressible fluid with a viscosity of 1.00 mPa s and a density of 1000 kg/m^3.

The two meningeal barrier models matched the 3D geometry of the chambers above and below the barrier TEM. The above meninges model was comprised of two cylindrical chambers: the fluid inside the transwell, with a diameter of 10 mm and a height of 3 mm, and the chamber above the transwell, with a diameter of 15 mm and a height of 2.5 mm. The inlet and outlet channel were on the same z plane intersecting the chamber above the transwell (0.5 x 0.5 mm, total length = 30 mm). The plug was modeled as a cut into the chamber above the transwell and the fluid inside the transwell, where an 8 mm wide cut was made in the chamber above the transwell parallel to the channels that was 2.5 mm thick and a cylinder with a diameter of 8 mm and a height of 2 mm was cut into the top of the fluid inside the transwell region. The below meninges model was comprised of a single cylindrical chamber with a diameter of 14 mm and a

height of 1.5 mm. The inlet and outlet channel were on the same z plane intersecting the chamber below the transwell (0.5 x 0.5 mm, total length = 30 mm), with a 3 mm long triangular widening at the intersection of the chamber on either side of the chamber. Aqueous media was modeled as an incompressible fluid with a viscosity of 1.00 mPa s and a density of 1000 kg/m^3.

For all models, a "normal" triangular mesh was used as generated by the software. The simulation was solved in time-dependent mode, and the reports were arbitrarily reported at 5 min unless stated otherwise. The simulation was solved in time-dependent mode, and the readouts were reported at 5 min after reaching steady state unless noted otherwise. For the LN model, the inlet velocity was set to 750 µm/s. A range of inlet velocities were tested for the brain model (no plug): 450 µm/s, 750 µm/s, 1120 µm/s, 1850 µm/s, and 3300 µm/s. For the above meninges model, the inlet velocity was set to either 450 µm/s (AD brain) or 3300 µm/s (naive brain), while the below meninges model had an inlet velocity of 750 µm/s. For hydrogel-based models, the velocity was measured along a central cutline as well as a cutline 10 µm from the top and 10 µm from the bottom, all in the x and y direction. For the barrier models, the velocity was measured along a cutline in the x and y direction either 5 µm above or 5 µm below the 10 mm region where the cell monolayer would be in either model.

5.3.6 Measurement of maximum channel velocity in barrier chip

The maximum velocity was experimentally measured as described previously.[16] In brief, a drop of blue dye (McCormick culinary blue dye, Maryland, USA) was inserted into a port within the device and recorded using the Timestamp Camera Basic application on an iPhone 12 mounted on a tripod. A small ruler was included to scale each recording. Images were taken from the recorded video at different times after dye insertion, and the distance the dye front moved over time was measured using ImageJ. When measuring velocity on the barrier chip, the device

was loaded with a glued transwell, with glue added on the side of the transwell membrane that would not impact fluid flow (i.e. glued below membrane for fluid loop that went above the membrane). Both fluid loops were filled with rotating stir bars for all velocity measurements.

5.3.7 Fluid recirculation tests in single-media chip with gel-filled transwells

Single-media chips were loaded with an o-ring before adding a cut transwell, either empty or containing 100 µL or 50 µL of collagen hydrogel. The chip was filled with 1200 µL of PBS containing blue dye (McCormick culinary blue food coloring, Maryland, USA) as described above. A 10 mm stir bar was added to the pump well, and the chip was loaded onto a pump where the motor circuit was set to 1.7 V. After a 5 min equilibration period, 10 µL of red dye (McCormick culinary red food coloring, Maryland, USA) was added to the pump well. The recirculation test was recorded using an iPhone as described above.

5.3.8 Barrier permeability assay using fluorescent dextran

For off-chip permeability tests, 300 µL of PBS was placed under the standard transwell and 300 µL of 10 kDa dextran labeled with AlexaFluor 647 was added in the transwell at a concentration of 10 µg/mL. After a period of time ranging from 1 hr to 6 hrs, the PBS below the transwell was sampled in triplicate and the fluorescent intensity was measured using a CLARIOstar plate reader (BMG LabTech, Germany). The background fluorescence from PBS only was subtracted for each condition.

For on-chip permeability tests, the o-ring and transwell were loaded into an empty device and the LN media loop (L) was filled first with 1200 µL of PBS. Then, the brain media loop (R) was filled with 1200 µL of 10 kDa dextran labeled with FITC or AlexaFluor 647 at 10 µg/mL. The left motor circuit was set to 1.5 V, and the right motor circuit was set to 2.7 V. After 2 hrs, fluid from the LN media loop (L) was sampled in triplicate either from the downstream port or

the pump well. The fluorescent intensity was measured using a CLARIOstar plate reader and the background fluorescence from PBS only was subtracted from each condition. For all experiments, the fluorescent intensity was converted to dextran concentration by measuring the fluorescent intensity at a range of known concentrations to create a calibration curve. The barrier-only devices were coated in parylene-C prior to use with the meningeal lymphatic TEMs as described previously.[15]

5.4 Results and Discussion

5.4.1 Concept of dual-media brain-immune chip

The major design goals when developing the brain-immune chip were 1) separate fluid compartments for brain and LN media; 2) interface with commercially available transwells; 3) accessible for media or tissue sampling over the course of the experiment; 4) fast and reproducible fabrication; 5) controllable recirculating fluid flow within each media compartments with biomimetic fluid flow through or across tissue models; and 6) user-friendly device interface to be able to share with collaborators. Having multiple media loops (item 1) was essential to address the "common media" challenge often faced by MOOCs, in which cells in various organs are not compatible with a shared culture media. This challenge is especially relevant for neurons and T cells, which each have unique media requirements. Therefore, our strategy was to separate the media into two distinct loops and maintain them using the meningeal lymphatics TEM. Inspired by the principles of our previous hand-built PDMS prototype,[18] we developed a monolithic 3D-printed device that consisted of two loops of channels that connected culture wells for transwell-based tissue models in line with a pump well[16] for recirculation of media and secreted molecular cues (Figure 5.1a,b).

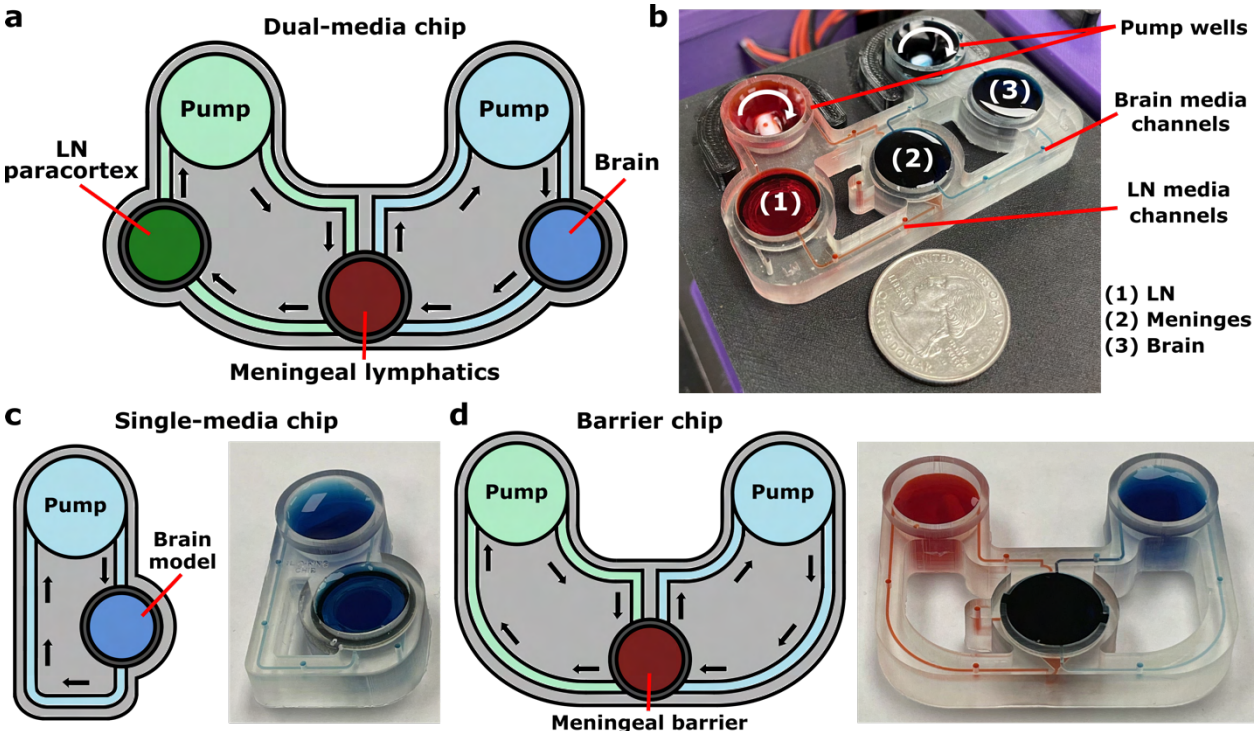

Figure 5.2 . Overview of devices for transwell tissue model culture. *(a) A schematic of the brain-immune chip for co-culture of the lymph node (LN) paracortex, meningeal lymphatics barrier, and brain TEM. The device contains two media loops each with separate pump wells that intersects at the meningeal barrier well. (b) An image of the dual-media brain-immune chip where the LN loop (L) was filled with red dye and the brain loop (R) was filled with blue dye. The chip was placed on a dual-motor pump to rotate the stir bars in the pump wells for fluid recirculation. A US quarter was shown for scale. (c) A schematic (left) and image (right) of the single-media chip for brain or LN paracortex culture in isolation. The chip was loaded with an empty cut transwell and filled with blue dye. (d) A schematic (left) and image (right) of the barrier-only chip for culture of the meningeal lymphatics barrier under recirculating fluid flow of both media loops. The chip was loaded with an empty cut transwell and filled with red dye in the LN loop (L) and blue dye for the brain loop (R).*

5.4.2 Single-media and barrier-only chips developed for individual TEM characterization

Before we co-culture all three TEMs on the brain-immune chip, we wanted to culture each model individually under fluid flow to confirm cell viability and function. Two additional devices were designed for independent TEM culture: 1) a single-media chip for flow through a hydrogel TEM (Figure 5.2a), and 2) a barrier-only chip for dual-media culture of a barrier TEM (Figure 5.2b). The single-media chip contains a single media loop, with a similar channel length compared to each of the dual-media chip loops. The barrier-only device was designed to

replicate the full geometry of the brain-immune chip, only with the brain and LN culture wells removed. While these devices were designed for use with these specific TEMs, they can be applied to other hydrogel tissue models (e.g. adipose tissue) or barriers (e.g. blood-brain barrier).

5.4.3 Interface with commercially available transwells for TEM culture

Within the device, it was critical to develop a method to culture transwell-based tissue models without fluid leaking around the transwell. We designed a culture well that contained an o-ring to act as a gasket between the 3D-printed material and the plastic transwell walls to develop a leak-free reversible seal(Figure 5.1b). The open culture wells and reversible transwell seal enable media and tissue sampling throughout an experiment via pipetting directly out of the well or removing the TEM entirely, respectively. To enable fluid flow both above and below the transwell models, we generated a method to cut commercially available transwells from a height of 10 mm to ~3 mm using a hot wire foam cutter. We improved the transwell cutting reproducibility by mounting the hot wire foam cutter on an FDM printed holder that held a transwell in place at a specific height and enabled the user to slide the foam cutter similar to an electric saw.

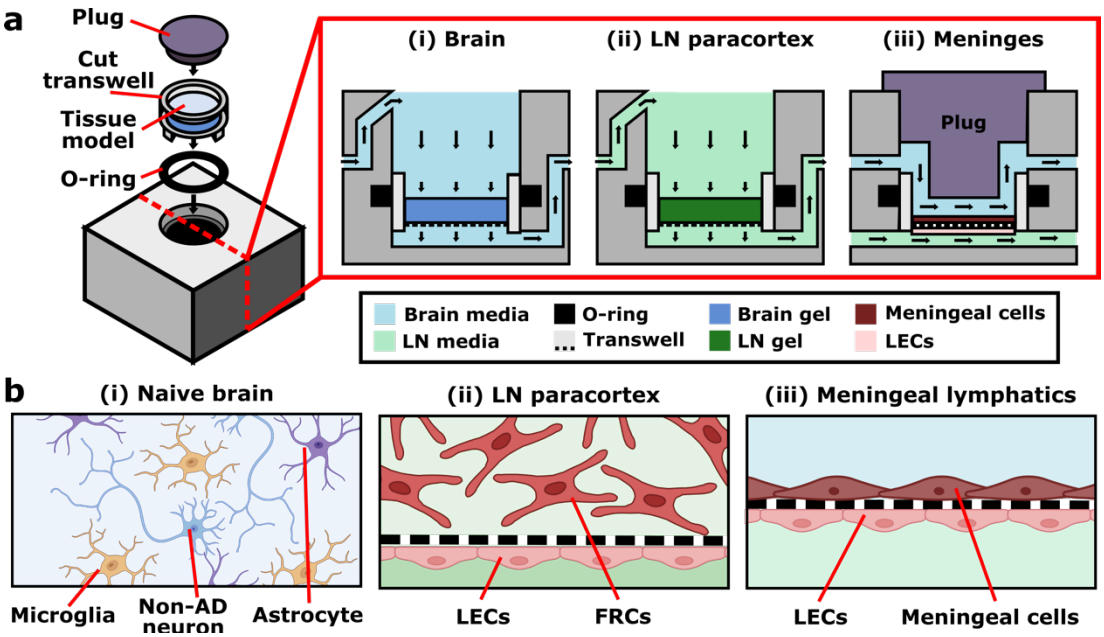

Figure 5.3 Cellular and fluidic environment of each tissue engineered model (TEM). *(a) Within each culture well, an o-ring rests between the 3D-printed material and a cut commercially available transwell and are inserted vertically into the well. For the (i) brain and (ii) lymph node (LN) paracortex TEMs, fluid flow enters the chamber from the top of the culture well and flows down through the cell-laden gel and out through an outlet channel at the base of the culture well. To generate flow across both cell monolayers in the (iii) meningeal lymphatics barrier TEM, the LN media flows through the chamber below the transwell while the brain media flows above the transwell. Here, a plug was utilized to drive brain media closer to the meningeal cell layer. (b) 3D cultures of each modeled tissue were designed to incorporate key cell types, structural components, and features of disease to mimic features found* in vivo.

5.4.4 Unique flow paths for each TEM cultured on-chip

We created two different culture wells with different flow paths to fit the needs of different organ models (Figure 5.3a). For the brain and LN paracortex TEMs, fluid entered the chamber above the cell-laden hydrogen and flowed through the gel perpendicular to the transwell membrane and exited the chamber in an outlet channel below the transwell (Figure 5.3ai,ii). The meningeal lymphatics TEM will act as a barrier between the brain and LN media compartments. As a result, there will be brain media flowing across the meningeal cell monolayer on the top of the transwell membrane and LN media flowing across the lymphatic endothelial cell (LEC) monolayer on the bottom of the transwell membrane (Figure 5.3aiii). To generate this flow

regime on-chip, a channel perfuses the chamber below the transwell, while a plug system is used in the chamber above the transwell to drive fluid flow closer to the membrane.

5.4.5 Brain, LN paracortex, and meningeal lymphatics TEMs

We aim to incorporate TEMs established by our collaborators in the Munson lab to model the brain-LN lymphatic connection. Each TEM includes relevant cell types to generate models of each respective tissue. To model the brain, a triculture containing neurons, microglia, and astrocytes were suspended in hydrogel within a transwell (Figure 5.3bi). To generate neurodegenerative models, the naive neurons can be replaced with neurons from diseased brains and accumulated proteins can be added (e.g. amyloid-ß for Alzheimer's disease). Instead of attempting to recreate the full complexity of the LN tissue, we initially focused on modeling the paracortex, where stromal cells (fibroblastic reticular cells, FRCs) were cultured within a hydrogel with a lymphatic endothelial cell (LEC) monolayer along the base of the transwell membrane (Figure 5.3bii). With many *in vitro* barrier models, a key feature is tight junctions between endothelial cells. To generate a barrier between the brain and LN compartments, we modeled the meningeal lymphatics by culturing a LEC layer to mimic the lining of lymphatic vasculature, where the tight junctions between cells retain barrier function (Figure 5.3biii). A meningeal cell monolayer was cultured on the top of the transwell membrane on the brain media-facing side to make up the meninges layer that surrounds the meningeal lymphatics *in vivo*.

5.4.6 Adapted impeller pump for fluid recirculation in multiple fluidic loops on a single chip

A key feature of the brain-immune chip is distinct media loops for brain and LN co-culture that will interface across the meningeal lymphatics barrier. To that end, each media loop required separate fluidic control. We adapted the motor-based impeller pump design described in Chapter 4 to include two motor circuits within a single pump housing to enable tubing-free fluid

recirculation (Figure 5.4a). Each media loop on-chip contains a pump well, where the rotating stir bar generates recirculating fluid flow through the connected loop of channels. Within the pump box, the two motor circuits each have voltage control and readout through a potentiometer (POT) and voltmeter, respectively. By maintaining separate voltage control, each fluidic loop on the brain-immune chip can be recirculating at different speeds depending on the needs of the modeled tissue. Once assembled, the brain-immune chip fits into two chip holders on top of the pump housing, which was optimized to keep the stir bars centered within both pump wells (Figure 5.4b). Six of the dual-motor pump boxes can be cultured on a single shelf within a standard cell culture incubator, resulting in a total of approximately 24 pumps and chips per incubator (Figure 5.4c).

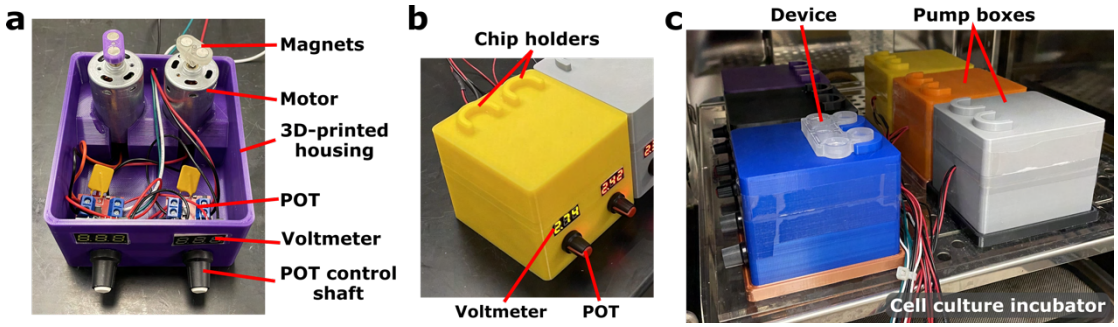

Figure 5.4 Dual-motor impeller pump. *(a) An image of the dual-motor pump housing without a lid showing the two distinct motor circuits.(b) An image of a single assembled dual-motor pump. (c) An image of six dual-motor pumps sitting on a single shelf in a cell culture incubator.*

5.4.7 Predicted fluidic environment on-chip in brain, LN paracortex, and meningeal lymphatics TEMs using 3D finite element models

The speed at which fluid is moving either through a tissue (i.e. interstitial fluid flow) or through a vessel (i.e. lymphatic vasculature) can be indicative of inflammation. In instances of neurodegenerative disease like Alzheimer's disease (AD), the interstitial fluid flow within brain parenchyma drastically slows down, dropping from ~5-10 µm/s to <1 µm/s in humans.[19,20]

Within the lymph node, there is limited research on the magnitude of the interstitial fluid velocity, but it is thought to be on the order of 1-2 μm/s.

When integrating tissue models into the brain-immune chip, a major design challenge was to recapitulate the fluidic environment within or surrounding these tissues in both naive and disease conditions, with Alzheimer's being our disease test case. With that in mind, we had three fluid flow goals: 1) achieve an approximate velocity through the LN paracortex model of 1-2 μm/s, 2) achieve an approximate velocity of both 5-10 μm/s and <1 μm/s within the bran model without changing the culture well geometry, and 3) achieve an approximate speed across the meningeal lymphatics model at all fluid speeds required for the brain and LN models. First, we generated a 3D finite element model using COMSOL Multiphysics where the model geometry consisted of the tissue culture well with an inlet and outlet channel above and below the modelled transwell (Figure 5.5a). The hydrogel for both brain and LN paracortex were modeled as a porous matrix with different gel depths depending on the tissue to match existing TEMs (200 μm thick for brain, 100 μm thick for LN paracortex). For the culture well model, the entire geometry was designed to match the 3D-printed device and cut transwell insert.

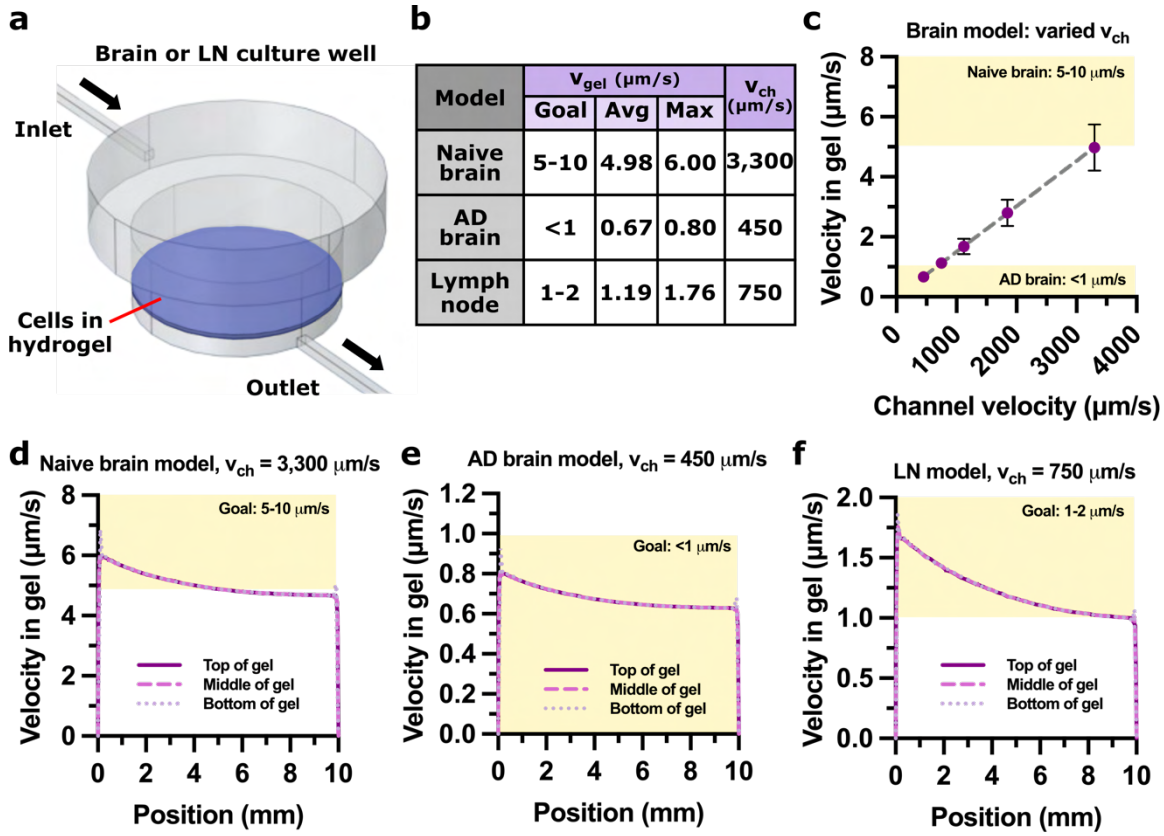

Figure 5.5 3D COMSOL model to predict flow through brain and LN models. *(a) Geometry of the 3D COMSOL model for the brain or LN paracortex TEMs colored to show the cell-laden hydrogen region. Black arrows represent the direction of fluid flow. (b) A table of the goal, predicted average, and predicted maximum velocity through the gel (v_{gel}) and the corresponding channel velocities (v_{ch}) for each tissue model. (c) The predicted velocity in gel (v_{gel}) at a range of channel speeds (v_{ch}) for the brain COMSOL model. The goal v_{gel} ranges for naive and Alzheimer's disease (AD) brain are shown in yellow boxes. (d-f) The predicted velocity in gel (v_{gel}) at cutlines in the top, middle, and bottom of the gel for the (d) naive brain model, (e) AD brain model, and (f) LN paracortex model. The goal v_{gel} ranges for each tissue are noted in yellow boxes.*

We focused on the brain model initially, and tested a range of inlet speeds to determine what channel speeds were within our goals for both naive and AD brain tissue (Figure 5.5b, c). As expected, the lower channel speeds resulted in slower predicted velocity in gel (v_{gel}). We found that a channel speed of 3,300 μm/s resulted in an average (4.98 μm/s) and maximum (6.00 μm/s) v_{gel} generally within the goal speed of 5-10 μm/s for the naive brain TEM (Figure 5.5d). At a much lower channel speed of 450 μm/s, the v_{gel} dropped to an average (0.67 μm/s) and maximum (0.80 μm/s) velocity both less than 1 μm/s for the neurodegenerative brain TEM

(Figure 5.5e). Finally, we found that a channel speed of 750 μm/s achieved a predicted average (1.19 μm/s) and maximum (1.76 μm/s) v_{gel} within the 1-2 μm/s range for the LN paracortex TEM (Figure 5.5f). For all three conditions, there was little to no variability in v_{gel} through the depth of the gel.

Next, we used the channel speeds determined in the brain and LN finite element models to optimize the geometry of the meningeal lymphatics culture well. Both media loops will perfuse through the brain and LN paracortex TEMs as well as across the meningeal lymphatics TEM, so it is important to have the channel speeds match for the hydrogel-based tissue models and their corresponding barrier side (e.g. the brain loop will perfuse through the brain TEM and across the meningeal cell monolayer on the barrier model). For the regions above the meninges (brain loop) and below the meninges (LN loop), our goal velocity across the membrane was 1-2 μm/s. We generated two separate 3D finite element models using COMSOL Multiphysics, where the model geometry was split into the chamber above the meninges and the chamber below the meninges that matched the culture well within the 3D-printed device (Figure 5.6a). As this model was designed to measure the flow across a cell monolayer, the model consisted of the fluid-filled chambers only, where the cells were assumed to be spread evenly across the surface.

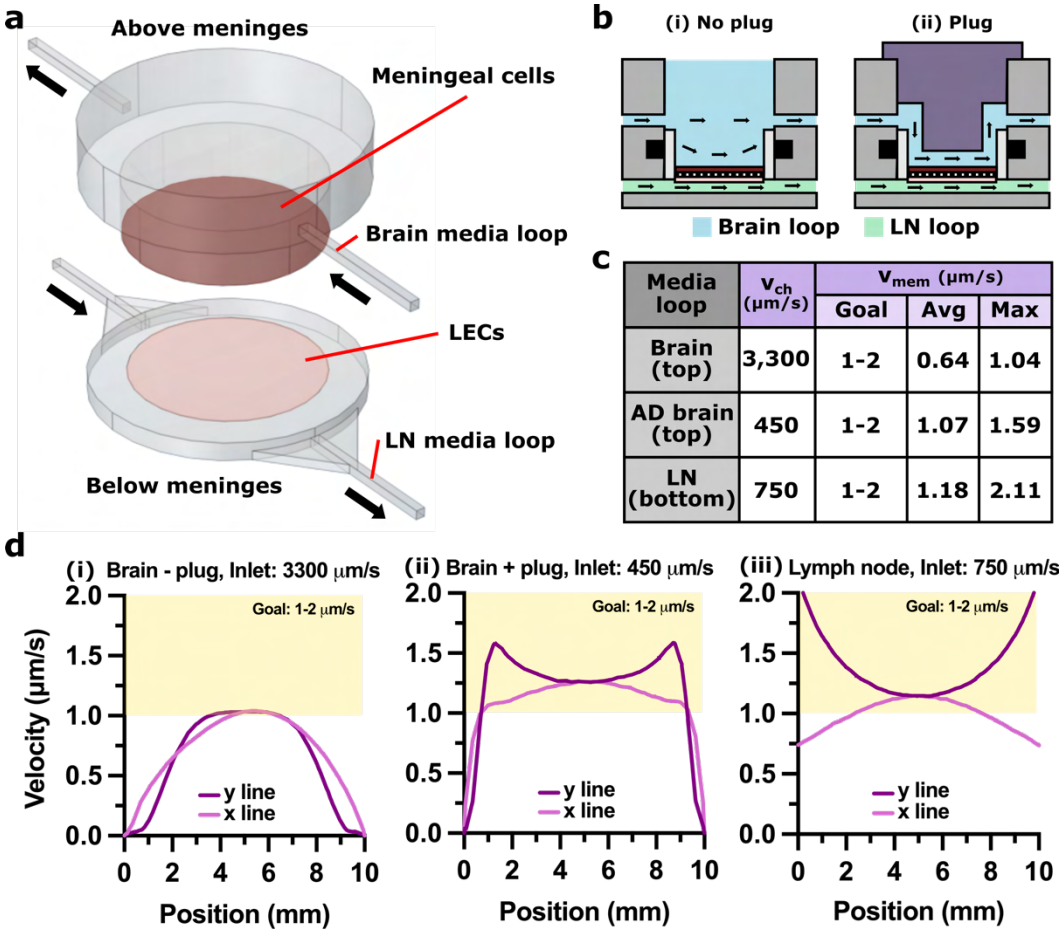

Media loop	v_{ch} (μm/s)	v_{mem} (μm/s)		
		Goal	Avg	Max
Brain (top)	3,300	1-2	0.64	1.04
AD brain (top)	450	1-2	1.07	1.59
LN (bottom)	750	1-2	1.18	2.11

Figure 5.6 3D COMSOL models to predict flow across meningeal barrier. *(a) Geometry of the 3D COMSOL simulations for the chamber above the meninges and the chamber below the meninges. The geometry was artificially colored to demonstrate the location of the meningeal cell layer and the LEC layer. The black arrows represent the fluid flow direction within each model. (b) A schematic of the flow regime across the meningeal lymphatic barrier (i) with no plug and (ii) with a plug. (c) A table of different channel velocities (v_{ch}) and the corresponding goal, predicted average, and predicted maximum velocity across the membrane (v_{mem}) for each media loop. (d) The predicted velocity along the membrane across a y and x cutline in the top chamber with the (i) brain - plug flow regime and (ii) brain + plug flow regime, as well as the (iii) bottom chamber with LN flow regime. The goal v_{mem} range was denoted with a yellow box on each graph.*

The first major challenge arose with the significant difference in channel speeds required between the naive brain (3,300 μm/s) and AD brain (450 μm/s) conditions. In the chamber above the meninges, there was a large fluid volume the fluid flow had to pass through, so we used that feature to our advantage. With a large, unblocked well, any fluid entering the well from the inlet channel would slow down immensely, with a limited portion of the fluid flow reaching the

membrane except at high channel speeds (Figure 5.6bi). When a plug was added to the well, the total volume of the culture well was decreased and the fluid path was driven closer to the membrane, resulting in a greater velocity across the membrane (Figure 5.6bii). After optimizing the chamber size and plug dimensions, we achieved our goal v_{mem} for the naive brain channel speed with a plug-free well and the AD brain channel speed with the addition of a plug (Figure 5.6c,di-ii). While the average v_{mem} in the plug-free well (0.64 μm/s) was below the goal range (1-2 μm/s) (Figure 5.6c,di), we felt that the ease of use with the use of only one plug would be preferrable. For the chamber below the transwell, the height of the chamber were optimized to achieve the goal v_{mem} (1-2 μm/s) with a channel speed of 750 μm/s (Figure 5.6c,diii). We widened the inlet and outlet channels where they intersect with the chamber to improve the fluid distribution across the LEC culture area, though there is still variability across the membrane region (Figure 5.6diii).

5.4.8 Controllable fluid recirculation within barrier-only chip

As fluid recirculation is a critical feature within the device, we confirmed fluid recirculation with the addition of a transwell in the barrier-only chip. The device was loaded with a cut transwell where the membrane was glued to prohibit mixing across the barrier. Once pre-filled with PBS, a small volume of blue dye was inserted into a port using a procedure reported previously.[16] Dye recirculated within the channels in both the LN loop (Figure 5.7a) and in the brain loop (data not shown). In addition to confirming fluid recirculation, we measured the maximum channel velocity at three different pump speeds for the LN loop (L) and the brain loop (R), with and without the plug (Figure 5.7b). As expected, the channel velocity increased linearly as the stir bar rotations per minute (RPM) increased. As there was little difference in channel velocity between all three conditions, we concluded that the resistance across both media loops

was comparable, even with the differences in chamber dimensions above and below the transwell culture well and the addition of the plug (Figure 5.7b).

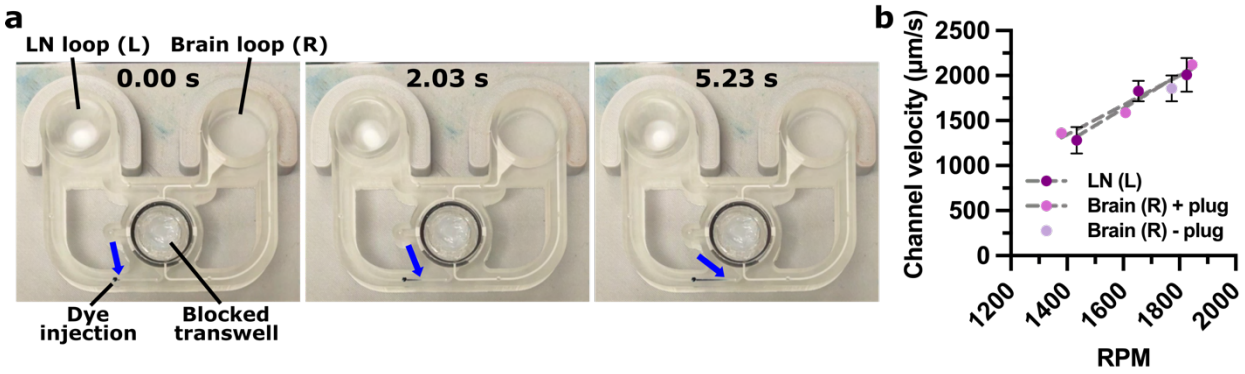

Figure 5.7 Experimental fluid recirculation and velocity. *(a) Time-lapse images of the barrier-only chip with the LN loop (L) filled with PBS. Blue dye was injected in one of the channel ports and flowed counter-clockwise towards the transwell where the membrane was sealed with glue. The dye front was marked with blue arrows. (b) Experimentally measured maximum velocity in the LN loop (L) and brain loop (R), with and without the plug present, at three different stir bar rotational speeds. Dots and error bars represent mean and standard deviation across four measurements.*

5.4.9 Mimic interstitial fluid flow through hydrogel-based TEMs using single-media chip

Tissues in the body are constantly perfused by interstitial fluid flow ranging from 0.01 – 10 µm/s in physiological and pathological conditions.[21,22] Here, we aimed to mimic interstitial fluid flow through hydrogel-based TEMs by driving flow transversely through the hydrogel. As the impeller pump is sensitive to added resistance within the fluidic loop,[16] we hypothesize that there will be a cutoff for gel thickness or permeability where recirculating flow can be achieved. First, we tested different gel thicknesses while holding permeability constant (Figure 5.8a). We found that both the empty transwell and the thinner gel (590 µm) achieved recirculating fluid flow, whereas the thicker gel (785 µm) inhibited flow (Figure 5.8b,c). When resistance is too high within the fluid loop, the vortex formed within the pump well will push small pulses of fluid down either channel, resulting in some dye entering the culture well or opposite channel instead of circulating in one direction (Figure 5.8c). After 65 min, both the empty transwell and thinner

gel resulted in a fully mixed chip, while the thicker gel had minimal dye in the culture well and channel loop. We started with 100 µL here as this is the volume of gel used when making the brain and LN TEMs, and if this volume is critical for TEM function, we can further optimize the fluid recirculation by increasing gel permeability by decreasing the concentration of collagen used when making the gels.

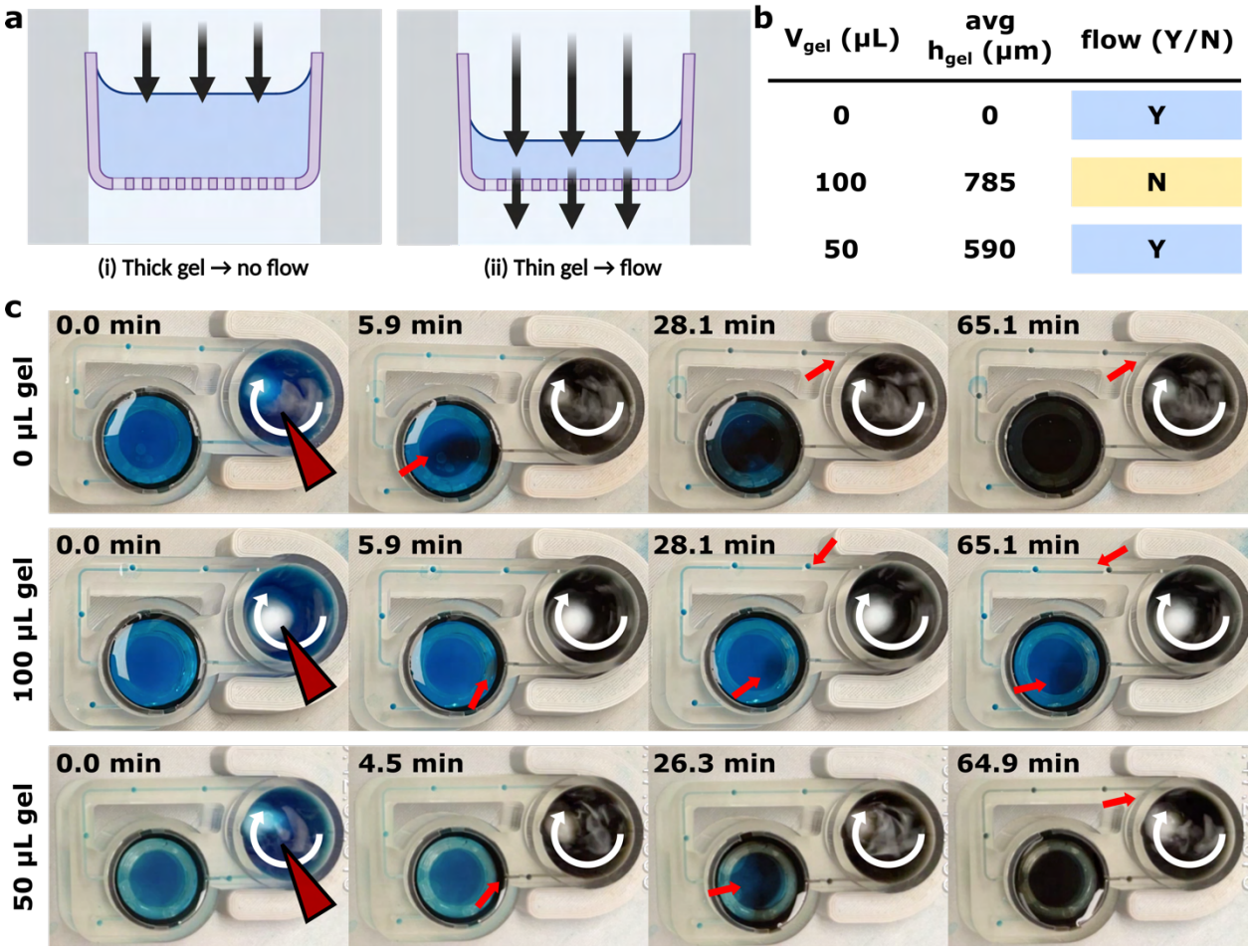

Figure 5.8 Optimization of flow through gel with varied gel height in single-media chip. *(a) Within a transwell on-chip, the thickness of the gel impacted the ability to achieve recirculating fluid flow (Created using BioRender.com) (b) The volume and average height of Collagen I gel added to a cut transwell impacted the ability to achieve flow through the gel. (c) Time-lapse images of the single-media chip with 0 µL, 100 µL, and 50 µL of gel filled with PBS dyed blue. Red dye was injected in the pump well and flowed clockwise towards the transwell culture well. The dye front was marked with red arrows.*

5.4.10 Semi-permeable barrier TEM separated the media compartments on-chip

There are many barriers *in vivo* that separate different tissues fluidically, e.g. the blood-brain barrier or meninges for the brain or the gut mucosal barrier.[2,23,24] While these barriers aim to separate different regions of the body, cross-talk across the barrier is required for each part of the body to work in concert. We aim to mimic this feature on-chip by separating media compartments with a semi-permeable barrier model, with the aim to allow molecules and/or cells to cross, depending on the modeled barrier and inflammatory state, while keeping the different media types distinct enough to maintain cell viability of all cultured TEMs. For our initial brain-immune device design, we are incorporating a TEM of the meningeal lymphatics to focus on the drainage of antigens from the brain to the lymph node, though a blood-brain barrier TEM could be added in the future. One method to probe barrier function is through measuring molecular permeability, where a fluorescent dextran is added to the brain-facing side of the transwell and the amount of dextran that crosses the barrier can be measured by sampling the liquid from the LN-facing side of the transwell (Figure 5.9a). As the barrier becomes more permeable, more dextran will cross the barrier.

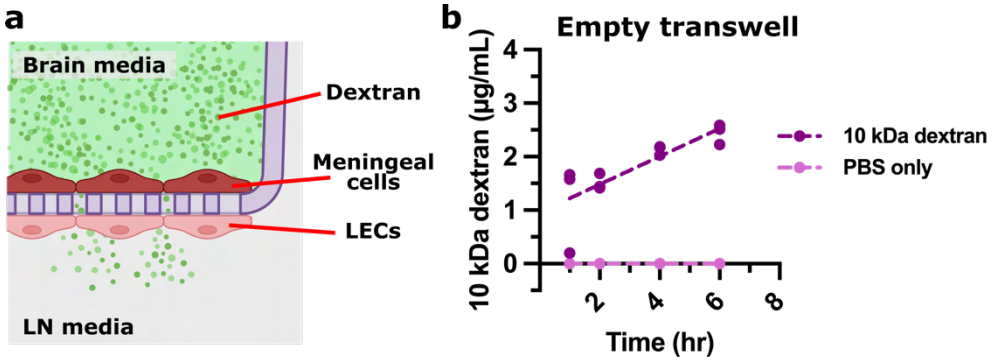

Figure 5.9 Barrier permeability assay using fluorescent dextran. *(a) A schematic of the off-chip permeability assay design, where fluorescent dextran above the barrier can pass through the cell monolayers of the meningeal lymphatics barrier. The amount of dextran crossed can be quantified by measuring fluorescent intensity of the liquid below the barrier (Created using BioRender.com). (b) The concentration of 10 kDa dextran that passed through an empty transwell off-chip over time with and without dextran present.*

First, we tested the permeability assay in empty standard transwells off-chip, where more dextran had crossed the empty membrane as time passed, as expected (Figure 5.9b). After testing permeability off-chip, we adapted the assay to measure barrier permeability on-chip. Using either an empty transwell or a meningeal lymphatics TEM, the barrier chip was loaded with 10 kDa dextran in the brain media loop (R) at 10 µg/mL while the LN media loop (L) contained no dextran (Figure 5.10a). First, we measured the permeability of an empty transwell both off-chip and on-chip with flow. The amount of dextran passing through the membrane on-chip was highly variable, ranging from 2 µg/mL to 6 µg/mL, whereas the off-chip condition were all around 1.5 µg/mL (Figure 5.10b). Due to this variability, the off-chip and on-chip conditions were not significantly different, though with more replicates and a longer culture time on-chip, the differences between conditions may be more evident.

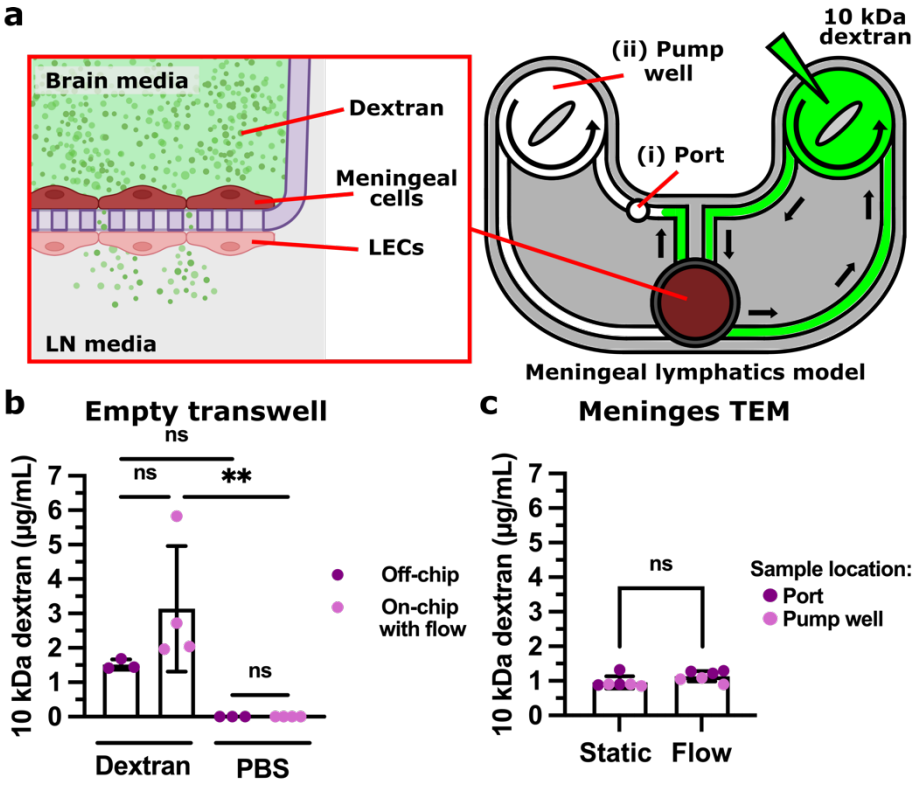

Figure 5.10 Barrier function on-chip using dextran permeability assay. *(a) A schematic of the permeability assay design on the barrier chip where 10 kDa dextran was added to the right*

*media loop (green) and sampled from the left media loop (white) at the (i) downstream port or the (ii) pump well after 2 hrs at 37 °C. A portion of the figure was created using BioRender.com. (b) The concentration of 10 kDa dextran that passed through an empty transwell off-chip and on-chip with flow after 2 hrs. Dots represent an average of three samples from a single chip at a sample location. Error bars represent the standard deviation. Results were compared using a one-way ANOVA with Tukey post-hoc tests. ns indicates $p > 0.2$, ** indicates $p < 0.01$. (c) The concentration of 10 kDa dextran that passed through the meningeal lymphatics TEM on-chip under static and flow conditions after 2 hrs. Dots represent an average of three samples from a single chip at a sample location. Error bars represent the standard deviation. Results were compared using a paired t test. ns indicates $p > 0.05$.*

Next, we measured the permeability of the meningeal lymphatics TEM under static and flow conditions on-chip. Based off of preliminary results, we saw that there was ~1 μg/mL in the LN media for both static and flow conditions after 2 hrs, with no statistical difference between the two conditions (Figure 5.10c). Based off of these results, we conclude that the meningeal lymphatics retains some barrier function, where fluid flow did not negatively impact permeability. Further tests are required to determine if this permeability is sufficient for cell viability of downstream TEMs.

5.5 Conclusions

Here, we describe the development of a 3D-printed multi-media device to co-culture multiple transwell-based engineered models in distinct media compartments. Each media loop had separate fluidic control using the dual-motor impeller pump to achieve biologically relevant flow profiles for each TEM. We designed leak-free culture wells to interface the 3D-printed material with commercially available transwells to enable either flow through or across the TEMs. We developed the barrier-only chip and single-media chip to characterize each individual TEM under flow separately before co-culturing them all together on the dual-media brain-immune chip. In ongoing work, we continue to probe meningeal lymphatics permeability on-chip with recirculating fluid flow in both naive and inflamed (+TNFa) conditions as well as optimize fluid recirculation through cell-laden gel TEMs. In future work, we aim to co-culture the brain,

meningeal lymphatics, and LN paracortex TEMs together to build a platform to study brain-immune interactions in instances of neuroinflammation and neurodegeneration.

5.6 References

1. Yankova, G., Bogomyakova, O. & Tulupov, A. The glymphatic system and meningeal lymphatics of the brain: new understanding of brain clearance. *Reviews in the Neurosciences* **32**, 693–705 (2021).
2. Louveau, A. *et al.* CNS lymphatic drainage and neuroinflammation are regulated by meningeal lymphatic vasculature. *Nat Neurosci* **21**, 1380–1391 (2018).
3. Albayram, M. S. *et al.* Non-invasive MR imaging of human brain lymphatic networks with connections to cervical lymph nodes. *Nat Commun* **13**, 203 (2022).
4. Papadopoulos, Z., Herz, J. & Kipnis, J. Meningeal Lymphatics: From Anatomy to Central Nervous System Immune Surveillance. *J.I.* **204**, 286–293 (2020).
5. Pappolla, M. *et al.* Evidence for lymphatic Aβ clearance in Alzheimer's transgenic mice. *Neurobiology of Disease* **71**, 215–219 (2014).
6. Picollet-D'hahan, N., Zuchowska, A., Lemeunier, I. & Le Gac, S. Multiorgan-on-a-Chip: A Systemic Approach To Model and Decipher Inter-Organ Communication. *Trends in Biotechnology* S0167779920303097 (2021) doi:10.1016/j.tibtech.2020.11.014.
7. Wang, Y. I., Carmona, C., Hickman, J. J. & Shuler, M. L. Multiorgan Microphysiological Systems for Drug Development: Strategies, Advances, and Challenges. *Adv Healthcare Materials* **7**, 1701000 (2018).
8. Hajal, C. *et al.* Engineered human blood–brain barrier microfluidic model for vascular permeability analyses. *Nat Protoc* **17**, 95–128 (2022).

9. Oddo, A. *et al.* Advances in Microfluidic Blood–Brain Barrier (BBB) Models. *Trends in Biotechnology* **37**, 1295–1314 (2019).
10. Park, J. *et al.* Three-dimensional brain-on-a-chip with an interstitial level of flow and its application as an in vitro model of Alzheimer's disease. *Lab Chip* **15**, 141–150 (2015).
11. Huang, Y., Williams, J. C. & Johnson, S. M. Brain slice on a chip: opportunities and challenges of applying microfluidic technology to intact tissues. *Lab on a Chip* **12**, 2103 (2012).
12. Park, J. *et al.* A 3D human triculture system modeling neurodegeneration and neuroinflammation in Alzheimer's disease. *Nat Neurosci* **21**, 941–951 (2018).
13. Trapecar, M. *et al.* Human physiomimetic model integrating microphysiological systems of the gut, liver, and brain for studies of neurodegenerative diseases. *Sci. Adv.* **7**, eabd1707 (2021).
14. Edington, C. D. *et al.* Interconnected Microphysiological Systems for Quantitative Biology and Pharmacology Studies. *Sci Rep* **8**, 4530 (2018).
15. Musgrove, H. B., Cook, S. R. & Pompano, R. R. Parylene-C Coating Protects Resin-3D-Printed Devices from Material Erosion and Prevents Cytotoxicity toward Primary Cells. *ACS Applied Bio Materials* **6**, 3079–3083 (2023).
16. Cook, S. R., Musgrove, H. B., Throckmorton, A. L. & Pompano, R. R. Microscale impeller pump for recirculating flow in organs-on-chip and microreactors. *Lab Chip* **22**, 10.1039.D1LC01081F (2022).
17. Ng, C. P. & Swartz, M. A. Fibroblast alignment under interstitial fluid flow using a novel 3-D tissue culture model. *American Journal of Physiology-Heart and Circulatory Physiology* **284**, H1771–H1777 (2003).

18. Shim, S., Belanger, M. C., Harris, A. R., Munson, J. M. & Pompano, R. R. Two-way communication between ex vivo tissues on a microfluidic chip: application to tumor–lymph node interaction. *Lab on a Chip* **19**, 1013–1026 (2019).
19. Yue, X. *et al.* New insight into Alzheimer's disease: Light reverses Aβ-obstructed interstitial fluid flow and ameliorates memory decline in APP/PS1 mice. *Alzheimer's & Dementia: Translational Research & Clinical Interventions* **5**, 671–684 (2019).
20. Jin, P. & Munson, J. M. Fluids and flows in brain cancer and neurological disorders. *WIREs Mechanisms of Disease* **15**, e1582 (2023).
21. Swartz, M. A. & Fleury, M. E. Interstitial Flow and Its Effects in Soft Tissues. *Annu. Rev. Biomed. Eng.* **9**, 229–256 (2007).
22. Munson, J. & Shieh, A. Interstitial fluid flow in cancer: implications for disease progression and treatment. *CMAR* 317 (2014) doi:10.2147/CMAR.S65444.
23. France, M. M. & Turner, J. R. The mucosal barrier at a glance. *Journal of Cell Science* **130**, 307–314 (2017).
24. Serlin, Y., Shelef, I., Knyazer, B. & Friedman, A. Anatomy and physiology of the blood–brain barrier. *Seminars in Cell & Developmental Biology* **38**, 2–6 (2015).

Chapter 6. Conclusions and Future Directions

6.1 Conclusions

In summary, we developed a customizable, user-friendly multi-organs-on-chip (MOOC) platform for tissue slice and 2D/3D cell culture that connected different tissue models using a simple loop of channels containing recirculating fluid flow. The devices had complex, 3D architecture achievable using resin 3D printing, where the material was made biocompatible using parylene-C coating. Tissue models, either fragile slices or transwell-based engineered models, were easily added and removed from the device through the open culture wells found within each device, resulting in the ability for repeated timecourse imaging. Recirculating fluid flow was achieved using the impeller pump, where a rotating impeller or stir bar within a large cylindrical well generated flow on-chip without the use of tubing. A wide range of biologically relevant speeds were achievable using this pump method by altering the device geometry and size of the rotating stir bar.

In conclusion, this work provided a strong foundation to study multi-organ immunity in the lab using a versatile 3D-printed device and tubing-free impeller pump platform. This technology has the potential to enable future lab members to study communication with the lymph node in the context of vaccination, tumor metastasis, neurodegenerative disease, autoimmunity, and more.

6.2 Future Directions to Address Current Limitations of Impeller Pump and MOOC System

6.2.1 Optimization of flow through the device using computational modeling

In prior work in **Chapter 2**, we developed a computational model to predict fluid speeds and shear stress as a result of impeller rotation. However, there are still many features of the

impeller pump that require optimization, and the use of computational modeling will streamline this process.

6.2.1.1 Reduction of total chip volume

A major challenge when building organs-on-chip is determining which readouts are both relevant for the model and feasible for the device geometry. With the current state of the device design, tissue slices or 3D cell cultures can be removed to assess cell viability, image a range of different markers, or measure gene expression. However, especially with immune cells and tissue, it is important to be able to measure what these tissue models are secreting (e.g. cytokines) following stimulation. A major roadblock for measuring secretions is on-chip dilution, primarily with the large size of the pump well (Table 6.1). When looking at cytokine secretion in murine lymph node slices, it is common to culture an individual slice in 500 µL of media,[1] whereas the 2T multi-tissue chip from **Chapter 4** has a more than three-fold greater fill volume (Table 6.1). With the 2T chip specifically, the geometry was optimized to reduce the fluid flow speed within the channel, and one major way to achieve that is to increase the size of the pump well and increase the channel-well intersection height. Here, we can use a computational model to quickly run a range of pump well and channel geometries to decrease the overall chip volume to be 500 µL or less while maintaining biologically relevant flow speeds.

Table 6.1 Fill volumes for each device.

Device	Pump well diameter (mm)	Impeller	Current fill volume (mL) per media loop
Cell recirculation chip (Ch. 2)[2]	26	Cross impeller	6.4 mL
2T chip for LN slice culture (Ch. 4)	15	5 mm stir bar	1.8 mL
Barrier-only chip (Ch. 5)	15	10 mm stir bar	1.2 mL/loop 2.4 mL total

6.2.1.2 Optimization of device geometry for consistent flow direction

A major challenge since the conception of the impeller pump has been a consistent fluid flow direction. The flow direction is critical for chip function as the tissue culture well for both tissue slices and hydrogel tissue engineered models (TEMs) require an inlet channel at the top of the culture well and an outlet channel below the slice or transwell for transverse perfusion. In addition, we have previously shown that on-chip orientation can impact the timing of molecular drainage, with a faster route of delivery directly through the channels or a delayed route of delivery through the pump well (**Chapter 4**).

The driving force behind impeller pump function is the generation of a vortex within the pump well, which in turn pushes and pulls liquid in the outlet and inlet channels, respectively. As a result, there is a favored fluid flow direction based off of the direction the stir bar rotation (i.e. clockwise stir bar rotation results in clockwise fluid flow on-chip). However, this pump method is sensitive to added resistance in the channel loop, and we hypothesize that a small channel restriction or bubble within the channels may cause the fluid flow direction to change. We recently attempted to address this issue by generating an enlarged inlet within the barrier-only chip to catch more rotating fluid in the pump well and encourage fluid direction one way over the other. Based off of preliminary results, this method significantly helped drive fluid flow one way consistently (Figure 6.1), but we have found that this is not enough for consistent fluid flow direction in other device designs.

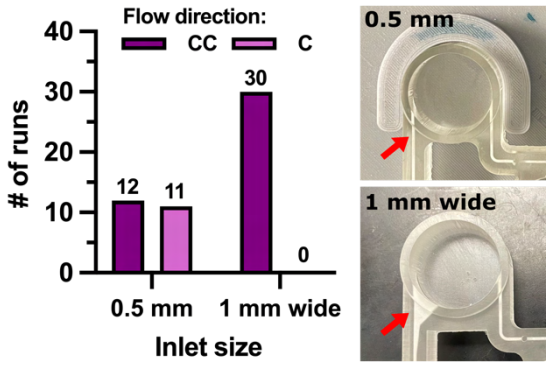

Figure 6.1 Fluid flow direction can be variable dependent on the device geometry. *With a stir bar rotating counterclockwise, fluid flow was fluctuating between counterclockwise (CC) and clockwise (C) with a standard 0.5 mm inlet, but went consistently CC with a widened 1 mm inlet.*

A challenge with measuring flow direction is that it may be consistent the first few times tested, but will switch flow directions in later, more critical, experiments. The use of a computational model can help with rapid testing of different geometries as well as combinations of geometries to predict the best method for consistent flow direction. In addition to the enlarged inlet, we propose a channel geometry where the inlet channel is intersecting the pump well much closer to the rotating stir bar and the outlet channel is closer to the top of the well to make one flow direction much more favorable over the other (Figure 6.2). In addition, check valves can be incorporated within the device to increase the resistance in the less-desired flow direction.

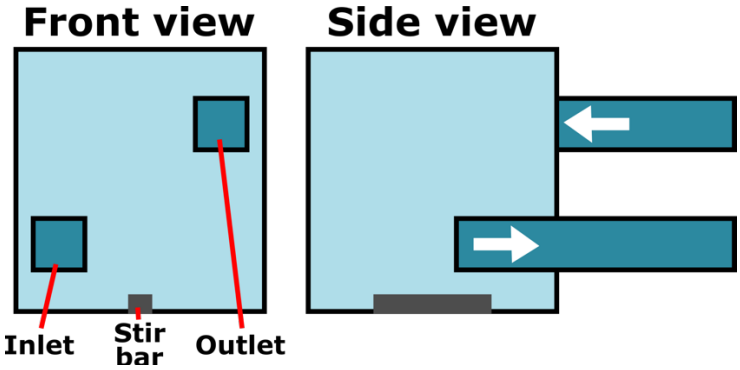

Figure 6.2 Proposed channel geometry to drive flow reproducibly in one direction.

6.2.1.3 Limit shear stress from stir bar rotation for immune cell recirculation

A major goal with this technology is the ability to recirculate immune cells on-chip. However, even with the help of parylene-C coating, the stir bar rotation was cytotoxic for recirculating murine splenocytes, with decreased cell viability at faster rotational speeds (Figure 6.3). We hypothesize that this is due to the high shear stress surrounding the rotating impeller or stir bar, where there is a rotations per minute (RPM) of 700 or greater. It is incredibly challenging to predict the shear stress surrounding the rotating impeller, and in previous work, we utilized a computational model that predicted the shear stress surrounding the 3D-printed cross impeller ranged from 100-400 dyn/cm^2, where physiological shear stress ranges from 0.6-12 dyn/cm^2 for lymphatic vessels and 0.35-70 dyn/cm^2 for blood vessels (**Chapter 2**).[2] Through the use of an updated computational model, we can optimize the pump conditions (impeller RPM, chip geometry, etc.) to either decrease the impeller/stir bar shear stress or create a geometry that encourages limited contact between recirculating cells and the rotating stir bar. We predict that, to start, a slower stir bar rotational speed would decrease the shear stress surrounding the rotating stir bar, which would also provide a means to decrease the pump well volume while maintaining physiological flow speeds.

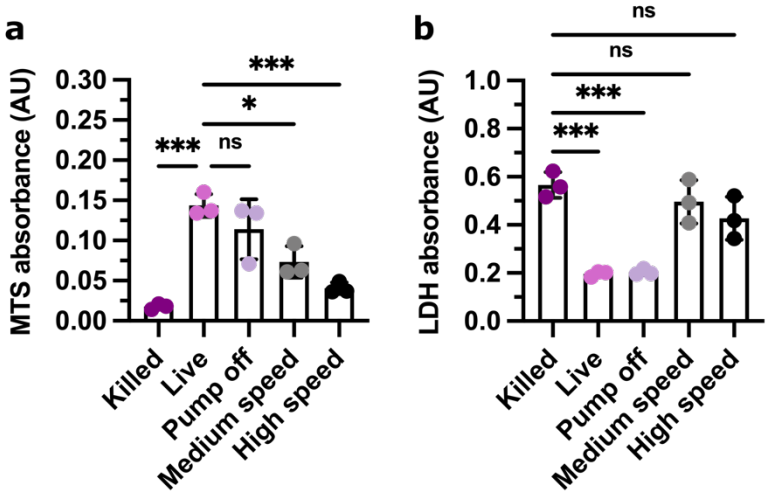

Figure 6.3 Stir bar rotation is cytotoxic to recirculating immune cells after 24 hr culture. *(a) MTS assay absorbance and (b) LDH assay absorbance of primary murine splenocytes cultured off-chip and in parylene-coated 2T chips with no stir bar rotation (pump off), medium pump*

*speed (V = 1.4 V), and high pump speed (1.7 V). Assay results were compared using a one-way ANOVA with Tukey post-hoc tests (n = 6). ns indicates p > 0.1, * indicates p < 0.02, *** indicates p < 0.0007. Each dot represents one sample. Error bars represent standard deviation.*

6.2.2 Adjust removable mesh design to drive fluid flow through lymph node slices at biologically relevant speeds

To build a biomimetic organs-on-chip model using lymph node slices, we aimed to drive fluid flow transversely through the tissue slice at a fluid velocity similar to interstitial fluid flow found *in vivo.* However, it was challenging to drive flow through slices using the multi-tissue chip when paired with the impeller pump (**Chapter 4**). The removable mesh support was designed to leave gaps around a tissue slice to limit the resistance added to the fluidic loop. As a result, the computational models predicted that the flow through the slice was incredibly low if fully negligible as a feature of tissue permeability (more permeable = higher fluid velocity in tissue). Here, we aim to resolve this issue by optimizing the removable mesh support design to encourage fluid to pass through a LN slice at biologically relevant speeds without adding enough resistance to cause pump failure. Changes to the geometry could include decreasing the gaps around the slice or removing them altogether, or altering the pump well and channel geometry to drive flow faster through the channels. We can rapidly test different iterations using the established 3D finite element modeling (**Chapter 4**) and confirm fluid recirculation experimentally by injecting dye in the channels in the presence of mock tissue.

6.2.3 Modification and commercialization of impeller pump external housing

Since conception in the summer of 2019, the impeller pump platform has undergone many alterations to decrease pump size and improve reproducible assembly. When switching from the original computer fan-based design (**Chapter 2**) to a motor-based design with printed housing (**Chapter 4**), the overall pump footprint decreased 2-fold. However, the current design,

both the single-motor and dual-motor design, use a fully printed housing, lid included, and when the seal was epoxied, as in **Chapter 4**, it is impossible to open the pump box to do routine maintenance and fix any issues that may come up. To address this issue, we designed an updated housing that used laser-cut acrylic lids with a rubber gasket as a lid (Figure 6.4-5).

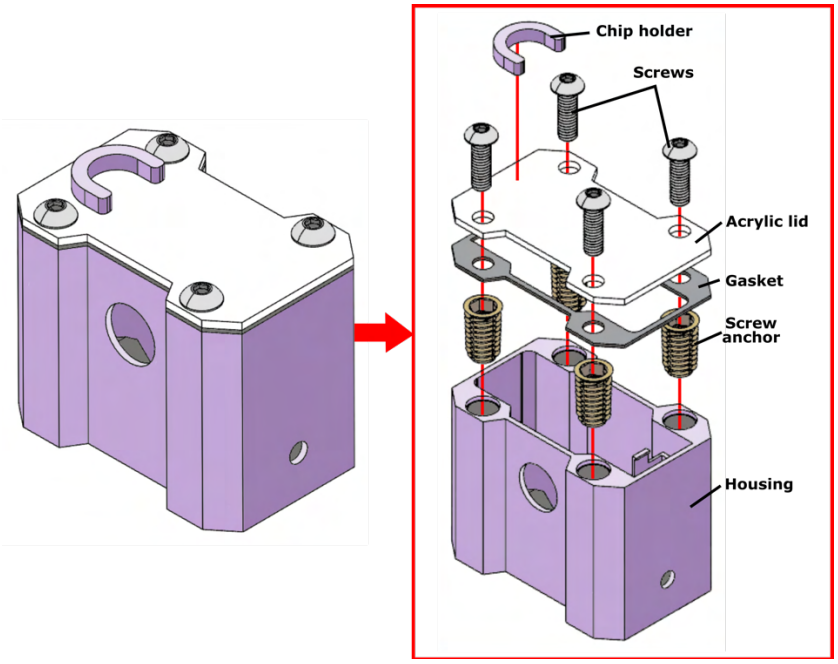

Figure 6.4 Assembly of single-motor pump with acrylic lid.

To guarantee a long-lasting use, we inserted screw anchors into the printed base in lieu of designing threaded holes in the base itself. The acrylic lid was screwed into the pump base, allowing for easy access to the motor circuit inside (Figure 6.4). The lid-based design was incorporated for both the single-motor and dual-motor pump design (Figure 6.5a) and incorporated a switch on the side to enable users to turn the pump on and off easily (Figure 6.5b).

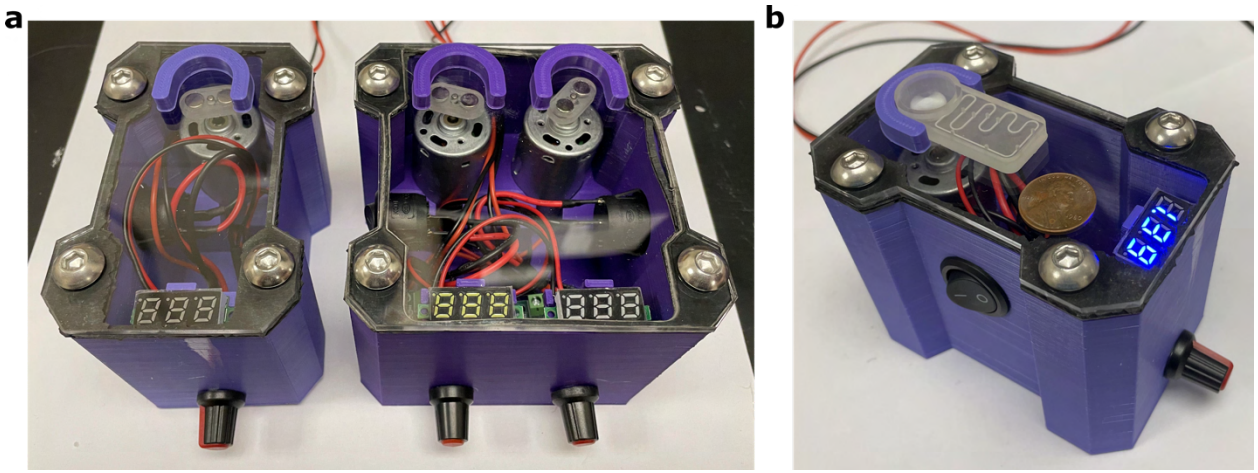

Figure 6.5 Updated impeller pump housing with acrylic removable lids. *(a) Image of a single-motor pump (left) and a dual-motor pump (right). (b) Image of a single-motor pump at 1.39 V with a device resting in the chip holder. A US penny was included for scale.*

While the acrylic lid-based design solved one issue, namely being able to open the pump to perform maintenance, there are still additional areas for improvement. First, certain elements of the motor circuit can be replaced to improve ease of use and decrease pump size. The current potentiometer is single-turn, which means that a minor adjustment of the external knob could result in a drastic change in pump voltage. Replacing this part with a 10-turn potentiometer would imrpove sensitivity while making pump channel velocities more reproducible between rounds (i.e. consistently 1.30 V instead of 1.29 V – 1.35 V). In addition, the DC motor can be replaced with either a motor or computer fan that is both smaller in size and has a wider range of rotational speeds. The motor that is currently used was selected specifically to limit heat output, and while it is smaller than the computer fans used in the initial design, there are much smaller motor options available. As for rotational speeds, the motor has a minimum voltage before it will begin to rotate which achieved an RPM of ~700, where the initial computer fan minimum RPM was ~500. This issue can be mitigated by switching to a motor with a lower RPM range, though this is likely to introduce more heat in the system. We plan to screen multiple motor or computer fan options for wide (and low) RPM range, low tempterature output, and small size. Computer

fans may be a good alternative as they have a low heat output and come in a wide range of sizes, but their speed capabilities are unclear without further testing. Once elements of the motor circuit are replaced/reduced, the pump housing can be redesigned to accomodate the new parts and the open space can be decreased to improve pump footprint.

Next, once we have a finalized pump housing design, we can begin to transition to commercially available manufacturing, i.e. injection molding. The current lengthy print time for the pump housing limits the amount of pumps than can be made at a time, where the single-motor pump box takes ~1 day to print and the dual-motor pump box takes ~2 days to print. This may work in some settings if a lab contains many FDM printers, but that is not commonplace. The circuit assembly takes 1-2 hrs, even when making 6-12 circuits, so the lengthy print time is the limiting factor as far as pump scale up is concerned. The next step would be to transition fabrication to injection molding, where we would outsource fabrication to a manufacturing company, where the major barrier for this fabricaiton method is cost. The individual pieces will have a low cost ($7.97 - $8.44), but the mold(s) developed for the injection molding process drives up the cost considerably, with mold costs ranging from $19,000 to $29,000 (Table 6.2). If this cost barrier can be overcome, the next step would be to outsource the motor circuit assembly and insertion into the pump housing. This process would enable users to just submit an order online and have fully assembled pumps delivered. This would extend the potential reach for the impeller pump system to many other collaborators, where we are currently responsible for pump assembly for any user. This process may result in an increase in pump cost, but we predict it will still be affordable compared to many commercially available alternatives.

Table 6.2 Approximate cost of molds and individual parts for impeller pump housing manufacturing using injection molding. *Prices based off of quote from ProtoLabs.*

Item	Cost
Prototype mold	$19,195
On-demand manufacturing mold	$28,790
Individual part	$7.97 - $8.44
Total for 100 parts	$20,040 - $29,590

6.2.4 Translate multi-tissue chip for scale-up microfabrication techniques

The current fabrication method for all chips described has been digital light processing (DLP) 3D printing, which is a viable method to quickly prototype devices with complex 3D geometry and maintains cell and tissue viability for at least 24 hrs with parylene-C coating (**Chapter 3** and **4**). This fabrication technique lends itself to small-batch fabrication, where 2-4 devices can be printed at a time in < 1 hr. However, these devices are prone to delamination after repeated use (3-5 times), where cracks begin to form within the material even with parylene-C coating. This may lead to toxins leaching from the device even with the biocompatible coating, or generate leaks within the device. Due to the limited reusability and small-batch nature of DLP 3D printing, we aim to translate the devices for tissue slice and tissue engineered models to CNC machining or injection molding fabrication techniques, where the device would be fully reusable with the ability to easily manufacture many device replicates. Changing to a new fabrication method would likely require a redesign of different features of the device, though it would use fully biocompatible plastics and would be more accessible for collaborators in biological fields where they can just purchase a set of chips instead of repeated 3D printing and coating steps.

6.2.5 Expand mock skin to generate a robust vaccination model on-chip

In **Chapter 4**, we used the multi-tissue chip to model a vaccine injection draining to the LN by co-culturing vaccinated mock skin with a LN slice in the 2T device. However, these initial experiments used a simplified skin model: soft hydrogel. Vaccine drainage to local LNs is dependent on size, where 20-100 nm particles will easily enter the lymphatic vascular, where the lymph flow will carry the molecules to local LNs. However, larger molecules, typically >500 nm, cannot drain to LNs alone and are picked up by tissue-resident immune cells and carried to LNs.[3,4] The current hydrogel-only model would be sufficient to model smaller vaccines and would limit the vaccines screened on-chip in the future. To address this issue, we can incorporate immune cells (e.g. dendritic cells) within the mock skin hydrogel where, once optimized, the immune cells can pick up larger vaccine components and drain on-chip to the downstream LN slice (Figure 6.6a). As vaccine size dictates drainage method *in vivo*, the mock skin model can be tested with a range of sizes of adjuvant to test drainage method, i.e. passively diffusing out with <100 nm molecules and cell-assisted delivery for >500 nm molecules.

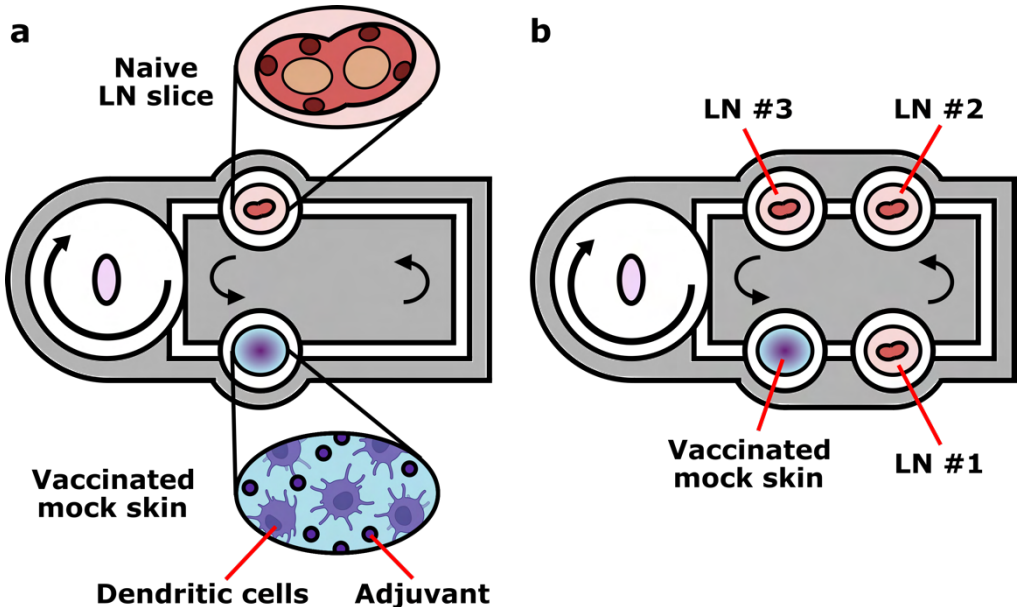

Figure 6.6 Expansion of mock skin in vaccination model. *(a) Schematic of a mock skin gel model (blue) containing skin-resident dendritic cells and adjuvant co-cultured with a downstream naive lymph node (LN) slice using the 2T device. (b) Schematic of vaccine from mock skin co-cultured with a daisy-chain of downstream LN slices using the 4T device.*

Once the mock skin model incorporates more biomimetic elements (i.e. immune cells), we can add additional LN slices on-chip to better mimic the chains of LNs found *in vivo*. LNs are found throughout the body, where humans have 500-600 and mice have 22-38.[5–7] With a vaccine injection in the skin or muscle, the draining LN closest to the injection site will receive the strongest vaccine dose, however other LNs in the region will also see the vaccine, albeit a more dilute amount. We can model this process using the four-tissue (4T) device, where the vaccinated mock skin would be inserted into the upstream culture well, and three LN slices would be added to the downstream culture wells in a daisy chain (Figure 6.6b). Based off of this layout, we hypothesize that the LN closest to the mock skin (LN #1) would be activated much faster as it receives the vaccine first, with a sequential delay for each downstream tissue (LN #2 and 3).

6.2.6 Generate a murine brain-immune chip using brain and lymph node slices

When incorporating models of the lymph node in organs-on-chip models, it is critical to decide which feature is the most relevant for the proposed question: 1) maintain spatiotemporal organization native to LN structure *in vivo* using murine LN slices, and 2) use human-based TEMs for clinical relevancy. In **Chapter 5**, we build towards a brain-immune chip using human TEMs, where the LN model is comprised of stromal cells in gel with a lymphatic endothelial cell (LEC) monolayer. This TEM is a simple representation of the paracortex within the LN, lacking other cell types (macrophages, T cells, B cells, etc.) and organization (sinus, B cell follicle, etc.) found *in vivo*. In the Pompano lab, we are currently developing a technique to slice portions of human tonsil tissue (lymph nodes commonly removed from patients) to retain tissue organization. However, this process is relatively new, and is not yet translatable for on-chip

culture. As a result, we aim to use murine LN and brain slices to generate a brain-immune chip that retains spatial organization.

Prior work described in **Chapter 4** established a method to culture LN slices on-chip. Here, the main challenge is to develop a culture system for murine brain slices. Brain tissue is highly sensitive to oxygen. As a result, a common culture method within organs-on-chip is to keep the brain slices at an air-liquid interface,[8] where nutrients and molecular signals are delivered passively from the liquid below the slice while the top surface of the slice is exposed to the air (Figure 6.7). This would require optimization of the removable mesh design to support the fragile brain tissue while allowing for enough contact with the media flowing below. In addition to slice optimization, any barrier used between brain and LN slices on-chip would have to be made using mouse cells, a process currently underway within the Munson lab with the meningeal lymphatics TEM. Once developed, this model can be used to model diseases like Alzheimer's (AD) or Multiple Sclerosis (MS) similar to the human brain-immune chip, with one key advantage: incorporation of tissue slices from murine disease models. For MS specifically, experimental autoimmune encephalomyelitis (EAE) has been commonly used to model some features of the disease within mice.[9] While this animal model has its limitations, the brain or LN tissue from an EAE mouse would be a good place to begin when building an MS model on-chip.

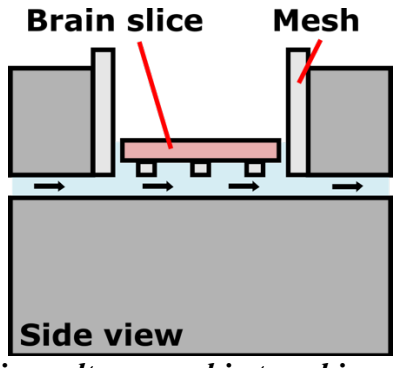

Figure 6.7 Flow path of brain slice culture on-chip to achieve an air-liquid interface.

6.3 Future Applications of the Brain-Immune MOOC

6.3.1 Model features of Alzheimer's disease on-chip by co-culturing human Alzheimer's brain, meninges, and lymph node TEMs in dual-media brain-immune chip

The work described in **Chapter 5** was building towards a dual-media device to co-culture engineered models of brain, meningeal lymphatics, and LN paracortex to model brain-immune interactions. Once the individual engineered models are characterized under flow on-chip using the single-media chip and the barrier-only chip, we can bring them all together within a single device under both naive and disease conditions. While there are many different neuroinflammatory and neurodegenerative diseases that involve the immune system, we will start with a model of Alzheimer's disease (AD), where hallmarks of the disease include the formation of amyloid-ß plaques, reduced waste clearance and interstitial fluid flow in the brain parenchyma, and the formation of neurofibrillary Tau tangles.[10–12] Immunity can either be beneficial or detrimental to the outcome of AD. Brain-resident immune cells called microglia have been found to clear damaging Aß or remain chronically active, which results in increased neurodegeneration in later stages of the disease.[10,13] While there has been many studies on the involvement of immune cell infiltration in AD, little is known about the role of the LN in neurodegenerative diseases. A study from Pappolla et al. found increasing levels of drained Aß oligomers in the cervical and axillary LNs over time, similar to the increased Aß present in the brain in early stages of AD, however, it is still unknown how this influences the LN function.[14] Here, we aim to model AD on-chip by including two major features: 1) AD brain TEM established previously by the Munson lab, and 2) reduced brain interstitial flow speeds by decreasing the channel speed in the brain media loop (R) (Figure 6.8).

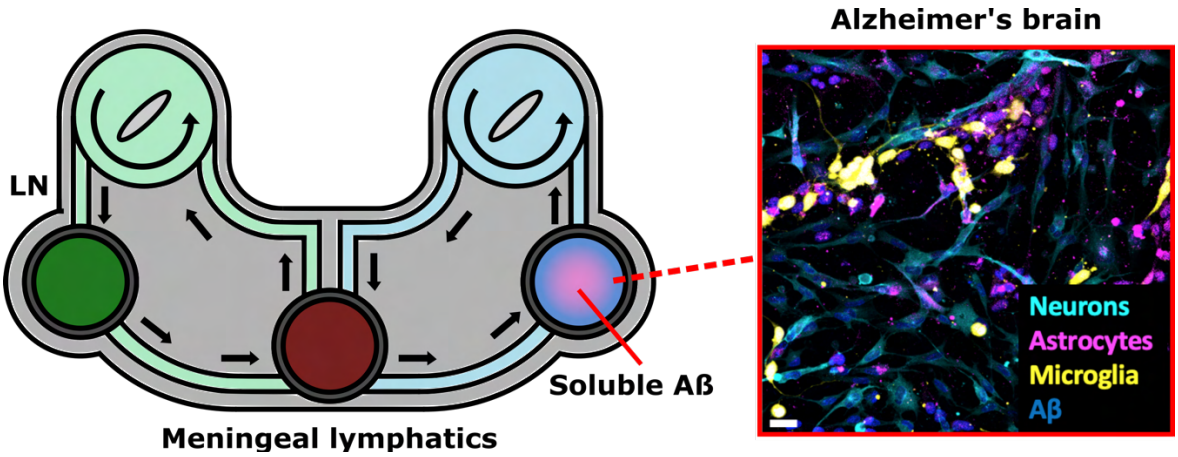

Figure 6.8 Brain-immune chip to model Alzheimer's disease. *A schematic of LN, meningeal lymphatics, and Alzheimer's brain TEM co-cultured on-chip. Fluorescent image (right) of AD brain TEM with neurons in cyan, astrocytes in magenta, microglia in yellow, and Aß in dark blue (provided by Dr. Kinsley Tate, Munson lab).*

The AD brain-immune chip is similar in design to the naive brain-immune chip proposed in **Chapter 5**, where we include an Alzheimer's brain model containing a triculture of microglia, astrocytes, and patient-derived neurons dosed with amyloid oligomers or plaques (Figure 6.8). We aim to model a reduction of interstitial flow by adding the plug in the meningeal lymphatics culture well and reducing the channel speed to 450 µm/s as described in **Chapter 5**, resulting in a drop in brain gel velocity from 5-10 µm/s (naive brain) to <1 µm/s (AD brain) (Figure 5.5-5.6). Using this platform, we can model the drainage of Aß from the AD brain model through the meningeal lymphatics to the LN paracortex on-chip (Figure 6.9). Based off of the plug-and-play nature of the device, we can also selectively inflame different tissue models off-chip and co-culture them with naive TEMs to study the impact of Aß drainage. For example, we can measure how much Aß drains to the LN model with a naive meningeal barrier and with a leaky inflamed barrier. In addition, we can begin to probe the downstream effects of Aß within the LN model by measuring immune cell activation and cytokine secretion.

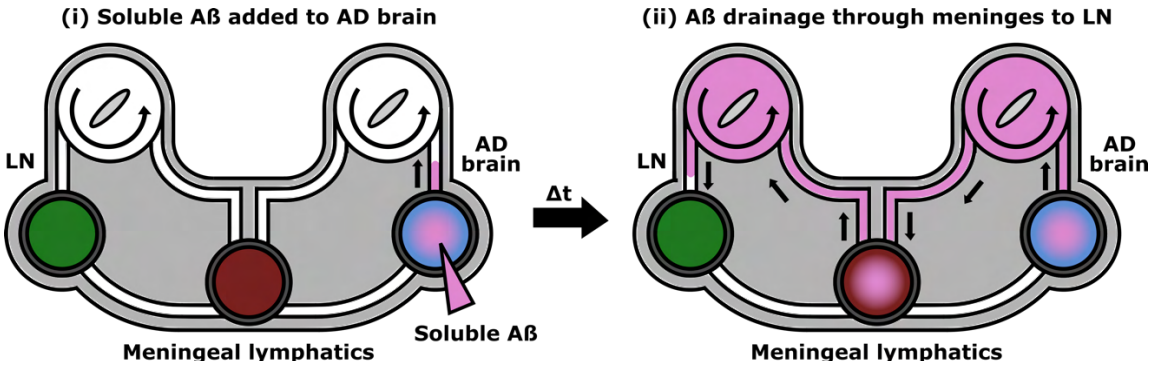

Figure 6.9 Workflow of Amyloid-ß (Aß) drainage from AD brain to LN on-chip. *When co-culturing the AD brain TEM with the meningeal lymphatics and LN TEM, (i) soluble Aß will be added to the brain TEM where (ii) it will pass through the meningeal lymphatics barrier and drain to the LN TEM.*

6.3.2 Develop four-tissue device to co-culture human brain, meningeal lymphatics, blood-brain barrier, and lymph node TEMs to model immune cell infiltration into the CNS in instances of neuroinflammation

The environment within the brain is heavily regulated to maintain normal brain function.[15,16] To maintain this, the brain is essentially separated from the rest of the body through various cellular barriers, one of them being the blood-brain barrier (BBB), a cellular roadblock lining the blood vessel capillaries within the brain and spinal cord. Under naive conditions, the BBB restricts passage of potentially harmful immune cells recirculating in the blood. However, in states of inflammation, the tight junctions between endothelial cells break down, allowing immune cells to infiltrate into the brain parenchyma (Figure 6.10a). Prior work focused on the pathway from the brain to the lymph node through the meningeal lymphatics, which is of particular interest in neurodegenerative diseases like Alzheimer's where brain antigens have been shown to drain to deep cervical lymph nodes.[17] In autoimmune diseases such as MS, immune cell infiltration and demyelination is a key feature as the disease progresses.[18] Here, we aim to build a transwell model of the BBB and incorporate it into the existing dual-media brain-

immune chip to model communication from the lymph node to the brain, with a particular focus on immune cell infiltration in instances of inflammation.

To develop a BBB transwell model, we will culture astrocytes and pericytes in collagen-fibrinogen hydrogel in a transwell with a brain endothelial cell (EC) monolayer on the base of the transwell membrane (Figure 6.10b), a layout similar to existing BBB models.[19] With this layout, the "blood"-like fluid would be below the transwell, while the "CSF"-like fluid would be above the transwell. We plan to confirm barrier function using the fluorescent dextran permeability assay described in **Chapter 5** as well as measuring the transendothelial electrical resistance (TEER) across the barrier.

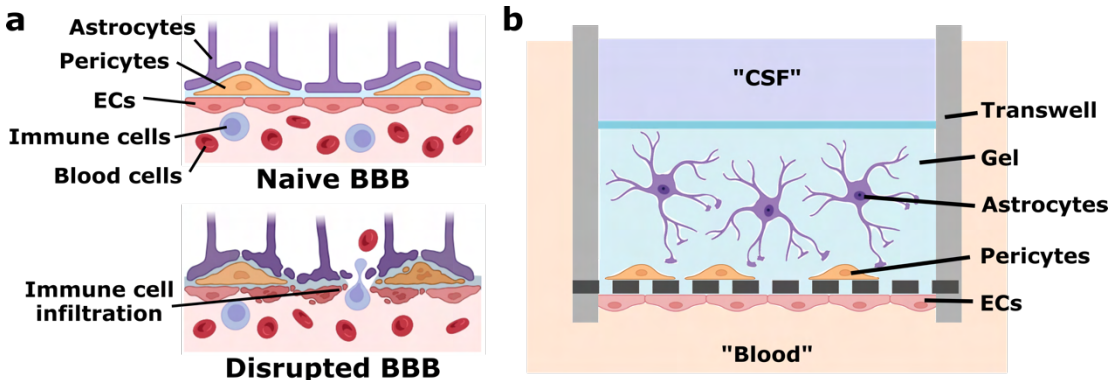

Figure 6.10 Blood-brain barrier (BBB) TEM. *(a) In naive conditions, the BBB is a selective barrier that limits immune cell entry into the CNS. When disrupted, the BBB becomes permeable, allowing immune cell infiltration (Created using BioRender.com). (b) The BBB tissue-engineered model would consist of a hydrogel containing astrocytes and pericytes within the transwell with a brain endothelial cell (EC) monolayer on the base of the transwell membrane (Cell cartoons from BioRender.com).*

Once the BBB TEM retains barrier function off-chip, we will first culture it under fluid flow conditions using the barrier-only chip, where the "blood" fluid would recirculate in the left media loop (red) and the "CSF" fluid would recirculate in the right media loop (blue) (Figure 6.11). Here, we can compare barrier function using dextran permeability and TEER in both naive and inflammatory (+ TNFa) conditions as well as test the passage of different therapeutics across the barrier.

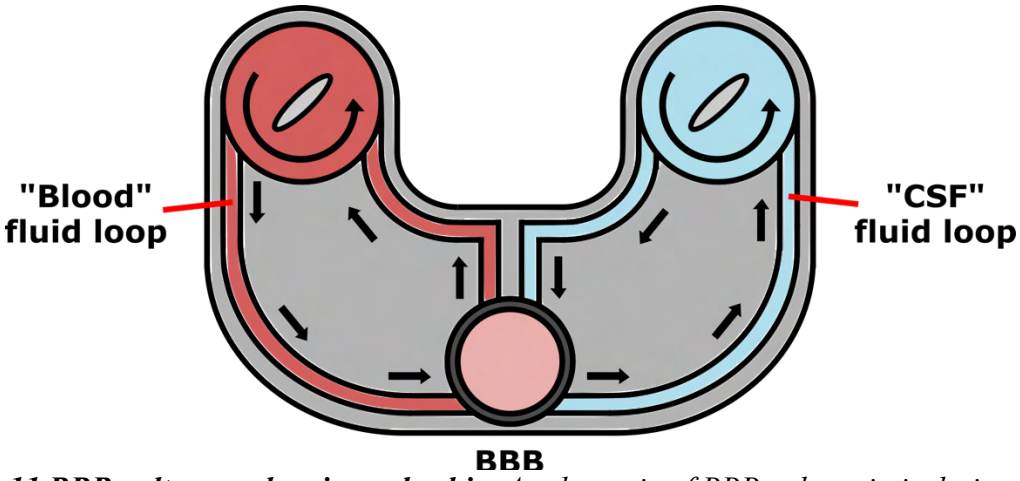

Figure 6.11 BBB culture on barrier-only chip. *A schematic of BBB culture in isolation on the barrier-only chip, where the "blood" fluid loop (L) would pass below the transwell and the "CSF" fluid loop (R) would pass above the transwell.*

Next, we will culture the BBB TEM on a four-tissue dual-media device where the meningeal lymphatics TEM and BBB TEM will act as barriers between both the LN paracortex TEM and brain TEM (Figure 6.12). Within the LN media compartment, the culture wells are arranged to enable fluid flow to pass from the meningeal lymphatics to the LN paracortex (brain antigens draining to local lymph nodes), then on to the BBB model (immune cell trafficking from the LN to the brain). Similarly, in the brain compartment, the flow passes from the BBB to the brain (delivery of nutrients or infiltrating immune cells into the brain), then on to the meningeal lymphatics (lymphatic clearance of the brain).

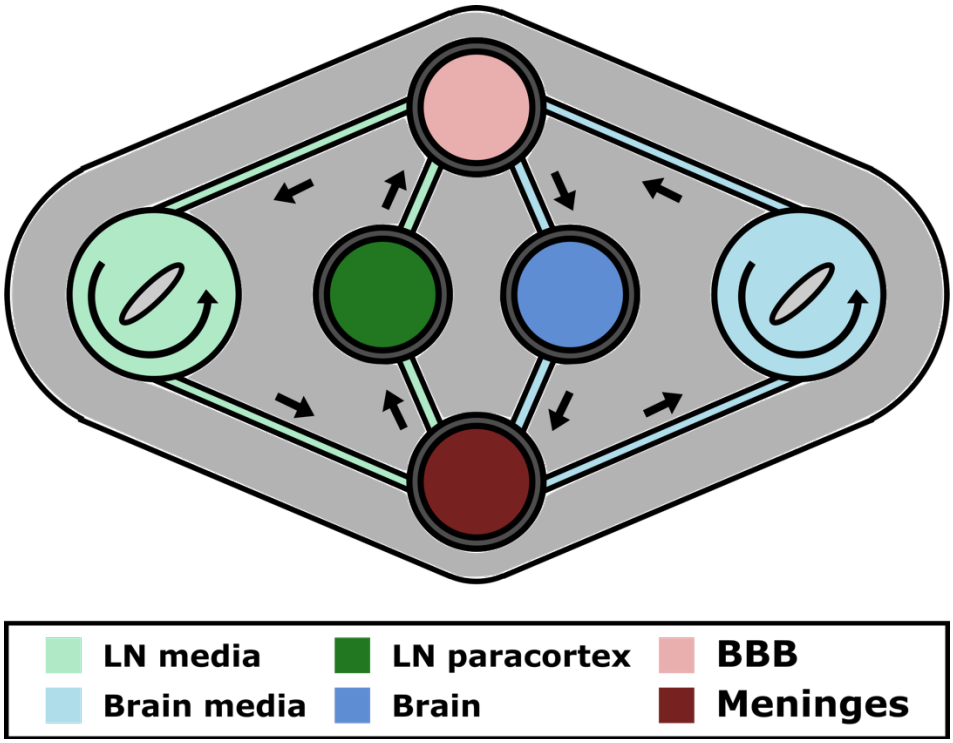

Figure 6.12 Co-culture of four organ models to study brain-immune interactions. *A schematic of the four-tissue chip with the co-culture of brain, meningeal lymphatics, BBB, and LN.*

Once established, this device can be used to model immune cell infiltration by recirculating immune cells in the LN media loop (L) in both naive and inflammatory conditions. In addition, we can build towards a MS-on-chip model by incorporating primary cells from MS patients in the engineered models, similar to the Alzheimer's brain TEM developed in the Munson lab. With the development of models of autoimmunity that incorporate models of primary immune organs like the lymph node, we can begin to understand the development and progression of autoimmune diseases as well as develop and test more effective therapeutics. Additional tissue models can be incorporated within the LN media loop where relevant, such as a gut model to mimic the gut-immune-brain axis involved in neuroinflammatory diseases.[20]

6.3 References

1. Belanger, M. C. *et al.* Acute Lymph Node Slices Are a Functional Model System to Study Immunity Ex Vivo. *ACS Pharmacol. Transl. Sci.* **4**, 128–142 (2021).
2. Cook, S. R., Musgrove, H. B., Throckmorton, A. L. & Pompano, R. R. Microscale impeller pump for recirculating flow in organs-on-chip and microreactors. *Lab Chip* **22**, 10.1039.D1LC01081F (2022).
3. Roozendaal, R. *et al.* Conduits Mediate Transport of Low-Molecular-Weight Antigen to Lymph Node Follicles. *Immunity* **30**, 264–276 (2009).
4. Roth, G. A. *et al.* Designing spatial and temporal control of vaccine responses. *Nat Rev Mater* **7**, 174–195 (2021).
5. Grant, S. M., Lou, M., Yao, L., Germain, R. N. & Radtke, A. J. The lymph node at a glance – how spatial organization optimizes the immune response. *Journal of Cell Science* **133**, jcs241828 (2020).
6. Ozulumba, T., Montalbine, A. N., Ortiz-Cárdenas, J. E. & Pompano, R. R. New tools for immunologists: models of lymph node function from cells to tissues. *Front. Immunol.* **14**, 1183286 (2023).
7. Van Den Broeck, W., Derore, A. & Simoens, P. Anatomy and nomenclature of murine lymph nodes: Descriptive study and nomenclatory standardization in BALB/cAnNCrl mice. *Journal of Immunological Methods* **312**, 12–19 (2006).
8. Huang, Y., Williams, J. C. & Johnson, S. M. Brain slice on a chip: opportunities and challenges of applying microfluidic technology to intact tissues. *Lab on a Chip* **12**, 2103 (2012).

9. Gold, R. Understanding pathogenesis and therapy of multiple sclerosis via animal models: 70 years of merits and culprits in experimental autoimmune encephalomyelitis research. *Brain* **129**, 1953–1971 (2006).
10. Jorfi, M., Maaser-Hecker, A. & Tanzi, R. E. The neuroimmune axis of Alzheimer's disease. *Genome Med* **15**, 6 (2023).
11. Silva, I., Silva, J., Ferreira, R. & Trigo, D. Glymphatic system, AQP4, and their implications in Alzheimer's disease. *Neurol. Res. Pract.* **3**, 5 (2021).
12. Zhang, F. & Jiang, L. Neuroinflammation in Alzheimer's disease. *NDT* 243 (2015) doi:10.2147/NDT.S75546.
13. Doty, K. R., Guillot-Sestier, M.-V. & Town, T. The role of the immune system in neurodegenerative disorders: Adaptive or maladaptive? *Brain Research* **1617**, 155–173 (2015).
14. Pappolla, M. *et al.* Evidence for lymphatic Aβ clearance in Alzheimer's transgenic mice. *Neurobiology of Disease* **71**, 215–219 (2014).
15. Kadry, H., Noorani, B. & Cucullo, L. A blood–brain barrier overview on structure, function, impairment, and biomarkers of integrity. *Fluids Barriers CNS* **17**, 69 (2020).
16. Serlin, Y., Shelef, I., Knyazer, B. & Friedman, A. Anatomy and physiology of the blood–brain barrier. *Seminars in Cell & Developmental Biology* **38**, 2–6 (2015).
17. Louveau, A. *et al.* Structural and functional features of central nervous system lymphatic vessels. *Nature* **523**, 337–341 (2015).
18. Ransohoff, R. M., Schafer, D., Vincent, A., Blachère, N. E. & Bar-Or, A. Neuroinflammation: Ways in Which the Immune System Affects the Brain. *Neurotherapeutics* **12**, 896–909 (2015).

19. Katt, M. E., Linville, R. M., Mayo, L. N., Xu, Z. S. & Searson, P. C. Functional brain-specific microvessels from iPSC-derived human brain microvascular endothelial cells: the role of matrix composition on monolayer formation. *Fluids Barriers CNS* **15**, 7 (2018).
20. Carabotti, M., Scirocco, A., Maselli, M. A. & Severi, C. The gut-brain axis: interactions between enteric microbiota, central and enteric nervous systems. *Annals of Gastroenterology*.